Microvesicles and Migratory Heterogeneity in Breast Cancer Progression

By

Samantha Christine Schwager

Dissertation

Submitted to the Faculty of the

Graduate School of Vanderbilt University

in partial fulfillment of the requirements

for the degree of

DOCTOR OF PHILOSOPHY

in

Biomedical Engineering

May 13th, 2022

Nashville, Tennessee

Approved:

Cynthia A. Reinhart-King, Ph.D.

Marjan Rafat, Ph.D.

W. David Merryman, Ph.D.

Robert Coffey, M.D.

Alissa Weaver, M.D., Ph.D.

Francois Bordeleau, Ph.D.

ACKNOWLEDGEMENTS

TABLE OF CONTENTS

LIST OF FIGURES

LIST OF TABLES

LIST OF ABBREVIATIONS

18-FDG	Fluorodeoxyglucosse F 18
2-DG	2-Deoxy-D-glucose
2-NBDG	2-(N-(7-Nitrobenz-2-oxa-1,3-diazol-4-yl)Amino)-2-Deoxyglucose
2D	2-dimensional
3D	3-dimensional
3T3	NIH 3T3 mouse embryonic fibroblast
A_{50}	Half the maximum area of the cell
ADP	Adenosine diphosphate
AFM	Atomic force microscopy
AMA	Antimycin-A
ANOVA	Analysis of variance
αSMA	Alpha smooth muscle actin (protein)
ACTA2	Alpha smooth muscle actin (gene)
ARF6	ADP Ribosylation Factor 6
Arp2/3	Actin-related proteins-2/3
ATP	Adenosine triphosphate
CAF	Cancer-associated fibroblast
CAT	Collective-to-amoeboid transition
Cav-1	Caveolin-1
CMAC	Cell-matrix adhesion complex
COL1	Collagen 1
CT	Computerized tomography
Ctrl	Control
DAPI	4',6-diamidino-2-phenylindole
Dbl	Diffuse B-lymphoma
ECM	Extracellular matrix
EdU	5-ethynyl-2'-deoxyuridine
EGF	Epidermal growth factor
EMT	Epithelial-mesenchymal transition
ER	Estrogen receptor
ERK	Extracellular signal-regulated kinase
ETC	Electron transport chain

EV	Extracellular vesicle
FAK	Focal adhesion kinase
Fap	Fibroblast activation protein
FBS	Fetal bovine serum
FLIM	Fluorescent lifetime imaging microscopy
Flot-2	Flotillin-2
Fn1	Fibronectin-1
FRET	Förster resonance energy transfer
FUW	Empty lentiviral backbone
GAPDH	Glyceraldehyde-3-phosphate dehydrogenase
GFP	Green fluorescent protein
GLUT	Glucose transporter
GTP	Guanosine triphosphate
HeLa	Immortal cervical cancer cell line
HEPES	4-(2-hydroxyethyl)-1-piperazineethanesulfonic acid
HIF-1	Hypoxia-inducibe factor
HSP	Heat shock protein
HRP	Horseradish peroxidase
IA	Iodoacetate
IDH	Isocitrate dehydrogenase
IκBα	Nuclear factor of kappa light polypeptide gene enhance in B-cell inhibitor, alpha
LIMK	Lim kinase
LOX	Lysyl oxidase
LSM	Laser scanning microscope
MAT	Mesenchymal-to-amoeboid transition
MCF10A	Human breast epithelial cell
MCF7	Human invasive breast ductal carcinoma, ER+, PR+, HER2- (luminal A)
MCT	Monocarboxylate transporter
MDA-MB-231	Human triple negative mammary adenocarcinoma
MDA$^+$	Highly migratory subpopulation of MDA-MB-231
MDA$^-$	Weakly migratory subpopulation of MDA-MB-231
miRNA	microRNA
MK2	Mitogen-activated protein kinase-activated protein kinase 2
MLC	Myosin light chain

MLCK	Myosin light chain kinase
MMP	Matrix metalloproteinase
MRI	Magnetic resonance imaging
mRNA	Messenger RNA
MT-MMP	Membrane-type matrix metalloproteinase
MV	Microvesicle
MV^+	MV isolated from MDA^+
MV^-	MV isolated from MDA^-
MVB	Multivesicular body
NaOH	Sodium hydroxide
OSCC	Oral squamous cell carcinoma
OxPhos	OxPhos
PA	Polyacrylamide
PBS	Phosphate buffered saline
PCG-1α	Peroxisome proliferator-activated receptor-gamma coactivator-1 alpha
Pdgfr	Platelet-derived growth factor receptor
PDH	Pyruvate dehydrogenase
PEI	Polyethylenimine
pFAK	Phosphorylated focal adhesion kinase
PET	Positron emission tomography
PLD	Phospholipase D
Postn	Periostin
PPP	Pentose Phosphate Pathway
PYR	Pyruvate
qRT-PCR	Quantitative real time polymerase chain reaction
Rac1	Ras-related C3 botulinum toxin substrate 1
ROCK	Rho-associated protein kinase
ROS	Reactive oxygen species
scr	Scrambled control vector
SEM	Standard error of the mean
shTg2	Short hairpin RNA targeting Tg2
SUM159PT	Human triple negative breast cancer cell line
SUM^+	Highly migratory subpopulation of SUM159PT
SUM^-	Weakly migratory subpopulation of SUM159PT

T101	Cell impermeable inhibitor of Tg2
T47D	Human invasive breast ductal carcinoma, ER+, PR+, HER2- (luminal A)
t_{50}	Time at which the cell has spread to half its maximum
TAM	Tumor-associated macrophage
TAZ	Transcriptional coactivator with PDZ-binding motif
TCA	Tricarboxylic acid
TFM	Traction force microscopy
Tg2	Tissue transglutaminase 2
TGF-β1	Transforming growth factor beta-1
TME	TME
TMRM	Tetramethylrhodamine methyl ester perchlorate
TNBC	Triple negative breast cancer
TnC	Tenascin C
TNF	Tumor necrosis factor
Triton	Octyl phenol ethoxylate
TSG101	Tumor susceptibility gene 101 protein
Tween20	Polyoxyethylene 20 sorbitan monolaurate
VEGFR-2	Vascular endothelial growth factor receptror-2
YAP	Yes-associated protein

CHAPTER 1: INTRODUCTION

Portions of this chapter were published as reviews in *Cellular and Mechanical Bioengineering*[1] and *Clinical and Experimental Metastasis*[2] and as a book chapter in *Current Topics on Membranes*[3].

1.1   Breast cancer metastasis

Cancer is the second leading cause of death in the United States with breast cancer being the most commonly diagnosed cancer among women[4]. Breast cancer malignancy stems from the ability of cancer cells to metastasize to other organs in the body. The five-year survival rate of patients with breast cancer localized to the breast is 99 percent; however, if the cancer spreads to a distant part of the body, this five-year survival rate drops to 26 percent, highlighting the inability to treat metastatic cancer with current therapies[5]. Current cancer therapies, including chemotherapy, radiation, targeted therapy, and immunotherapy, treat cancer as a homogenous disease and target individual cancer hallmarks, including sustained proliferation, genomic instability, and altered cancer cell metabolism[6,7]. The inability to treat metastatic cancer with current therapies is highly attributed to heterogeneity within a single tumor.

1.2   Intratumor heterogeneity

Tumors are made up of a heterogeneous collection of cells, including cancer, stromal, and immune cells, and a dynamic extracellular matrix (ECM) with broad variations in architecture and stiffness[8]. Cancer cells within a single tumor are heterogeneous with distinct genetic and phenotypic traits. These traits are regulated by both intrinsic factors, such as cell lineage, genetic instability, and epigenetic modifications, and extrinsic factors imposed by the tumor microenvironment (TME)[7,9]. While it is known that tumors are mechanically diverse and tumor cells can vary in metabolic and migratory states[10], the direct impact of intratumor heterogeneity on cancer progression is poorly understood.

1.3   Components of the breast tumor microenvironment

Fibroblasts are one of the most abundant stromal cells in the TME[11]. Cancer-associated fibroblasts (CAFs) located in the TME mediate cancer cell invasion and metastasis through ECM remodeling[12]. CAFs secrete soluble factors and directly remodel the matrix to generate tracks, tunnels, and aligned fibers which cancer cells can sense and use to invade away from the primary tumor[13]. It is currently hypothesized that a large portion of CAFs in the TME are derived from fibroblasts adjacent to the primary tumor that have been transformed to a more contractile, activated state that remodels the ECM[14]. While the mechanisms that cancer cells use to transform fibroblasts are poorly understood, microvesicles (MVs) have recently been implicated in cancer cell-mediated fibroblast activation[15–17].

1.4   Cell-cell mechanical communication in cancer

Communication between cells in the TME enables cancer progression and metastasis. While cell-cell communication in cancer has primarily been examined through chemical mechanisms, recent evidence suggests that mechanical communication through cell-cell junctions and cell-ECM linkages is also an important mediator of cancer progression. Cancer and stromal cells remodel the ECM through a variety of mechanisms, including matrix degradation, matrix cross-linking, matrix deposition, and physical means. Cancer cells sense these mechanical environmental changes through cell-matrix adhesion complexes (CMACs) and subsequently alter the force landscape within the microenvironment. This communication permits cancer cells to communicate with each other but and communication between stromal and cancer cells in the TME.

1.4.1   Mechanical communication through the ECM

Cancer cells mechanically communicate with neighboring cells without direct cell-cell contact by exerting forces through the matrix. Cells bind to the matrix through cell-matrix adhesion complexes (CMACs), composed of integrin ECM receptors that bind ECM ligands, including collagen and fibronectin, and adaptor molecules that link integrins with the actin cytoskeleton (**Figure 1.1**)[18–24]**.** Cells in contact with the ECM also receive mechanical signals from the surrounding matrix through these CMACs. More specifically, integrins within CMACs sense both the chemical composition of the surroundings (i.e., which ECM ligands are present) and the mechanical properties of the surrounding matrix (i.e., ECM stiffness)[22,25]. The composition of ligands in the ECM dictates which signaling pathways will be activated based on integrin signaling; the spatial architecture of ECM fibers determines the stability and size of the CMACs[20,26–28]. Specifically, the chemical composition and physical properties of the ECM can regulate integrin-mediated cytoskeletal assembly and tyrosine phosphorylation to generate different types of adhesions with different downstream pathways[29]. The transmission of mechanical signals from the ECM is additionally dependent upon matrix mechanical properties. Different ECM proteins, including collagen I and fibronectin, can transmit or inhibit mechanical forces depending upon matrix tension, subsequently regulating downstream signaling events[30].

Cells within the TME transmit mechanical forces by directly altering the mechanical landscape of the surrounding matrix through numerous mechanisms including physical reorganization, matrix degradation, cross-linking, and deposition (**Table 1.1**). Matrix remodeling alters the local mechanical properties surrounding cells, resulting in direct changes to cell behavior as well as altering mechanical communication between cells within the matrix.
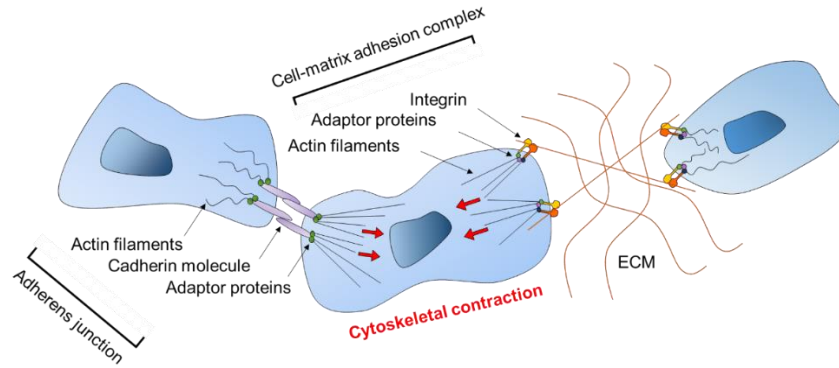
Figure 1.1. Cellular transmission and reception of mechanical signals. Transmission of intercellular mechanical signals through adherens junctions and cell-matrix adhesion complexes. Cancer cells transmit intercellular signals to neighboring cells through two mechanisms. Cancer cells can directly transmit forces to adjacent cells through cell-cell adhesions, specifically adherens junctions, or cancer cells can transmit forces to cells without direct contract through CMACs. Briefly, cellular contractility pulls on the ECM through CMACs which provides tension in ECM fibers resulting in aligned ECM fibers. Other cells in contact with the matrix sense these changes through their CMACs resulting in phenotypic changes.
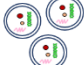
1.4.1.1   Physical Remodeling

Cells transmit forces through the matrix by reorganizing their actin cytoskeleton controlled by activation of Rho GTPase and Rho-associated protein kinase (ROCK) signaling[31–37]. Activation of ROCK, downstream of Rho GTPase, results in the phosphorylation of myosin light chain (MLC)[35,38,39]. This pathway promotes the contraction of actin fibers which pull on the ECM through CMACs and transmit traction forces through the ECM (**Figure 1.1**)[40–43]. These cell-generated contractile forces are used by cancer and stromal cells to remodel the ECM in two ways: deformation and fiber alignment. Physical deformation of the matrix is used by invading cancer cells to maneuver dense ECM without using matrix degrading proteases, and has been shown to be dependent on cell contractility through the ROCK pathway[44]. However, cancer cells also physically deform collagen fibers with protease activity present. Thus, physical deformation and matrix degradation can be used in concert. Additionally, stromal cells physically deform the matrix to assist in cancer cell migration. It was recently shown that CAFs are able to deform the basement membrane to promote cancer cell invasion[45].

Physical alignment of collagen fibers has also been shown to enhance cancer cell invasion. Collagen fibers aligned normal to the tumor boundary were identified as a tumor-associated collagen signature (**Figure 1.2**)[46]. In these regions of aligned fibers, groups of cancer cells migrating away from the tumor boundary were observed, indicating local invasion through collective cell migration. The alignment of collagen fibers into bundles parallel to the contractile force exerted by cancer cells provides contact guidance for migrating cancer cells and enhances migration persistence in the direction of the aligned collagen[47,48]. Additionally, this alignment of fibers has been shown to facilitate long range cell-cell

communication. Mammary acini can interconnect by aligning collagen fibers that coordinate and accelerate the transition of acini to an invasive state[114]. More recently, mechanical signaling resulting from ECM fiber alignment was shown to promote cancer cell protrusion frequency, persistence, and lengthening along the alignment axis to promote migration efficiency, thus facilitating metastatic cell invasion through the ECM during metastasis (**Figure 1.2**)[50,51]. Physical remodeling provides contact guidance for invading cancer cells, longer distance force transmission, and a method to deform and reorganize the ECM, resulting in a protease-independent mechanism of traversing the ECM.

Table 1.1. Players, mechanisms, and implications of ECM remodeling in cancer. Cancer cells, CAFs, and EVs are the major players involved in cancer ECM remodeling. All three players have large roles in ECM degradation through the release of MMPs, leading to altered ECM topography and the generation of tracks in the ECM. Additionally, cancer cells, CAFs, and EVs have all been implicated in matrix deposition of various proteins, leading to matrix stiffening. Cancer cells, CAFs, and EVs are involved in matrix crosslinking to stiffen the matrix through TG2 and LOX. Lastly, both cancer cells and CAFs are highly involved in physical remodeling of the ECM, both through actomyosin contractility and CMACs.

	Degradation Enzymes	Matrix Deposition	Crosslinking Enzymes	Physical Remodeling
Cancer cells	MMPs	Collagen, Fibronectin, Tenascin C	TG2, LOX	Actomyosin Contractility, CMACs
CAFs	MMPs	Collagen, Fibronectin, Tenascin C, Laminin	LOX	Actomyosin Contractility, CMACs
EVs	MMPs	Fibronectin	TG2	

	• Altered topology
	• Microtracks
		• Matrix stiffening
		  • Increased adhesion
		  • Increased traction forces
		  • Increased proliferation
		  • Activation of CAFs, TAMs
				• ECM deformation
				• Fiber alignment
				  • Contact guidance
				  • Force transmission

1.4.1.2   Matrix Stiffening

Cancer and stromal cells transmit mechanical signals to the matrix in the forms of matrix crosslinking and matrix deposition, resulting in increased ECM stiffness in cancerous tissue compared to healthy tissue[52]. Enzymatic crosslinking can alter the structural integrity of the ECM without greatly altering the overall organization and composition of the proteins in the matrix. The two main enzymes responsible for ECM crosslinking in the TME are lysyl oxidase (LOX) and tissue transglutaminase 2 (Tg2) (**Table 1.1**). LOX is an extracellular copper-dependent enzyme, secreted from a variety of cells including fibroblasts and endothelial cells, that can crosslink collagen and elastin molecules via an oxidation reaction[53]. High LOX expression has been correlated with poor prognosis in oral squamous cell caricnoma

and estrogen receptor negative (ER-) breast cancer patients and has become an attractive target for cancer therapies[54,55]. Additionally, downregulation of LOX expression significantly decreased metastases in mice[55]. Similarly, Tg2 is multifaceted enzyme expressed in cancer cells that participates in protein crosslinking, ATP/GTP hydrolysis, signal transduction, and even displays protein disulfide isomerase activity[56]. Cell surface Tg2 interacts with fibronectin and promotes fibronectin dimerization. Tg2 complexed with fibronectin in the ECM can also bind to the heparan sulphate chains of syndecan 4 to promote cell adhesion[56]. Additionally, high expression of Tg2 by breast cancer cells increases survival, invasion, motility, and metastasis[56–59].

In conjunction with enzymatic crosslinking, the mechanical properties of ECM can change due to alterations in ECM deposition by cells within the TME. Both cancer and stromal cells upregulate matrix protein expression to secrete increased matrix components into the surrounding environment resulting in desmoplasia[52,60–62]. CAFs deposit significant amounts of fibronectin, collagen, tenascin C, and laminin, to contribute to the dense tumor stromal matrix (**Table 1.1**)[61,63–65]. While matrix protein secretion is dependent upon cancer cell type, it has been shown that malignant cells deposit significant amounts of collagen, fibronectin, and tenascin C (**Table 1.1**)[62]. Through the deposition of various ECM components, CAFs and cancer cells construct a fibrotic stroma, leading to altered tissue mechanical properties and altered mechanically-induced signaling in cells.

Matrix stiffness effects how cancer and stromal cells interact with and communicate through the ECM. Durotaxis, or the cellular preference for stiffer substrates, revealed that direction of cell migration can be manipulated by changing substrate mechanical properties[66]. With increased mechanical tension, integrins and downstream mechanosensing equipment become activated and further strengthen focal adhesion and actin stress fiber formation[67,68]. While changes in ECM stiffness can make the matrix more resistant to cell-mediated physical reorganization, increased matrix stiffening can also alter cellular contractility[69]. Increased matrix stiffness has been associated with increased F-actin bundling, the formation of stress fibers, mature focal adhesions, increased cancer cell adhesion, traction forces, and proliferation[69–74]. Importantly, this increased stiffness can differentiate fibroblasts into their cancer-supporting counterparts[75,76]. In summary, matrix stiffening resulting from increased matrix crosslinking and matrix deposition mechanically signals to both cancer cells and stromal cells to promote cancer progression.

1.4.1.3   Matrix Degradation

Matrix degradation in the TME primarily occurs through proteolytic enzymes. Importantly, remodeling via proteolytic degradation results in alterations to the physical properties of the ECM, including changes in topography, which directly influence cell behavior. Various matrix-degrading proteases are upregulated in cancer and stromal cells and degrade a variety of matrix proteins found in the

basement membrane and ECM to facilitate cancer cell invasion (**Figure 1.2**)[77–80]. Metalloproteinases are the most prominent protease family involved in mechanical communication in cancer progression.

Matrix metalloproteinases (MMPs) are typically secreted into the TME and digest numerous ECM proteins to allow cells to breach the basement membrane and traverse the ECM[78–81]. Both cancer cells and CAFs are major sources of secreted MMPs in the TME. MMP-2, as one example, is expressed in several cancer cell lines and primarily degrades collagen to promote cancer cell migration (**Figure 1.2**)[82]. Alternatively, MMP-9 has little to no expression in cancer cells, but is secreted from CAFs and endothelial cells and is involved in both matrix degradation and vascular remodeling (**Figure 1.2**)[83,84]. MMPs can be released directly by cells or they can be contained within extracellular vesicles (EVs)[85,86]. Numerous cancer types release EVs containing MMPs. As one example, melanoma cells release EVs containing enzymatically active MMPs capable of matrix degradation[87]. Similarly, EVs released from prostate cancer cells have been shown to contain enzymatically active MMP2 and MMP9[88,89]. Notably, the presence of matrix degradation enzymes in EVs likely results in matrix remodeling far from the primary tumor as EVs can travel far distances before rupturing[90–92].

A subset of MMPs, termed membrane-type metalloproteinases (MT-MMPs), are anchored to cell membranes. MT-MMPs have been identified on invadopodia structures of migrating cancer cells[93,94]. These protease rich invadopodia degrade the matrix as the cell invades to form tube-like microtracks (**Figure 1.2**)[95,96]. Cancer cells migrate independently of MMP activity when using microfabricated 3D collagen microtracks which emulate paths left behind by invasive cells[97]. Further investigation revealed that cancer cells in these tracks did not require cell-matrix mechanocoupling but were more dependent on internal cytoskeletal dynamics to drive migration through the microtracks[98]. Thus, cells in contact with these microtracks may use them as easy passage through the ECM to the bloodstream to eventually colonize a secondary site. Stromal fibroblasts have also been implicated in leading collective cancer cell invasion using protease-dependent pathways (**Figure 1.2**). As fibroblasts remodel the matrix through Rho-mediated myosin light chain activity and MMP-dependent matrix degradation, cancer cells can retain an epithelial phenotype and invade away from the primary tumor[45,99]. In summary, matrix degradation is routinely used to remodel the ECM during cancer progression, and degradation-based remodeling modifies physical properties of the ECM, including altered topology such as microtracks, which is sensed by cancer and stromal cells within the TME to promote cancer progression and metastasis.

1.4.2   *Mechanical cell-cell communication at adherens junctions*

Cytoskeletal dynamics drive cell protrusion, adhesion, and contraction, allowing cancer cells to migrate[100]. However, intercellular cytoskeletal forces generated by cancer cells are also transmitted to adjacent cells as a form of mechanical communication. Epithelial cells directly transmit intercellular forces to neighboring cells through adherens junctions (AJs) (**Figure 1.1**). AJs mechanically link the cytoskeletons

of adjacent cells and are the primary mechanism of cell contact-mediated intercellular force transmission[101]. The extracellular domain of cadherins on opposing cells interact to form a stable adhesion between cells[102]. Intercellular domains of cadherins are linked to the actomyosin cytoskeleton through a complex supramolecular interface of adaptor proteins, including α-catenin, β-catenin, and vinculin, which add mechanical integrity to the junction and act as mechanotransducers[101,103]. The vinculin interface and α-catenin binding are important to mechanotransduction mechanisms of E-cadherin based adhesions and these proteins change conformation under applied force to induce signaling pathways and cytoskeletal remodeling[103]. The alignment of the actomyosin bundles relative to the junction allows for normal and shear stresses to be applied across the junctions between cells[104]. Additionally, cells can coordinate tissue-level contractile forces through these mechanical linkages[105,106].

The contractile forces generated by actomyosin bundles are transmitted across the mechanical linkages and sensed by cadherins and adapter proteins on adjacent cells. Cadherins sense tensile forces and rigidity of contacts[104]. Different types of cadherins, including E-, N-, and P-cadherin, are expressed on distinct cell types and play a range of roles in intercellular force transmission in cancer. In an epithelial state, cancer cells predominantly express E-cadherin with low expressions of N- and P-cadherin[107]. Single molecule analysis of cadherin bonds has revealed differential mechanics between E- to E-cadherin bonds and N- to N-cadherin bonds[108]. The E- to E-cadherin bonds are able to withstand larger forces before breaking when compared to the N- to N-cadherin bonds[108]. Upon epithelial-to-mesenchymal transition, cancer cells reduce E-cadherin expression and increase N- and P-cadherin expression, supporting the hypothesis that cell-cell adhesions decrease after EMT[107]. Furthermore, CAFs and cancer cells are able to form E-cadherin/N-cadherin adhesions which transmit intercellular forces and aid in cancer cell invasion[109]. Thus, it is possible that both the composition of intercellular contacts and the ratio of the different cadherins expressed are important regulators of cell-cell adhesion strength.

1.4.3 *Consequences of cell-cell mechanical signaling on cancer cell migration*

The degradation, stiffening, and physical remodeling of the ECM, initiated by both stromal and cancer cells, contributes to cancer cell migration. Cancer cells exhibit two modes of migration during invasion: single cell migration or collective migration. The increased matrix stiffness associated with increased contractility, matrix deposition and crosslinking has been shown to promote single cell migration. Although stiff matrices often have smaller pores, cancer cells can remodel the matrix by exerting elevated traction forces[69]. Elevated matrix stiffness in tumors has been shown to promote Rho/ROCK activity, focal adhesion assembly, and contractility of the actin cytoskeleton to induce cancer cell dissemination[110–112]. Additionally, increased ECM stiffness alters cell-matrix adhesions to promotes tumor cell metastatic potential and invasiveness through increased integrin clustering and subsequently enhanced integrin signaling through focal adhesion proteins such as paxillin and vinculin[113,114]. With this, stiff matrices

increase the number of focal adhesions and traction force generated compared to compliant matrices thereby altering cell-ECM mechanical communication (**Figure 1.2**)[114,115]. As such, tissue stiffness can drive single cell migration by increasing Rho/ROCK signaling, focal adhesion assembly, and cellular contractility.

During collective migration, an aggregate of cells coupled through cell-cell contacts migrate as a unit with leader cells at the front of the pack and follower cells behind them. The chemical and mechanical mechanisms driving collective motions are currently being investigated. Collective migration is an inherently more complicated process as cellular forces are transmitted to the matrix and to numerous adjacent cells. Studies investigating monolayer dynamics have revealed the importance of intercellular force transmission through cell-cell contacts in coordinating collective migration[116]. Coordination of traction forces via intercellular forces is evident in cell monolayers. The highest traction forces can be found towards the leading edge, where leader cells are mechanically coupled via actin cables where they exert strong traction forces that propagate into the monolayer and help orient migration direction of follower cells[117,118]. The dynamics of intercellular stresses distributed throughout a cellular monolayer also help coordinate the migration of cells during plithotaxis, or the guidance mechanism by which cells collectively migrate in the direction that minimizes local shear stresses[119,120]. Because cells are mechanically linked during collective migration, they exert forces directly onto one another and redistribute forces throughout the monolayer. Interestingly, mechanical interactions of follower cells, including a mechanical pull on the future leader, have been implicated in the selection of leader cells as the mechanical pull induced by follower cells aids in leader cell polarization and protrusion[121]. Another emerging mechanism of collective cell guidance is collective durotaxis[122]. Interestingly, cells that do not undergo durotaxis as individuals still utilize collective durotaxis[122]. The ability of cells to follow rigidity gradients as a group is dependent on local stiffness sensing at the periphery and long-range force transmission through cell-cell mechanical linkages[122]. Atomic force microscopy (AFM) measured local mechanical changes generated by cells in collagen matrices and observed strain stiffening at the leading edge of cancer cells in collective migration[123]. This finding highlights the reciprocal nature of invasion, as cells sense the "traveling wave" of stiffened substrate as they invade[123]. These studies reveal the contribution of matrix mechanics and mechanical signals to both single cell and collective migration in cancer progression.
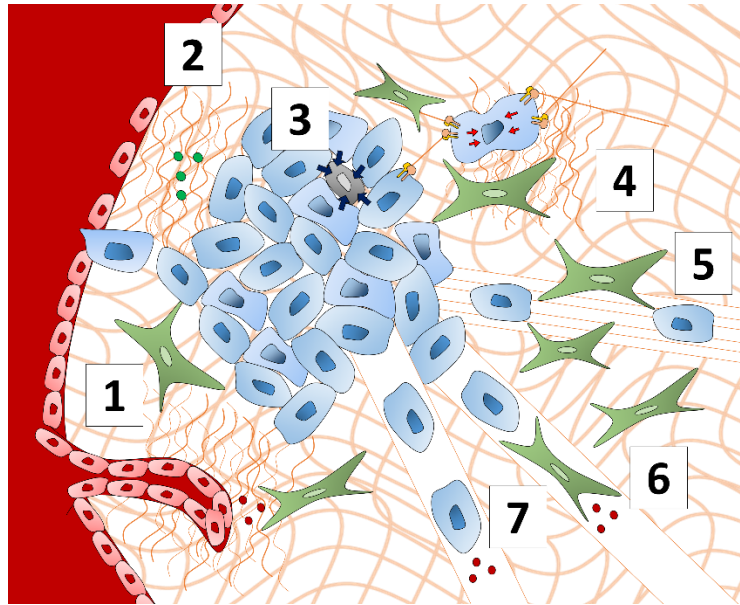
Figure 1.2. Consequences of cell-cell communication in cancer. (1) Increased ECM crosslinking via LOX and ECM remodeling via proteases enhances angiogenesis and enables endothelial cells to migrate through the ECM and form capillaries. (2) Increased ECM rigidity decreases the structural integrity and barrier function of blood vessels. (3) Cancer cells exhibit mechanical competition as they must outcompete less-mechanically fit neighboring cells via compressive forces that induce apoptosis. (4) Cancer cells sense increased matrix stiffness through cell-matrix adhesion complexes and can transmit these mechanical signals to nearby cells by exerting traction forces on the matrix. (5) Cancer-associated fibroblasts in the tumor stroma align matrix fibers which cancer cells can use as tracks to invade away from the primary tumor. (6) Fibroblasts act as leader cells, using matrix-degrading proteases to form tunnels in the ECM, which cancer cells follow to invade away from the primary tumor in a form of collective migration. (7) Cancer cells secrete matrix-degrading proteases to form tunnels in the ECM to invade away from the primary tumor.

1.5   Mechanobiology of microvesicle signaling

1.5.1   Microvesicle overview

Extracellular vesicles (EVs) have recently emerged as important mediators of cell communication and disease progression. The term "extracellular vesicles" refers to lipid bilayer-bound vesicles released from cells and include exosomes, microvesicles (MVs), large oncosomes, and apoptotic bodies[124,125]. Exosomes, 50-150 nm in diameter, are formed via the endocytic pathway as secretory multi-vesicular bodies (MVBs) fuse with the plasma membrane[124]. Exosomes are distinguished from other EVs by the presence of endosomal sorting complex required for transport (ESCRT) proteins that regulate MVB transportation, including Alix, TSG101, HSP70, and HSP90[126]. Additionally, exosome release relies on the neutral sphingomyelinase pathway, resulting in the enrichment of CD63, CD9, and CD81 tetraspanins in exosomes[126]. MVs, 100 or 200 nm -1 μm in diameter, are formed via the budding and subsequent shedding of the plasma membrane[124]. As a result, MVs primarily contain cytosolic and plasma membrane associated proteins, including tetraspanins[126]. Cytoskeletal proteins, heat shock proteins, integrins, and glycosylated

and phosphorylated proteins are also commonly identified in MVs[126]. Large oncosomes, classified as EVs larger than 1 μm in diameter, are produced by plasma membrane blebbing but differ in their buoyant density from other EVs[124,127]. Large oncosomes are believed to only be released from cancer and cancer-associated cells, with the number of large oncosomes released correlating with cancer aggressiveness[128]. As such, oncosomes primarily contain oncogenic proteins[128]. Lastly, apoptotic bodies are approximately 50 nm - 5 μm in diameter and are shed from the plasma membrane of apoptotic cells[125]. Unlike other EVs, apoptotic bodies contain complete organelles and higher levels of proteins associated with the nucleus, mitochondria, Golgi apparatus, and endoplasmic reticulum[126].

The role of MVs in disease progression are newly emerging. MVs were first described in 1967 after particulate material, described as "dust", was observed to be released from platelets[129]. It has now been determined that this "dust" is plasma membrane bound vesicles that are shed from the plasma membrane of both healthy and diseased cells. Now termed microvesicles, these vesicles contain a variety of cargo not typically thought to be released from cells, including receptor tyrosine kinases, cytosolic signaling proteins, and microRNAs. MVs are believed to play a prominent role in disease progression as they have been detected in body fluids including blood, urine, and synovial fluid from diseased patients, and elevated MV counts have been observed in cardiovascular diseases and cancerous tissue[130–132]. The transfer of cargo via MVs can result in the transformation of recipient cells to support disease progression. For example, MV signaling can promote extracellular matrix and vascular remodeling, recruit tumor-promoting stromal cells, and induce transformed phenotypes within neighboring cells[15–17,133–136].

The mechanobiology and membrane dynamics of MV release and uptake are under investigation. As MV uptake by recipient cells can modulate cell function, understanding the mechanisms of MV release, internalization, and the resulting signaling is crucial to fully comprehend the roles of MVs in disease progression. Here, we review recent advances in the understanding of actomyosin-regulated MV biogenesis, MV uptake via pinocytosis, and subsequent MV signaling. We additionally investigate the roles of altered cell contractility, mode of cell migration, and matrix compliance in regulating MV signaling.

1.5.2 *Mechanobiology of MV biogenesis*

1.5.2.1 Intracellular contractility and MV biogenesis

The release of MVs from the plasma membrane of cells is integral to MV-mediated communication during disease progression. While the complete mechanism of MV release is not defined, MV biogenesis is believed to be a multistep process that includes the trafficking of cellular cargo to the plasma membrane, a rearrangement of membrane lipids, and vesicle pinching mediated by contractile machinery[137]. As contractile machinery is essential for MVs release, altered cell contractility likely affects MV release and is an area currently being investigated[138,139].

Recent work has outlined a contractility-based MV release pathway regulated by ARF6, a small GTP-binding protein that regulates membrane trafficking and actin cytoskeleton remodeling[138–140] (**Figure 1.3**). Briefly, activation of phospholipase D (PLD) by ARF6-GTP promotes ERK activation. ERK subsequently activates myosin light chain kinase (MLCK) which signals through myosin light chain (MLC) to induce the actomyosin-based contraction required for MV release [140].

Downstream of ARF6 signaling, a separate RhoA GTPase signaling pathway highly regulates MV release[138,139] (**Figure 1.3**). RhoA activation targets both Rho-associated protein kinase 1 (ROCK1) and Rho-associated protein kinase 2 (ROCK2). Together, ROCK1 and ERK inhibit myosin light chain phosphatase (MLCP) which reduces the inactivation of MLC, further inducing actomyosin-based contractility and MV formation[138]. Alternatively, ROCK2 activates Lim kinase (LIMK), resulting in the inactivation of the actin-binding disassembly factor cofilin, resulting in the stabilization of F-actin necessary for MV generation[139].

Importantly, a variety of external stimuli that alter cellular contractility also affect MV release dynamics[139]. Inhibition of ROCK-1 and ROCK-2 in cancer cells using the small molecule Y-27632 inhibitor resulted in decreased cell contractility and eliminated the appearance of MVs on the cell surface[139], suggesting that cells with reduced ROCK-mediated contractility have decreased MV release. Additionally, it is well-established that contractile forces can be modulated by MLCK, which promotes MLC phosphorylation and the assembly of actin-myosin filaments[141]. Overexpression of MLCK in HeLa cells increased MV formation[139]. Similarly, treatment of melanoma cells with blebbistatin, a small molecule inhibitor of myosin II, or with latrunculin A, an actin-binding toxin that inhibits actin polymerization, both reduced MV release[140]. Altogether, these results suggest that external stimuli that alter actomyosin dynamics have profound effects on MV release. Further work is required to determine whether additional external stimuli, such as growth factors or cytokines, released by surrounding cells regulate MV release.
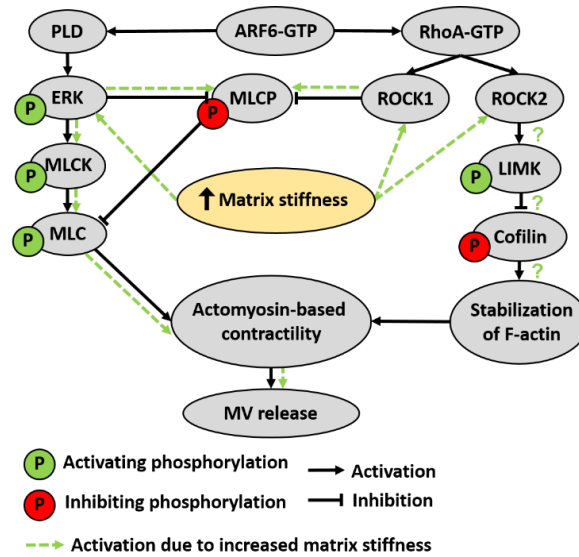
Figure 1.3. Proposed pathway of intracellular contractility and matrix stiffness regulation of MV release. MV release is regulated by ARF6-GTP signaling through ERK and RhoA-GTP pathways. Increased matrix stiffness may regulate this pathway through a variety of pathways. Green dashed lines represent pathways activated by matrix stiffness.

1.5.2.2   Amoeboid migration promotes MV release

Cell migration is a fundamental behavior in a variety of tissue processes and disease states, including development, wound healing, diabetes, and cancer[142–144]. During cell migration, cells primarily display two distinct modes of motility: amoeboid and mesenchymal. Amoeboid migration is classically defined as cell migration that exhibits fast speeds, high levels of actomyosin contractility, round cell shapes, and little to no matrix adhesion[145]. Amoeboid migration is protease-independent; cells squeeze through preexisting gaps or tracks in the ECM[146] (**Figure 1.4A**). Alternatively, cells undergoing mesenchymal migration move much slower, are weakly polarized, and exhibit multiple types of protrusions, including lamellipodia and filopodia[143]. Mesenchymal migration relies on strong integrin-mediated adhesions to the matrix and proteases to degrade the matrix[143] (**Figure 1.4B**). Amoeboid and mesenchymal migration are highly regulated by the Rho GTPases, RhoA and Rac1 GTPase, respectively. As intracellular actin dynamics and Rho GTPase activity are required for both MV release and regulation of cell migration mode, mode of cell migration appears to be linked to MV release.

In amoeboid migration, activation of RhoA GTPase at the cell rear leads to the assembly of contractile actin and myosin filaments. Actomyosin-based contractility at the cell rear generates hydrostatic pressure and cytoplasmic flow to form plasma membrane blebs at the leading edge, which are believed to be due to a decrease in membrane-actin cortex attachment or a local rupture of the actin cortex[146–148]. Blebs are distinct from other cellular protrusions as their formation is pressure-driven rather than actin polymerization-driven[149]. For blebbing to induce amoeboid cell migration, blebs need to be formed at the

leading edge of the cell, resulting in a transfer of cytoplasm in the direction of migration[148] (**Figure 1.4A**). As previously described, RhoA GTPase has been implicated in contractility-based MV formation through ROCK1 and ROCK2 signaling. Thus, RhoA GTPase activation may link amoeboid migration with increased MV release.

Whether MVs are released from the leading edge or trailing edge of migrating amoeboid cells is not currently defined and evidence suggests both scenarios may be possible. During amoeboid migration, directional membrane flow is generated by RhoA polarization to the cell rear, which creates force and pressure for membrane blebbing at the leading edge[145,150] (**Figure 1.4A**). As RhoA expression is enriched in MVs and required for contractility-based MV release[139], RhoA polarization to the cell rear suggests that MV release is enhanced at the cell rear during amoeboid migration. Live cell imaging of migrating amoeboid cells has also revealed a trail of MVs in the wake of the migrating cells[138]. To promote their directional migration, polarized amoeboid cells also express ezrin, a actin binding protein that links the plasma membrane to the actin cytoskeleton, at the cell rear[151]. Conflicting evidence exists as to whether ezrin expression prevents or contributes to MV release. Because ezrin links the plasma membrane to the cytoskeleton, it is speculated that ezrin prevents the membrane and actin cortex detachment required for blebbing at the cell rear, thereby promoting directional migration[151]. This implies that MVs are not released from the cell rear during active amoeboid cell migration but rather from RhoA rich regions of the membrane during moments of reduced cell polarity. Interestingly, a smaller amount of RhoA is expressed at the leading edge of a cell during amoeboid migration[152]. While RhoA at the rear edge appears to be constitutively active, RhoA expression at the leading edge is highly variable and may only last for seconds[152]. It is perhaps during these moments of leading edge RhoA expression that MVs are released from the front edge of a migrating cell (**Figure 1.4C**).

Importantly, ezrin has been identified in MVs released from a variety of cell types, including T-lymphocytes and cancer cells[153,154], highlighting that ezrin might actually contribute to MV release. Modulation of ezrin expression and localization has direct impacts on MV release[153,155]. Expression of CD82, a metastasis suppressing tetraspanin that inhibits tumor cell migration, resulted in ezrin expression in membrane bleb-like structures at the cell periphery and promoted ezrin release to the extracellular space via MVs[155]. While CD82 expression impairs cell migration, it may also promote cancer progression due to increased MV release and signaling. Similarly, induction of an amoeboid phenotype resulted in the redistribution of fascin, an actin-binding protein, ezrin, and podocalyxin, a cell-adhesion glycoprotein, to the neck of budding MVs at the cell periphery to promote MV release[154]. Importantly, during plasma membrane blebbing, ezrin is recruited to plasma membrane blebs in a spatially and temporally-dependent fashion, potentially explaining the conflicting role of ezrin in blebbing[156]. While ezrin is the first protein recruited to plasma membrane blebs, it is not enriched in the membrane during bleb expansion[156]. It later

re-localizes to the blei as expansion slows[156], potentially to reattach the plasma membrane to the cytoskeleton as the MV is released. In summary, RhoA GTPase regulation of amoeboid migration links amoeboid migration with MV release. Further work is necessary to determine the relationship between amoeboid cell polarization, ezrin localization, and MV release.

In mesenchymal migration, Rac1 GTPase is exclusively active at the leading edge to promote invadopodia formation[150] (**Figure 1.4B**). In contrast, RhoA GTPase is expressed in lower amounts at the cell rear[150]. Rac1 and RhoA GTPases have a complex, balanced relationship in cell migration[157–159]. Inhibition of one GTPase leads to activation of the other[159]. Recent work has studied the direct link between Rac1 GTPase expression and MV release[138]. Sustained Rac1 activation abrogated MV release from cancer cells on compliant matrices, supporting that Rac1 expression does not promote MV release. Treatment of Rac1-expressing cells with the Rac1 small molecule inhibitor NSC23766 or transfection with the dominant-negative Rac1 mutant Rac1(T17N) resulted in decreased invadopodia and invadopodia-mediated proteolysis, large focal adhesions, RhoA activation, and increased MV release on compliant matrices, but not on stiff matrices[138]. This implies that Rac1 inhibition promotes MV release on compliant matrices by a switch to RhoA GTPase expression **(Figure 1.4D)**. As Rac1 inhibition could not promote MV release on stiff matrices, a mechanosensitive pathway independent from RhoA/Rac1 signaling also likely mediates MV release.

A third Rho GTPase, Cdc42, is also involved in the formation of invadopodia and appears linked to MV shedding from the cell surface. Constitutive expression of Cdc42 in HeLa cells did not induce MV generation[139], suggesting that Cdc42 expression does not drive MV formation. Interestingly, very few MVs were observed on the surface of diffuse B-lymphoma (Dbl)-transformed fibroblasts[160]. As Dbl is a known activator of Cdc42[161], Cdc42 likely either inhibits MV formation or stimulates MV shedding from the cell surface. An activated-mutant of Cdc42 capable of constitutive GDP-GTP exchange increased the amount of MVs shed by HeLa cells into surrounding culture medium[162], suggesting that Cdc42 actually stimulates MV shedding from the cell surface. As a result, invadopodia formation and MV shedding may be linked through Cdc42 expression.

Importantly, cancer cells exhibit plasticity in which they can switch between amoeboid and mesenchymal motility depending on their environment[147]. Recently, mesenchymal-to-amoeboid transition (MAT) has been described in which cells exhibit a motility shift due to environmental signals, including MMP activity and cytokine signaling[163]. This suggests that both RhoA/Rac1 signaling and MV release may be altered by environmental cues that alter mode of cell migration. Altogether, MV release appears linked to RhoA GTPase activity in amoeboid migration, with cells undergoing RhoA-mediated amoeboid migration releasing increased numbers of MVs compared to cells undergoing Rac1-mediated mesenchymal migration. While the relationship between mode of cell migration and MV release is highly regulated by

14

RhoA/Rac1 expression, a separate mechanosensitive pathway may also regulate this relationship due to Rac1 inhibition not promoting MV release on stiff matrices.
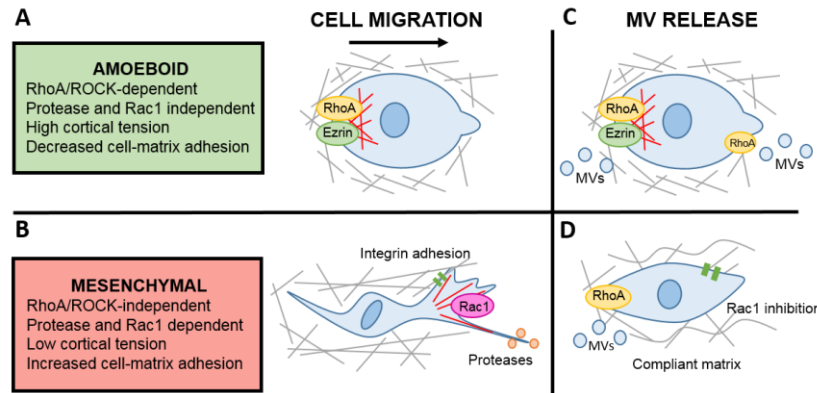
Figure 1.4. RhoA regulates MV release. (A) In amoeboid migration, actomyosin contractility and cytoplasmic flow form membrane blebs at the leading edge. RhoA and ezrin are polarized to the rear edge. (B) In mesenchymal migration, Rac1 expression at the leading edge drives actin polymerization in lamellipodia and filopodia protrusions which, along with increased cell-matrix integrin adhesion and protease activity, drive migration. (C) In amoeboid migration, MVs are likely released from both the leading edge, with short-lived RhoA expression, and the trailing edge where RhoA is constitutively expressed. (D) In mesenchymal migration, evidence suggests that to release substantial quantities of MVs, Rac1 inhibition is required. Inhibition of Rac1 increases RhoA activation, resulting in increased MV release on compliant matrices, but not stiff matrices.

1.5.2.3   Matrix stiffness alters cell contractility and cell migration to regulate MV release

Altered ECM mechanical properties occur in a variety of disease states, including pulmonary disease, Alzheimer's disease, diabetes, and cancer[164]. While changes to the ECM are known to directly impact cell contractility and cell migration[165], the direct relationship between ECM mechanics and MV release have yet to be thoroughly investigated.

Altered ECM mechanical properties directly affect the intracellular contractile machinery previously implicated in MV release. Increased matrix stiffness increases cell spreading and cell contractility in a variety of cell types, including fibroblasts, epithelial cells, and endothelial cells[17,166,167]. As increased cell spreading and cytoskeletal tension promote MLC phosphorylation in vascular smooth muscle cells[168], matrix stiffness likely additionally regulates the MLCK-dependent step of MV release (**Figure 1.3**). Additionally, ECM stiffening induces integrin clustering which enhances ERK activation[169] (**Figure 1.3**). This suggests that stiffening of the microenvironment in various disease states may promote MV release from resident cells through MLCK- and ERK-mediated cell contractility. This enhanced MV release from diseased cells may work to further promote disease progression by promoting MV signaling to healthy cells. Increased substrate stiffness also increases RhoA and ROCK1 mRNA and protein in breast cancer cells[170]. Integrin clustering associated with increased matrix stiffness increases Rho-mediated, ROCK1-generated myosin contractility and force generation[169]. As a result, increased matrix stiffness may also

enhance MV release through ROCK1 signaling (**Figure 1.3**). While increased extracellular matrix stiffness activates a variety of pathways associated with MV release, including MLCK, ERK, RhoA, and ROCK1 signaling, the direct effect of increased matrix stiffness on contractility-based MV release is not yet known.

While ERK and ROCK1 signaling are upregulated by increased matrix stiffness, the impact of increased matrix stiffness on ROCK2 signaling is less clear. Similarly to RhoA and ROCK1, increased substrate stiffness increases ROCK2 mRNA and protein in breast cancer cells[170–172] which may also promote contractility-based MV release (**Figure 1.3**). However, the impact of increased matrix stiffness on downstream ROCK2 signaling is unclear. It was recently shown that cofilin phosphorylation, required for F-actin stabilization in MV release, does not appear to be altered by substrate stiffness. However, only a range of 10 kPa to 57 kPa was tested, ignoring the effects of softer tissues on cofilin phosphorylation[170]. Additional work is required to reveal whether ROCK2 signaling in MV release is regulated by matrix stiffness.

The role of matrix stiffness in RhoA -dependent MV release additionally suggests a relationship between cell differentiation and MV release, as substrate stiffness is known to regulate stem cell differentiation[173]. The expression of smooth muscle-specific differentiation proteins was found to be dependent on matrix rigidity in 3D when RhoA is constitutively activated[174]. This implies that different amounts of MVs and MV cargo may be released by cells differentiated on compliant and stiff ECM.

Changes in matrix stiffness can also alter mode of cell migration to impact MV release. It was recently shown that cancer cells on compliant matrices adopted a rounded, blebbing, amoeboid morphology associated with RhoA GTPase activity[138]. Conversely, cancer cells on stiff matrices exhibited a flattened, spread, mesenchymal morphology associated with Rac1 GTPase activity[138]. These stiffness-mediated morphologies were determined to be associated with different MV release properties, with cells on soft matrices releasing more MVs than cells on stiff matrices[138]. While consistent with previous findings that RhoA signaling is required for MV release, these results suggest that decreased matrix stiffness is correlated with increased MV release due to the switch to an amoeboid phenotype. Importantly, matrix stiffness in this system was modulated by changing gelatin thickness and gelatin percentage in 2D[138]. Investigation of 3D environments and physiologically relevant biomaterials and stiffness would further enhance our understanding of stiffness-mediated MV release.

Altered matrix mechanics may also induce MAT. Increased cell confinement due to decreased pore size in the ECM results in cells that exhibit traits of both mesenchymal and amoeboid migration, with rounded morphology, increased migration speed, and large vinculin-adhesion sites[175]. While MV release in this intermediate mode of migration has yet to be investigated, the rounded cell morphology paired with large matrix adhesion sites may increase the effects of matrix stiffness on MV release.

In summary, MV release is highly dependent upon intracellular actin dynamics, mediated by ARF6 signaling through ERK and RhoA GTPase. The pathways downstream of ARF6 are highly dependent on altered intracellular contractility and matrix stiffness, indicating that soluble and mechanical signals in the TME may influence MV release and contribute to disease progression. Lastly, mode of cell migration, regulated by environmental signals and mechanical properties, regulates MV release through RhoA GTPase activity.

1.5.3   *Mechanobiology of MV transport and uptake*

As MV uptake by recipient cells is known to modulate cell function, understanding the mechanisms of MV transport and internalization are crucial to fully understand their function in disease progression. MVs have been detected in a variety of bodily fluids from cardiovascular disease, rheumatoid arthritis, and cancer patients[130–132], suggesting that MVs are transported away from diseased tissue where they may interact with healthy cells. Mechanical signals generated by the diseased tissue likely play a role in regulating MV transport away from diseased tissue. First, decreased epithelial barrier integrity, induced by increased epithelial cell contractility and decreased cell adhesion, may regulate the transport of MVs in a variety of diseases, including cancers, gastrointestinal diseases, and pulmonary fibrosis[176–182]. The increased epithelial permeability induced by these diseases may promote MV transport away from the diseased tissue to signal to healthy cells. However, the direct relationship between MV transport and epithelial barrier function have yet to be investigated. Additionally, altered vascular permeability may similarly regulate MV transport into the blood stream. Increased vascular permeability, common in both atherosclerosis and cancer, is induced by altered tissue mechanics and arterial stiffening[183–185]. Increased vascular permeability is known to enhance leukocyte extravasation and cancer cell intravasation[185–187]. It is likely that MVs similarly exhibit enhanced transport into the vasculature in conditions of increased vascular permeability. As a result, mechanics of the vasculature likely regulate transport of MVs away from diseased tissues but have yet to be directly investigated.

The mechanisms of EV uptake by recipient cells has been thoroughly researched and reviewed in recent years[188–193]; however, these studies refer to their vesicle population as the generic class of EVs and do not distinguish based on vesicle type. As a result, the specific mechanisms of MV uptake are largely undefined. Current evidence suggests that while EVs can be taken up by direct fusion with the plasma membrane[194], they are primarily taken up by endocytosis[188,195–197]. EV uptake via endocytosis can occur through a variety of endocytic pathways, including clathrin-mediated endocytosis, lipid raft-mediated endocytosis, caveolin-mediated endocytosis, pinocytosis, and phagocytosis[188]. As these studies focused on uptake of the generic EV population, it is unclear how MVs are internalized by recipient cells and whether MV internalization is a mechanosensitive process.

Uptake of MVs released from alveolar macrophages by alveolar epithelial cells was shown to more closely resemble pinocytosis, or the non-specific uptake of extracellular fluid, rather than receptor-mediated endocytosis[198]. This result is significant in suggesting that MVs likely do not use specific transmembrane proteins to dock on receptor cells. Instead, uptake of MVs by alveolar epithelial cells is dependent upon recipient cell dynamin function[198]. Dynamin, a GTPase that is required for clathrin-dependent endocytosis, is recruited and assembled at the neck of clathrin-coated pits. Activated dynamin then catalyzes membrane fission to induce endocytosis[199,200]. Importantly, while MV uptake was greatly inhibited by the dynamin inhibitor dynasore, clathrin expression by MVs was not required for dynamin-mediated endocytosis[198], suggesting that MV uptake does not depend upon clathrin-mediated endocytosis. This reveals a dynamin-dependent clathrin-independent endocytic pathway that regulates MV uptake. Interestingly, membrane tension, regulated by matrix stiffness and cellular contractility, is known to affect endocytosis[201–204]. Decreased membrane tension is associated with increased endocytosis while increased membrane tension decreases endocytosis[201,202]. While certain endocytic responses correlate with a reduction in membrane tension, these responses are dynamin-independent[205]. This suggests that dynamin-dependent MV endocytosis may be independent of recipient cell membrane tension. However, other methods of MV endocytosis not currently defined may be regulated by membrane tension.

MV uptake has also been found to be dependent upon recipient cell actin polymerization[198]. MV uptake by alveolar epithelial cells was disrupted using the actin polymerization inhibitor cytochalasin D. As actin polymerization is required for endocytosis, the interaction between actin and dynamin likely regulates MV uptake. While the relationship between cell contractility and MV uptake have not yet been investigated, this evidence suggests that increased cell contractility, which is associated with increased actin polymerization and actin remodeling, may correlate with increased MV uptake.

Actin dynamics in cell migration may additionally affect MV uptake but have yet to be investigated. RhoA regulates actin polymerization in amoeboid cells through mammalian homolog of Drosophila diaphanous 1 (mDia1) signaling, which catalyzes actin nucleation and polymerization[206]. Together, mDia1 and ROCK interact downstream of RhoA to induce actomyosin bundling[206]. As a result, increased RhoA signaling in amoeboid cells may enhance their ability to uptake MVs. Conversely, Rac1 and Cdc42, associated with invadopodia formation, control actin polymerization through Wiskott-Aldrich syndrome protein (WASP) and WASP-family verprolin-homologous protein (WAVE) regulation[207]. Specifically, the interactions of WASP and WAVE with Arp2/3 promotes formation of the actin network at the leading edge of mesenchymal cells[207]. Thus, the leading edge of cells undergoing mesenchymal migration, rather than the trailing edge, may be more equipped for MV uptake due to increased actin polymerization.

In summary, the mechanisms of MV transport and internalization are vastly understudied. Increased epithelial and vascular permeability likely enhance transport of MVs away from diseased tissue

and into the vasculature. However, the relationship between barrier integrity and MV transport have not yet been investigated. Additionally, recipient cell mechanics regulate MV uptake through actin polymerization[198]. Currently, the only known mechanism of MV uptake is via dynamin-dependent endocytosis which may not be affected by matrix stiffness and cell contractility. However, MV uptake does appear to be dependent on recipient cell actin polymerization, potentially through a mechanism other than the previously described dynamin-dependent endocytosis. As a result, recipient cell RhoA and Rac1 GTPase dynamics may regulate the ability of cells to uptake MVs via actin polymerization.

1.5.4   Mechanobiology of MV-mediated cell activation

Uptake of MVs can differentiate and transform recipient cells leading to altered cellular function. It is known that MVs can signal to and transform epithelial cells, endothelial cells, immune cells, and stromal fibroblasts[15–17,133,135,136,208–210]. Importantly, we have recently shown that MV-mediated transformation is mechanosensitive, as MV-mediated fibroblast activation was enhanced on stiff matrices mimicking the breast tumor periphery, compared to soft matrices mimicking healthy breast tissue[17]. This finding emphasizes that stiffer tumorigenic matrices may further promote cancer progression through enhanced MV signaling. However, the mechanism behind this enhanced MV signaling on stiff matrices is unclear. We speculate that it may be due to a heightened response to the MV cargo on stiff matrices or increased MV uptake, potentially due to increased fibroblast contractility on stiff matrices. It is additionally unclear whether this phenomenon is fibroblast-specific or whether matrix stiffness regulates MV-induced transformation in a variety of cell types. Further investigation is required to determine whether stiffened matrices associated with diseases such as lung fibrosis, atherosclerosis, or diabetes will enhance MV signaling to epithelial, endothelial, or immune cells.

Previous research has suggested that matrix stiffness sensitizes cells to various chemical cues. For example, increased matrix stiffness enhances vascular endothelial growth factor receptor-2 (VEGFR-2) internalization in endothelial cells and sensitizes epithelial cells to epidermal growth factor (EGF), resulting in increased epithelial cell proliferation[211,212]. Together, these results suggest that matrix stiffness may increase cell sensitivity to MV cargo. This may be cargo-specific and recipient cells may only exhibit increased sensitivity to select MV cargo, such as growth factors, cytokines, or other soluble factors. Future investigation into the sensitivity of fibroblasts to specific MV cargo on a variety of substrate stiffness will elucidate the mechanism of this stiffness-dependent MV-mediated fibroblast activation.

Alternatively, an enhanced response to MVs on stiff matrices may be a result of increased MV uptake via increased actin polymerization and cell contractility, as previously described. As fibroblasts exhibit increased contractility on stiff matrices[17], this may provide them with the necessary actin polymerization required for MV uptake. Similarly, increased substrate stiffness may alter recipient cell membrane tension to increase MV uptake via a form of endocytosis not yet implicated in MV uptake.

MVs may also be involved in a mechanosensitive feedback loop in the TME to promote cancer progression. As previously described, increased matrix stiffness enhances fibroblast response to MV cargo[17]. This results in increased fibroblast activation to further remodel and stiffen the TME[17], which may ultimately further amplify fibroblast response to MVs, both through increased MV release by resident cancer cells, increased MV uptake by resident fibroblasts, and increased remodeling by activated fibroblasts. Matrix remodeling by cancer-associated fibroblasts may have significant effects on cancer progression by inducing increased cancer cell invasion away from primary tumors and promoting pre-metastatic niche formation[12,213,214]. As a result, this mechanosensitive MV signaling feedback loop may further promote cancer metastasis.

MVs may also alter the mode of migration in recipient cells. Metastatic amoeboid cancer cells transferred their amoeboid phenotype to other cancer cells via exosomes to induce a more aggressive cancer phenotype[215]. This signaling was shown to be a result of cargo transfer that activated the RhoA/ROCK signaling pathway[215]. While MVs have not yet been studied in this context, components of the RhoA signaling pathway in MV cargo may also induce amoeboid signaling in recipient cells. If true, MV-induced MAT may enhance MV release from transformed recipient cells to further promote disease progression.

The effects of matrix stiffness and other environmental factors on MV signaling are poorly understood. While recent work suggests that increased matrix stiffness may enhance MV-mediated fibroblast activation, the mechanism behind this phenomenon is unknown. Further work is necessary to understand the role of matrix stiffness in the delivery of specific MV cargo to specific cell types and the effects on their downstream signaling. Additionally, investigation of MV regulation of MAT will further elucidate the roles of MVs in cancer progression.

1.6 Cancer cell metabolism, migration, and metastasis

1.6.1 *Primer on cancer cell metabolism*

Reprogramming of glucose metabolism is an important hallmark of cancer that supports cell survival during the metastatic cascade. Cancer cells are able to dynamically switch between two modes of glucose metabolism, glycolysis and oxidative phosphorylation (OxPhos), based on nutrient availability and energy demands[216]. Glycolysis, which can occur anaerobically, is a highly inefficient mode of glucose metabolism, yielding just 2 ATP per mole of glucose (**Figure 1.5**). Mitochondrial OxPhos is an aerobic process that occurs in the mitochondria of cells and is highly efficient at generating ATP, yielding 36 ATP per mole of glucose[217] (**Figure 1.5**). Generally, healthy cells only switch between glycolysis or OxPhos based on oxygen availability. In hypoxic conditions, healthy cells must switch to anaerobic glycolysis to maintain ATP generation. As the processes can occur simultaneously in the presence of oxygen, it is rare that a cell can be classified as driven wholly by glycolysis or OxPhos. However, the predominant source of energy utilization is often determined by the cellular process being fueled or by cues from the surrounding

microenvironment. Additionally, though cells must use glycolysis to produce pyruvate to fuel OxPhos, they can also be redirected to produce energy via aerobic and anaerobic branches of the Pentose Phosphate Pathway (PPP), which is primarily responsible for the redox status of the cell[218]. In contrast, a separate metabolic pathway that catabolizes glutamine is thought to be heavily utilized in some cancers, while not in others[219]. As such while glycolysis and OxPhos are the two primary and most heavily studied modes of glucose metabolism, it is important to note that cells can undergo a variety of metabolic processes to fuel migration, proliferation, and metastasis.
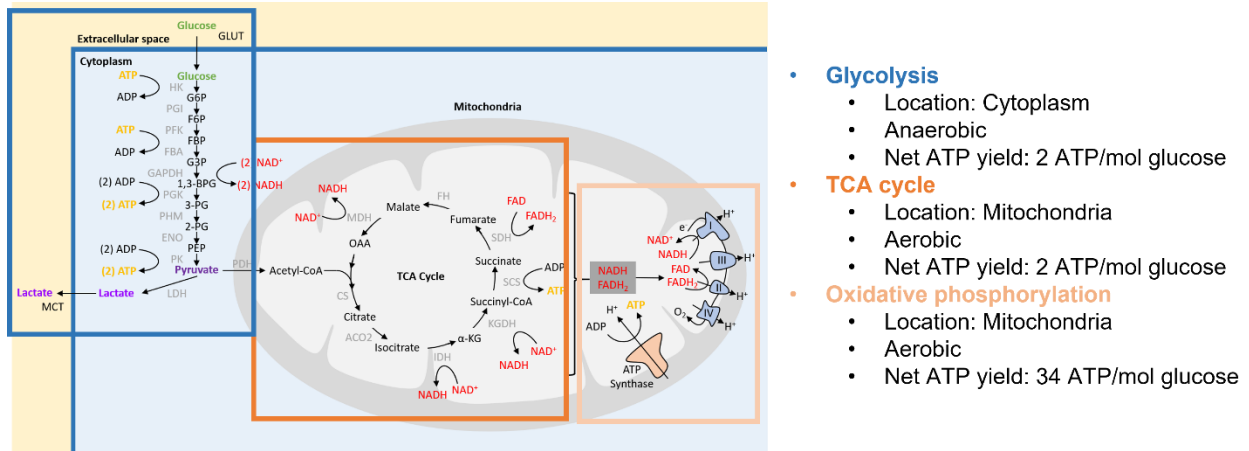
Figure 1.5. Overview of glucose metabolism. Cancer cells generate large amounts of ATP through glucose metabolism. Glucose metabolism is composed of three interconnected pathways: glycolysis, the TCA cycle, and OxPhos. Glycolysis occurs anaerobically in the cytoplasm and produces 2 ATP/mol glucose. The TCA cycle and OxPhos are aerobic processes that occur in the mitochondria and together generate 36 ATP/mol glucose.

Cancer cells are uniquely metabolically plastic and can dynamically switch between the two main modes of glucose metabolism, even when oxygen availability remains high[220–222]. In contrast to normal cell function, cancer cells often preferentially use glycolysis for ATP generation under aerobic conditions, termed "the Warburg Effect"[223]. Importantly, Warburg's observations focused on comparing the metabolism of "growing tissue" to "resting tissue" and thereby focused on the metabolism of highly proliferative cancer cells[223]. Initially, this metabolic switch was attributed to mitochondrial impairment and dysfunction but was later found that the switch to glycolysis was independent of mitochondrial health in most cancers and rather occurred as the result of metabolic reprogramming in cancer cells[224,225]. Specifically, mutations in signaling pathways that regulate glucose uptake, such as Akt or Myc, have shown to be responsible for the Warburg Effect[226–228]. While glycolysis has been shown to enhance cancer cell proliferation, it is still unclear how cancer cell glucose metabolism relates to migratory and metastatic capability.

1.6.2   Bioenergetics of single cell and collective migration

In the early steps of the metastatic cascade, cancer cells detach from the primary tumor, invade through the basement membrane, and navigate through the ECM. Completion of these steps is thought to be required for a cell to successfully colonize new tissues and form secondary tumors[229]. Importantly, successful invasion and migration relies on the metabolic and migratory plasticity of cancer cells to meet changing energetic demands of unique microenvironments[230]. Understanding the nuances of how cellular metabolism regulates cancer cell invasion and migration is essential to target the cancer cells that are capable of escaping the primary tumor. Migration away from the primary tumor can occur as either single cell or collective migration[231–234]. Further analysis of these mechanisms reveals that multiple different modes exist, epithelial and mesenchymal single cell migration and leader and follower cells in collective migration[235–238]. The migratory potential and metabolism of migrating cells is heavily dependent on mode of migration and is further complicated by intratumor metabolic heterogeneity that is mediated in part by spatial cues.

Single cell migration *in vitro* has been heavily studied to parse apart the particular mechanisms cells use to navigate the TME[116,239,240]. Briefly, cancer cells utilize various migratory modes to traverse the TME, transitioning first from a non-migratory epithelial state to a more migratory mesenchymal mode[241–243]. During epithelial-to-mesenchymal transition (EMT), cells transition to a more aggressive phenotype characterized by a change in both morphology and invasive capability[244]. Numerous aspects of migration and EMT are linked both directly and indirectly to metabolism. Importantly, EMT is characterized by cytoskeletal reorganization and formation of protrusions which can alter energy production and consumption[245]. EMT is due in part to upregulation of specific transcriptional factors like Snail, Slug, and TWIST which have previously been associated with altered cell metabolism[246]. Specifically, Snail has been linked with altered glucose flux in cancer cells by regulating glycolysis and the pentose phosphate pathway[247]. Additionally, hypoxia-induced HIF-1 signaling is known to induce EMT through TWIST signaling[248,249]. However, the respective roles of glycolysis and OxPhos during these transitions, especially in oxygen-rich conditions, are relatively unknown.

Recent evidence points to a prominent, understudied role for OxPhos during single cell cancer migration[250]. An increase in mitochondrial biogenesis and OxPhos via upregulated expression of peroxisome proliferator-associated receptor gamma, coactivator 1-alpha (PCG-1α) has been strongly correlated with a more invasive cancer cell phenotype and an increase in the formation of distal tumors[250]. Additionally, relocation of mitochondria to the leading edge of cells and to forming protrusions is thought to enable increased ATP production to fuel migration and invasion[251,252]. Mitochondrial function, in contrast to what was previously proposed by the Warburg Effect, is not impaired in more aggressive phenotypes. In fact, in super-invasive and super-metastatic phenotypes, created through rounds of *in vitro* and *in vivo*

sorting, respectively, a mitochondrial shift occurs in which cells maintain levels of OxPhos without an increase in glycolysis[253]. This metabolic switch is also thought to be mediated by the availability of TNF-receptor associated protein-1 (TRAP1) which is expressed in lower levels in cancerous tissue than normal tissue. TRAP1 deficiency *in vitro* was found to correlate with increased OxPhos, intermediates of the TCA cycle, and ATP and ROS production to increase the invasiveness of migrating cells[254]. Thus, data suggests that OxPhos may play an equally important role in the aggressive phenotype of migrating cells compared to glycolysis, though it may be more context-dependent to provide ATP to localized regions where it can be utilized efficiently.

In contrast to single cell migration in cancer, collective migration describes cells that move cooperatively in groups that has been observed in many cancers, including breast, prostate, colorectal, and lung cancers[255]. Importantly, the collective behaviors of cancer cell clusters has been suggested to lead to increased invasion, metastasis, and therapeutic resistance compared to single cells[256–259]. In collective migration, a leader cell guides clusters of follower cells coupled with cell-cell junctions through the TME. To guide collective strands, leader cells utilize actin-rich protrusions and proteases, including MMPs and Cathepsin B[260–262]. Conversely, follower cells exhibit high levels of cell-cell adhesions, such as cadherin-based adherens junctions[263,264]. Given the very different mode of migration utilized when cells move collectively compared to single cell movement, the energetic needs for two modes are likely very different.

It was recently reported that the collective invasion of cancer cells is regulated by the energy status of leader and follower cells[265,266]. Leader cells of breast cancer cell spheroids exhibit higher glucose uptake compared to follower cells, suggesting that leader cancer cells rely more heavily on glucose flux than follower cells[265]. Similarly, glycolytic ATP production was reported to regulate the collective invasion of endothelial cells in vessel branching[267,268]. Additionally, recent data suggests that breast cancer leader cells must overcome a threshold level of intracellular ATP/ADP to successfully invade[265]. As leader cells invade, their energy gradually depletes, leading to leader-follower cell transition in which a follower cell becomes a new leader cell[265]. Importantly, as invading strands encounter a physically challenging environment, they exhibit more frequent leader-follower switching to overcome the high energy barrier of their invasion[265]. This result suggests that cancer cells exhibit phenotypic plasticity, regulated by energetically demanding microenvironmental challenges, during collective migration. Interestingly, it was also recently reported that lung cancer leader cells preferentially utilize mitochondrial OxPhos regulated by pyruvate dehydrogenase (PDH), and lung cancer follower cells rely on elevated glucose uptake regulated by GLUT1 to fuel collective invasion in tumor spheroids[266]. This finding is consistent with other collective migration studies describing leader cells as more migratory but less proliferative than follower cells[266,269]. Co-targeting of PDH and GLUT1 dramatically reduced spheroid invasion, suggesting that co-targeting glycolysis and mitochondrial OxPhos to inhibit the invasion of a metabolically heterogeneous cancer cell population holds

potential for drug development[266]. The reason for these contrasting findings may lie in the context of the metabolism measurements. The dynamic, real-time switching of a heterogenous leader/follower cell population invading from spheroids provides a transient context for cell metabolism, where greater energy demands in the leader cell position lead to increased uptake of glucose that may suggest an increase of glycolysis independent of a change in OxPhos. However, when cells are sorted to create distinct, leader and follower cell populations, a more permanent, lasting metabolic signature is characterized in which leader cell populations generally increase OxPhos compared to follower cells. By taking these two studies together, a more complete insight into the metabolic behavior of leader and follower cells reveals a highly context-dependent relationship.

1.6.3   Interactions with stromal cells that regulate metabolism during cancer cell migration

Communication between fibroblasts and infiltrating leukocytes in the TME and cancer cells can affect both metabolism and migration. In the primary tumor, cancer cells secrete hydrogen peroxide which induces oxidative stress and caveolin-1 (Cav-1) degradation in fibroblasts[270,271]. The loss of Cav-1 enhances fibroblast aerobic glycolysis, inducing the release of energy-rich metabolites, including lactate, pyruvate, and ketone, into the microenvironment[272,273]. In addition to oxidative stress, cancer-derived MVs can also signal to fibroblasts to increase aerobic glycolysis through Cav-1 degradation[16]. These activated fibroblasts subsequently become more glycolytic and release higher levels of lactate into the TME[16]. Uptake of these metabolites by cancer cells can directly fuel mitochondrial OxPhos[16,272,273]. Additionally, evidence suggests that matrix mechanics regulate MV signaling[1,17,274]. Specifically, increased matrix stiffness enhances MV-induced fibroblast activation[17]. As MV-induced activation was previously shown to increase fibroblast aerobic glycolysis[16], increased matrix stiffness in the TME may further promote this metabolic switch in fibroblasts through enhanced MV signaling. This observation, in which fibroblasts in the tumor stroma exhibit enhanced glycolysis to fuel cancer cell mitochondrial OxPhos, has been termed the Reverse Warburg Effect[272]. These tumor-stromal metabolic interactions within the context of confinement were recently investigated using a unique, micropatterned tumor-stroma interface model[275]. Cancer cells at the center of the micropattern, mimicking high confinement at the tumor core, upregulated expression of glycolysis genes. Cancer cells at the tumor-stromal interface, recapitulating low confinement at the tumor periphery, upregulated expression of OxPhos genes, further supporting a metabolic relationship between tumor and stromal cells[275].

As cancer-associated fibroblasts located in the TME are known mediators of cancer cell invasion and metastasis through ECM remodeling[1,12,46,276], metabolic coupling between cancer cells and stromal fibroblasts likely regulates cancer cell escape from the primary tumor and subsequent metastasis. Fibroblast-enhanced cancer cell OxPhos can increase cancer cell migration and invasion *in vitro*[16]. Additionally, this metabolic coupling can enhance cancer cell resistance to cancer therapies. Specifically,

fibroblast-induced epithelial cancer cell mitochondrial activity has been shown to enhance cancer cell tamoxifen resistance in breast cancer cells *in vitro*[273].

Metabolic interactions between cancer cells and infiltrating leukocytes may also affect cancer migration and metastasis. Similar to cancer cells, activated T cells exhibit enhanced aerobic glycolysis to support their proliferation and effector function[277,278]. As a result, infiltrating leukocytes and cancer cells compete for nutrients in the TME[279]. Decreased T cell glucose uptake has direct implications on their anti-tumor efficacy and thereby affects cancer cell progression[280,281]. While the majority of research on the leukocyte-cancer cell metabolic relationship has focused on the effects on T cell efficacy, increased T cell glucose uptake in the TME may induce a similar response to the Reverse Warburg Effect in cancer cells, where cancer progression is fueled by metabolic intermediates released by T cells.

1.6.4   *Metabolic signatures of metastatic cancer cells*

To effectively target metastatic cancer cells with metabolic inhibitors, it is essential to determine the bioenergetics of cancer cells that regulate their progression during the metastatic cascade and subsequent tissue colonization. A variety of evidence suggests that metastatic cancer cells may rely more on mitochondrial OxPhos while primary tumors rely more on glycolysis to fuel primary tumor growth. The direct role of OxPhos in metastatic cancer cells was initially observed by removing mitochondrial DNA from cancer cell lines and observing their effect *in vitro* and *in vivo*[282,283]. Breast and brain cancer cells devoid of mitochondrial DNA lost their tumorigenic phenotype that was only restored upon the transfer of normal mitochondria to the cells[282]. Similarly, removal of mitochondrial DNA in cervical and ovarian carcinoma lines resulted in decreased tumor growth when subcutaneously injected in mice[283]. Later, it was observed that brain metastases of breast cancers exhibited increased OxPhos compared to primary tumors[284]. Similar reports found circulating cancer cells from a 4T1 mouse model to be enriched for OxPhos transcripts compared to their primary tumor counterparts[250]. This enhanced OxPhos in circulating cancer cells was found to be associated with PGC-1α expression[250]. Silencing of PGC-1α reduced both cancer cell invasion and metastasis without affecting cancer cell proliferation, primary tumor growth, or EMT status[250]. Taken together, these studies suggest that mitochondrial OxPhos plays an essential role for cancer cell tumorigenicity and metastasis. Comparison of metastatic melanoma cells with their primary tumor counterparts revealed enhanced mitochondrial OxPhos in the metastatic cancer cells. Specifically, production of mitochondrial superoxide, a byproduct of cellular respiration, distinguished highly metastatic melanoma cells from weakly metastatic cells[285]. Similarly, metabolic profiling of parental breast cancer epithelial cells compared to their metastatic counterparts collected from secondary sites *in vivo* has revealed differential utilization of key metabolic factors[286]. Specifically, metastatic subclones boasted increased metabolic flexibility and redox control, allowing cells to proliferate even under high stress conditions. Analysis of highly metastatic parental ductal carcinoma cells collected from liver metastases *in vivo* showed

increased OxPhos regulated via myoferlin, a protein associated with vesicle trafficking, compared to less metastatic subclones[287]. This study highlights another potential metabolic target in metastasis, myoferlin, that has already shown to be effective in mouse models[288].

Recently, single-cell RNA sequencing has been used to distinguish metabolic differences between primary tumors and metastases. Single-cell RNA sequencing of matched primary tumors and micrometastases revealed mitochondrial OxPhos as the top pathway upregulated in micrometastases compared to higher levels of glycolytic enzymes in primary tumors[289]. This finding suggests that enhanced glycolysis may aid in primary tumor cell growth while mitochondrial OxPhos may be more important in a variety of metastatic stages and colonization. Additionally, this finding of differentially enriched metabolic pathways in primary tumors versus micrometastases highlights that different metabolism-targeting therapies may be advantageous in different stages of cancer progression. Importantly, transcriptional heterogeneity was still apparent in these micrometastases[289], proving that one metabolic therapy may not be capable of targeting all metastatic cells found in a lesion. Altogether, these findings reemphasize the importance of the "migration-proliferation dichotomy" and suggest a similar "metastasis-proliferation dichotomy" may also exist. It is likely that microenvironmental cues then signal to these metastatic cancer cells to return to a glycolytic phenotype to fuel proliferation of the secondary tumor.

Reports of upregulated glycolysis, rather than mitochondrial OxPhos, have also been associated with increased metastasis. In hepatocellular carcinoma cells, overexpression of glycolytic enzymes results in increased metastasis in a mouse model[290]. Similarly, increased glycolysis has been linked to antioxidant-driven metastasis in lung tumors in addition to increased glucose uptake and lactate secretion[291]. Sorting the conflicting evidence regarding whether metastatic cancer cells rely more heavily on OxPhos or glycolysis may lie in the location of the metastatic spread, as metastatic breast cancer cells that preferentially use glycolysis tend to metastasize to the liver, while those utilizing OxPhos target lung or bone secondary sites[292]. These glycolytic breast cancer cells are thought to be specifically tuned for liver metastasis via increased HIF-1α and PDK-1 activity that is essential in regulating metabolic pathways. Further, aggressive 4T1s metastasizing to liver, bone, and lung utilized a combination of mitochondrial OxPhos and glycolysis, suggesting that secondary site colonization is dependent on the metabolic state of the cells[292]. Additionally, patient data suggests that within the secondary sites, the presence of glycolytic markers was dependent on the specific site location, where metastatic cells at brain and lung sites were more likely to maintain a glycolytic phenotype than other secondary sites[293]. Still others report that brain metastases *in vivo* have higher expression of both glycolytic and OxPhos-associated enzymes[284], suggesting that while differential metabolic programming may be elevated in specific secondary sites, metastatic cells likely use a combination of the pathways to meet energetic requirements.

Table 1.2. Cancer therapies targeting glucose metabolism

Drug	Target enzyme	Approval stage	Ref
Enasidenib	IDH-2	Approved	[294]
Metformin	ETC complex I	Approved for type 2 diabetes, clinical trials for cancer	[295,296]
2-DG	HK	Clinical trials	[297,298]
3-BrPa	HK, GAPDH	Clinical trials	[299]
AT-101	LDH-A	Clinical trials	[300]
AZD3965	MCT1	Clinical trials	[301]
CPI-613	PDH, α-KGDH	Clinical trials	[302]
DCA	PDK1	Clinical trials	[303,304]
FK866	GAPDH	Clinical trials	[305]
IDH305	IDH	Clinical trials	[306]
Ivosidenib	IDH	Clinical trials	[307]
Lonidamine	HK	Clinical trials	[308,309]
Marizomib	ETC complex II	Clinical trials	[310,311]
Polyphenon E	LDH-A	Clinical trials	[312]
Resveratrol, chrysin	HK2	Clinical trials	[313]
Ritonavir	GLUT1	Clinical trials	[314]
TT-232	PKM2	Clinical trials	[315]
PFK158	PFKFB3	Clinical trials	[316–318]
3PO	PFKFB3	Research	[316,318]
Fasentin	GLUT1, GLUT4	Research	[319]
GEN-27	GLUT1, HK	Research	[320]
Koningic acid	GAPDH	Research	[321]
STF-31	GLUT1	Research	[322]
VK3	PKM2	Research	[315]
VK5	PKM2	Research	[315]
WZB117	GLUT1	Research	[323]

1.6.5 *Anti-metastatic therapies and metabolism-targeting drugs*

While most cancer therapies exclusively target proliferation, recent understanding of the role of glucose metabolism in cancer cell proliferation, migration, and metastasis lays a strong foundation towards the development of anti-metastatic drugs targeting metabolic processes essential in the metastatic cascade. Enasidenib, a selective inhibitor of mutant isocitrate dehydrogenase 2 (IDH-2), an enzyme that mediates progression through the TCA cycle, is already approved to treat patients with IDH-2-mutated myeloid leukemia[294] (**Table 1.2**). Similar IDH-inhibiting drugs have been shown to abrogate both invasion and

migration of chondrosarcoma cells *in vitro* while their proliferation remained unaffected, which may point to a prominent role of mitochondrial metabolism in metastasis[324]. Additionally, a variety of metabolism-targeting agents are currently in clinical trials (**Table 1.2**). For example, AZD-3965, which inhibits MCT1, reportedly exhibits anti-tumorigenic properties by preventing cellular acidification during increased glycolysis[301]. However, while MCT4 inhibitors reportedly decrease pancreatic ductal adenocarcinoma cell migration *in vitro,* MCT1 inhibitors have little effect on migration. Interestingly, inhibiting either MCT1 or MCT4 significantly reduces cell invasion, again pointing to the role of individual components of metabolic pathways on specific steps in the metastatic cascade[325]. Another potential therapeutic, CPI-613, disrupts mitochondrial metabolism to induce reactive oxygen species (ROS)-associated apoptosis[326] and significantly decrease collective cancer cell invasion *in vitro*[266], and is currently undergoing clinical trials with pancreatic cancer patients[327]. Metformin, a drug approved for the treatment of Type 2 Diabetes, is currently undergoing clinical trials to treat cancer[295] including its use in combination therapy with chemotherapeutic drugs, including cisplastin and doxycycline, as it is hypothesized that metformin may increase cancer cell sensitivity to chemotherapy[295]. Interestingly, metformin is effective at inhibiting both proliferation and migration in breast cancer cells *in vitro*[328,329]. As metformin predominantly inhibits progression of OxPhos by inhibiting the ETC Complex I, this finding points to the powerful role of OxPhos in key steps in the metastatic cascade. In part due to the complexities described above identifying the predominant metabolic pathways for a given cancer in a given patient, cancer therapies that target both glycolysis and mitochondrial OxPhos are undergoing clinical trials, as both metabolic pathways have been deemed important for cancer progression (**Table 1.2**).

Drugs and therapies simultaneously targeting both glycolysis and OxPhos are being pursued to combat compensatory mechanisms upon the inhibition of one of the pathways. Recently, the drug Marizomib was combined with a glycolysis inhibitor to reduce metastatic spread in mice[311]. When treated with Marizomib, which acts to downregulate mitochondrial OxPhos through inhibiting Complex II of the ETC, cells were found to increase glycolysis to provide necessary energy for proliferation and metastasis[311]. Similarly, *in vitro*, the drug significantly decreased the migratory ability of TNBCs, correlating with the downregulation of PGC-1α and EMT genes[311]. These data led to the combination therapy of Marizomib and 2-deoxy D-glucose (2-DG), a glycolysis inhibitor, which was shown to significantly inhibit tumor growth. Thus, in moving to clinical trials and designing anti-metastatic therapies, understanding site-specific bioenergetics and compensatory mechanisms is essential to inhibit metastasis without off-target effects. Additionally, because cells are reprogrammed at different stages of metastasis to rely more on glycolysis or OxPhos, it is necessary to understand which pathway is dominant at each stage. Recently, a targeted tumor-specific inhibition of cell metabolism using a ginsenoside derivative was found to decrease tumor growth in a xenograft model[330]. By downregulating both OxPhos and glycolysis in tumor cells only,

while leaving normal, healthy cells unchanged, this promising therapy could decrease metastasis without altering normal cell function.

CHAPTER 2: MATRIX STIFFNESS REGULATES MICROVESICLE-INDUCED FIBROBLAST
ACTIVATION

This chapter was published in AJP-Cell Physiology[17] and has been reproduced with the permission of the
publisher and my co-authors.

2.1 Abstract

Extracellular vesicles released by cancer cells have recently been implicated in the differentiation of stromal cells to their activated, cancer-supporting states. Microvesicles, a subset of extracellular vesicles released from the plasma membrane of cancer cells, contain biologically active cargo, including DNA, mRNA, and miRNA, which are transferred to recipient cells and induce a phenotypic change in behavior. While it is known that microvesicles can alter recipient cell phenotype, little is known about how the physical properties of the TME affect fibroblast response to microvesicles. Here, we utilized cancer cell-derived microvesicles and synthetic substrates designed to mimic the stiffness of the tumor and tumor stroma to investigate the effects of microvesicles on fibroblast phenotype as a function of the mechanical properties of the microenvironment. We show that microvesicles released by highly malignant breast cancer cells cause an increase in fibroblast spreading, α smooth muscle actin expression, proliferation, cell-generated traction force, and collagen gel compaction. Notably, our data indicate that these phenotypic changes occur only on stiff matrices mimicking the stiffness of the tumor periphery and are dependent upon the cell type from which the microvesicles are shed. Overall, these results show that the effects of cancer cell-derived microvesicles on fibroblast activation are regulated by the physical properties of the microenvironment, and these data suggest that microvesicles may have a more robust effect on fibroblasts located at the tumor periphery to influence cancer progression.

2.2 Introduction

The stromal microenvironment plays a crucial role in the determination of cancer cell metastatic potential. Signaling molecules, extracellular components, and cells within the stroma can increase or decrease the metastatic potential of cancer cells[331]. This relationship is bidirectional as the microenvironment is often manipulated by cancer cells through both direct and indirect mechanisms. Recent studies have shown that EVs secreted by cancer cells, specifically exosomes and MVs, communicate with stromal cells to alter the local TME[15,332–334]. MVs originate from the plasma membrane of cells and range from 200 nm–1 μm in diameter[335]. They contain a wide variety of cargo, including ECM components, cytoskeletal proteins, and signaling molecules[15,90,336]. The interaction of cancer cell-derived MVs with recipient cells promotes cancer-supporting characteristics, including increased cell growth and survival[15,133]. The effects of MV components within the TME are just beginning to be uncovered.

Cancer cell invasion through the basement membrane and metastasis to a secondary site are highly dependent upon cell-cell and cell-matrix interactions[1]. Specifically, CAFs located in the TME have been shown to mediate cancer cell invasion and metastasis through the direct remodeling of the ECM[46,276,337]. CAFs use contractile forces to generate tracks in the ECM to guide cancer cell invasion and promote metastasis[46]. It is currently hypothesized that a large portion of CAFs in the TME are derived from fibroblasts adjacent to the primary tumor that have been transformed to an activated state[14]. It was recently established that MVs released from MDA-MB-231 breast cancer cells transform normal fibroblasts to exhibit increased survival capability and the ability to grow under low-serum conditions[15]. Proteomic screens of MDA-MB-231 MVs were carried out to determine the MV-associated proteins responsible for fibroblast transformation, specifically tissue transglutaminase and fibronectin [15].

Fibroblasts in the tumor stroma are exposed to both compliant healthy tissue and the increasingly stiff tissue of the primary tumor. Specifically, increased matrix stiffness has been shown to promote fibroblast spreading, traction force, and proliferation[338,339]. Here, we examined the effects of breast cancer cell-derived MVs on fibroblast function on substrates mimicking both healthy and tumorigenic tissue. We show that MVs increase fibroblast cell area, contractility, and proliferation in a manner that is dependent upon matrix stiffness. We additionally show that the ability to activate fibroblasts on stiff matrices is dependent upon the cell type from which the MVs are shed. Together, these results demonstrate the role of the mechanical properties of the matrix in regulating MV-induced fibroblast activation and matrix remodeling.

2.3   Materials and methods

Cell culture and reagents: MDA-MB-231 malignant mammary adenocarcinoma cells (HTB-26, ATCC, Manassas, VA), MDA-MB-231 cells (HTB-26, ATCC) transfected to express Lifeact-GFP, and NIH 3T3 fibroblasts were maintained in Dulbecco's Modified Eagle's Media (DMEM) (Thermofisher Scientific, Waltham, PA) supplemented with 10% FBS (Atlanta Biologicals, Flowery Branch, GA) and 1% penicillin-streptomycin (ThermoFisher Scientific). MCF10A mammary epithelial cells (CRL-10317; ATCC) were maintained in DMEM-F12 (ThermoFisher Scientific) supplemented with 5% horse serum (ThermoFisher Scientific), 0.5 µg ml^{-1} hydrocortisone (Sigma, St. Louis, MO), 20 ng ml^{-1} hEGF (ThermoFisher Scientific), 10 µg ml^{-1} insulin (Sigma), 100 ng ml^{-1} insulin (Sigma), and 1% penicillin-streptomycin. MCF7 mammary adenocarcinoma cells (HTB-22, ATCC) were maintained in Minimum Essential Medium (MEM) (ThermoFisher Scientific) supplemented with 10% FBS and 1% penicillin-streptomycin. All cells were cultured at 37°C and 5% CO_2. Primary antibodies used were rabbit anti-flotillin-2 (#3436; Cell Signaling Technology, Danvers, MA), rabbit anti-IκBα (#9242; Cell Signaling Technology), mouse anti-alpha smooth muscle actin (M0851, DAKO, Santa Clara, CA), and mouse anti-beta actin (A5316, Sigma).

Secondary antibodies used were HRP anti-rabbit (Rockland, Limerick, PA), HRP anti-mouse (Rockland), and AlexaFluor 488 conjugated to donkey anti-mouse (Life Technologies, Carlsbad, CA).

MV isolation and characterization: Sub confluent MDA-MB-231, MCF10A, and MCF7 cells were incubated overnight in serum-free DMEM, serum-free DMEM-F12, or serum-free MEM, respectively. The conditioned media was removed from the cells and centrifuged at 400 RPM. The supernatant was removed and again centrifuged at 400 RPM. The medium was then filtered through a 0.22 μm SteriFlip filter unit (EMD Millipore, Billerica, MA) and rinsed with serum-free media. The MVs retained by the filter were resuspended in their respective serum-free media. Nanoparticle tracking analysis (ZetaView ParticleMetrix, Germany) was used to determine the size and number of isolated MVs. N=3 independent sets of MV isolations.

Western blotting: Isolated MVs were rinsed with PBS on a 0.22 μm SteriFlip filter unit and lysed with Laemmli buffer. MDA-MB-231 cells were cultured on tissue culture plastic dishes, rinsed with PBS, and lysed with Laemmli buffer. Lysates were resolved by SDS-PAGE. The proteins were then transferred to PVDF membranes. Transferred membranes were blocked with 5% milk in TBS-Tween. Membranes were incubated overnight in IκBα (1:1000), Flotillin-2 (1:1000), and beta-actin (1:1000) in 5% milk in TBS-Tween at 4°C. Membranes were then incubated in horseradish peroxidase-conjugated secondary antibody (1:2000) in 5% milk in TBS-Tween for 1 hour at room temperature. Samples were imaged with a LAS-4000 imaging system (Fujifilm Life Science, Japan) after the addition of SuperSignal West Pico or West Dura Chemiluminescent Substrates (ThermoFisher Scientific). N=3 independent sets of MV isolations.

Polyacrylamide gel preparation: Polyacrylamide (PA) gels were fabricated as described elsewhere[340]. Briefly, the ratio of acrylamide (40% w/v; Bio-Rad, Hercules, CA) to bis-acrylamide (2% w/v; Bio-Rad) was varied to tune gel stiffness from 1 to 20 kPa to mimic the heterogeneous stiffness in the TME[8]. Moduli were changed by varying ratios of bis-acrylalmide:acrylamide [% acrylamide:% bis-acrylamide (Young's modulus (kPa))]; [3:0.1 (1)], [7.5:0.175 (5)], [12:0.19 (20)]. The PA gels were coated with 0.1 mg/ml rat tail type I collagen (Corning, Corning, NY).

Cell spreading assays: NIH 3T3 fibroblasts were seeded on 1, 5, or 20 kPa PA gels in 1.6 mL of DMEM + 1% FBS. Cell media was additionally supplemented with either 400 μL of serum-free media or approximately $5.5*10^7$ MVs suspended in 400 μL serum-free media. Phase contrast images were acquired at 20 minute intervals using a 10x/0.3 N.A. objective on a Zeiss Axio Observer Z1.m microscope. Only cells without contact with adjacent cells that spread to an area of at least 30% greater than its initial area were analyzed. For area analysis, cells were outlined in ImageJ (NIH, Bethesda, MD) and area was quantified. The data were regressed via a nonlinear least-squares regression to a modified error function of the form

$$A = \left[\text{erf}\left(\frac{t-t_{50}}{\tau}\right) + 1\right] \times A_{50} \tag{1}$$

previously used to describe cell spreading dynamics[341]. Briefly, A is the area of the cell, t is the time after plating, t_{50} is the time at which the cell has spread to half its maximum, and A_{50} is half the maximum area of the cell. N=3+ independent sets of PA gels and MV isolations.

Phalloidin and αSMA immunofluorescence and analysis: NIH 3T3 fibroblasts were seeded on 1, 5, or 20 kPa PA gels in 1.6 mL of DMEM + 1% FBS. Cell media was supplemented with either 400 μL of serum-free media or approximately $5.5*10^7$ MVs suspended in 400 μL serum-free media. After 24 hours, cells were fixed with 3.2% v/v paraformaldehyde (Electron Microscopy Sciences, Hartfield, PA) and permeabilized with 0.1% Triton-X-100 (J.T. Baker, Phillipsburg, NJ). Cells were blocked with 3% bovine serum albumin in 0.02% Tween in PBS and then incubated for 3 hours at room temperature with mouse anti-alpha smooth muscle actin (1:100). After being washed, cells were incubated for 1 hour with AlexaFluor 488 conjugated to donkey anti-mouse (1:200). The cells were washed and F-actin and nuclei were stained with AlexaFluor 568 phalloidin (1:500, Life Technologies, Carlsbad, CA) and DAPI (1:500, Molecular Probes, Eugene, OR), respectively. To image, gels were inverted onto a drop of Vectashield Mounting Media (Vector Laboratories, Burlingame, CA) placed on a glass slide. Fluorescent images were acquired with a 20x/1.0 N.A. water-immersion objective on a Zeiss LSM700 Upright laser-scanning microscope. For αSMA expression, cells stained with phalloidin were outlined in ImageJ. Cell area was overlaid onto αSMA images and integrated density was measured. Corrected total cell αSMA fluorescence was calculated by subtracting the cell area multiplied by the mean fluorescence of the background by the integrated density of the cell. N=3 independent sets of PA gels and MV isolations.

Cell proliferation assays: NIH 3T3 fibroblasts were serum-starved for 6 hours and subsequently seeded on 1, 5, or 20 kPa PA gels in 1.6 mL of DMEM + 1% FBS. Cell media was supplemented with either 400 μL of serum-free media or approximately $5.5*10^7$ MVs suspended in 400 μL serum-free media. After 24 hours, 10 μM 5-ethynyl-2'-dexoyuridine (EdU; ThermoFisher Scientific) was added to the culture media for 2 hours. Cells were fixed with 3.2% v/v paraformaldehyde (Electron Microscopy Sciences) and stained with the Click-iT EdU Kit (ThermoFisher Scientific) following the manufacturer's instructions. Nuclei were counterstained with DAPI (1:500). Cells were imaged with a 20x/1.0 N.A. water-immersion objective on a Zeiss LSM700 Upright laser-scanning microscope. The percentage of EdU incorporation was calculated as the ratio of EdU positive cells to the total number of cells. N=3 independent sets of PA gels and MV isolations.

Traction force microscopy: Traction force microscopy was performed as previously described[167]. Briefly, polyacrylamide (PA) gels, embedded with 0.5 μm diameter fluorescent beads (Life Technologies), were prepared with Young's moduli of 1 kPa, 5 kPa, and 20 kPa. Some traction force experiments were only conducted on 5 kPa and 20 kPa PA gels due to the difficulty of cell adhesion onto soft gels in low serum conditions. NIH 3T3 fibroblasts were allowed to adhere for 24 hours in 1.6 mL of DMEM + 1% FBS

supplemented with either 400 μL of serum-free media, approximately 5.5*10^7 MVs suspended in 400 μL serum-free media, 400 μL of conditioned media, or approximately 5.5*10^7 MVs suspended in 400 μL conditioned media. After 24 hours, phase contrast images of single fibroblasts and fluorescent images of the bead field at the surface of the PA gel were acquired. Fibroblasts were removed from the PA gel using 0.25% trypsin/EDTA (Life Technologies) and a fluorescent image of the bead field was acquired after cell removal. Bead displacements between the stressed and null states and fibroblast area were calculated and analyzed using the LIBTRC library developed by M. Dembo (Dept. of Biomedical Engineering, Boston University)[342]. The overall cellular force is the integral of the traction vectors over the total cell area. Outliers were removed using the ROUT method with Q = 0.2%. N=3 independent sets of PA gels and MV isolations.

Collagen gel contraction: Type I collagen was isolated from rat tail tendons (Rockland) and solubilized to form 10 mg/mL stock solutions as previously described[343]. Briefly, collagen stock solutions were mixed with 0.5 M ribose to form collagen solutions containing a final concentration of 100 mM ribose in 0.1% sterile acetic acid and incubated at 4°C for 5 days. Glycated collagen solutions were neutralized with 1 M sodium hydroxide (Sigma) in 10X PBS buffer (Life Technologies) and mixed with HEPES (EMD Millipore) and sodium bicarbonate (JT Baker) in 10X PBS to form 1.5 mg/mL collagen gels. When added to collagen, ribose interacts with amino groups on proteins to form Schiff bases that rearrange into Amadori products. Amadori products form advanced glycation endproducts (AGE) that accumulate on proteins and result in cross-link formation [343]. 3T3 fibroblasts were seeded at a density of 200,000 fibroblasts per mL of collagen gel for a final volume of 500 μL collagen gels. Collagen gels were cultured in 1.1 mL DMEM+1% FBS and supplemented with either 400 μL of serum-free media or approximately 5.5*10^7 MVs suspended in 400 μL serum-free media. Gels were unattached from the well-plate by tracing around the outward edge of the gel with a pipet tip. Gels were allowed to contract for 48 hours and subsequently imaged. N=4 independent sets of collagen gels and MV isolations.

Statistical analysis All statistical analysis was performed using GraphPad Prism 7 (GraphPad Software, La Jolla, CA) or Excel 2016 (Microsoft, Redmond, WA). Where appropriate, data were compared with a student's t-test or with a two-way analysis of variance (ANOVA) with Sidak multiple comparisons test. All data is reported as mean ± standard error (SE).

2.4 Results

2.4.1 *Highly malignant breast cancer cells release MVs.*

To examine the role of cancer cell-derived MVs on fibroblasts, we first isolated MVs from the highly malignant MDA-MB-231 breast cancer cells. The release of MVs by breast cancer cells was visualized by culturing LifeAct-GFP MDA-MB-231 breast cancer cells in serum-free media (**Figure 2.1A**). MVs were isolated from breast cancer cells using centrifugation and subsequent filtration. Isolated MVs

were confirmed to be within the expected size distribution (200 nm-1 μm) using nanoparticle tracking analysis (**Figure 2.1B**). Western blot analysis confirmed the expression of the MV marker flotillin-2 in MV lysates and the absence of the cytosolic marker IκBα, showing no cytosolic contamination from intact cells in the MV samples (**Figure 2.1C**). These results are consistent with prior studies suggesting that MDA-MB-231 breast cancer cells release extracellular vesicles within the MV class[15,133,344].
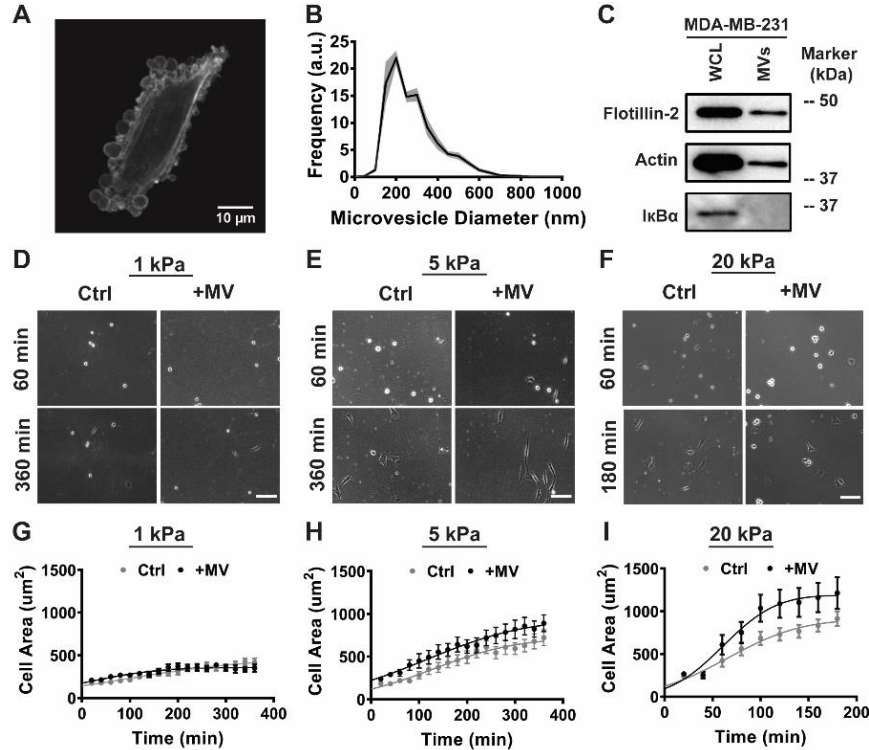
Figure 2.1. Cancer cell-derived MVs increase fibroblast early spreading dynamics on stiff matrices.
(**A**) Fluorescent image of MDA-MB-231 cell in serum-free media. (**B**) Size distribution of isolated MVs.
(**C**) Representative immunoblots of actin, the MV marker flotillin-2, and the cytosolic-specific marker IκBα in whole cell lysates (WCL) and MV lysates (MVs). (**D-F**) Representative images of early spreading in fibroblasts treated with serum-free media alone (Ctrl) or MVs (+MV) on (**D**) 1 kPa, (**E**) 5kPa, and (**F**) 20 kPa PA gels. Scale bar = 100 μm. (**G-I**) Measurements of fibroblast cell area during early cell spreading, taken every 20 minutes, on (**G**) 1 kPa (Ctrl: n=24, +MV: n=14), (**H**) 5 kPa (Ctrl: n=34, +MV: n=27), and (**I**) 20 kPa PA gels (Ctrl: n=30, +MV: n=28). Data points fit to a nonlinear least-squares regression of a modified error function. Plots are mean ± SE. N=3+ independent sets of PA gels and MV isolations.

Table 2.1. Regression parameter values for data presented in Figure 2.1.

	1 kPa		5 kPa		20 kPa	
	Ctrl	+MV	Ctrl	+MV	Ctrl	+MV
R^2	0.9701	0.89	0.9745	0.9845	0.9782	0.9766
t_{50}	95.72	5.069	130.5	113.6	65.58	62
A_{50}	227.2	179.6	359.9	462.6	451.2	593.1

2.4.2   Cancer cell-derived MVs increase fibroblast early spreading dynamics on stiff matrices.

Fibroblasts in the tumor stroma are exposed to a range of matrix stiffness due to heterogeneities in ECM composition. As increased matrix stiffness has been shown to directly promote fibroblast spreading and the ability of a cell to spread directly affects its function, we investigated the relationship between matrix stiffness and MV-mediated fibroblast spreading[339,345–348]. MVs were applied to fibroblasts at the time of seeding on PA gels of varying stiffness (1-20 kPa), spanning the range of matrix stiffness in physiologically relevant breast tissue[8]. Cell spreading was monitored using time-lapse microscopy, and the data were fit to a modified error function to obtain the half-maximum spreading area, A_{50}, and the half-maximum spreading time, t_{50}[341] (**Table 2.1**, see Methods for details). As expected, significant differences in A_{50} were calculated between increasing PA gel stiffness within control or MV conditions (**Table 2.2**), highlighting the role of matrix stiffness in fibroblast spreading. At a stiffness mimicking healthy breast tissue (1 kPa), MVs did not affect early fibroblast spreading dynamics or fibroblast cell area after 24 hours of culture (**Figure 2.1D,G**, **Figure 2.2A-B**); no change in the A_{50} was observed between control and MV conditions (**Table 2.2**). However, on moderately stiff PA gels mimicking tumorigenic breast tissue (5 kPa), culture with MVs increased the rate of early fibroblast spreading (**Figure 2.1E,H**). Likewise, a significant difference in the A_{50} was calculated between control and MV conditions on the 5 kPa PA gel (**Table 2.2**). After 24 hours of culture, no change in fibroblast cell area was noted between control and MV conditions on 5 kPa PA gels (**Figure 2.2A,B**). Additionally, increased rate of early fibroblast spreading was evident in fibroblast culture with MVs on the stiffest substrate tested (20 kPa), where the rate of early spreading was increased as well as fibroblast cell area throughout the entire observation period (**Figure 2.1F,I, Figure 2.2A-B**). A significant difference in A_{50} was observed between control and MV conditions on the 20 kPa gel (**Table 2.2**) as well as a significant difference between cell area after 24 hours of culture (**Figure 2.2A-B**). These results indicate that MVs derived from highly malignant breast cancer cells cause an increase in early fibroblast spreading on stiff matrices, highlighting the role of matrix mechanical properties in regulating cellular interactions and fibroblast function in the TME.

Table 2.2. Statistical comparison of regression parameter values using two-way ANOVA with Sidak test for multiple comparisons. *p<0.05, ***p<0.001, ****p<0.0001.

	A_{50}
1 kPa Ctrl vs 1 kPa +MV	N.s.
5 kPa Ctrl vs 5 kPa +MV	***
20 kPa Ctrl vs 20 kPa +MV	***
1 kPa Ctrl vs 5 kPa Ctrl	****
5 kPa Ctrl vs 20 kPa Ctrl	*
1 kPa +MV vs 5 kPa +MV	****
5 kPa +MV vs 20 kPa +MV	***
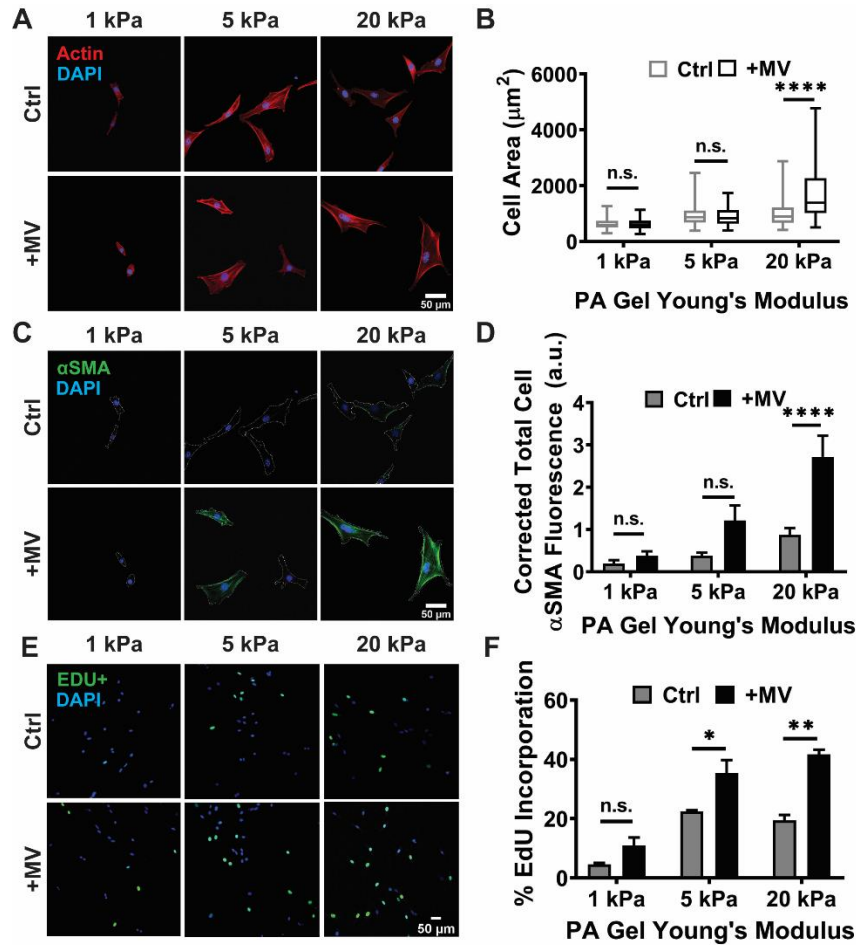
Figure 2.2. Cancer cell-derived MVs induce CAF-like fibroblast phenotypes on stiff matrices. (A) Representative images of fibroblast actin (red) after culture in serum-free media alone (Ctrl) or MVs (+MV) on 1, 5, or 20 kPa PA gels. **(B)** Measurements of fibroblast cell area after 24 hours of culture on 1 (Ctrl: n= 75, +MV: n= 75), 5 (Ctrl: n= 80, +MV: n= 80), and 20 kPa PA gels (Ctrl: n= 80, +MV: n= 80) in Ctrl and +MV conditions. Plots are median ± the minimum and maximum values. **(C)** Representative images of fibroblast αSMA (green) after 24 hours of culture in Ctrl and +MV conditions. Cell perimeter outlined in dashed white line. **(D)** Measurements of fibroblast αSMA fluorescence after 24 hours of culture on 1 (Ctrl: n=67, +MV: n=64), 5 (Ctrl: n= 66, +MV: n= 68), and 20 kPa PA gels (Ctrl: n= 80, +MV: n= 75) in Ctrl and +MV conditions. **(E)** Representative fluorescent images of fibroblast EdU incorporation after treatment with serum-free media alone (Ctrl) or MVs (+MV) for 24 hours on 1, 5, or 20 kPa PA gels. EdU+ cells in green. DAPI in blue. **(F)** Fibroblast proliferation after culture in Ctrl or +MV conditions for 24 hours as determined by Click-iT EdU staining. Percentages are relative to total cell number. 10 representative images taken for each conditions; over 500 cells analyzed for each condition. N=3 independent sets of PA gels and MV isolations. Plots are mean ± SE. Scale bar = 200 μm. *$p<0.05$, **$p<0.01$, ****$p<0.0001$ from two-way ANOVA with Sidak test for multiple comparisons. N.s. not significant.

2.4.3   *Cancer cell-derived MVs induce CAF-like fibroblast phenotypes on stiff matrices.*

After 24 hours of culture with cancer cell-derived MVs, fibroblasts on 1 and 5 kPa PA gels exhibited no change in cell area compared to control conditions while fibroblasts on 20 kPa PA gels exhibited significantly larger cell area following treatment with MV (**Figure 2.2A-B**). Since MVs induce a

more robust spreading response when cells are on stiff substrates, we hypothesized that cancer cell-derived MVs in conjunction with a stiff microenvironment may help activate fibroblasts to their cancer-associated state. αSMA expression, a marker of fibroblast activation[349–351], was quantified to measure fibroblast activation. In control conditions, αSMA expression slightly increased with increasing matrix stiffness. After 24 hours of culture with MVs, fibroblasts on 1 and 5 kPa PA gels exhibited no significant increase in αSMA expression, compared to control conditions (**Figure 2.2C-D**). However, a robust increase in αSMA expression was evident in fibroblasts cultured with MVs on 20 kPa PA gels, compared to control conditions (**Figure2.2C-D**). These results suggest that MV-induced fibroblast activation increases with matrix stiffness. Given that the ability of cells to spread and fibroblast activation have been shown to be related to proliferation [14,345], and our data indicates MVs affect spreading and activation, we sought to determine if cancer cell-derived MVs affect fibroblast proliferation on matrices of varying physiological stiffness. Fibroblast proliferation in control conditions increases on stiffer (5 and 20 kPa) matrices compared to more compliant (1 kPa) matrices, and MVs significantly increased fibroblast proliferation on both 5 and 20 kPa matrix conditions (**Figure 2.2E-F**). These results indicate that matrix stiffness enhances MV-induced fibroblast proliferation.

2.4.4 *Cancer cell-derived MVs increase fibroblast contraction on stiff matrices.*

As we observe increased cell spreading and αSMA expression on stiff substrates in response to MVs, we sought to assess whether cell contractility also increases. For a fibroblast to remodel its surrounding matrix, it uses actomyosin contractility to generate force to rearrange the matrix[352]. To assess the effects of cancer cell-derived MVs on fibroblast-matrix interactions, we utilized traction force microscopy to measure cellular contractile force following MV treatment. Given that our data indicates that matrix stiffness alters fibroblast spreading in response to MVs, and given that fibroblasts encounter heterogeneous stromal environments with varying stiffness during cancer progression[353–356], we measured fibroblast traction force on substrates of varying stiffness (1-20 kPa). At a stiffness mimicking healthy breast tissue (1 kPa), fibroblasts exhibited no change in total traction force per cell or traction stress when cultured with MVs for 24 hours (**Figure 2.3A-C**). Likewise, no statistically significant change in total traction force or traction stress was exhibited in fibroblasts cultured on a moderate stiffness mimicking tumorigenic conditions in breast tissue (5 kPa) (**Figure 2.3A-C**). However, on 20 kPa substrates, mimicking the highest ECM stiffness found in breast cancer[8], MVs induced a robust increase in fibroblast traction force (**Figure 2.3A**). Since the force is the traction stress integrated over the area, these data indicate that this change is not simply a result of the increased cell area observed in Figure 2. Fibroblasts cultured with MVs on the stiff matrices also exhibited an increase in traction stress, indicating an increase in the ability of fibroblasts to contract the matrix (**Figure 2.3B-C**). These data suggest that increasing matrix stiffness enhances the effects of cancer cell-derived MVs on fibroblast contractility.

To further investigate the increased traction force initiated by cancer-derived MVs, we assessed the ability of fibroblasts to contract collagen gels. The stiffness of collagen gels was modulated by non-enzymatic glycation without altering the density of collagen gel[343]. Fibroblasts were cultured in non-glycated and glycated 1.5 mg/mL collagen gels, with Young's Moduli of approximately 175 Pa and 575 Pa, respectively [343], for 48 hours in control or MV conditions. Fibroblasts cultured in control conditions exhibited greater collagen gel contraction in more compliant matrices compared to stiffer matrices (**Figure 2.3D-E**). Fibroblasts cultured with MVs exhibited significantly increased collagen gel contraction compared to control conditions in glycated matrices (**Figure 2.3D-E**). These data reveal that MVs increase fibroblast collagen gel contraction to a greater magnitude on stiffer, glycated matrices. These results are consistent with our data on 2D substrates (**Figure 2.3A-C**) which indicates cancer cell-derived MVs increase the ability of fibroblasts to contract stiffer matrices. Specifically, this system extends the effects of MVs on fibroblasts to more physiologically relevant 3D microenvironments.
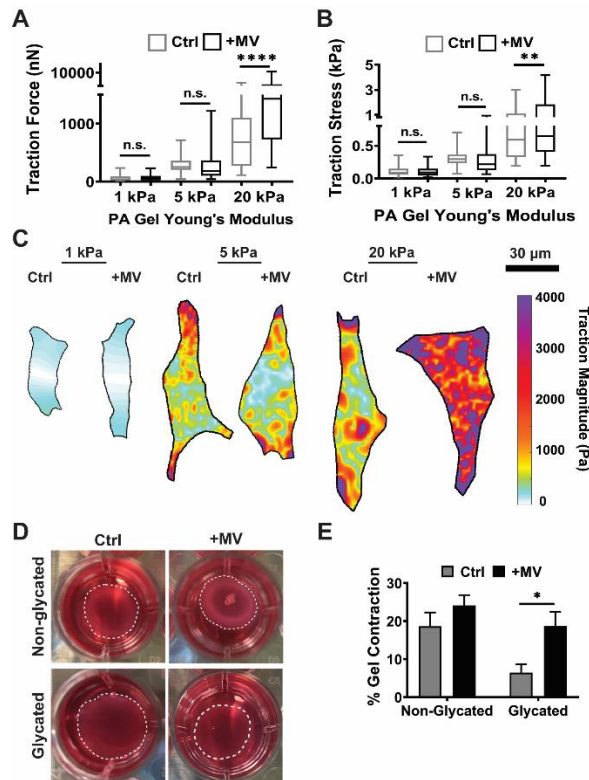
Figure 2.3. Cancer cell-derived MVs increase fibroblast contraction on stiff matrices. (A) Traction force measurements of fibroblasts treated with serum-free media alone (Ctrl) or MVs (+MV) on 1 (Ctrl: n=64, +MV: n=44), 5 (Ctrl: n=47, +MV: n=51), and 20 (Ctrl: n=39, +MV: n=42) kPa PA gels. **(B)** Traction stress measurements (Traction Force/Cell Area) of fibroblasts in Ctrl and +MV culture conditions on 1 (Ctrl: n=64, +MV: n=44), 5 (Ctrl: n=47, +MV: n=51), and 20 (Ctrl: n=39, +MV: n=42) kPa PA gels. N = 3 independent sets of PA gels and MV isolations. Plots are median ± the minimum and maximum values. **(C)** Representative traction stress maps of fibroblasts in Ctrl and +MV culture conditions on 1, 5, and 20 kPa PA gels. **(D)** Representative images of collagen gel contraction after 48 hours. **(E)** Collagen gel contraction by fibroblasts treated with serum-free media alone (Ctrl) or MVs (+MV) for 48 hours in non-

glycated (n=12) or glycated (n=12) matrices. N = 4 independent sets of collagen gels and MV isolations. *p<0.05, **p<0.01, ****p<0.0001 from two-way ANOVA with Sidak test for multiple comparisons. N.s. not significant.

2.4.5 Cancer-cell derived MVs are significant regulators of fibroblast function independently of the overall cancer cell secretome.

Cancer cells release a variety of components into the extracellular space, including cell motility factors, growth factors, proteases, and cytokines, in addition to extracellular vesicles[357]. As MVs are just one of the many components released from cancer cells, we sought to determine whether MVs are a physiology significant regulator of fibroblast function in the TME compared to the overall secretome. To compare the effects of MVs to other components of the cancer cell secretome, isolated MVs were resuspended in cancer cell conditioned media and applied to fibroblasts. On stiff 20 kPa PA gels, fibroblasts cultured with MVs suspended in conditioned media exhibited increased cell area (**Figure 2.4A**), traction force (**Figure 2.4B**), and traction stress (**Figure 2.4C-D**), compared to fibroblasts cultured with conditioned media alone. This data indicates that MVs are not outcompeted by other components of the cancer cell secretome.
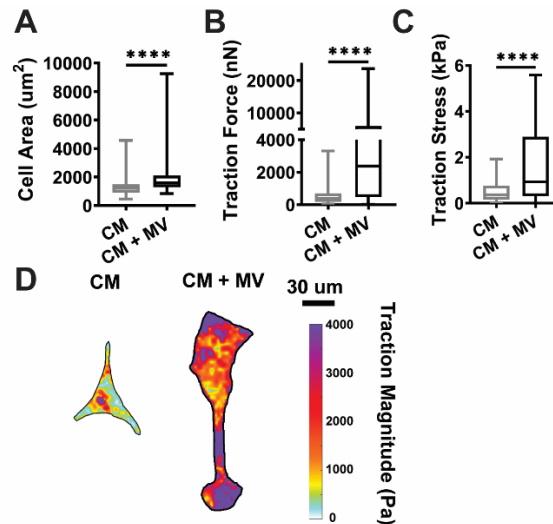
Figure 2.4. Cancer-cell derived MVs alter fibroblast function independently of other secreted factors. **(A)** Cell area of fibroblasts treated with conditioned media (CM) or conditioned media supplemented with MVs (CM + MV) for 24 hours on 20 kPa PA gels (CM: n=72, CM + MV: n=78). **(B)** Traction force measurements of fibroblasts in CM and CM + MV culture conditions on 20 kPa PA gels (CM: n=41, CM + MV: n=50) **(C)** Traction stress measurements (Traction Force/Cell Area) of fibroblasts in CM and CM + MV culture conditions on 20 kPa PA gels (CM: n=41, CM + MV: n=50). **(D)** Representative traction stress maps of fibroblasts in CM and CM + MV culture conditions on 20 kPa PA gels. N = 3 independent sets of PA gels and MV isolations. Plots are median ± the minimum and maximum values. ****p<0.0001 from student's unpaired t-test.

2.4.6   MV-induced fibroblast activation is MV cell-type dependent.

To determine whether the cell type from which the MVs are shed influences the matrix stiffness-dependent effect of MVs on fibroblasts, MVs were isolated from the MCF10A breast epithelial cells and MCF7 breast cancer cells, which are considered less aggressive than MDA-MB-213 cells. MCF10As, MCF7s, and MDA-MB-231 cells all released comparable numbers of MVs (**Figure 2.5A**). MVs isolated from MCF7 and MDA-MB-231 cells had similar size distributions, while MCF10A MVs shift towards larger diameters (**Figure 2.5B**). To investigate the effects of these MVs on fibroblast function, fibroblasts were cultured with MCF10A or MCF7 MVs on both 5 and 20 kPa PA gels. Fibroblasts cultured with MCF10A MVs exhibited no change in cell area, traction force, or traction stress on either 5 or 20 kPa PA gels (**Figure 2.5C-F**). Fibroblasts cultured with MCF7 MVs exhibited no change in cell area on either 5 or 20 kPa PA gels (**Figure 2.5G**), but cell contractility increased on stiff 20 kPa PA gels (**Figure 2.5H-J**). This data indicates that the effect of MVs on fibroblast function is cell-type dependent, as MVs from non-malignant epithelial cells had no influence upon fibroblast cell area or traction force. This data also suggests that the effect may be dependent upon cancer cell malignancy, as the magnitude of change in fibroblast contractility appeared to increase from non-malignant (MCF10A), to weakly metastatic (MCF7), to more aggressive (MDA-MB-231) cancer cells. However, MVs from additional cell lines from different cancer types would need to be tested to fully address this finding.
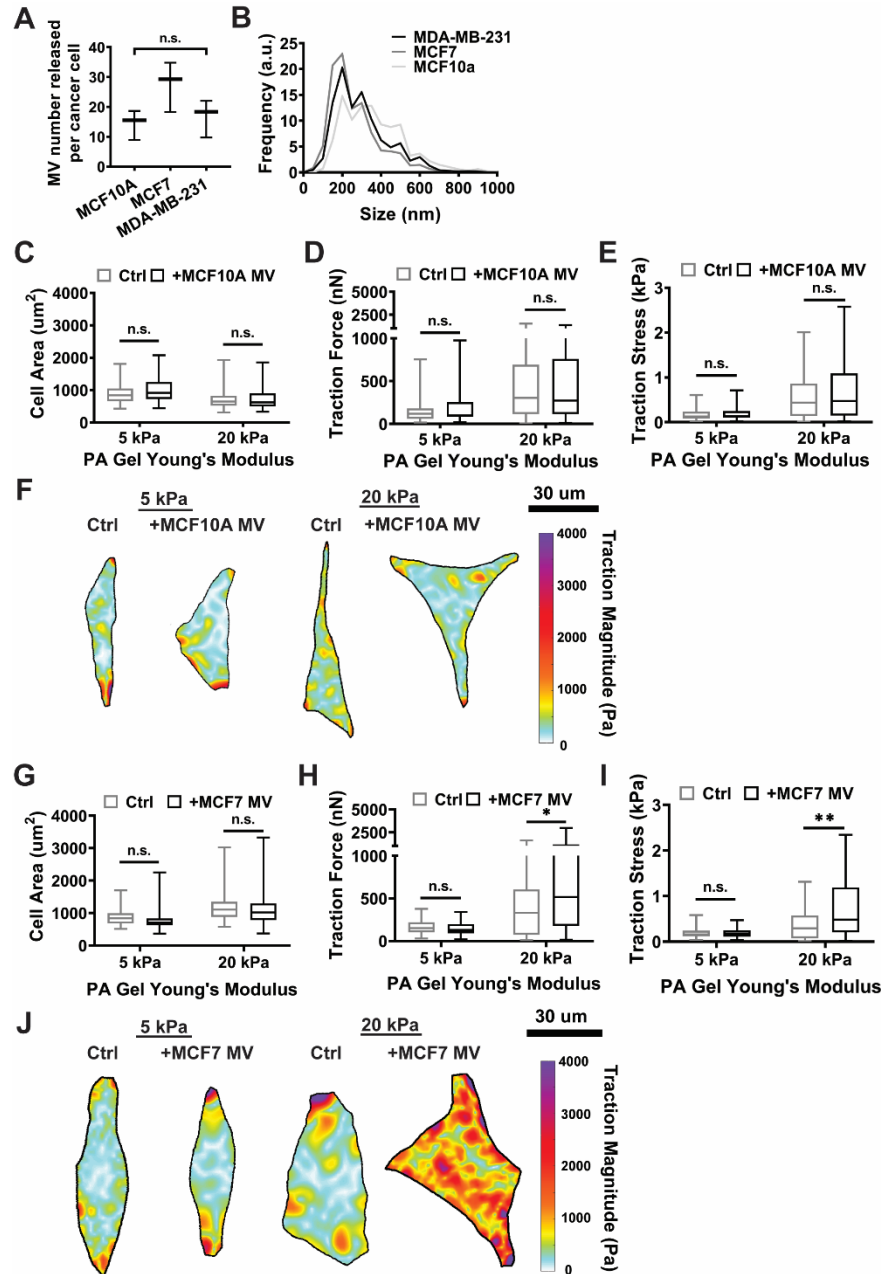
Figure 2.5. MV-induced fibroblast activation is MV cell-type dependent. (**A**) Number of MVs released by MCF10A, MCF7, and MDA-MB-231 cancer cells. (**B**) MCF10A, MCF7, and MDA-MB-231 MV size distributions. N=3 independent MV isolations. (**C**) Cell area measurements of fibroblasts treated with serum-free media alone (Ctrl) or MCF10A MVs (+MCF10A MV) on 5 (Ctrl: n=67, +MCF10A MV: n=66) and 20 (Ctrl: n=75, +MCF10A MV: n=75) kPa PA gels. (**D**) Traction force measurements of fibroblasts in Ctrl and +MCF10A MV culture conditions on 5 (Ctrl: n=42, +MCF10A MV: n=33) and 20 (Ctrl: n=51, +MCF10A MV: n=49) kPa PA gels. (**E**) Traction stress measurements (Traction Force/Cell Area) of fibroblasts in Ctrl and +MCF10A MV culture conditions on 5 (Ctrl: n=42, +MCF10A MV: n=33) and 20 (Ctrl: n=51, +MCF10A MV: n=49) kPa PA gels. (**F**) Representative traction stress maps of fibroblasts in Ctrl and +MCF10A MV culture conditions on 5 and 20 kPa PA gels. (**G**) Cell area measurements of fibroblasts treated with serum-free media alone (Ctrl) or MCF7 MVs (+MCF7 MV) on 5 (Ctrl: n=63, +MCF7 MV: n=63) and 20 (Ctrl: n=68, +MCF7 MV: n=69) kPa PA gels. (**H**) Traction force measurements

42

of fibroblasts in Ctrl and +MCF10A MV culture conditions on 5 (Ctrl: n=30, +MCF7 MV: n=30) and 20 (Ctrl: n=42, +MCF7 MV: n=40) kPa PA gels. **(I)** Traction stress measurements (Traction Force/Cell Area) of fibroblasts in Ctrl and +MCF10A MV culture conditions on 5 (Ctrl: n=30, +MCF7 MV: n=30) and 20 (Ctrl: n=42, +MCF7 MV: n=40) kPa PA gels. **(J)** Representative traction stress maps of fibroblasts in Ctrl and +MCF7 MV culture conditions on 5 and 20 kPa PA gels. N = 3 independent sets of PA gels and MV isolations. Plots are median ± the minimum and maximum values. *$p<0.05$, **$p<0.01$ from two-way ANOVA with Sidak test for multiple comparisons. N.s. not significant.

2.5   Discussion

Recent evidence has highlighted the ability of EVs to transform epithelial and stromal cells to promote cancer progression. Specifically, exosomes have been implicated in the promotion of cancer cell migration, chemotaxis, tumorigenicity, and chemoresistance, and the transformation of stromal fibroblasts and macrophages to cancer-promoting states[213,332,358–363]. These phenotypes are the result of the transfer of oncogenic proteins from cancer cells, including mutant KRAS proteins, TGF-β1, and microRNA[213,332,360,363]. However, the effects of MVs, a distinct class of EVs released from the plasma membrane of cancer cells, on the TME are just beginning to be uncovered. Here, we show that MVs induce changes in fibroblast spreading, αSMA expression, proliferation, cell-generated traction forces, and collagen gel compaction. Importantly, the MV-induced phenotypes assessed in this study were enhanced with matrix stiffness.

Our data suggests that matrix stiffness may prime non-transformed fibroblasts for activation by MV cargo. Previously, matrix stiffness was shown to sensitize various cells to respond to growth factors. Matrix stiffening was shown to sensitize cells to EGF, with implications in epithelial cell proliferation[211]. Similarly, increased matrix stiffness was shown to increase EGF-dependent growth in epithelial cells[169]. Additionally, matrix stiffness enhances VEGFR-2 internalization, signaling, and proliferation in endothelial cells[212]. As such, matrix stiffness may play a role in the sensitivity of fibroblasts to MV cargo.

Other than priming cells for response to MVs, the stiffness-dependent differences that we have identified may also be due to differences in MV uptake. Conflicting evidence exists as to whether endocytosis is altered with matrix stiffness. Epithelial cells cultured on varying PA gel stiffness showed increased nanoparticle uptake on 20 kPa PA gels relative to 1 kPa gels[364]. However, it has also been shown that epithelial cells cultured on soft matrices had significantly enhanced EV uptake, compared to tissue culture polystyrene[365]. Additionally, uptake of MK2 by mesothelial cells is increased on soft substrates, compared to stiff substrates[366]. As such, matrix stiffness may play a role in MV uptake by stromal cells; however, it is not yet clear and requires further investigation.

Previously, matrix stiffness was identified as a central regulator of fibroblast activation and fibroblast-induced fibrosis in the lung. Specifically, TGF-β1 was shown to enhance fibroblast traction forces on stiff matrices mimicking fibrotic lung tissue, but not on matrices mimicking the stiffness of

healthy lung tissue[339]. Additionally, YAP and TAZ were identified as mechano-activated regulators of the matrix stiffness-driven feedback loop that amplifies lung fibrosis[367]. Together, these results suggest a role for matrix stiffness in fibroblast-induced fibrosis of the lung, where the fibrotic ECM is both a cause and a consequence of fibroblast activation. We identify a similar phenomenon in the TME. We speculate that a feedback loops exists where matrix stiffness amplifies MV-induced fibroblast activation, which further stiffens the matrix to activate both fibroblasts and other cell types in the TME. As a whole, these results suggest that the compliance of healthy tissue may inhibit MV-induced fibroblast activation.

Interestingly, MV release from cancer cells is also likely regulated by matrix stiffness, further adding to the consequences of this feedback loop. Previously, MV shedding was determined to be regulated by the GTPase RhoA[368]. Significant evidence exists to suggest that RhoA activity in cells is highly regulated by matrix stiffness[174]. As such, it is likely that the increased matrix remodeling by MV-activated fibroblasts also results in increased MV release from cancer cells to further activate stromal cells. This feedback loop would then result in further matrix stiffening.

Here, we focus on the primary TME; however, it is known that MVs have been identified in the circulation of cancer patients[132]. The transfer of exosomal contents to recipient cells is believed to play a role in the preparation of the premetastatic niche[91,369]. Exosomal integrins were found contribute to the premetastatic niche and direct organ-specific colonization by fusing with cells in a tissue-specific fashion, shown to play roles in brain, lung, and liver metastasis[369]. Additionally, exosomal microRNA associated with osteoblast differentiation was identified in cancer exosomes, believed to play a role in the preparation of the premetastatic niche for bone metastasis[91]. Interestingly, it has also been shown that CAFs in breast tumors select for cancer cell clones that are more equipped for bone metastasis[370]. Consequently, MVs released by the primary tumor may both travel to distant sites in the body to prime the pre-metastatic niche as well as activate fibroblasts surrounding the primary tumor involved in metastatic cell selection. Further studies are required to determine if the MV class of extracellular vesicles are identified in distant tissues. Based on our data, it is possible that MVs may play a role in the development of the pre-metastatic niche of stiffer tissues, such as breast to bone metastasis. While we focus here on contractility, it is also possible that MVs may induce the release of soluble signals from fibroblasts that may also play a role in priming.

Overall, our work reveals a novel mediator in the bidirectional relationship between cancer cells and fibroblasts in the TME. As fibroblast activation is associated with cancer progression, cancer-derived MVs appear to play a role in transforming fibroblasts to an activated state to prime the TME for metastasis. We hypothesize that a matrix stiffness feedback loops exists in which MV-induced fibroblast activation further stiffens the matrix promote cancer progression. Additionally, the robust response of fibroblasts to culture with MVs on matrices ranging from 5-20 kPa highlights the sensitivity of fibroblasts to MV contents at the tumor periphery. Significantly, this region is where fibroblasts form tracks in the matrix or align

fibers to promote cancer cell invasion. Future studies should assess the ability of cancer cells to sense MV-mediated fibroblast remodeling.

CHAPTER 3: WEAKLY MIGRATORY METASTATIC BREAST CANCER CELLS ACTIVATE FIBROBLASTS VIA MICROVESICLE-ASSOCIATED TG2 TO FACILITATE DISSEMINATION AND METASTASIS

This chapter is in revision and is available on BioRxiv[371] and has been reproduced with permission of the publisher and my co-authors.

3.1   Abstract

Cancer cell migration is highly heterogeneous, and the migratory capability of cancer cells is thought to be an indicator of metastatic potential. It is becoming clear that a cancer cell does not have to be inherently migratory to metastasize, with weakly migratory cancer cells often found to be highly metastatic. However, the mechanism through which weakly migratory cells escape from the primary tumor remains unclear. Here, utilizing phenotypically sorted highly and weakly migratory breast cancer cells, we demonstrate that weakly migratory metastatic cells disseminate from the primary tumor via communication with stromal cells. While highly migratory cells are capable of single cell migration, weakly migratory cells rely on cell-cell signaling with fibroblasts to escape the primary tumor. Weakly migratory cells release microvesicles rich in tissue transglutaminase 2 (Tg2) which activate fibroblasts and lead weakly migratory cancer cell migration *in vitro*. These microvesicles also induce tumor stiffening and fibroblast activation *in vivo* and enhance the metastasis of weakly migratory cells. Our results identify microvesicles and Tg2 as potential therapeutic targets for metastasis and reveal a novel aspect of the metastatic cascade in which weakly migratory cells release microvesicles which activate fibroblasts to enhance cancer cell dissemination.

3.2   Introduction

It is known that cancer cell migration *in vivo* can be highly heterogeneous with cells exhibiting a wide range of migratory phenotypes, including amoeboid, mesenchymal, single cell, and collective migration[242,372,373]. Even within a single population, cells can exhibit different migration phenotypes[374–377] resulting from intrinsic cancer cell genetic differences[378–381] and extrinsic factors, such as interactions with the extracellular matrix or stromal cells[175,214,372,382–385]. As the first step in the metastatic cascade involves the migration and invasion of cancer cells away from the primary tumor, migratory capability is largely believed to be an indicator of cancer progression[229,386–388]. However, it is now becoming clear that a cancer cell does not have to be inherently migratory to metastasize[377,389–393]. In fact, some of the highly metastatic phenotypes in breast and colorectal cancers are often less migratory than the weakly metastatic phenotypes, yet they are still able to enter the circulation as efficiently[377,390,392–394]. While enhanced clustering, survival, and proliferation have been suggested as potential mechanisms for why weakly migratory cells can outperform their highly migratory counterparts in the late stages of the metastatic cascade thus contributing

to metastasis[377,392], it is not clear how these weakly migratory cells can efficiently escape from the primary site.

To escape the primary site during local invasion, cancer cells navigate through a heterogeneous TME, where they interact with the extracellular matrix and a diverse collection of stromal cells. Chemical, physical, and metabolic interactions with the TME are known to alter the invasion capacity of cancer cells[214,395,396]. CAFs are a stromal cell in the TME that can lead and promote tumor cell invasion and metastasis through extracellular matrix (ECM) remodeling[13,46,214,383,397–399]. CAFs at the primary tumor are largely derived from fibroblasts that have been transformed to a more contractile, activated state[14], and cancer-derived MV) have recently been implicated in fibroblast activation[15–17]. Thus, we hypothesized that while highly migratory cells can escape the primary tumor independently, CAFs facilitate weakly migratory cancer cell escape from the primary tumor.

Here, we identify a novel aspect of the metastatic cascade by which weakly migratory cancer cells release Tg2-rich MVs to activate fibroblasts and enhance cancer cell dissemination. Moreover, highly and weakly migratory cells release MVs which differentially signal to the TME. MVs from highly migratory cells have little effect on fibroblast activation, and highly migratory cells do not require activated fibroblasts to migrate. In contrast, MVs from weakly migratory cells are rich in Tg2 and activate fibroblasts which enhance fibroblast-led weakly cancer cell migration *in vitro*. These MVs also induce tumor stiffening and fibroblast activation *in vivo* and enhance the metastasis of weakly migratory cells. Our findings highlight MVs and Tg2 as potential targets for developing therapeutics to prevent metastasis.

3.3   Materials and methods

Cell culture and reagents: MDA-MB-231 malignant mammary adenocarcinoma cells (HTB-26, ATCC, Manassas, VA), NIH 3T3 fibroblasts, and all modified cell lines were maintained in Dulbecco's Modified Eagle's Media (DMEM) (ThermoFisher Scientific, Waltham, PA) supplemented with 10% fetal bovine serum (FBS) (Atlanta Biologicals, Flowery Branch, GA) and 1% penicillin-streptomycin (ThermoFisher Scientific). MCF7 mammary adenocarcinoma cells (HTB-22; ATCC) were maintained in minimum essential medium (MEM) (ThermoFisher Scientific) supplemented with 10% FBS and 1% penicillin-streptomycin. All cells were cultured at 37°C and 5% CO_2. Primary antibodies used were rabbit anti-flotillin-2 (3436; Cell Signaling Technology, Danvers, MA), mouse anti-α smooth muscle actin (M0851, DAKO, Santa Clara, CA), mouse anti-beta actin (A5316, Millipore Sigma, Burlington, MA), mouse anti-tissue transglutaminase 2 (ab2386, Abcam, Cambridge, UK), goat anti-fibronectin (sc6953, Santa Cruz, Dallas, TX), rabbit anti-fibronectin (F3648, Millipore Sigma), rabbit anti-focal adhesion kinase (3285, Cell Signaling Technology, Danvers, MA), rabbit anti p-focal adhesion kinase (Tyr397) (3283, Cell Signaling Technology), and mouse-anti GAPDH (MAB374, Millipore Sigma). Secondary antibodies used were HRP anti-rabbit (Rockland, Limerick, PA), HRP anti-mouse (Rockland), AlexaFluor 488 conjugated to donkey

47

anti-goat (Life Technologies, Carlsbad, CA), AlexaFluor 488 conjugated to donkey anti-rabbit (Life Technologies), AlexaFluor 488 conjugated to donkey anti-mouse (Life Technologies), and AlexaFluor 568 conjugated to donkey anti-mouse (Life Technologies). Actin was stained using Texas Red Phalloidin (Life Technologies).

Phenotypic sorting of MDA-MB-231 breast cancer cells: MDA-MB-231 breast cancer cells were phenotypically sorted based on their ability to migrate through a collagen gel on top of a Transwell insert as previously described[377]. Briefly, cancer cells were seeded on a thin layer of 1 mg/ml collagen (Corning, Corning, NY) on top of a Transwell insert with 8 μm pores (Greiner Bio-One, Kremsmunster, Austria). A serum gradient was applied and cancer cells were allowed to migrate for four days. After four days, highly migratory and weakly migratory cells were collected and reseeded in fresh Transwells. After 20 rounds of purification, cells that repeatedly migrated through the assay were termed 'highly migratory' (MDA$^+$) and cells that never migrated through the assay were termed 'weakly migratory' (MDA$^-$).

Modified cell lines: MDA$^+$ and MDA$^-$ were stably transduced with either FUW-GFP-E2A-fluc or FUW-mCherry-E2A-rluc, both created in-house. NIH 3T3 fibroblasts were transduced with either Life-Act eGFP (#84383, Addgene, Watertown, MA) or FUW-mCherry-E2A-rluc. To generate a Tg2-knockdown and a scrambled control cell line, MDA$^{- (GFP/luc)}$ were subjected to lentiviral transduction with either the Tg2-targeting MISSION shRNA plasmid (SHCLND-NM_004613: TRCN0000272816) (MDA$^{- (scr)}$) or the MISSION scr.1-puro scrambled control plasmid DNA (SHC001; Millipore Sigma) (MDA$^{- (shTg2)}$). To generate Tg2 overexpressing cell lines, MDA$^+$ and MCF7 were stably transduced with an FUW-Tg2 plasmid created in-house.

Orthotopic mammary metastasis mouse model : Orthoptic injection of NOD SCID gamma (NSG) mice was conducted as previously described[377]. Briefly, female NSG mice, 6-8 weeks of age, were injected subcutaneously at the fourth mammary fat pad with either MDA$^+$, MDA$^-$, MDA$^{- (scr)}$, or MDA$^{- (shTg2)}$, lentivirally transduced with GFP and firefly luciferase tags. In mouse experiments with MVs, either serum-free media alone or approximately $1*10^7$ MV$^-$ suspended in serum-free media were injected subcutaneously at the primary tumor site every three days from one to six weeks post cancer cell injection. For bioluminescent imaging, mice were injected with 30 mg/mL D-luciferin (Gold-Bio, St Louis, MO) and imaged weekly on an IVIS Lumina III Series (Caliper LifeSciences, Hopkinton, MA). After 4-6 weeks, primary tumors were removed using sterile surgical technique. Primary tumor size was measured with calipers. Primary tumors were cut in half and either snap-frozen in dry ice or fixed with 4% v/v paraformaldehyde (Electron Microscopy Sciences, Hartfield, PA). At the endpoint, mouse lung and liver were collected and fixed in 4% v/v paraformaldehyde for 24 hours and sent to the Vanderbilt Tissue Pathology Shared Resource for paraffin embedding and sectioning.

Atomic force microscopy of primary mouse tumors: Primary tumor samples cryopreserved in O.C.T compound were cut into 20 μm sections. Prior to AFM stiffness measurements, samples were thawed at room temperature for 3 minutes, and maintained in 1X Halt Protease Inhibitor Cocktail (78438, ThermoFisher Scientific). A thermoplastic coverslip (ThermoFisher Scientific) with a 6 μm biopsy punch hole was superglued on top of the tumor section. An ImmEdge hydrophobic pen (Vector Laboratories, Burlingame, CA) was used to draw a small circle around the biopsy punch hole. AFM measurements were performed using a MFP3D-BIO inverted optical AFM (Asylum Research, Santa Barbara, CA), with an inverted fluorescent Zeiss Observer Z.1 microscope with a 10x/0.3 N.A. objective. A silicon nitride cantilever with a 5 μm diameter spherical borosilicate glass tip and a spring constant of 0.06 N/m (Novascan Technology, Boone, IA) was used. Samples were indented at a 2 μm/second loading rate, with a maximum indentation force of 5 nN. To obtain tumor stiffness measurements, IGOR PRO Software (Asylum Research) was used. At least two force maps of each primary tumor sample were obtained. AFM data was fit to a Hertz model with a Poisson's ratio of 0.5.

qPCR of tumors Snap frozen primary tumors were prepared for RNA isolation by TRIZOL digestion and subsequent homogenization using a TissueLyser II (Qiagen, Hilden, Germany) with a 5 mm stainless steel bead for 2 min at 30 Hz. After homogenization, samples were incubated at room temperature for 5 minutes in TRIZOL. Chloroform was added to the homogenized sample and incubated at room temperature for 3 minutes. Samples were centrifuged at 10,000 x g for 30 minutes at 4C. The upper aqueous phase was separated and mixed with 70% ethanol. RNA was subsequently isolated using the RNeasy Mini Kit (Qiagen). DNA was synthesized from RNA using the iScript cDNA Synthesis Kit (Bio-Rad Laboratories, Hercules, CA). qPCR was performed with the iQ SYBR Green Supermix (Bio-Rad Laboratories) per manufacturer protocols. The primer sequences for each gene are listed in Supplementary Table 1.

Table 3.1. Primer sequences used for quantitative real-time PCR.

Gene	Forward Primer (5'-3')	Reverse Primer (5'-3')
Acta2	TGTAGCCCTGGCCTAGCAAC	TGCCATCCATGCCTGGGAATA
Fap	GTGGAAGACAGACTTGCTTCTTTT	CAGGTTTGTAAACTCTTGAGGGACG
Pdgfrα	AAACCCGGTGGGTGTCCTAA	CGGGATCCATCCAAGCCATCA
Pdgfrβ	CCCTCGAGGAAAGCCCTTGG	GACCTTCCCGAGGCAGAGTT
Gapdh	CTGGTAAAGTGGATATTGTTGCCAT	TGGAATCATATTGGAACATGTAAACC
Col1A1	CTGGACAGCCTGGACTTC	TTCATCATAGCCATAGGACATC
Fn	CAGAAATGACCATTGAAGGT	ATGAGTCCTGACACAATCAC
Col4A1	GAAGGGTAGCATCGGGGGAC	GTGGCCCTATTCCTGGGACC
Tenascin C	ACCATGCTGAGATAGATGTTCCAAA	CTTGACAGCAGAAACACCAATCC

| Periostin | TGCTGCCCTGGCTATATGAG | GTAGTGGCTCCCACAATGCC |

Immunohistochemical staining of mouse tissues: Primary tumors were fixed, paraffin-embedded, and mounted into 5 μm thick sections at the Vanderbilt Tissue Pathology Shared Resource. For collagen staining, tumors were stained using the picrosirius red stain kit (Polysciences Inc., Warrington, PA). For fibronectin staining, tumors were stained using the Abcam IHC-Paraffin Protocol. Briefly, 5 μm thick sections of primary tumors were deparaffinized and rehydrated using a series of washes of xylene, ethanol, and water. Heat-induced epitope retrieval was completed using a sodium citrate buffer. Tumor sections were blocked for 2 hours in tris buffered saline (TBS) + 10% fetal bovine serum + 1% bovine serum albumin at room temperature. Samples were incubated overnight in rabbit anti-fibronectin (1:500) in TBS + 1% bovine serum albumin. After washing, samples were incubated in TBS + 0.3% hydrogen peroxide for 15 minutes to suppress endogenous peroxidase activity. Samples were incubated in HRP anti-rabbit (1:200) for 1 hour. Staining was developed using the DAB chromogen (8059S, Cell Signaling Technology) and samples were subsequently counterstained using Mayer's hematoxylin (Millipore Sigma). Tumor samples were then dehydrated, cleared, and mounted. Anti-GFP staining of liver and lungs was completed by the Vanderbilt Tissue Pathology Shared Resource. Whole slide imaging and quantification of immunostaining were performed in the Digital Histology Shared Resource at Vanderbilt University Medical Center (www.mc.vanderbilt.edu/dhsr).

Immunofluorescent staining of mouse tissues: Primary tumors were frozen and cut into 20 μm thick sections at the Vanderbilt Tissue Pathology Shared Resource. Tumor sections were thawed, fixed for 10 minutes in 4% v/v paraformaldehyde, and permeabilized in 1% Triton X-100 (Millipore Sigma). Sections were blocked for 2 hours in PBS + 10% fetal bovine serum + 5% donkey serum + 5% goat serum. Samples were incubated overnight in mouse anti-αSMA (1:200). After washing, samples were incubated in AlexaFluor 568 conjugated to donkey anti-mouse (1:200) and DAPI (1:500) for 2 hours. Sections were mounted for imaging using Vectashield Mounting Media (Vector Laboratories). Sections were imaged with a 10x/0.3 N.A. objective on a Zeiss LSM800 confocal laser-scanning microscope.

MV isolation and characterization: MVs were isolated as previously described. MDA-MB-231 and MCF7 were incubated overnight in serum-free media. The conditioned media was removed from the cells and centrifuged at 400 RPM. The supernatant was removed and again centrifuged at 400 RPM. The medium was then filtered through a 0.22 μm SteriFlip filter unit (Millipore Sigma) and rinsed with serum-free media. The MVs retained by the filter were resuspended in serum-free media. Nanoparticle tracking analysis (ZetaView ParticleMetrix, Germany) was used to determine the size and number of isolated MVs.

Western blotting: Isolated MVs were rinsed with PBS on a 0.22 μm SteriFlip filter unit and lysed with Laemmli buffer. MDA$^+$, MDA$^-$, and NIH 3T3 fibroblasts were lysed with Laemmli buffer. For T101 experiments, MV$^-$ were incubated for 30 minutes with either DMSO or 10 μM T101. MVs were re-filtered

and resuspended in serum-free media. NIH 3T3 fibroblasts were cultured with either MV$^{-\text{(DMSO)}}$ or MV$^{-\text{(T101)}}$ for 24 hours before lysis with Laemmli buffer. All lysates were resolved by SDS-PAGE and transferred to PVDF membranes. Transferred membranes were blocked with either 5% milk or 5% bovine serum albumin in TBS-Tween. Membranes were incubated overnight in mouse anti-α smooth muscle actin (1:1000), rabbit anti-flotillin-2 (1:1000), mouse anti-tissue transglutaminase 2 (1:1000), rabbit anti-focal adhesion kinase (1:1000), rabbit anti-phospho focal adhesion kinase (1:1000), and mouse anti-GAPDH (1:2000) at 4°C. Membranes were then incubated in horseradish peroxidase-conjugated secondary antibody (1:2000) in 5% milk or 5% bovine serum albumin in TBS-Tween for 1 hour at room temperature. Samples were imaged with an Odyssey Fc (LI-COR Biosciences, Lincoln, NE) after the addition of SuperSignal West Pico or West Dura Chemiluminescent Substrates (ThermoFisher Scientific).

Polyacrylamide gel preparation: Polyacrylamide (PA) gels were fabricated as described elsewhere[340]. Briefly, the ratio of acrylamide (40% w/v; Bio-Rad, Hercules, CA) to bis-acrylamide (2% w/v; Bio-Rad) was varied to tune gel stiffness to 20 kPa, previously shown to enhance fibroblast response to MVs[17]. 20 kPa PA gels were fabricated using an acrylamide: bis-acrylamide ratio of 12%:0.19%. PA gels were coated with 0.1 mg/ml rat tail type I collagen (Corning).

Fibronectin immunofluorescence and analysis: NIH 3T3 fibroblasts were seeded on 20 kPa PA gels in 1.6 mL of DMEM + 1% FBS. Cells were treated with either 400 μL of serum-free media or approximately $3*10^7$ MVs suspended in 400 μL serum-free media for 24 hours. Cells were first fixed with 3.2% v/v paraformaldehyde and subsequently permeabilized with a 3:7 ratio of methanol to acetone. Cells were incubated with goat anti-fibronectin (1:100) overnight. The cells were washed and incubated with AlexFluor 488 conjugated to donkey anti-goat (1:200), TexasRed phalloidin (1:500), and DAPI (1:500) for 1 hour. To image, gels were inverted onto a drop of Vectashield Mounting Media placed on a glass slide. Fluorescent images were acquired with a 20x/1.0 N.A. water-immersion objective on a Zeiss LSM700 Upright laser-scanning microscope. Cells stained with phalloidin were outlined in ImageJ to calculate cell area. Area of fibronectin was measured by using the threshold function in ImageJ to calculate area of positive stain. The ratio of fibronectin area to cell area was calculated.

Phalloidin and αSMA immunofluorescence and analysis: NIH 3T3 fibroblasts were seeded on 20 kPa PA gels in 1.6 mL of DMEM + 1% FBS. Cell media was additionally supplemented with either 400 μL of serum-free media or approximately $3*10^7$ MVs suspended in 400 μL serum-free media. After 24 hours, cells were fixed with 3.2% v/v paraformaldehyde and permeabilized with 1% Triton X-100. Cells were blocked with 3% bovine serum albumin in 0.02% Tween in PBS and then incubated for 3 hours at room temperature with mouse anti-alpha smooth muscle actin (1:100). After being washed, cells were incubated for 1 hour with AlexaFluor 488 conjugated to donkey anti-mouse (1:200). The cells were washed and F-actin and nuclei were stained with TexasRed phalloidin (1:500) and DAPI (1:500), respectively. To image,

gels were inverted onto a drop of Vectashield Mounting Media placed on a glass slide. Fluorescent images were acquired with a 20x/1.0 N.A. water-immersion objective on a Zeiss LSM700 Upright laser-scanning microscope.

EdU proliferation assay: NIH 3T3 fibroblasts were serum-starved for 6 hours and subsequently seeded on 20 kPa PA gels in 1.6 mL of DMEM + 1% FBS. Cell media was additionally supplemented with either 400 μL of serum-free media or approximately $3*10^7$ MVs suspended in 400 μL serum-free media. After 24 hours, 10 μM 5-ethynyl-2'-dexoyuridine (EdU, ThermoFisher Scientific) was added to the culture media for 2 hours. Cells were fixed with 3.2% v/v paraformaldehyde and stained with the Click-iT EdU Kit (ThermoFisher Scientific) following the manufacturer's instructions. Nuclei were counterstained with DAPI (1:500). Cells were imaged with a 20x/1.0 N.A. water-immersion objective on a Zeiss LSM700 Upright laser-scanning microscope. The percentage of EdU incorporation was calculated as the ratio of EdU positive cells to the total number of cells.

Traction force microscopy: Traction force microscopy was performed as previously described[167]. Briefly, 20 kPa PA gels, embedded with 0.5 μm diameter fluorescent beads (ThermoFisher Scientific), were prepared. NIH 3T3 fibroblasts were allowed to adhere for 24 hours in 1.6 mL of DMEM + 1% FBS supplemented with either 400 μL of serum-free media or approximately $3*10^7$ MVs suspended in 400 μL serum-free media. After 24 hours, phase contrast images of fibroblasts and fluorescent images of the beads at the surface of the PA gel were acquired. Fibroblasts were removed from the PA gel using 0.25% trypsin/EDTA (Life Technologies) and a fluorescent image of the beads was acquired after cell removal. Bead displacements between the stressed and null states and fibroblast area were calculated and analyzed using the LIBTRC library developed by M. Dembo (Dept. of Biomedical Engineering, Boston University)[342]. Outliers were removed using the ROUT method with Q = 0.2%.

Spheroids: MDA-MB-231, MCF7, and/or NIH 3T3 fibroblasts, transduced with either GFP or mCherry, were resuspended in spheroid compaction media containing 0.25% methylcellulose (STEMCELL, Vancouver, Canada), 4.5% horse serum (ThermoFisher Scientific), 18 ng/mL EGF (ThermoFisher Scientific), 90 ng/mL cholera toxin (Millipore Sigma), 90 U/mL penicillin (Life Technologies), and 90 ug/mL streptomycin (Life Technologies) in DMEM/F12 (ThermoFisher Scientific). A 2:1 ratio of cancers cells to fibroblasts (1:1 for MCF7:3T3 spheroids) were added to wells of a round-bottom 96 well plate to generate 5,500 cell spheroids. The plate was centrifuged at 1100 rpm for 5 minutes at room temperature and subsequently incubated at 37 degrees for 72 hours (24 hours for MCF7+3T3 spheroids) to allow for spheroid compaction.

After spheroid compaction, spheroids were embedded into 4.5 mg/mL collagen gels. Briefly, 4.5 mg/mL collagen gels were generated by mixing 10 mg/ml stock collagen (Rockland), 0.1% acetic acid, culture media, 10x HEPES (Millipore Sigma), and 1 N NaOH (Millipore Sigma) and added to wells of a

24 well plate. Compacted spheroids were placed into the middle of the collagen gel without touching the bottom of the well plate. The embedded spheroids were placed in a 37°C incubator for 10 minutes to polymerize, then the plate was flipped upside-down for another 30 minutes to avoid spheroid adhesion on the bottom of the well. Spheroids were rehydrated every 24 hours with 300 μL of 1% DMEM and supplemented with either 200 μL of serum-free DMEM or $1.5*10^7$ MVs suspended in 200 μL serum-free DMEM. Spheroids were imaged every 24 hours for 48 hours (72 hours for MCF7+3T3 spheroids) using a Zeiss LSM800 inverted confocal microscope equipped with an environmental control chamber. Spheroid images were captured using a 10X/0.3 NA objective. The projected spheroid area, the spheroid diameter, and the maximum cancer cell migration distance from the spheroid core was measured. The expansion index (A_i/A_0-1) was calculated to quantify spheroid outgrowth.

iTRAQ Proteomics and Analysis: After MV isolation, MVs were lysed in a buffer composed of 2% Nonidet P-40 (Millipore Sigma), 0.5% sodium deoxycholate (Millipore Sigma), 300 mM sodium chloride (Millipore Sigma), and 50 mM Tris pH 8. Lysates were incubated for 30 minutes at 4°C and centrifuged at 14,000 x g for 15 minutes at 4°C to pellet non-solubilized proteins. iTRAQ proteomics of lysates was completed by the Vanderbilt Mass Spectrometry Research Center Proteomics Core. Briefly, enzyme digestion of lysates was used to generate proteolytic peptides. MV^+ and MV^- peptides were labeled with 117 and 115 iTRAQ reagents, respectively. Samples were subsequently mixed, fractioned using liquid chromatography, and analyzed via tandem mass spectrometry. A database search using the fragmentation data identified the labeled peptides and their corresponding proteins. Protein set enrichment analysis was completed using the PSEA-Quant algorithm[400]. The REVIGO web tool was used to remove redundant GO terms[401].

Statistical analysis: All statistical analysis was performed using GraphPad Prism 7 (GraphPad Software, La Jolla, CA) or Excel 2016 (Microsoft, Redmond, WA). Where appropriate, data were compared with a student's t-test or with a two-way analysis of variance (ANOVA) with Sidak multiple comparisons test. All data is reported as mean ± standard error (SE) unless otherwise notated.

3.4   Results

3.4.1   *Highly and weakly migratory breast cancer subpopulations form tumors with distinct matrix and fibroblast populations*

To investigate the mechanism through which weakly migratory cells locally invade and disseminate, MDA-MB-231 breast cancer cells were phenotypically sorted based on migration through a collagen coated transwell[377]. Twenty rounds of sorting resulted in the isolation of two stable subpopulations of breast cancer cells: highly migratory MDA$^+$ and weakly migratory MDA$^-$ (**Fig. 3.1A**). Consistent with our previous *in vivo* findings[377], highly and weakly migratory tumors grew at comparable rates (**Fig. 3.1B-C**) and the highly migratory MDA$^+$ subpopulation was weakly metastatic in an orthotopic mouse model

53

while the weakly migratory MDA$^-$ subpopulation was highly metastatic (**Fig. 3.1D**). Given the differing migratory and metastatic capabilities of MDA$^+$ and MDA$^-$, we sought to characterize the tumor microenvironment formed by highly and weakly migratory cell *in vivo* to determine the impact of the tumor microenvironment on cancer cell dissemination and subsequent metastasis.

Since increased collagen and fibronectin deposition and increased tumor stiffness have been linked to tumor progression[52,402,403], we investigated the mechanical properties of MDA$^+$ and MDA$^-$ tumors to assess whether altered tumor matrix mechanics may contribute to metastatic potential. Based on Atomic Force Microscopy measurements, MDA$^-$ primary tumors exhibited significantly higher tumor stiffness compared to MDA$^+$ tumors (**Fig. 3.1E**). qPCR of tumors revealed significantly higher amounts of mouse-derived matrix, including collagen I (Col1A1), fibronectin 1 (Fn1), collagen IV (Col4A1), tenascin-C (Tnc), and periostin (Postn), in MDA$^-$ tumors compared to MDA$^+$ tumors (**Fig. 3.1F**). Similarly, increased collagen and fibronectin was evident via immunohistochemical staining in MDA$^-$ tumors compared to MDA$^+$ tumors (**Fig. 3.1G**). These results indicate that the weakly migratory, highly metastatic MDA$^-$ form stiffer tumors with increased ECM.

Given that MDA$^-$ produce stiffer tumors than MDA$^+$, and CAFs are a major stromal component of breast tumors that mediate matrix deposition[404], we investigated the CAF component of tumors from each subpopulation. MDA$^-$ tumors exhibited increased levels of several CAF markers, including α-smooth muscle actin (Acta2), fibroblast activation protein (Fap), and platelet-derived growth factors α and β (Pdgfrα, Pdgfrβ) (Fig. 1h). MDA$^-$ tumors also exhibited an increased fraction of αSMA positive tissue area compared to MDA$^+$ tumors (**Fig. 3.6I-J**). Given that αSMA is the primary marker of myofibroblast-like CAFs (myCAFs), that myCAFs and matrix-CAFs (mCAFs) express high levels of FAP, PDGFRα, and PDGFRβ [405–407], and that myCAFs are highly contractile and deposit high levels of ECM [406,408], these results suggest that MDA$^-$ tumors are enriched for a myCAF-like fibroblast population. These findings reveal that the weakly migratory, highly metastatic MDA$^-$ primary tumors have increased myCAF-like fibroblasts.

Since MDA$^-$ tumors are stiffer and have a larger population of CAFs compared to MDA$^+$ tumors, we investigated the mechanisms by which MDA$^-$ may activate fibroblasts using RNA-seq. Previously published genes involved in cancer cell-induced fibroblast activation[409–412] were used to generate a Stroma-Activating Score (**Fig. 3.1K-L**). No significant difference in Stroma-Activating Score was calculated between MDA$^+$ and MDA$^-$ (**Fig. 3.1L**). However, when separated into several Stroma-Activating Groups (Inflammatory, Matrix Ligands, Cell-Cell Adhesion, and Secreted), MDA$^+$ scored significantly higher on Matrix Ligands, while MDA$^-$ scored significantly higher on Cell-Cell Adhesion and Secreted genes (**Fig. 3.1M-P**). This suggests that MDA$^-$ mediate fibroblast activation through Cell-Cell Adhesions and Secreted factors. To further investigate the secreted factors that may influence fibroblast activation, RNA-seq counts of genes involved in fibroblast activation through secreted factors was assessed (**Fig. 3.1Q**). Both TGFB2

and TGM2 were significantly enriched in MDA⁻ compared to MDA⁺. These findings reveal that MDA⁻ may activate fibroblasts through secreted factors.
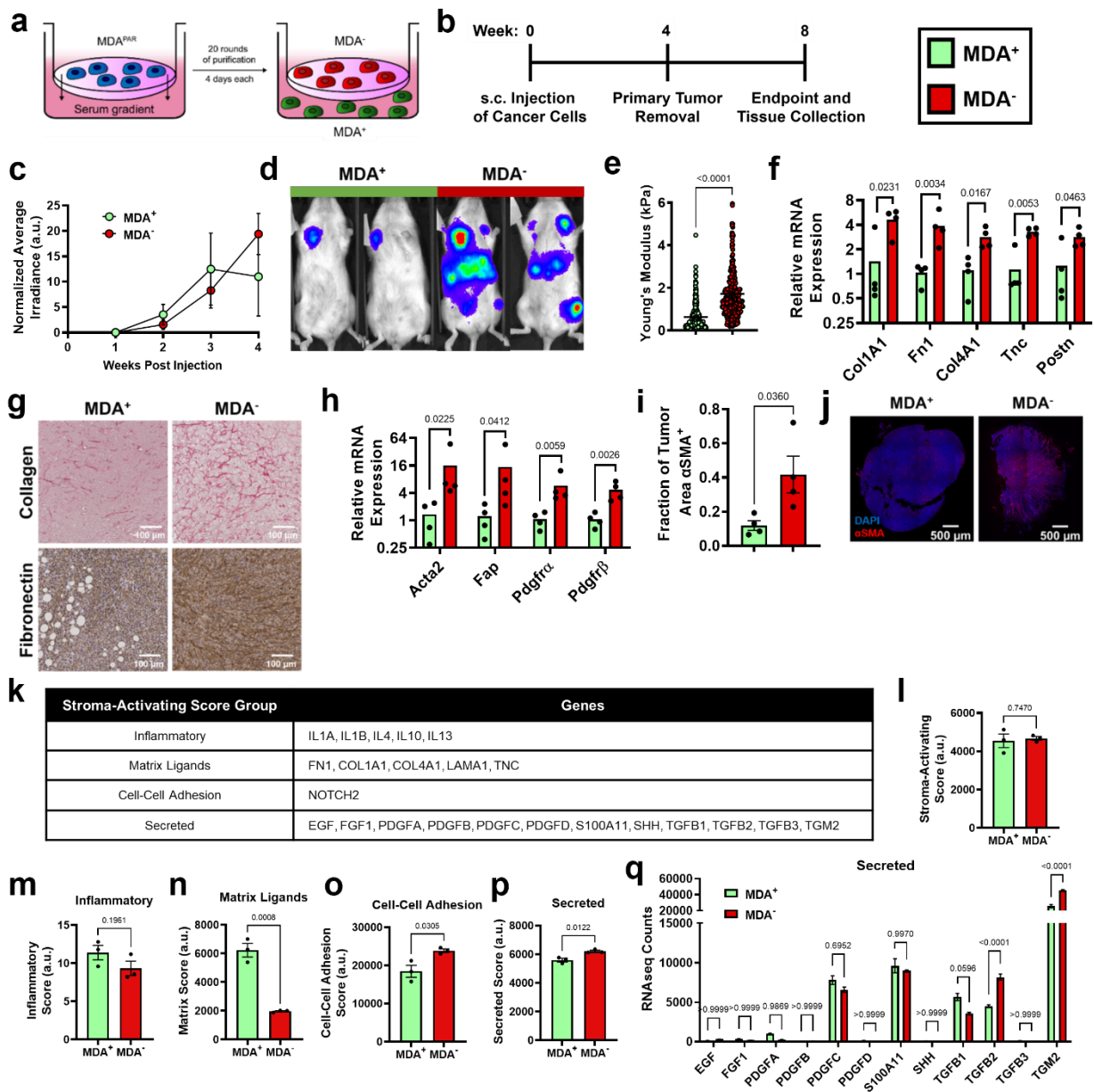
Figure 3.1. Highly and weakly migratory breast cancer subpopulations form tumors with distinct matrix and fibroblast populations. (a) Schematic of phenotypic sorting. (b) Timeline of orthotopic mammary metastasis model. (c) Normalized average irradiance of MDA⁺ and MDA⁻ primary tumors (N=3 mice). (d) Representative BLI of MDA⁺ and MDA⁻ metastasis. (e) AFM stiffness measurements of MDA⁺ and MDA⁻ primary tumors. (N=3+ tumors per condition; n = 254, 280). (f) Relative mRNA expression of mouse-derived matrix components in MDA⁺ and MDA⁻ primary tumors. (N=4 tumors per condition). (g) Immunohistochemical staining of collagen and fibronectin in MDA⁺ and MDA⁻ primary tumors. (h) Relative mRNA expression of stromal CAF markers in MDA⁺ and MDA⁻. (N=4 tumors per condition). (i) Fraction of tumor area positive for αSMA (N=4). (j) Representative images of αSMA (red) and DAPI (blue) in MDA⁺ and MDA⁻ tumors. (k) Stroma-Activating Score Group genes identified in RNAseq of MDA⁺ and

MDA[-]. (l) Stroma-Activating Score of MDA[+] and MDA[-] (N=3). (m) Inflammatory Score of MDA[+] and MDA[-] (N=3). (n) Matrix Score of MDA[+] and MDA[-] (N=3). (o) Cell-Cell Adhesion Score of MDA[+] and MDA[-] (N=3). (p) Secreted Score of MDA[+] and MDA[-] (N=3). (q) Inflammatory Score of MDA[+] and MDA[-] (N=3). Secreted Score of MDA[+] and MDA[-], separated by gene (N=3). mRNA graphs show mean + individual data points. Bar graphs shown mean +/- SEM. P-values determined using an unpaired Student's t-test.

3.4.2   *MVs released from weakly migratory cancer cells are potent activators of fibroblasts in vitro*

Since our data indicate that MDA[-] may activate fibroblasts using secreted factors, and it is known that MVs can induce fibroblast activation[15,17], we compared the MVs released from MDA[+] and MDA[-]. MVs were collected from the MDA[+] and MDA[-] subpopulations after culture in serum-free conditions. Isolated MVs were purified using centrifugation and size-based filtration and termed MV[+] and MV[-], respectively. MDA[-] released significantly more MVs than MDA[+] (**Fig. 3.2A**) but both MV[+] and MV[-] had similar size distributions and were within the expected 200 nm – 1 µm range (**Fig. 3.2B**). To probe MV signaling to fibroblasts, fibroblast phenotypes associated with fibroblast activation and cancer progression were examined after culture with MV[+] and MV[-] on 20 kPa polyacrylamide gels, representing the stiffness of breast ECM at the tumor periphery[8] (**Fig. 3.2C**). MV[-] caused focal adhesion kinase (FAK) Tyr397 phosphorylation in fibroblasts, as increased FAK phosphorylation (pFAK) was evident in fibroblasts cultured with MV[-] compared to control and MV[+] conditions (**Fig. 3.2D-E**), consistent with previous findings that MDA-MB-231 MVs regulate fibroblast FAK activation[15]. Additionally, fibroblasts cultured with MV[-] exhibited increased α-smooth muscle actin (αSMA) expression, a marker of fibroblast activation, and cell area compared to both control and MV[+] conditions (**Fig. 3.2F-H, Supp. Fig. 3.1A**). Fibroblasts cultured with MV[+] displayed no change in αSMA expression or cell area compared to control conditions (**Fig. 3.2F-H, Supp. Fig. 3.1A**). Fibroblasts cultured with MV[-] also displayed increased positive fibronectin staining (**Fig. 3.2I, Supp. Fig. 3.1B-C**), suggesting the MV[-] increased fibronectin deposition by fibroblasts. Fibroblasts cultured with MV[-] exhibited increased EdU incorporation compared to MV[+] and control conditions, indicative of increased proliferation (**Fig. 3.2J, Supp. Fig. 3.1D**). Increased traction force and traction stress was evident in fibroblasts cultured with MV[-], compared to control conditions, but not in fibroblasts cultured with MV[+] (**Fig. 3.2K, Supp. Fig. 3.1E-F**). Overall, this data indicates that MV[-] activate fibroblasts to a more proliferative, contractile state compared to MV[+] and control conditions.
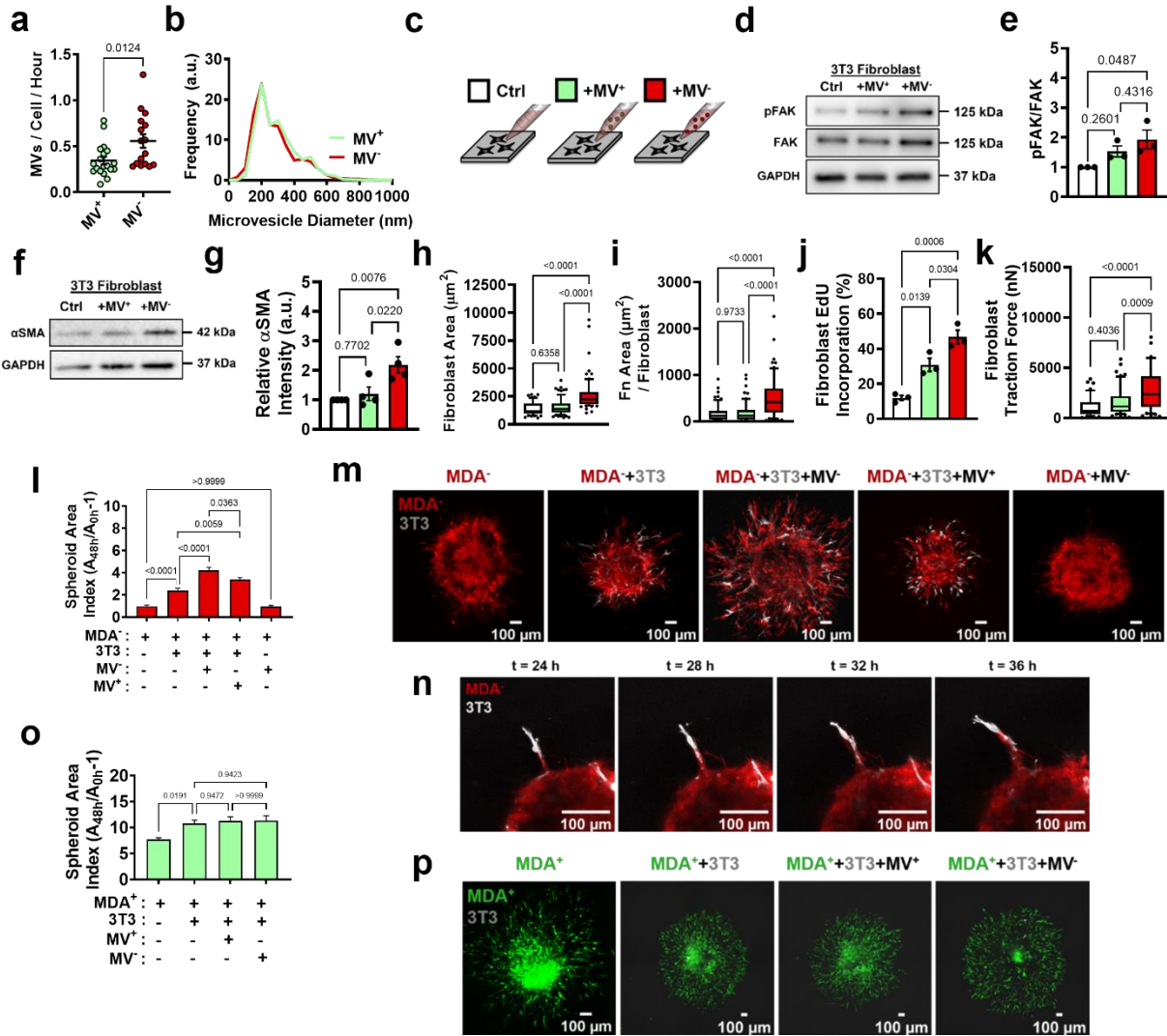
Figure 3.2. MV⁻ are potent activators of fibroblasts *in vitro*. (a) Number of MVs released from MDA⁺ and MDA⁻ per hour (N=19, 16). (b) Size distribution of MVs isolated from MDA⁺ and MDA⁻. (c) Schematic overviewing fibroblast culture with MVs. (d) Western blot of pFAK, FAK, and GAPDH in fibroblasts cultured in cultured in control conditions (Ctrl), with MV⁺ (+MV⁺), or with MV⁻ (+MV⁻). (e) Quantification of western from (d) (N=3). (f) Western blot of αSMA and GAPDH in fibroblasts cultured in in Ctrl, +MV⁺, or +MV⁻ conditions (g) Quantification of western from (f) (N=4). (h) Fibroblast cell area after culture in Ctrl, +MV⁺, or +MV⁻ conditions. (N=3; n=69, 75, 77). (i) Area of fibronectin deposited per fibroblast cultured in Ctrl, +MV⁺, or +MV⁻ conditions. (N=3; n=66, 66, 61). (j) Percentage of fibroblasts EdU positive after culture in Ctrl, +MV⁺, or +MV⁻ conditions. (N=3). (k) Fibroblast traction force after culture in Ctrl, +MV⁺, or +MV⁻ conditions. (N=3; n=41, 57, 58). (l) Representative images of spheroid outgrowth 48 hours post embedding. MDA⁻ (red); 3T3 fibroblast (gray). (m) Spheroid area index 48 hours post embedding. (N=3+; n=22, 31, 32, 22, 19). (n) Time series images of fibroblast leading MDA⁻ escape from spheroid. (o) Spheroid area index 48 hours post embedding. (N=3+; n=28, 62, 34, 28). (p) Representative images of spheroid outgrowth 48 hours post embedding. MDA⁺ (green); 3T3 fibroblast (gray). Bar graphs show mean +/- SEM. Box and whisker plots show median and 25ᵗʰ-75ᵗʰ (box) and 10ᵗʰ-90ᵗʰ (whiskers) percentiles. P-values determined using an unpaired Student's t-test or a one-way ANOVA with Tukey's test for multiple comparisons.
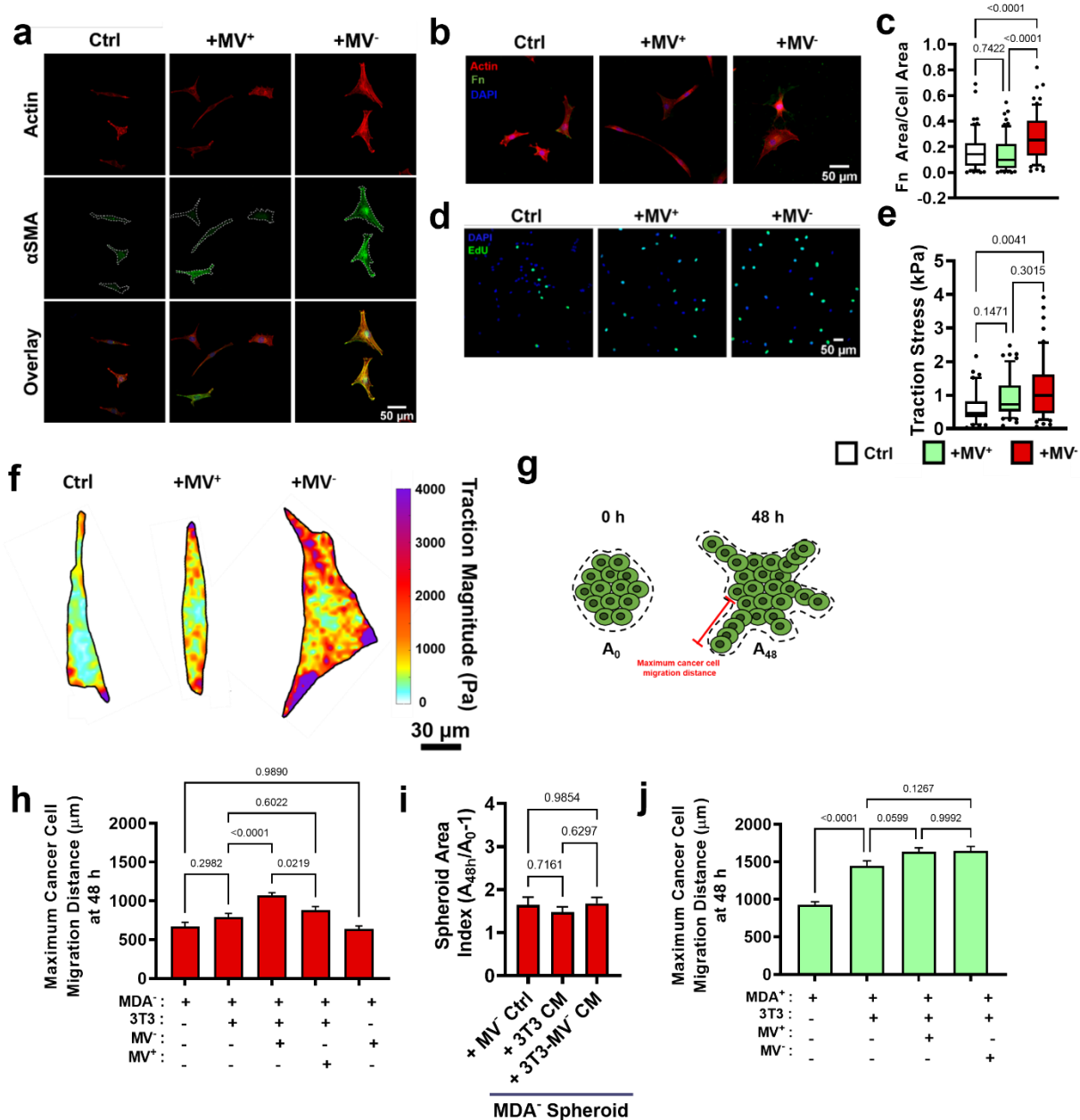
Supplemental Figure 3.1. (a) Representative images of fibroblast cell area (red) and αSMA expression (green) after culture in control conditions (Ctrl), with MV$^+$ (+MV$^+$), or with MV$^-$ (+MV$^-$). (b) Representative images of fibroblast fibronectin deposition after culture in Ctrl, +MV$^+$, or +MV$^-$ conditions. Actin (red); fibronectin (green); DAPI (blue). (c) To ensure that the increased fibronectin area was not a result of increased fibroblast spreading, fibronectin area was normalized to cell area. (N=3; n=66, 66, 61). (d) Representative images of fibroblast EdU incorporation after culture in Ctrl, +MV$^+$, or +MV$^-$ conditions. DAPI (blue); EdU (green). (e) Fibroblast traction stress (calculated as fibroblast traction force / cell area) after culture in Ctrl, +MV$^+$, or +MV$^-$ conditions. (N=3; n=41, 57, 58). (f) Representative fibroblast traction stress maps. (g) Schematic of spheroid outgrowth measurements. (h) Maximum distance of cancer cell migration away from spheroid core 48 hours post spheroid. (N=3+, n=22, 31, 32, 22, 19) (i) Maximum distance of cancer cell migration away from spheroid core 48 hours post spheroid embedding. (N=3, n = 19, 18, 17) (j) Maximum distance of cancer cell migration away from spheroid core 48 hours post spheroid

embedding. (N=3+; n=28, 32, 54, 24). Bar graphs show mean +/- SEM. Box and whisker plots show median and 25th-75th (box) and 10th-90th (whiskers) percentiles. P-values determined using a one-way ANOVA with Tukey's test for multiple comparisons.

3.4.3   *MV-mediated fibroblast activation increases weakly migratory cancer cell migration*

CAFs enable cancer cell migration and metastasis, in part, through matrix remodeling at the primary tumor[13,46,214,383,397–399]. Given that our data indicate that MDA⁻ cells induce fibroblast activation through the release of MV, we investigated whether MV-activated fibroblasts could promote the migration of MDA⁻ in a tumor spheroid model. After 48 hours of culture, MDA⁻ spheroids exhibited minimal spheroid outgrowth, measured using a spheroid area index (A_{48h}/A_{0h}-1) (**Fig. 3.2L-M, Supp. Fig. 3.1G-H**), while MDA⁺ spheroids exhibited high levels of spheroid outgrowth (**Fig. 3.2O-P, Supp. Fig. 3.1G, J**), consistent with our previous findings[377]. Coculture of MDA⁻ or MDA⁺ with 3T3 fibroblasts (MDA⁻+3T3, MDA⁺+3T3) resulted in significantly enhanced spheroid outgrowth compared to cancer cells alone (**Fig. 3.2L-M, O-P, Supp. Fig. 3.1G-H, J**). MDA⁻+3T3 spheroids displayed fibroblast-led strands of MDA⁻ migration away from the spheroid, suggesting that the fibroblasts physically lead the migration of MDA⁻ through the matrix (**Fig. 3.2N**). Importantly, MDA⁻+3T3 spheroids cultured with MV⁻ exhibited significantly enhanced spheroid outgrowth and MDA⁻ migration distance, compared to MDA⁻+3T3 control spheroids (**Fig. 3.2L-M, Supp. Fig. 3.1G-H**). MDA⁻+3T3 spheroids cultured with MV⁺ also showed increased outgrowth compared to MDA⁻+3T3 spheroids, but this outgrowth was significantly less than that induced by MV⁻ (**Fig. 3.2L-M, Supp. Fig. 3.1G-H**). Interestingly, MDA⁺+3T3 spheroids cultured with MV⁺ or MV⁻ exhibited no change in spheroid outgrowth and MDA⁺ migration distance compared to control conditions (**Fig. 3.2O-P, Supp. Fig. 3.1G, J**). This result suggests that MDA⁺ are capable of robust migration independently of MV-mediated fibroblast signaling. When MV⁻ were applied to MDA⁻ only spheroids, no increase in spheroid outgrowth was observed, highlighting the necessity of fibroblasts for this MV-induced cancer cell migration (**Fig. 3.2L-M, Supp. Fig. 3.1G-H**). Additionally, MDA⁻ spheroids cultured with fibroblast conditioned media or MV⁻-treated fibroblast conditioned media displayed no change in spheroid outgrowth (**Supp. Fig. 3.1I**), indicating that fibroblast-enhanced cancer cell migration is not a result of secreted factors but rather due to physical interactions. Altogether, these results indicate that MV⁻ are potent activators of fibroblasts and that MV⁻-induced fibroblast activation mechanically feeds back to induce the migration of MDA⁻.
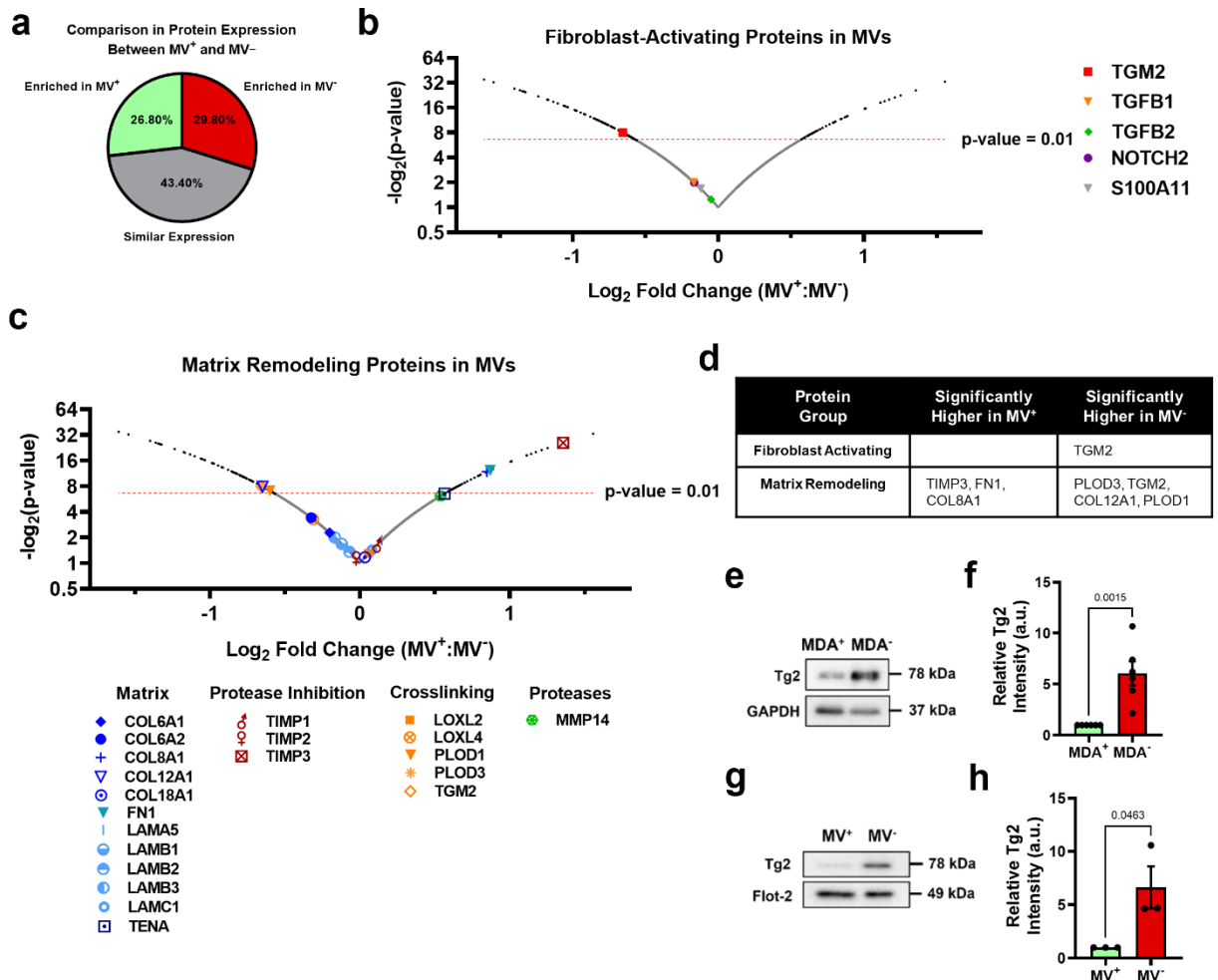
Figure 3.3. Phenotypically sorted breast cancer subpopulations release MVs with distinctly different contents. (a) Comparison of protein expression between MV$^+$ and MV$^-$. Enriched in MV$^+$ = FC≥1.1; similar expression = 0.9<FC<1.1; enriched in MV$^-$ = FC≤0.9. (b) Fibroblast-activating proteins identified in proteomics of MV$^+$ and MV$^-$. P-value cut-off of 0.01 indicated with red-dotted line. (c) Matrix remodeling proteins identified in in proteomics of MV$^+$ and MV$^-$. P-value cut-off of 0.01 indicated with red-dotted line. (d) Significantly upregulated genes (p<0.01) in MV$^+$ and MV$^-$ involved in fibroblast activation and matrix remodeling. (e) Western blot of Tg2 and GAPDH in MDA$^+$ and MDA$^-$. (f) Quantification of western in (e) (N=6). (g) Western blot of Tg2 and Flot-2 in MV$^+$ and MV$^-$. (h) Quantification of western in (g) (N=3). Proteomics graphs show log$_2$ Fold Change of MV$^+$:MV$^-$ and each data point represents a protein. Bar graphs shown mean +/- SEM. P-values of bar graphs determined using an unpaired Student's t-test.
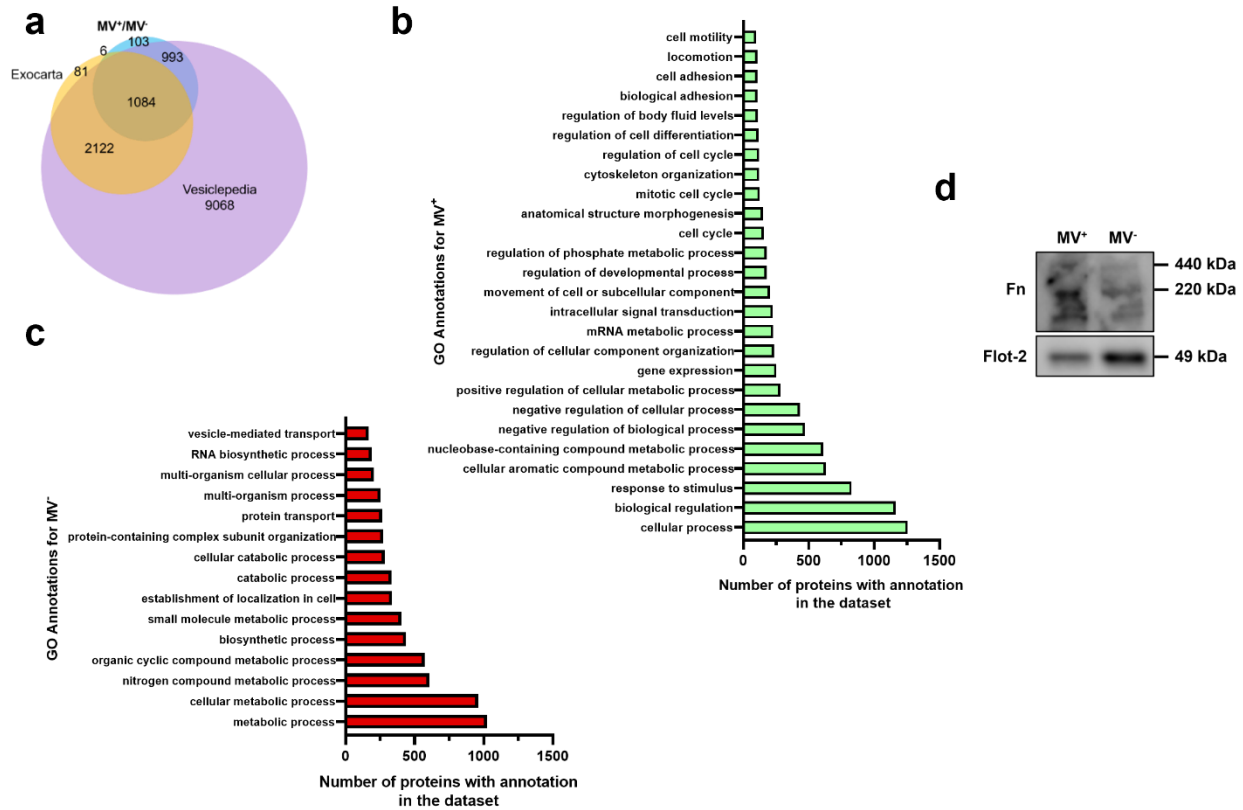
Supplemental Figure 3.2. (a) Comparison of proteomics of MV$^+$ and MV$^-$ to Exocarta and Vesiclepedia databases. (b) GO annotations for proteins enriched in MV$^+$. (c) GO annotations for proteins enriched in MV$^-$. (d) Western blot of Fn and Flot-2 in MV$^+$ and MV$^-$. (i) Western blot of Tg2 and GAPDH in MDA$^-$, MDA$^{- (scr)}$, and MDA$^{- (shTg2)}$.

3.4.4 *Highly and weakly migratory breast cancer cells release MVs with distinctly different contents*

To determine the MV cargo responsible for the activation of fibroblasts by the MDA$^-$ cells, iTRAQ proteomics was completed on MV$^+$ and MV$^-$. Identified proteins were compared to Exocarta and Vesiclepedia EV databases and exhibited significant overlap with both EV databases (**Supp. Fig. 3.2A**). Proteomics data suggests that MV cargo was different between highly migratory and weakly migratory subpopulations of breast cancer cells, with 26.8% of the identified proteins being more highly expressed by MV$^+$ (FC≥1.1) and 29.8% being more highly expressed by MV$^-$ (FC≤0.9) (**Fig. 3.3A**). 43.4% of identified proteins were similarly expressed between both MV populations (0.9<FC<1.1) (**Fig. 3.3A**). Protein set enrichment analysis (PSEA) of MV$^+$ and MV$^-$ cargo was performed using the PSEA-Quant algorithm[400]. PSEA revealed different GO annotations for MV$^+$ and MV$^-$ protein expression (**Supp. Fig. 3.2B-C**). Of note, MV$^+$ were enriched for cargo involved in biological adhesion, cell adhesion, location, and cell motility (**Supp. Fig. 3.2B**). MV$^-$ were enriched for cargo involved in various metabolic and catabolic processes and

vesicle-mediated transport (**Supp. Fig. 3.2C**). These findings indicate that cancer cells with varying migratory ability release MVs with distinctly different cargo.

Expression of proteins involved in fibroblast activation and matrix remodeling was assessed using proteomics (**Fig. 3.3B-C**). The fibroblast-activating proteins TGM2, TGFB1, TGFB2, NOTCH2, and S100A11 were identified in MV$^+$ and MV$^-$ (**Fig. 3.3B**). MV$^-$ had significantly higher expression of TGM2 compared to MV$^+$ while TGFB1, TGFB2, NOTCH2, and S100A11 had no significant difference in expression between MV$^+$ and MV$^-$ (**Fig. 3.3B, D**). Many matrix-remodeling proteins were identified in MV$^+$ and MV$^-$, including a variety of matrix ligands, protease inhibitors, crosslinking enzymes, and matrix-degrading proteases (**Fig. 3.3C**). TIMP3, FN1, and COL8A1 matrix-remodeling proteins were expressed significantly higher in MV$^+$ while PLOD3, TGM2, COL12A1, and PLOD1 were expressed significantly higher in MV$^-$ (**Fig. 3.3C-D**).

Tissue transglutaminase 2, also known as TGM2 or Tg2, identified as significantly enriched in MV$^-$ compared to MV$^+$, is a calcium-dependent enzyme that both crosslinks collagen and activates fibroblasts (**Fig. 3.3D**). EVs have previously been shown to transfer Tg2 to fibroblasts resulting in fibroblast activation[15,413]. Increased Tg2 expression in MDA$^-$ and MV$^-$, compared to MDA$^+$ and MV$^+$, was verified using western blot (**Fig. 3.3E-H**). More specifically, it has been shown that EV-Tg2 crosslinks EV-fibronectin (Fn) into dimers to potentiate fibroblast integrin signaling upon EV-fibroblast interactions[15,413]. While the Fn dimer was present in both MV$^+$ and MV$^-$, it was more highly expressed in MV$^+$ (**Supp. Fig. 3.2D**), suggesting that fibroblast activation by MV$^-$ does not solely rely on Fn dimer-mediated integrin signaling.
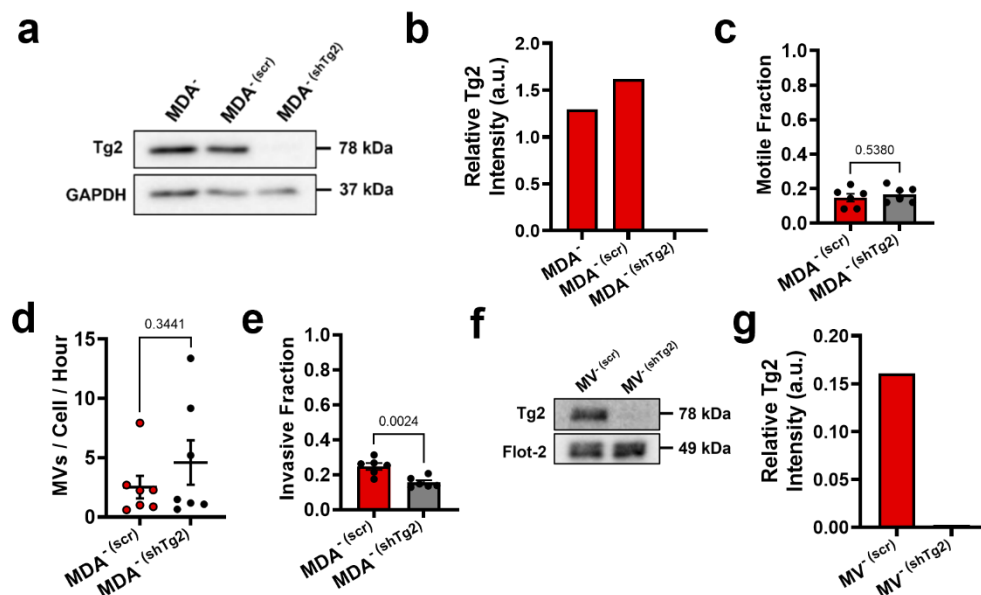
Supplemental Figure 3.3. (a) Western blot of Tg2 and GAPDH in MDA$^-$, MDA$^{-\,(scr)}$, and MDA$^{-\,(shTg2)}$. (b) Quantification of western in (a). (c) Motile fraction of MDA$^{-\,(scr)}$ and MDA$^{-\,(shTg2)}$ in 3D collagen. (N=3; n=6). (d) Number of MVs released from MDA$^{-\,(scr)}$ and MDA$^{-\,(shTg2)}$ per hour. (N=7). (e) Invasive fraction of MDA$^{-\,(scr)}$ and MDA$^{-\,(shTg2)}$ through collagen coated transwells. (N=3; n=6). (f) Western blot of Tg2 and Flot-2 in MV$^{-\,(scr)}$ and MV$^{-\,(shTg2)}$. (g) Quantification of western in (f). Bar graphs show mean +/- SEM. P-values determined using an unpaired Student's t-test.

3.4.5 *Modulation of MV-Tg2 expression regulates MV-mediated fibroblast activation*

Given that Tg2 is a known mediator of MV-induced fibroblast transformation[15], we investigated whether knockdown of Tg2 abrogates MV$^-$-induced fibroblast activation. MDA$^-$ was stably transduced with shRNA targeting Tg2 (MDA$^{-\,(shTg2)}$) (**Supp. Fig. 3.3A-B**). Knockdown of Tg2 resulted in no change in MDA$^-$ migration or MV release compared to the scrambled control (MDA$^{-\,(scr)}$) (**Supp. Fig. 3.3C-D**). A slight decrease in Transwell invasion was observed in MDA$^{-\,(shTg2)}$ compared to MDA$^{-\,(scr)}$ (**Supp. Fig. 3.3E**). MVs released from MDA$^{-\,(shTg2)}$ (MV$^{-\,(shTg2)}$) had reduced Tg2 expression compared to the scrambled control MVs (MV$^{-\,(scr)}$) (**Supp. Fig. 3.3F-G**).

Fibroblasts cultured with MV$^{-\,(shTg2)}$ exhibited decreased αSMA expression, cell area, fibronectin area, proliferation, and traction force, compared to culture with MV$^{-\,(scr)}$ (**Fig. 3.4A-F, Supp. Fig. 3.2A-G**). This suggests that knockdown of Tg2 in MDA- cells reduced the capacity of MV$^-$ to activate fibroblasts. Treatment of MV$^-$ with the Tg2 inhibitor, T101, decreased fibroblast αSMA expression compared to culture with MV$^-$, further supporting role of MV-Tg2 in fibroblast activation (**Fig. 3.4H-I**).

Spheroid cocultures of MDA$^{-\,(scr)}$ and MDA$^{-\,(shTg2)}$ with 3T3 fibroblasts were utilized to assess the effects of MV$^{-\,(shTg2)}$ on cell migration. MDA$^{-\,(scr)}$+3T3 spheroids cultured with MV$^{-\,(scr)}$ exhibited a significant increase in spheroid outgrowth compared to untreated conditions, consistent with our prior experiments (**Fig. 3.4J-K, Supp. Fig. 3.2G**). MDA$^{-\,(shTg2)}$+3T3 spheroids cultured with MV$^{-\,(shTg2)}$ exhibited no change in spheroid outgrowth compared to untreated control conditions (**Fig. 3.4J-K, Supp. Fig. 3.2G**), suggesting that without MV-induced fibroblast activation, fibroblasts could not increase cancer cell migration. MDA$^{-\,(shTg2)}$+3T3 spheroids cultured with MV$^{-\,(scr)}$ exhibited a significant increase in spheroid migration compared to untreated conditions, highlighting that MV-Tg2 is required for MV-mediated fibroblast-induced cancer cell migration (**Fig. 3.4J-K, Supp. Fig. 3.2G**).

To further investigate the role of Tg2 in MV-mediated fibroblast activation, Tg2 was overexpressed in MDA$^+$ using lentiviral transduction (MDA$^{+\,(FUW-Tg2)}$) (**Supp. Fig. 3.5A**). Fibroblasts cultured with MV$^{+\,(FUW-Tg2)}$ displayed increased cell area and increased traction force, compared to culture with MV$^+$ (**Supp. Fig. 3.2B-C**). These results were consistent with earlier findings suggesting that MV-Tg2 regulates MV-mediated fibroblast phenotype (**Fig. 3.4**).

Additionally, Tg2 was overexpressed in the weakly migratory, weakly metastatic MCF7 breast cancer cell line (**Supp. Fig. 3.5D**). Overexpression of Tg2 did not significantly change the motile fraction

of MCF7 in 3D collagen gels (**Supp. Fig. 3.5E**). Fibroblasts cultured with MV$^{MCF7\ (FUW-Tg2)}$ displayed significantly increased cell area compared to Ctrl and MV^{MCF7} and exhibited significantly increased traction force compared to control conditions (**Supp. Fig. 3.5F-G**). These findings confirm that addition of Tg2 to MVs from another weakly migratory breast cancer cell line regulates MV-mediated fibroblast phenotype. Additionally, spheroid cocultures of MCF7 with 3T3 fibroblasts were utilized to assess the effects of MV-Tg2 on cell migration. MCF7+3T3 spheroids cultured in control conditions or with MV^{MCF7} exhibited low levels of spheroid outgrowth at 72 hours (**Supp. Fig. 3.5H-I**). MCF7+3T3 spheroids cultured with MV^{MCF7} $^{(FUW-Tg2)}$ exhibited significantly higher levels of spheroid outgrowth and MCF7 cells migrating away from the spheroid core was observed (red arrows) (**Supp. Fig. 3.5H-I**). These results reveal that MV-mediated fibroblast activation through MV-Tg2 can enhance the dissemination of another weakly migratory breast cancer cell line.
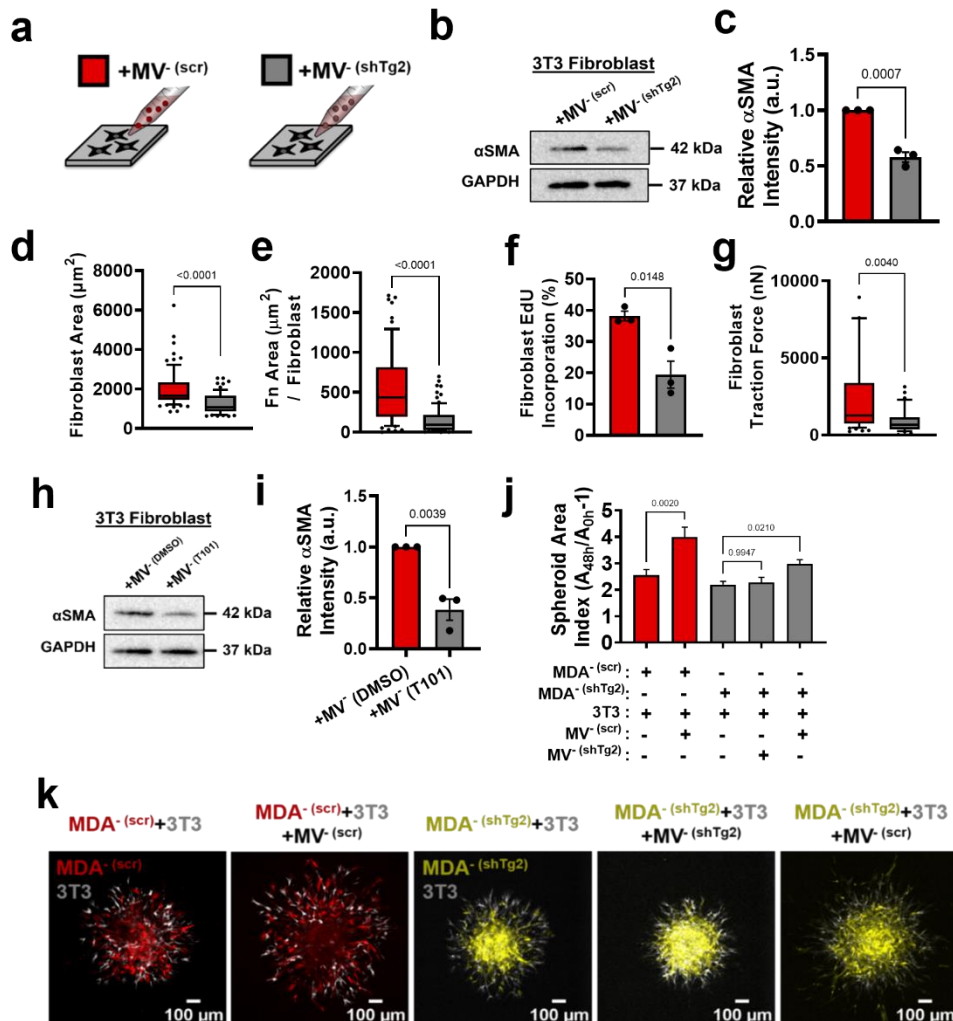
Figure 3.4. Modulation of Tg2 expression in MVs regulates MV-mediated fibroblast activation. (a) Schematic overviewing fibroblast culture with MVs. (b) Western blot of αSMA and GAPDH in fibroblasts

cultured with MV$^{-\text{(scr)}}$ (+MV$^{-\text{(scr)}}$) or with MV$^{-\text{(shTg2)}}$ (+MV$^{-\text{(shTg2)}}$). (c) Quantification of western in (b) (N=3). (d) Fibroblast cell area after culture in +MV$^{-\text{(scr)}}$ or +MV$^{-\text{(shTg2)}}$ conditions. (N=3; n=75,69). (e) Area of fibronectin deposited per fibroblast cultured in +MV$^{-\text{(scr)}}$ or +MV$^{-\text{(shTg2)}}$ conditions. (N=3; n=62, 82). (f) Percentage of fibroblasts EdU positive after culture in +MV$^{-\text{(scr)}}$ or +MV$^{-\text{(shTg2)}}$ conditions. (N=3). (g) Fibroblast traction force after culture in +MV$^{-\text{(scr)}}$ or +MV$^{-\text{(shTg2)}}$ conditions. (N=3; n=56, 33). (h) Western of blot of αSMA and GAPDH in fibroblasts cultured with MV$^{-\text{(DMSO)}}$ (+MV$^{-\text{(DMSO)}}$) or with MV$^{-\text{(T101)}}$ (+MV$^{-\text{(T101)}}$). (i) Quantification of western in (h) (N=3). (j) Spheroid area index quantification 48 hours post embedding. (N=3+; n=23, 23, 83, 60, 37). (k) Representative images of spheroid outgrowth 48 hours post embedding. MDA$^{-\text{(scr)}}$ (red); 3T3 fibroblast (gray); MDA$^{-\text{(shTg2)}}$ (yellow). Bar graphs show mean +/- SEM. Box and whisker plots show median and 25th-75th (box) and 10th-90th (whiskers) percentiles. P-values determined using an unpaired Student's t-test or a one-way ANOVA with Tukey's test for multiple comparisons.
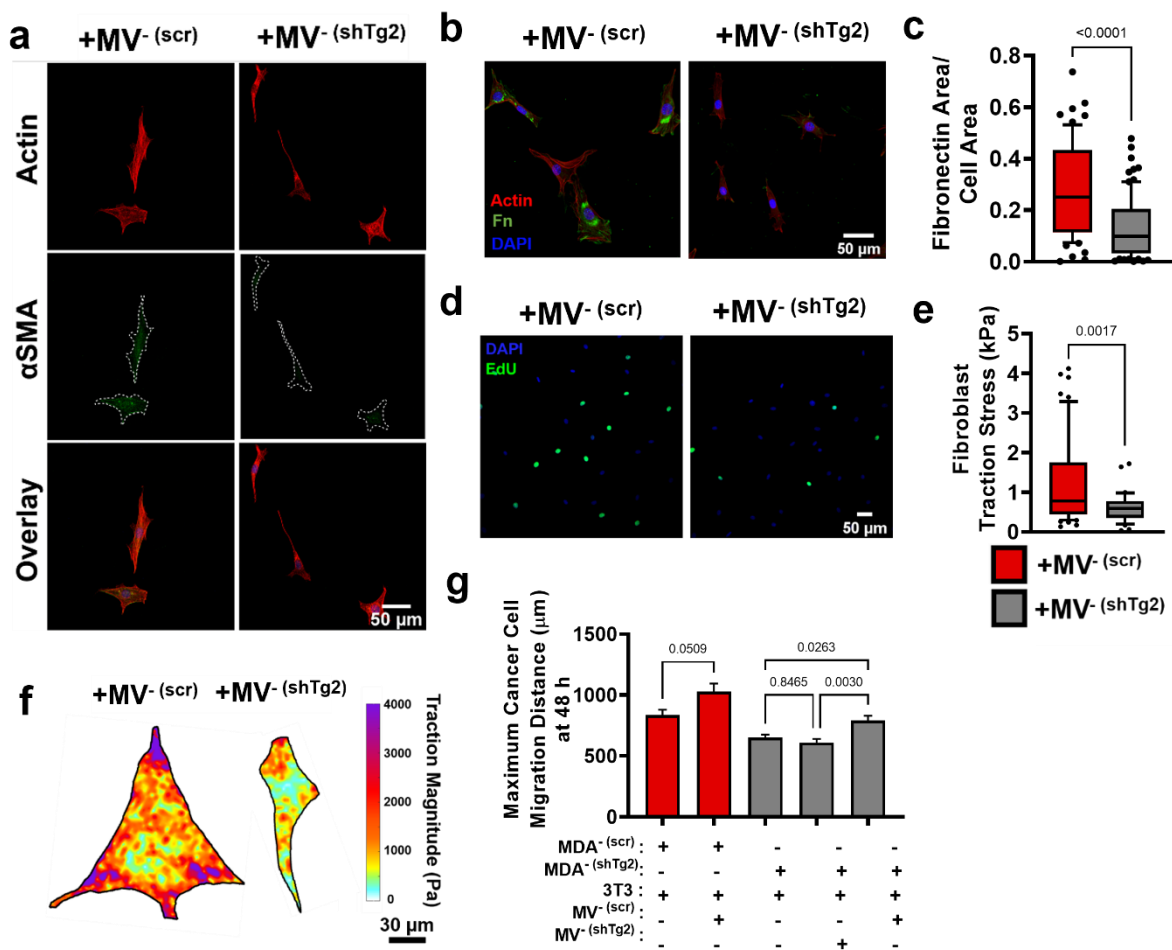
Supplemental Figure 3.4. (a) Representative images of fibroblast area (red) and αSMA expression (green) after culture with MV$^{-\text{(scr)}}$ (+MV$^{-\text{(scr)}}$) or MV$^{-\text{(shTg2)}}$ (+MV$^{-\text{(shTg2)}}$). (b) Representative images of fibroblast fibronectin deposition after culture in +MV$^{-\text{(scr)}}$ or +MV$^{-\text{(shTg2)}}$ conditions. Actin (red); fibronectin (green); DAPI (blue). (c) Fibronectin area normalized to fibroblast cell area. (N=3; n=62, 82). (d) Representative images of fibroblast EdU incorporation after culture in +MV$^{-\text{(scr)}}$ or +MV$^{-\text{(shTg2)}}$ conditions. DAPI (blue); EdU (green). (e) Fibroblast traction stress (calculated as fibroblast traction force / cell area) after culture in +MV$^{-\text{(scr)}}$ or +MV$^{-\text{(shTg2)}}$ conditions. (N=3; n=56, 33). (f) Representative fibroblast traction stress maps. (g)

Maximum distance of cancer cell migration away from spheroid core 48 hours post spheroid embedding. (N=3+; n= 23, 23, 83, 60, 37). Bar graphs show mean +/- SEM. Box and whisker plots show median and 25th-75th (box) and 10th-90th (whiskers) percentiles. P-values determined using an unpaired Student's t-test or a one-way ANOVA with Tukey's test for multiple comparisons.
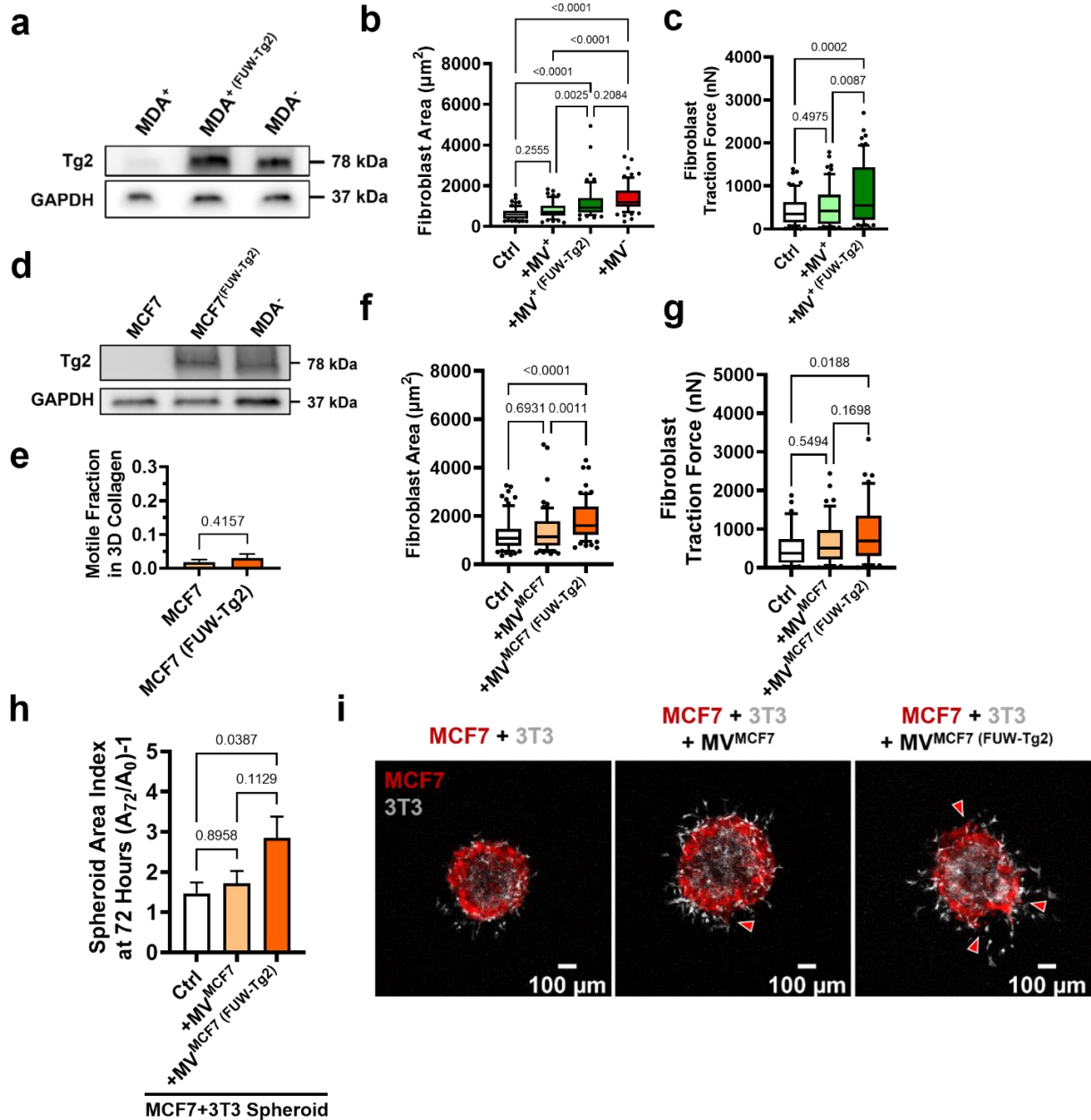
Supplemental Figure 3.5. (a) Western blot for Tg2 and GAPDH in MDA$^+$, MDA$^{+ \text{(FUW-Tg2)}}$, and MDA$^-$. (b) Fibroblast cell area after culture in control conditions (Ctrl), with MV$^+$ (+MV$^+$), with MV$^{+ \text{(FUW-Tg2)}}$ (+MV$^{+ \text{(FUW-Tg2)}}$), or with MV$^-$ (+MV$^-$). (N=3; n=70, 57, 56, 64). (c) Fibroblast traction force after culture in Ctrl, +MV$^+$, and +MV$^{+ \text{(FUw-Tg2)}}$ conditions (N=3, n= 61, 60, 60). (d) Western blot for Tg2 and GAPDH in MCF7, MCF7$^{\text{(FUW-Tg2)}}$, and MDA$^-$. (e) Motile fraction of MCF7 and MCF7$^{\text{(FUW-Tg2)}}$ in 3D collagen (N=3). (f) Fibroblast cell area after culture in control conditions (Ctrl), with MV$^{\text{MCF7}}$ (+MV$^{\text{MCF7}}$), or with MV$^{\text{MCF7 (FUW-Tg2)}}$ (+MV$^{\text{MCF7 (FUW-Tg2)}}$) (N=3, n = 76, 72, 71). (g) Fibroblast traction force after culture in Ctrl, +MV$^{\text{MCF7}}$,

66

+ MV$^{MCF7 (FUW-Tg2)}$ (N=3, n = 38, 47, 44). (h) Spheroid area index of MCF7+3T3 spheroids after 72 hours of outgrowth (N=3, n = 13, 12, 13) (i) Representative images of spheroid outgrowth 72 hours post embedding. MCF7 (red); 3T3 fibroblast (gray). Red arrows point to MCF7 cells migrating away from spheroid core. Bar graphs show mean +/- SEM. Box and whisker plots show median and 25th-75th (box) and 10th-90th (whiskers) percentiles. P-values determined using an unpaired Student's t-test or a one-way ANOVA with Tukey's test for multiple comparisons.

3.4.6 *Tg2 knockdown in MDA$^-$ reduces metastasis*

Given that MV-Tg2 activated fibroblasts *in vitro* and increased cancer cell migration in spheroid cocultures, we investigated whether knockdown of Tg2 in MDA$^-$ is sufficient to reduce MDA$^-$ metastasis in an orthotopic mammary metastasis mouse model (**Fig. 3.5A**). Six weeks post subcutaneous injection of MDA$^{- (scr)}$ and MDA$^{- (shTg2)}$ into the mammary fat pad, primary tumors were of similar volumes (**Fig. 3.5B**). MDA$^{- (shTg2)}$ tumors exhibited decreased stiffness compared to control tumors (**Fig. 3.5C**). Immunofluorescent staining of MDA$^{- (scr)}$ and MDA$^{- (shTg2)}$ tumors for the fibroblast activation marker αSMA revealed a decreased fraction of αSMA$^+$ tissue in MDA$^{- (shTg2)}$ tumors compared to control tumors (**Fig. 3.5D-E**), suggesting that knockdown of Tg2 reduced primary tumor fibroblast activation. Immunohistochemical staining for collagen and fibronectin also revealed decreased matrix in the MDA$^{- (shTg2)}$ tumors compared to control tumors (**Fig. 3.5F**). Three weeks post primary tumor removal, BLI imaging and tissue collection was completed. The metastasis of MDA$^{-(shTg2)}$ to the lungs and liver was greatly reduced compared to MDA$^{- (scr)}$ (**Fig. 3.5G-K**). Livers from MDA$^{- (shTg2)}$ mice displayed fewer macroscopic liver nodules compared to MDA$^{- (scr)}$ (**Fig. 3.5H**), and immunohistochemical staining for GFP$^+$ cancer cells in mouse liver and lungs revealed decreased GFP+ tissue area in the lungs and liver of MDA$^{- (shTg2)}$ mice (**Fig. 3.5I-K**). These findings reveal that knockdown of Tg2 in MDA$^-$ decreases tumor stiffness, fibroblast activation, ECM deposition, and metastasis.
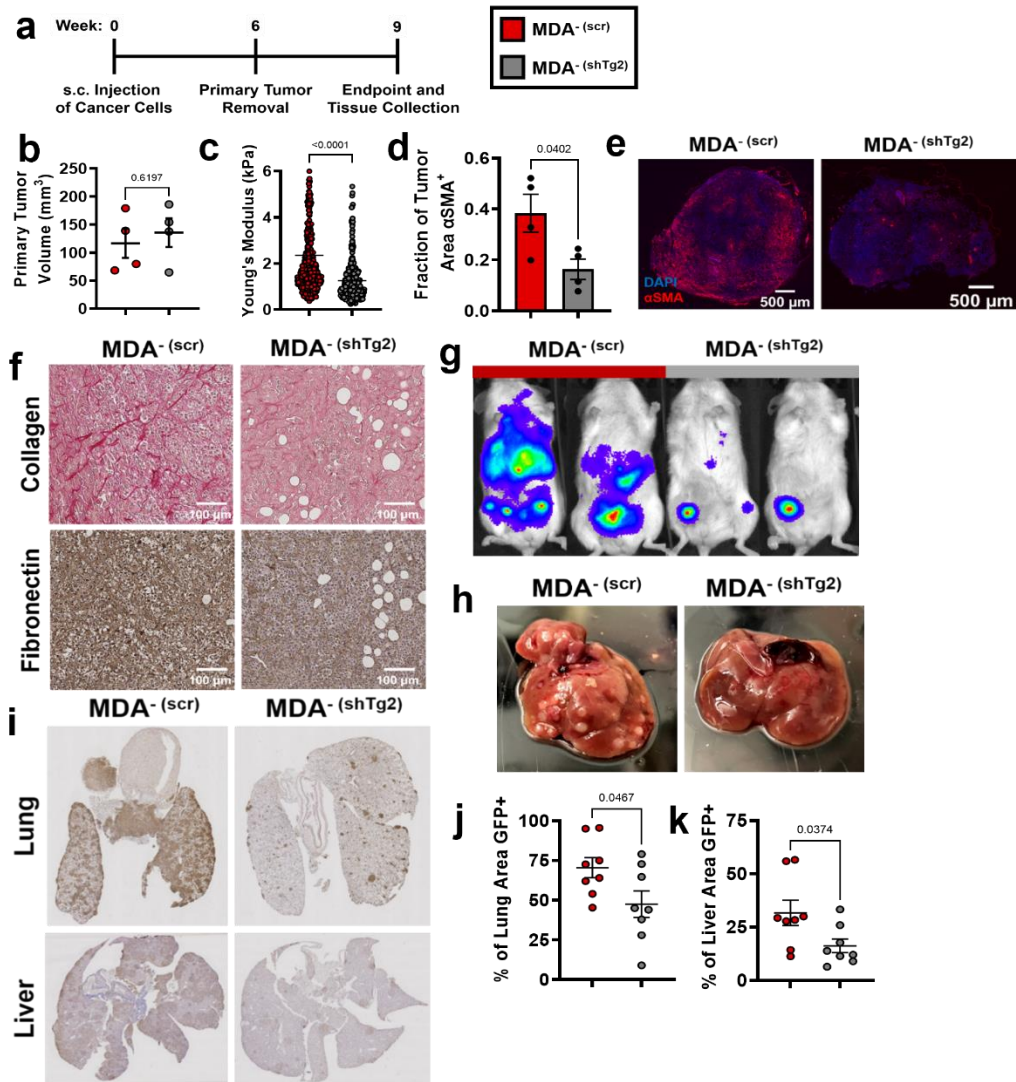
Figure 3.5. Knockdown of Tg2 in MDA⁻ subpopulation reduces metastasis. (a) Timeline of orthotopic mammary metastasis model. (b) Primary tumor volume after removal (N=4). (c) AFM stiffness measurements of MDA⁻ (scr) and MDA⁻ (shTg2) primary tumors. (N=3+ tumors per condition; n = 420, 379). (d) Fraction of tumor area positive for αSMA (N=4). (e) Representative images of αSMA (red) and DAPI (blue) in MDA⁻ (scr) and MDA⁻ (shTg2) primary tumors. (f) Immunohistochemical staining of collagen and fibronectin in MDA⁻ (scr) and MDA⁻ (shTg2) primary tumors. (g) Representative BLI of MDA⁻ (scr) and MDA⁻ (shTg2) metastasis. (h) Representative image of macroscopic liver nodules. (i) Anti-GFP immunohistochemical staining of lungs and liver from MDA⁻ (scr) and MDA⁻ (shTg2) mice. (j) Quantification of percentage of lung tissue area GFP-positive. (N=4, n=8). (k) Quantification of percentage of liver tissue area GFP-positive. (N=4, n=8). Data shown as mean +/- SEM. P-values determined using an unpaired Student's t-test.

3.4.7   *Tg2-rich MV⁻ are sufficient to induce MDA⁻ (shTg2) metastasis*

Since knockdown of Tg2 in MDA⁻ reduced MDA⁻ metastasis, we investigated whether supplementing primary tumors composed of MDA⁻ (shTg2) cells with Tg2-rich MV⁻ could induce the metastasis of MDA⁻ (shTg2). One week post-subcutaneous injection of MDA⁻ (shTg2) into the mammary fat pad,

mice were subcutaneously injected every three days for five weeks with either MV$^-$ suspended in serum-free media (MDA$^{-\,(shTg2)}$ + MV$^-$) or a serum-free (SF) media control (MDA$^{-\,(shTg2)}$ + SF) or (**Fig. 3.6A**). After six weeks of primary tumor growth, MDA$^{-\,(shTg2)}$ primary tumors supplemented with MV$^-$ were significantly larger than and exhibited increased primary tumor stiffness compared to control tumors (**Fig. 3.6B-C**). MDA$^{-\,(shTg2)}$ + MV$^-$ tumors also exhibited an increased fraction of αSMA$^+$ tissue area compared to control tumors (**Fig. 3.6D-E**). Immunohistochemical staining of tumors revealed increased collagen and fibronectin deposition in the MDA$^{-\,(shTg2)}$ + MV$^-$ primary tumors compared to control tumors (**Fig. 3.6F**). Three weeks post primary tumor removal, BLI imaging and tissue collection was completed. Supplementing MDA$^{-\,(shTg2)}$ primary tumors with MV$^-$ induced increased metastasis to both the lungs and liver of mice, compared to control mice (**Fig. 3.6G-K**). Livers from MDA$^{-\,(shTg2)}$ + MV$^-$ mice displayed increased numbers of macroscopic liver nodules compared to control mice (**Fig. 3.6H**). Immunohistochemical staining for GFP in mouse lungs revealed increased metastasis to the lungs of MDA$^{-\,(shTg2)}$ + MV$^-$ mice compared to control mice (**Fig. 3.6I-J**). Livers of MDA$^{-\,(shTg2)}$ + MV$^-$ mice had slightly increased but not significantly higher levels of metastasis compared to control mice (**Fig. 3.6J, K**). These results indicate that repeated injection of Tg2-rich wildtype MV$^-$ during the growth of MDA$^{-\,(shTg2)}$ primary tumors resulted in primary tumor stiffening, increased fibroblast activation, and increased metastasis of the Tg2-knockdown weakly migratory breast cancer subpopulation. Altogether, our results reveal a novel mechanism by which weakly migratory cancer cells release Tg2-rich MVs to activate fibroblasts and remodel the primary tumor to facilitate weakly migratory cancer cell migration and metastasis (**Fig. 3.6L**).
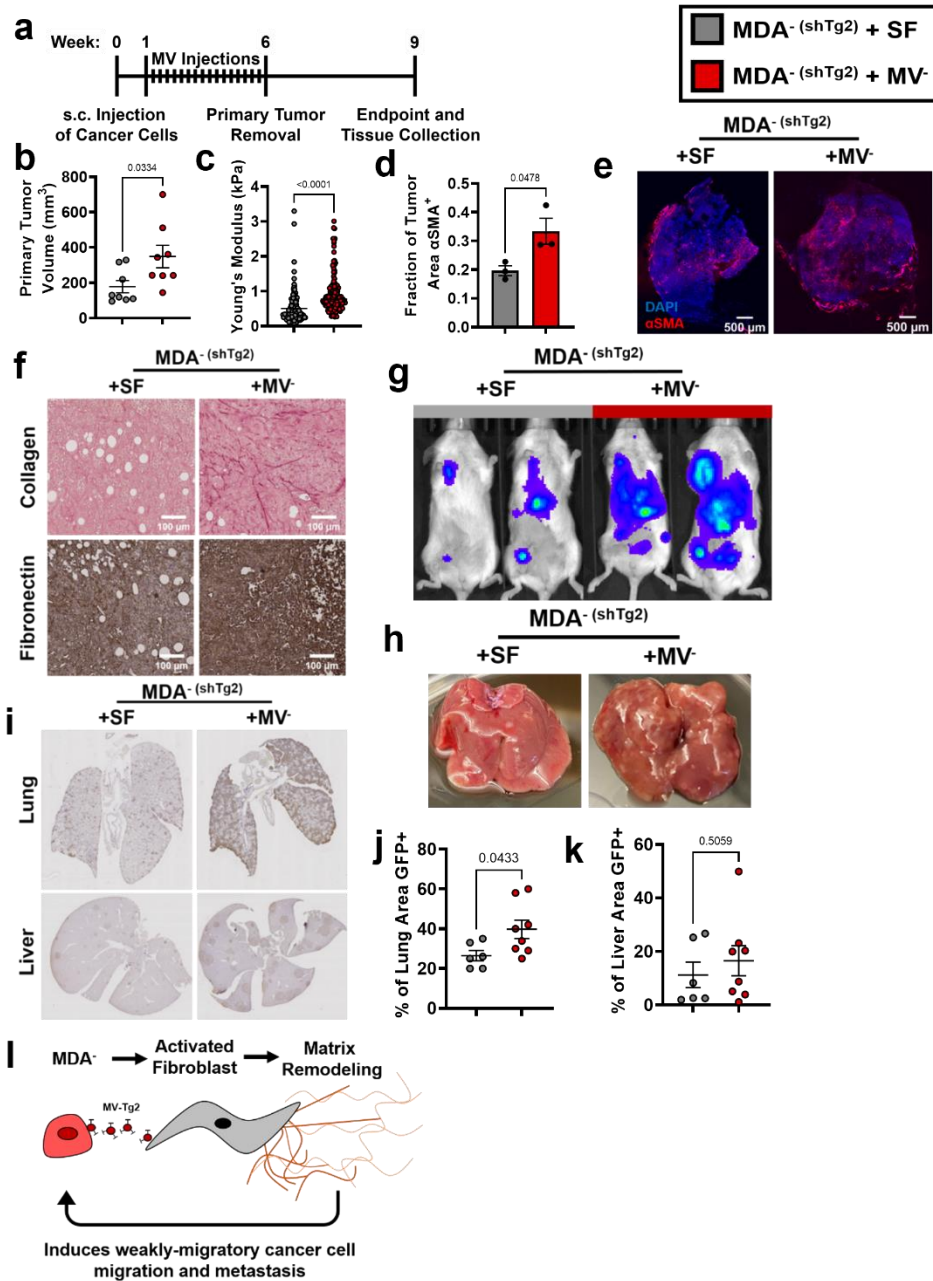
Figure 3.6. Tg2-rich wildtype MV⁻ are sufficient to induce the metastasis of MDA⁻ (shTg2). (a) Timeline of orthotopic mammary metastasis model with MV injections every 3 days. (b) Primary tumor volume after removal (N=8). (c) AFM stiffness measurements of MDA⁻ (shTg2) + SF and MDA⁻ (shTg2) + MV⁻ primary tumors. (N=3+ tumors per condition; n = 128, 140). (d) Fraction of tumor area positive for αSMA (N=3). (e) Representative images of αSMA (red) and DAPI (blue) in MDA⁻ (shTg2) + SF and MDA⁻ (shTg2) + MV⁻ primary tumors. (f) Immunohistochemical staining of collagen and fibronectin in MDA⁻ (shTg2) + SF and MDA⁻ (shTg2) + MV⁻ primary tumors. (g) Representative BLI of MDA⁻ (shTg2) metastasis. (h) Representative image of macroscopic liver nodules. (i) Anti-GFP immunohistochemical staining of lungs and liver from MDA⁻ (shTg2) + SF and MDA⁻ (shTg2) + MV⁻ mice. (j) Quantification of percentage of lung tissue area GFP-positive. (N=6, 8). (k) Quantification of percentage of liver tissue area GFP-positive. (N=6, 8). (l) Illustration overviewing the mechanism of MDA⁻ metastasis. Data shown as mean +/- SEM.

70

3.4.8   Clinical implications of Tg2 expression on breast cancer progression

Given that MV-Tg2 facilitate weakly migratory cancer cell metastasis, we investigated the clinical ramifications of these findings by examining Tg2 expression as a function of patient prognosis. Using the TNMplot database, we found that Tg2 expression of breast cancer patients increased from normal tissue to breast tumor tissue[414], indicating that Tg2 expression was correlated with breast cancer metastasis (**Fig. 3.7A**). Additionally, breast cancer patients exhibited significant decreased distant metastasis free survival with high Tg2 expression compared to low Tg2 expression[415] (**Fig. 3.7B**). This relationship between Tg2 expression and distant metastasis free survival was even more robust in triple negative breast cancer (TNBC) patients[415] (**Fig. 3.7C**). Lastly, using Tg2 co-expression data of breast invasive carcinoma patients, ACTA2, FAP, PDGFRα, and PDGFRβ were significantly correlated with Tg2 expression, indicating that Tg2 expression correlates with fibroblast activation in breast cancer patients [416,417] (**Fig. 3.7D**). Together, these findings further implicate Tg2 as an indicator of breast cancer progression and identify Tg2 as an important therapeutic target to prevent fibroblast activation and metastasis.
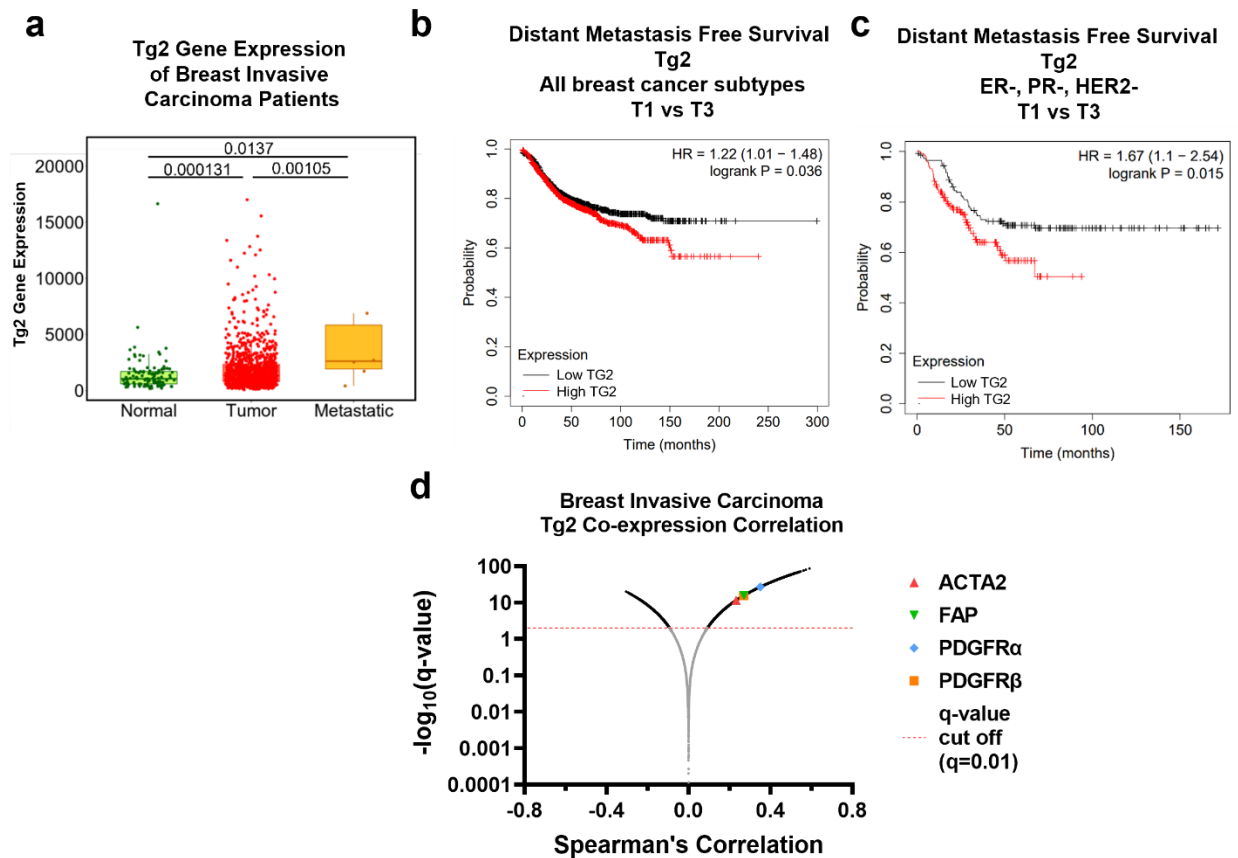
Figure 3.7. Clinical implications of Tg2 expression on breast cancer progression. (a) Tg2 gene expression, measured with RNA sequencing, of normal, tumor, and metastatic tissue from breast invasive carcinoma patients. (N=242, 7569, 82). Data adapted from TNMplot database. (b) Distant metastasis free survival Kaplan-Meier plot for Tg2 expression in all breast cancer subtypes. Data adapted from the Kaplan-

71

Meier Plotter database. (c) Distant metastasis free survival Kaplan-Meier plot for Tg2 expression in ER, PR, and HER2 negative breast cancer. Data adapted from the Kaplan-Meier Plotter database. (d) Tg2 co-expression correlation data for breast invasive carcinoma. Data adapted from cBioPortal using the Firehose Legacy dataset.

3.5   Discussion

Identifying the mechanisms of cancer cell dissemination away from the primary tumor is essential to develop new therapies to target metastatic cancer cells. Specifically, we show that in breast cancer, while highly migratory cells are capable of independent migration, weakly migratory cells release Tg2-rich MVs which activate fibroblasts which subsequently promote cancer cell dissemination and ultimately metastasis. Our data suggests that the interaction between weakly migratory cancer cells and stromal fibroblasts via MVs facilitates weakly migratory cancer cell dissemination and metastasis.

Our data supports the observation that cells do not need to be inherently migratory to metastasize[377,389–393]. Others have shown that MDA-MB-231 isolated from bone metastases were less migratory than their primary tumor counterparts[389] and that highly metastatic subpopulations of MDA-MB-231 selected through repeated *in vivo* isolation of metastases were weakly migratory[390,391]. Our work is the first to describe a mechanism by which cancer cells with a weak migration phenotype can manipulate cells within the TME to escape the primary tumor. Given the current emphasis on cell migration in cancer metastasis research, these findings highlight that cancer cell migration alone is not a sufficient indicator of metastatic potential. A focus on MV-mediated cell-cell signaling between cancer and stromal cells is crucial to fully understand the dynamics of cancer cell dissemination.

Our findings suggest a feedback loop between MV signaling, matrix remodeling, and fibroblast activation may exist. We previously reported that MV-mediated fibroblast activation was enhanced in high stiffness matrices mimicking the breast tumor periphery[17]. Here, we show that Tg2-rich MVs stiffen the primary tumor, induce matrix deposition by stromal cells, activate fibroblasts, and promote cancer metastasis. Together, these data indicate that MV-induced fibroblast activation leads to increased tumor stiffening through matrix remodeling and this increased stiffness may feedback to prime fibroblasts for continued activation to further enhance cancer metastasis. Additionally, previous work revealed that transformation of normal fibroblasts *in vivo* by MDA-MB-231 MVs was dependent upon Tg2[17]. Our results point to a role for these MV-Tg2-activated fibroblasts in mediating cancer cell escape from the primary tumor through matrix remodeling. As knockdown of Tg2 in MDA-MB-231 is known to decrease metastasis[418], we suspect this may due, in part, to reduced MV-mediated fibroblast activation and decreased cancer cell escape from the primary tumor.

Importantly, our work is the first to show that MV cargo varies based on cell phenotype. While it is known cancer cell phenotype affects the numbers of MVs released[274], our work reveals that differences in cancer cell phenotype within a single cell line actually correlates with differences in MV cargo.

Additionally, while previous work showed that highly migratory cancer cells package migration-promoting cargo into EVs[419], our results suggest that heterogeneity in MV cargo based on migratory phenotype has downstream effects on fibroblast activation, TME remodeling, and ultimately metastasis. Our findings specifically show that Tg2 is not uniformly expressed by all breast cancer-derived MVs but rather dependent upon the migratory phenotype of the MV releasing cell, with increased Tg2 expression in MVs released by the weakly migratory breast cancer cells. Interestingly, the weakly migratory cells express high levels of Tg2 and E-cadherin[377]. While Tg2 expression is generally linked with EMT and positively correlated with cancer cell invasion and migration[58,59,420] and E-cadherin is a marker of epithelial phenotypes and decreased cancer cell migration[377,392,421], Tg2 was recently identified as a marker of epithelial-mesenchymal plasticity and was found to be upregulated in cancer cells undergoing EMT only after a reversion to a secondary epithelial state[413]. Taken together, these findings reveal that MV cargo changes as cells plastically change their EMT phenotype during the metastasis.

Additionally, our findings suggest that not all MVs released from a cell population will homogenously communicate with surrounding cells. In cancer, targeting MV populations that contain cargo (such as Tg2) to remodel the TME may be crucial to reduce metastatic potential. Importantly, other groups have shown that exosomes affect later stages of cancer metastasis, including angiogenesis and pre-metastatic niche formation[213,413,422]. As exosomes and MVs contain many of the same cancer-promoting signaling proteins, such as Tg2, VEGF, and TGFβ[344,413,423–425], MVs may also signal to endothelial cells to promote angiogenesis and travel to secondary sites to promote pre-metastatic niche formation. Taken together, these findings reveal that identifying the MV populations and MV cargo capable of promoting progression through the metastatic cascade is essential to prevent metastasis and highlight MVs as a potential target for new anti-metastatic cancer therapies.

In summary, the relationship between cancer cell migratory ability and dissemination away from the primary tumor is complex. While highly migratory cells are capable of independent migration, our work identifies a population of weakly migratory, highly metastatic breast cancer cells which escape the primary tumor via MV-Tg2-mediated fibroblast activation. As we further define the relationship between cancer cell migration and metastatic potential and the consequences of MV signaling on cancer progression, these findings are likely to have broader implications in designing modalities and therapies to detect and target metastatic cancer cells.

CHAPTER 4: LINK BETWEEN GLUCOSE METABOLISM AND EMT DRIVES TRIPLE
NEGATIVE BREAST CANCER MIGRATORY HETEROGENIETY

This chapter is under review and has been reproduced with the permission of the publisher and my co-
authors. This work was completed in collaboration with co-first author Jenna A. Mosier.

4.1   Abstract

Intracellular and environmental cues result in heterogeneous cancer cell populations with different
metabolic and migratory behaviors. While glucose metabolism and EMT have previously been linked, it is
unclear how this relationship fuels cancer cell migration. Here, we show that while glycolysis drives single
cell confined migration in engineered microtracks, fast and slow cells display different migratory
sensitivities to glycolysis and OxPhos inhibition. Phenotypic sorting of highly and weakly migratory
subpopulations (MDA$^+$, MDA$^-$) reveals that more mesenchymal, highly migratory MDA$^+$ preferentially use
glycolysis while more epithelial, weakly migratory MDA$^-$ utilize OxPhos. These phenotypes are plastic and
MDA$^+$ can be made less glycolytic, mesenchymal, and migratory and MDA$^-$ can be made more glycolytic,
mesenchymal, and migratory via modulation of glucose metabolism or EMT. These findings reveal an
intrinsic link between EMT and glucose metabolism that controls migration. Identifying mechanisms
fueling phenotypic heterogeneity is essential to develop targeted metastatic therapeutics.

4.2   Introduction

Intratumor heterogeneity is an emerging hallmark of cancer that complicates clinical diagnostics
and therapeutics[7,377,426]. As cancer cells have uniquely high proliferation rates, cancer metabolism research
has historically focused on identifying aerobic glycolysis as the driving force behind this proliferation[223–
225,227,427]. Recent work has identified heterogeneity in breast cancer metabolic state in both primary tumors
and metastatic sites, with increased glycolysis in primary tumors and increased mitochondrial OxPhos at
metastatic sites[289]. Therefore, energy produced via glycolysis and OxPhos may fuel different cell behaviors
with different metastatic advantages.

One of the first steps of breast cancer metastasis is invasion through the basement membrane and
migration through the extracellular matrix[428–430]; therefore, migratory ability is often considered an indicator
of metastatic success[229,386–388]. To complete this first step and escape the primary tumor, cancer cells can
reprogram their metabolism to fuel migration through a mechanically and chemically complex TME[2]. It is
has been suggested that cancer cells undergo epithelial-to-mesenchymal transition (EMT) to promote
invasion and migration through the TME[431–434]. Cancer cell EMT phenotype and metabolic state appear to
exist in a dynamic, reciprocal relationship. Metabolic dysregulation and glycolytic enzymes can induce
EMT[435–439]. Alternatively, drivers of EMT can induce metabolic reprogramming and upregulate glycolysis

in transitioning cancer cells[247,438,440–444]. While it is known that cancer cell bioenergetics and EMT are intrinsically linked, the consequences of this relationship on intratumor migratory heterogeneity are unclear.

Here, we observe significant heterogeneity in the metabolic signatures and EMT phenotype of migrating breast cancer cells. Cell migration in the TME was modeled using microfabricated 3D microtracks which recapitulate matrix confinement encountered *in vivo*[97,445]. While MDA-MB-231 breast cancer cells primarily utilize glycolysis to fuel their migration in confinement, single cell analysis of MDA-MB-231 revealed that while highly migratory cells were sensitive to inhibition of glycolysis and unaffected by inhibition of OxPhos, inhibition of OxPhos increased weakly migratory cancer cell migration. To further investigate this migratory heterogeneity, MDA-MB-231 breast cancer cells were phenotypically sorted to obtain highly and weakly migratory subpopulations of MDA-MB-231 that were then thoroughly characterized. We show that highly migratory populations (MDA$^+$) exhibit increased mesenchymal features and increased glycolytic genes, while weakly migratory populations (MDA$^-$) are more epithelial and are more associated with OxPhos. Further exploration of this characterization revealed that migratory ability in confinement can be controlled by inducing EMT or modulating metabolic pathways utilized by cells. Thus, our findings reveal that a dynamic, complementary relationship between glucose metabolism and EMT phenotype drives heterogeneous migratory phenotypes in triple negative breast cancer.

4.3 Materials and methods

Cell culture and reagents: MDA-MB-231 mammary adenocarcinoma cells (HTB-26, ATCC, Manassas, VA) were maintained in Dulbecco's Modified Eagle's Media (DMEM) (ThermoFisher Scientific, Waltham, PA) supplemented with 10% fetal bovine serum (Atlanta Biologicals, Flowery Branch, GA) and 1% penicillin-streptomycin (ThermoFisher Scientific). Iodoacetate (10 µM, Millipore Sigma, I2512), sodium pyruvate (100 µM, ThermoFisher Scientific, 11360070), and antimycin-A (250 µM in 2D, 500 µM in microtracks, Millipore Sigma, A8674) were used to inhibit glucose metabolism. TGFβ (5 ng/mL in 2D, 50 ng/mL in microtracks) was used to induce EMT. SUM159PT cells (BioIVT) were maintained in Ham's F12 Medium (ThermoFisher Scientific) supplemented with 5% fetal bovine serum, 1 µg/mL hydrocortisone (Millipore Sigma), 5 µg/mL insulin (Millipore Sigma), and 1% penicillin-streptomycin. Cell culture and time-lapse imaging were performed at 37°C and 5% CO_2.

Microtrack fabrication: Collagen microtracks of 10 µm width were prepared as previously described[445]. Briefly, 100-mm diameter silicon wafer molds were coated with S1813 photoresist and Bosch etched to pattern with microtrack geometries. Polydimethylsiloxane (PDMS; Sylgard) was mixed in a 1:10 ratio of cross-linker to monomer, poured over the wafer, and cured to be used as a template stamp. Collagen Type I extracted from rat tail tendons was prepared in-house and resuspended as a 10 mg/mL stock solution in acetic acid. The stock solution was diluted to 3 mg/mL, neutralized with 1 N NaOH, and used to lightly coat PDMS stamps. Stamps were inverted onto a drop of diluted collagen between two thin PDMS spacers

and left to polymerize for 90 min at 37°C. To finalize 3D microtracks, patterned collagen matrices were seeded with either parental (MDA[PAR]), highly migratory (MDA[+]), or weakly migratory MDA-MB-231 (MDA[-]) (~100,000 cells/mL to achieve low seeding density) and left to settle for 2 minutes at 37°C. A thin layer of collagen was applied to a glass coverslip and inverted over the microtracks as a lid. Microtrack system was supplied with fresh media was fully polymerized, and cells were left to incubate overnight at 37°C. At ~18 hours post cell seeding, glucose metabolism inhibitors or vehicle controls were added to microtracks in fresh media. Timelapse images of cells were acquired every 20 minutes from 1-12 hours post inhibitor application, acquired using a Zeiss Axio Observer Z1 inverted microscope equipped with a Hamamatsu ORCA-ER camera with a 10×/0.3 NA objective for migration studies. AxioVision software was used to operate device. Where applicable, cells were supplemented with 50 ng/mL TGFβ 24 hours before imaging, followed by 100 nM of TMRM (Invitrogen, U34361) 2 hours before imaging. Timelapse images were acquired every 20 minutes 24-30 hours after TGFβ treatment using Zeiss LSM800 Confocal Microscope with a 10x/0.3 NA Zeiss Objective with a 10X objective.

Analysis of cell migration in microtracks: Cell migration was analyzed by using Fiji ImageJ (National Institute of Health, Bethesda, MD) to outline individual cells in collagen microtracks. The cell body was manually outlined, and cell area, centroid, and aspect ratio were quantified. Cell displacement was calculated as the distance between cell centroids between each frame. Average velocity was then calculated by dividing the displacement by the time step. For each frame, the number of microtrack walls the cell contacted was logged. For TGFβ studies, cell velocity was measured and TMRM corrected total cell fluorescence (CTCF = Integrated Density – (Mean Intensity of Background*Cell Area)) was calculated where applicable. Cells undergoing cell division, apoptosis, or interacting with other cells were excluded from analysis.

Phenotypic sorting of breast cancer cells: Breast cancer cell lines were sorted as previously described[377]. Briefly, breast cancer cells were seeded on top of a transwell insert (Greiner Bio-One, Kremsmunster, Austria) with 8 µm pores coated in 1 mg/ml collagen. A serum gradient was applied, and cells were able to migrate through the transwell insert for four days. After four days, highly migratory and weakly migratory cells were collected and purified over 20 rounds of sorting. Cells that repeatedly migrated through the transwell were termed 'highly migratory' (MDA[+], SUM^{+}) and cells that never migrated through the transwell were termed 'weakly migratory' (MDA[-], SUM[-]).

Motile fraction: MDA[+] or MDA[-] were seeded into 1.5 mg/mL collagen gels at a density of 200,000 cells/mL. Cells were incubated for 24 hours at 37°C. Timelapse images of cells were acquired every 20 minutes for 12 hours, acquired using a Zeiss Axio Observer Z1 inverted microscope equipped with a Hamamatsu ORCA-ER camera with a 10×/0.3 NA objective. AxioVision software was used to operate

device. Motile fraction was quantified as the fraction of cells that migrated at least one cell body every 2 hours. Aspect ratio of cells was quantified using ImageJ.

RNA sequencing: RNA was isolated using the RNeasy mini kit and RNAase-Free DNase Set according to manufacturer protocols. RNA sequencing was performed by the Vanderbilt Technologies for Advanced Genomics core (VANTAGE) as previously described[377]. EMT and Energy Scores were computed from the average normalized expression of manually curated lists of epithelial, mesenchymal, glycolysis, and OxPhos genes.

Glucose uptake: Cells were cultured for 24 hours in DMEM + 10% FBS. After 24 hours, fresh media supplemented with 0.146 mM 2-NBDG (Life Technologies) was added and cells were supplemented with 5 ng/mL TGFβ if applicable. After 24 hours, cells were fixed in 3.2% paraformaldehyde and imaged on a Zeiss LSM800 Confocal Microscope with a 10x/0.3 NA Zeiss Objective with a 10X objective. To calculate 2-NBDG uptake, cells were manually outlined and the corrected total cell fluorescence (CTCF = Integrated Density – (Mean Intensity of Background*Cell Area)) was calculated.

Mitochondrial membrane potential: Cells were cultured for 24 hours in DMEM + 10% FBS and cells were supplemented with 5 ng/mL TGFβ if applicable. After 24 hours, fresh media supplemented with 75 nM TMRM (Invitrogen, U34361) was added. After 30 minutes, cells were washed with PBS and fixed in 3.2% paraformaldehyde. Cells were imaged on a Zeiss LSM800 Confocal Microscope with a 10x/0.3 NA Zeiss Objective. To calculate TMRM, cells were manually outlined and the corrected total cell fluorescence (CTCF = Integrated Density – (Mean Intensity of Background*Cell Area)) was calculated.

Lactate Output: MDA$^+$ and MDA$^-$ were cultured for 24 hours in DMEM + 10% FBS. Conditioned media was removed, and lactate output was measured using the L-Lactate Assay Kit (Abcam, ab65331).

DNA constructs: FUW-E-cadherin-E2A plasmid was created in-house and was used to stably transduce MDA$^+$.

Quantitative PCR: mRNA was isolated from cells using PureZOL RNA isolation reagent (Bio-Rad). cDNA was synthesized from mRNA using iScript cDNA Synthesis Kit (Bio-Rad). QPCR was completed using SYBR green (Bio-Rad). Relative mRNA expression was calculated as 2^{-ddCt} and β-actin was used to normalize results.

Table 4.1. qPCR Primers

	Forward (5' to 3')	Reverse (5' to 3')
CDH1	GCCTCCTGAAAAGAGAGTGGAAG	TGGCAGTGTCTCTCCAAATCCG
VIM	AGGCAAAGCAGGAGTCCACTGA	ATCTGGCGTTCCAGGGACTCAT
ZEB1	GGCATACACCTACTCAACTACGG	TGGGCGGTGTAGAATCAGAGTC
SNAI1	TGCCCTCAAGATGCACATCCGA	GGGACAGGAGAAGGGCTTCTC

ACTB	CACAAGCAGAGTGCTGAAGGTG	GATTCCTGAGAGTCCAAAGACAG

Statistical analysis: All statistical analysis was performed using GraphPad Prism. Box-and-whisker plots show mean, $25^{th}/75^{th}$ percentile, and whiskers represent maximum and minimum values. Fold change bar graphs and dose curves show mean +/- SEM. Dot plots show individual data points.

4.4 Results

4.4.1 Glycolysis fuels breast cancer migration in confined environments

Both glycolysis and OxPhos have been implicated in single cell migration in cancer[250,252,446,447]. However, microenvironmental mechanical cues such as confinement are known to regulate cancer cell migration and bioenergetics[175,382]. To determine the mode of glucose metabolism that drives breast cancer migration in confined spaces, MDA-MB-231 breast cancer cell (MDA[PAR]) migration was analyzed with inhibitors of glycolysis or OxPhos in engineered, *in vitro* collagen microtracks which mimic the natural tracks and pores found in the TME, allowing accurate quantification of 3D, directional migration[97,445]. Microtracks were fabricated using custom-made PDMS template stamps on liquid collagen. After collagen polymerization, microtracks were seeded with low densities of cancer cells to permit single cell time-lapse imaging (**Figure 4.1A**). To modulate breast cancer glucose metabolism, MDA[PAR] were treated with either iodoacetate (IA), an inhibitor of GAPDH in glycolysis, or antimycin-A (AMA), an inhibitor of complex III of the electron transport chain in the mitochondria. MDA[PAR] treated with IA were additionally supplemented with 100 µM sodium pyruvate (PYR) to reduce toxicity from glycolysis inhibition and permit continued mitochondrial respiration[448,449]. MDA[PAR] treated with IA and IA + PYR (MDA[PAR] + IA, MDA[PAR] + IA + PYR) displayed significantly reduced migration velocity 6-12 hours after drug application compared to vehicle control conditions (MDA[PAR] Ctrl) (**Figure 4.1B,C**). MDA[PAR] treated with AMA (MDA[PAR] + AMA) displayed no change in velocity 6-12 hours after drug application compared to vehicle control conditions (**Figure 4.1D**). To directly compare response to different inhibitors with different vehicle controls, fold change of velocity was calculated. MDA[PAR] treated with IA and IA + PYR displayed significantly decreased fold changes in velocity compared to cells treated with AMA (**Figure 4.1E**). These data suggest that MDA[PAR] migration in confinement is primarily fueled by glycolysis compared to OxPhos.
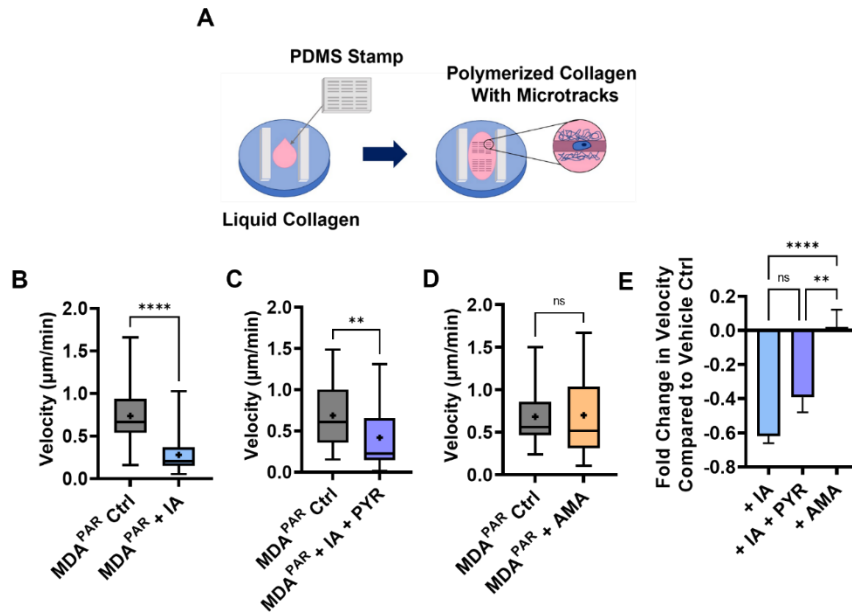
Figure 4.1. Glycolysis fuels MDA-MB-231 migration in confinement. (A) Schematic of microtrack micromolding. PDMS stamp used to mold collagen in between plastic spacers in a 6 well plate; Average MDA^{PAR} microtrack velocity 6-12 h after (B) vehicle control (diH$_2$O) (Ctrl) or IA application (+ IA) (n=42-46); (C) vehicle control (diH$_2$O) or IA + PYR application (+ IA + PYR) (n=35-36); (D) vehicle control (DMSO) or AMA application (+ AMA) (n=37-45); (E) Fold change in velocity compared to vehicle control from (D-F) (n=36-46); ** denotes p<0.01, **** denotes p<0.0001, ns = not significant. Mean + SEM shown for bar graphs and min to max for box-and-whisker plots with mean represented as "+".

4.4.2 *Breast cancer cells exhibit heterogeneous migration in response to glucose metabolism inhibitors*

Given that MDA^{PAR} breast cancer cells are highly heterogenous and display different morphologies, migration potentials, and EMT phenotypes[377,450–452], we investigated the distribution of MDA^{PAR} velocity in response to glucose metabolism inhibitors. MDA^{PAR} migration without glucose metabolism inhibition (MDA^{PAR} Ctrl) was largely heterogeneous with cells displaying a wide range of velocities in confinement (**Figure 4.2A-C**). MDA^{PAR} migration in response to IA was largely homogeneous, with a shift towards decreased velocities evident in the velocity histogram (**Figure 4.2A**). Migration response to IA+PYR also resulted in a shift in the velocity histogram towards decreased velocities (**Figure 4.2B**). MDA^{PAR} migration in response to AMA treatment was more heterogeneous, with certain cells exhibiting decreased migration velocities and others exhibiting increased migration velocities compared to MDA^{PAR} Ctrl (**Figure 4.2C**).

Given that cells within MDA^{PAR} exhibited different velocities in response to glucose metabolism inhibition, we investigated whether cells with low or high migration velocities responded differently to inhibition of glycolysis or OxPhos. Cells with migration velocities greater than 0.5 µm/min were considered to have high migration velocities, and cells with migration velocities less than 0.5 µm/min were considered to have low migration velocities. As inhibitors of glucose metabolism had no effect on cell velocity until 2 hours post drug application (data not shown), we analyzed the effects of glucose inhibitors on individual

cells by comparing velocity pre-inhibitor effect (1-2h after inhibitor application, Pre) to post-inhibitor effect (11-12h after inhibitor application, Post). MDA^{PAR} response to IA was largely homogenous, with cells displaying greatly decreased velocity post-inhibitor effect (**Figure 4.2D**). Interestingly, cells with initially high migration velocities had a significantly larger fold decrease in velocity compared to cells with initially low migration velocities suggesting that IA decreased velocity of highly migratory cells to a greater extent (**Figure 4.2E**). MDA^{PAR} response to IA + PYR was more heterogeneous, with cells with initially low migration velocities displaying very little change in velocity while cells with initially high migration velocities displayed significantly decreased velocity (**Figure 4.2F-G**). MDA^{PAR} treated with AMA exhibited highly heterogeneous responses in velocity. While MDA^{PAR} with initially high migration velocities displayed a slight decrease in velocity, cells with initially low migration velocities displayed a fold increase in velocity after AMA treatment (**Figure 4.2H-I**). These results reveal that the migration of highly and weakly migratory cells within the heterogeneous MDA^{PAR} cell line vary in their relationship to different routes of glucose metabolism. These findings suggest that metabolic heterogeneity within MDA^{PAR} may contribute to migratory heterogeneity.
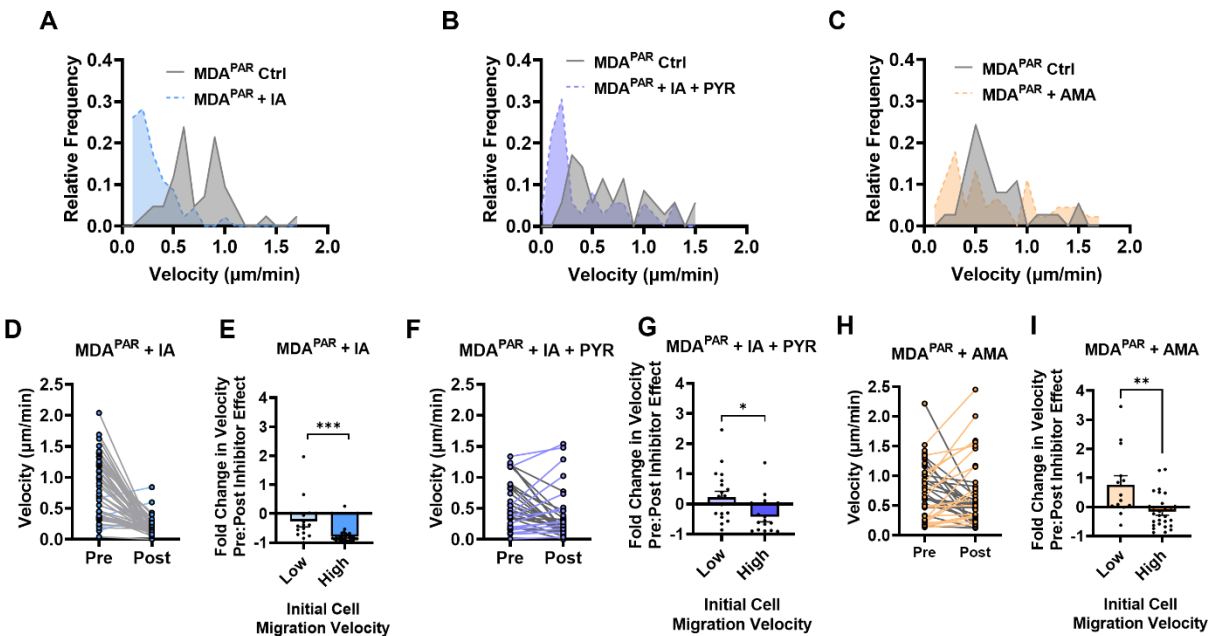
Figure 4.2. MDA-MB-231 exhibit heterogeneous migration in response to glucose metabolism inhibitors in confinement. (A) Average microtrack velocity histogram of MDA^{PAR} 6-12 h after vehicle control (Ctrl) or IA application (+ IA) (N=3, n=42-46); (B) Average microtrack velocity histogram of MDA^{PAR} 6-12 h after vehicle control (Ctrl) or IA+PYR application (+ IA + PYR) (N=3, n=35-36); (C) Average microtrack velocity histogram of MDA^{PAR} 6-12 h after vehicle control (Ctrl) or AMA application (+ AMA) (N=3, n=37-45); (D) Pre-treatment effect (1-2 h) and post-treatment effect (11-12 h) average microtrack velocity after IA application (N=3, n=46). Gray lines = decreasing velocity. Blue lines = increasing velocity; (E) Fold change of velocity shown in (D) for cells with low migration velocities (velocity<0.5 µm/min) and high migration velocities (velocity >0.5 µm/min); (F) Pre-treatment effect (1-2 h) and post-treatment effect (11-12 h) average microtrack velocity after IA + PYR application (N=3, n=35).

Gray lines = decreasing velocity. Purple lines = increasing velocity; (G) Fold change of microtrack velocity shown in (F) for cells with low migration velocities (velocity<0.5 µm/min) and high migration velocities (velocity >0.5 µm/min); (H) Pre-treatment effect (1-2 h) and post-treatment effect (11-12 h) average microtrack velocity after AMA application (N=3, n=44). Gray lines = decreasing velocity. Orange lines = increasing velocity; (I) Fold change of microtrack velocity shown in (H) for cells with low migration velocities (velocity<0.5 µm/min) and high migration velocities (velocity >0.5 µm/min); * denotes p <0.05, *** denotes p<0.001. Mean + SEM with dot plot shown for bar graphs.

4.4.3 *Phenotypically sorted weakly and highly migratory subpopulations preferentially utilize different pathways for glucose metabolism*

Given that MDA^{PAR} of low and high migration velocities displayed heterogeneous responses to glycolysis and OxPhos inhibition, we sought to determine whether weakly or highly migratory cancer cells preferentially utilize different pathways of glucose metabolism to fuel migratory heterogeneity. MDA^{PAR} were phenotypically sorted based on their ability to migrate through a collagen coated Transwell (**Figure 4.3A**)**.** Cells that migrated through the Transwell were purified over 20 rounds of sorting and termed highly migratory, or MDA$^+$. Cells that never migrated through the Transwell were purified over 20 subsequent rounds of sorting and termed weakly migratory, or MDA$^-$. Consistent with previous characterization[377], MDA$^+$ exhibited a higher motile fraction in 3D collagen gels compared to MDA$^-$ (**Figure 4.3B**).

Given that MDA$^+$ and MDA$^-$ vary in migratory capability and that migration after treatment with glucose metabolism inhibitors differed between MDA^{PAR} of low and high migration velocities, we investigated the metabolic behaviors of phenotypically sorted MDA$^+$ and MDA$^-$. MDA$^+$ displayed increased glucose uptake (**Figure 4.3C,D**), quantified via 2-NBDG uptake, increased lactate output (**Figure 4.3E**), and decreased mitochondrial membrane potential (**Figure 4.3D,F**), quantified via TMRM, compared to MDA$^-$. These findings suggest that the highly migratory MDA$^+$ rely more on glycolysis than MDA$^-$ and that MDA$^-$ rely more on OxPhos than MDA$^+$ (**Figure 4.3G**).
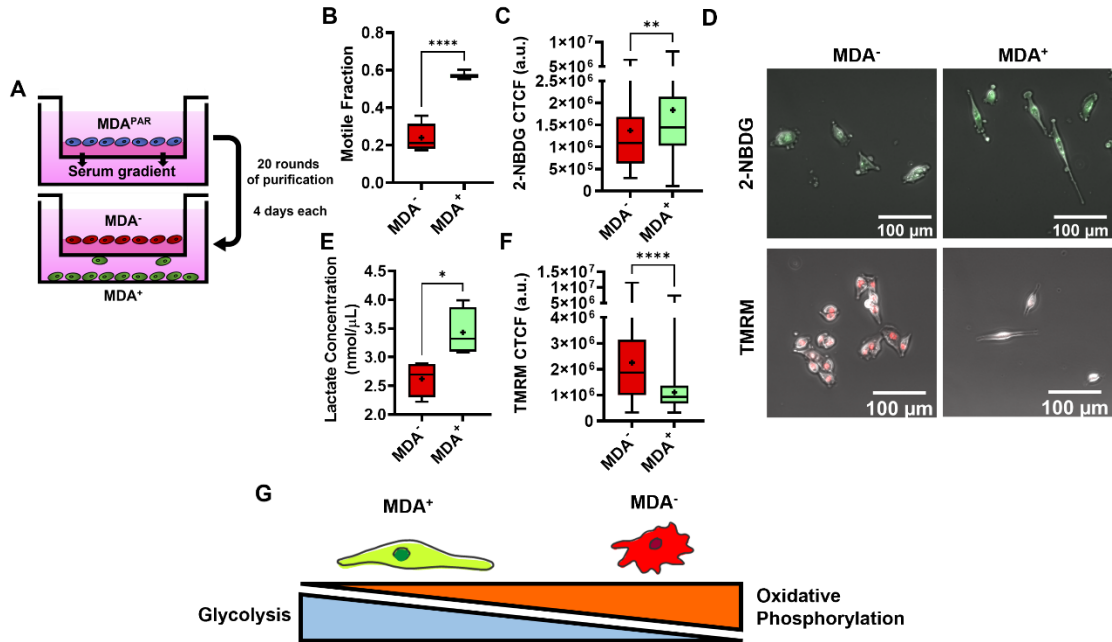
Figure 4.3. Weakly and highly migratory MDA-MB-231 subpopulations utilize different pathways for glucose metabolism. (A) Schematic of phenotypic sorting; (B) Motile fraction of weakly and highly migratory cells (N=3); (C) 2-NBDG of MDA⁻ and MDA⁺ (N=3, n=106-142); (D) Representative images of 2-NBDG (green) and TMRM (red) in MDA⁻ and MDA⁺. (E) Lactate concentration of MDA⁻ and MDA⁺ (N=3); (F) TMRM of MDA⁺ and MDA⁻ (N=3, n=157-160); (G) Schematic of metabolic differences between MDA⁻ and MDA⁺. * denotes $p<0.05$, ** denotes $p<0.01$, **** denotes $p>0.0001$. Min to max shown for box-and-whisker plots with mean represented as "+".

4.4.4 *Modulation of EMT phenotype regulates glucose metabolism to drive migration*

Given the known relationship between EMT and glucose metabolism[247,435–440,442–444], we sought to investigate the relationship between cancer cell bioenergetics, EMT phenotype, and migratory ability between phenotypically sorted triple negative breast cancer cells. In addition to MDA-MB-231, human triple negative SUM159 breast cancer cells were phenotypically sorted into highly migratory SUM⁺ and weakly migratory SUM⁻ subpopulations. MDA⁺, MDA⁻, SUM⁺, and SUM⁻ RNA sequencing was scored based on bioenergetics and EMT status. EMT Score was calculated as (Mesenchymal Score/Epithelial Score). Energy Score was calculated as (Glycolysis Score/OxPhos Score). Both MDA⁺ and SUM⁺ had higher EMT Scores (more mesenchymal) and higher Energy Scores (more glycolytic) than their weakly migratory counterpart (**Figure 4.4A**), revealing that phenotypic sorting of triple negative breast cancer cells isolates EMT and metabolically distinct subpopulations of cancer cells. For the cell types tested, highly migratory cells are more mesenchymal and rely more on glycolysis than weakly migratory cells. Taken together, these findings reveal that migratory heterogeneity within triple negative breast cancer cell lines may be driven by the link between glucose metabolism and EMT status.

To further determine how the link between metabolism and EMT can drive migratory heterogeneity, we investigated whether modulation of EMT phenotype conversely alters glucose metabolism to change migration capability. To induce EMT of the more epithelial MDA⁻, MDA⁻ were treated with TGFβ for 24 hours (**Figure 4.4B**). After treatment, MDA⁻ exhibited increased glucose uptake (**Figure 4.4C**), quantified with 2-NBDG, and decreased mitochondrial membrane potential (**Figure 4.4D**), measured with TMRM. These data are consistent with previous findings that cells undergoing EMT undergo metabolic reprogramming to increase glycolysis[247,438,440–443]. Conversely, MET of the more mesenchymal MDA⁺ was simulated by overexpression of E-cadherin using shRNA (**Figure 4.4B**). E-cadherin expressing MDA⁺ demonstrated increased mitochondrial membrane potential (**Figure 4.4E**) and decreased glucose uptake (**Figure 4.4F**), consistent with MET inducing a more mitochondrial energy phenotype[435,437,438,444].

As EMT and MET change glucose metabolism utilization, we investigated whether these altered bioenergetics regulate downstream migration. We previously showed that E-cadherin-overexpressing MDA⁺ exhibit reduced cell migration velocities in confined microtracks compared to MDA⁺ control cells[377]. These findings correlate a mitochondrial energy-dependent phenotype with decreased migratory ability. Conversely, treatment with MDA⁻ with TGFβ, known to induce a complete EMT phenotype[242], increased MDA⁻ migration velocities and decreased mitochondrial membrane potential relative to MDA⁻ control cells (**Figure 4.4G-H**). While it is widely known that EMT phenotype correlates with migratory ability[242,377], these findings reveal that EMT-induced metabolic reprogramming fuels enhanced migration.
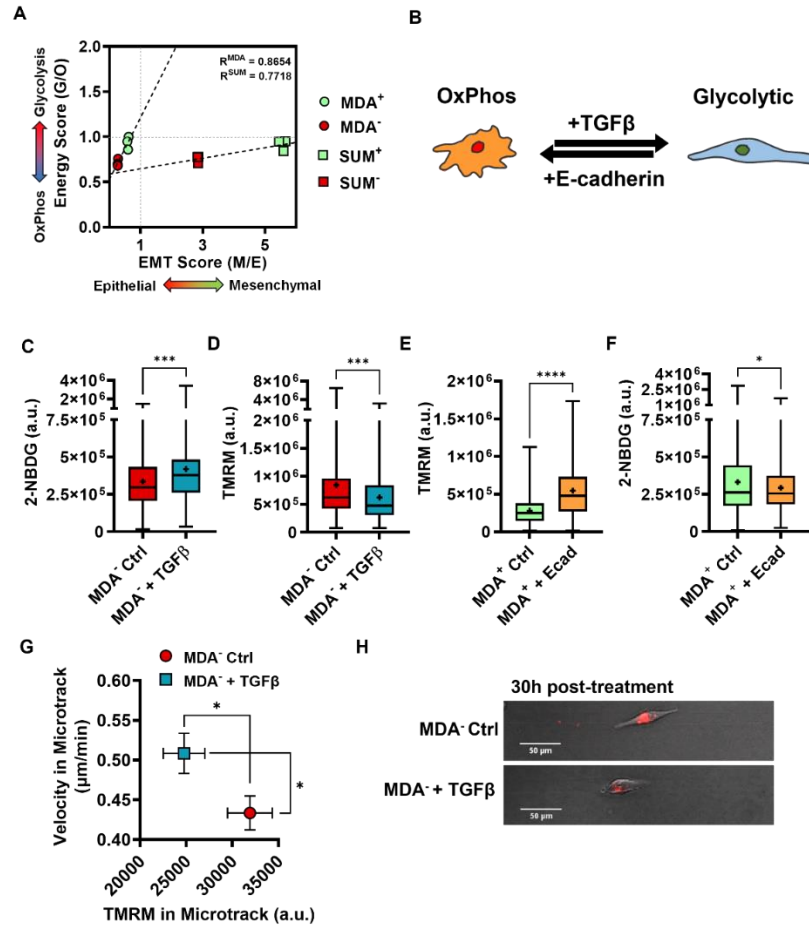
Figure 4.4. Modulation of EMT phenotype regulates glucose metabolism to drive migration. (A) Energy (Glycolysis/OxPhos) vs EMT (Mesenchymal/Epithelial) scores for highly and weakly migratory subpopulations for MDA-MB-231 cells (MDA+, MDA-) and SUM159 cells (SUM+, SUM-) as quantified using RNA sequencing, fit with linear regression. R values shown. (N=3); (B) Schematic of EMT regulation using E-cadherin and TGFβ; (C) 2-NBDG of MDA- and MDA- treated with TGFβ (N=3, n=191-239); (D) TMRM signal in MDA- and MDA- treated with TGFβ (N=3, n=236-258); (E) TMRM of MDA+ and MDA+ with E-cadherin overexpression (N=3, n=92-118); (F) 2-NBDG of MDA+ and MDA+ with E-cadherin overexpression (N=3, n=289-320); (G) Velocity and TMRM of MDA- and MDA- treated with TGFβ in microtracks (N=3, n=59-78); (H) Representative images of cells labeled with TMRM in microtracks; * denotes $p < 0.05$, *** denotes $p < 0.001$, **** denotes $p < 0.0001$. Mean + SEM shown for (G) and min to max for box-and-whisker plots with mean represented as "+".

4.4.5 *Modulation of glucose metabolism shifts migration phenotypes of weakly and highly migratory subpopulations*

Given that weakly and highly migratory subpopulations of MDA[PAR] differentially utilize glycolysis and OxPhos (**Figure 4.3**) and given that changes to EMT induce metabolic reprogramming to drive migration (**Figure 4.4**), we investigated whether modulation of glycolysis and OxPhos would be sufficient to alter the migration phenotypes of highly and weakly migratory breast cancer cells. As MDA+ are more glycolytic than MDA-, we first investigated whether inhibiting glycolysis was sufficient to block single cell

migration in confinement. MDA⁻ treated with IA + PYR displayed reduced migration velocity compared to control conditions (**Figure 4.5A,D**). Similarly, MDA⁺ treated with IA + PYR displayed significantly reduced migration velocity compared to vehicle control conditions (**Figure 4.5B,D**), revealing that glycolysis is essential for the migration of both weakly and highly migratory cancer cells. IA + PYR had a significantly greater effect on the migration of MDA⁺ compared to MDA⁻ (**Figure 4.5C**), highlighting that glycolysis is utilized to different extents by weakly and highly migratory cells for migration in confinement.

Given that migration is primarily thought to be glycolysis driven[245] and disruption of mitochondrial energy production can induce cell migration [444], we next investigated whether inhibition of mitochondrial energy production would increase cancer cell migration. MDA⁻ treated with AMA displayed a robust increase in migration velocity (**Figure 4.5D,E**), revealing that inhibition of OxPhos was sufficient to increase weakly migration cancer cell migration. Conversely, MDA⁺ treated with AMA displayed no significant change in migration velocity (**Figure 4.5D,F**), revealing that inhibition of OxPhos does not increase the migration of highly migratory cancer cells. Importantly, AMA had a significantly different effect on the migration of MDA⁻ compared to MDA⁺ revealing that inhibition of OxPhos energy production by weakly migratory cells that preferentially utilize mitochondrial energy can increase cell migration velocity (**Figure 4.3G**).
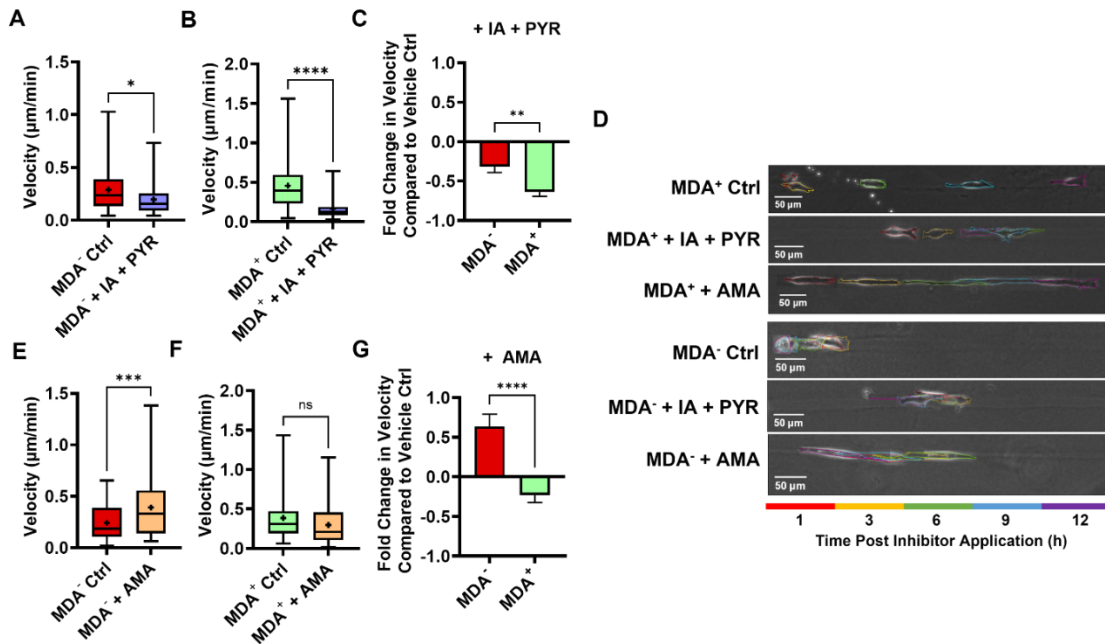
Figure 4.5. Modulation of glucose metabolism changes migration phenotypes of highly and weakly migratory subpopulations. (A) Average velocity of MDA⁻ 6-12 h after IA + PYR or vehicle control application (N=3+, n=46-51); (B) Average velocity of MDA⁺ 6-12 h after IA + PYR or vehicle control application (N=3+, n=34-36); (C) Fold change of velocity between treated and control conditions for MDA⁺ and MDA⁻ (A-B); (D) Representative images of cell migration in microtracks from 1-12 hours after vehicle control or inhibitor application; (E) Average velocity of MDA⁻ 6-12 h after AMA or vehicle control application (N=3+, n=57-69); (F) Average velocity of MDA⁺ 6-12 h after AMA or vehicle control

application (N=3+, n=48-57); (G) Fold change of velocity between treated and control conditions for MDA$^+$ and MDA$^-$ (E-F). * denotes p<0.05, ** denotes p<0.01, *** denotes p<0.001, **** denotes p<0.0001. Mean + SEM shown for bar graphs and min to max for box-and-whisker plots with mean represented as "+".

4.4.6   *Modulation of glucose metabolism regulates EMT phenotype to drive migration*

Given that weakly and highly migratory cells preferentially utilize different modes of glucose metabolism (**Figure 3**), that modulation of EMT phenotype reprograms metabolism to regulate migration (**Figure 4.4**), and that inhibition of OxPhos increases migration velocity of weakly migratory cancer cells (**Figure 4.5**), we sought to determine whether EMT status drives the differential migration response by weakly and highly migratory cancer cells to glucose metabolism inhibitors. Previous work suggests that glycolytic enzymes and mitochondrial dysfunction can induce EMT[435,437,438,444]. Thus, we investigated whether glucose metabolism inhibitors could shift EMT phenotype to drive migratory changes (**Figure 4.6A**). As mesenchymal cells display increased aspect ratios compared to epithelial cells[453–455], we first quantified cell aspect ratio after treatment with IA+PYR or AMA to assess changes in EMT status. MDA$^-$ exhibited decreased aspect ratios compared to MDA$^+$ in bulk collagen gels, consistent with more mesenchymal cells being more elongated **(Figure 4.6B)**. MDA$^-$ and MDA$^+$ treated with IA+PYR displayed no change in aspect ratio (**Figure 4.6C,D**), suggesting that IA+PYR has no effect on EMT status. Treatment with AMA significantly increased elongation of both the more epithelial, weakly migratory MDA$^-$ and the more mesenchymal, highly migratory MDA$^+$ (**Figure 4.6E,F**).

To further assess EMT phenotype after treatment with glucose inhibitors, RNA expression of epithelial marker E-cadherin (CDH1) and mesenchymal markers vimentin (VIM) and Zeb1 (ZEB1) were quantified using quantitative RT-PCR. Treatment of MDA$^-$ or MDA$^+$ with IA+PYR resulted in no significant change in CDH1, VIM, or ZEB1 mRNA (**Figure 4.6G,H**), further reinforcing that inhibition of GAPDH in glycolysis has no effect on EMT status of the phenotypically sorted weakly and highly migratory breast cancer cells. Conversely, treatment of MDA$^-$ with AMA significantly increased both CDH1 and ZEB1 mRNA (**Figure 4.6G**) and treatment of MDA$^+$ with AMA significant increased VIM and ZEB1 mRNA (**Figure 4.6H**). These results reveal that AMA increased mesenchymal gene expression in both MDA$^-$ and MDA$^+$. Interestingly, we show that treatment with AMA selectively increased MDA$^-$ migration and not MDA$^+$ migration compared to vehicle control conditions.

Altogether, these findings suggest that while glycolysis inhibition significantly impairs migration velocity, it has little effect on EMT phenotype. Instead, we observe a significant change in EMT markers upon mitochondrial impairment with AMA, indicating that while modulating glucose metabolism through glycolysis or mitochondrial inhibition can affect migration velocity, EMT phenotype is more dependent on mitochondrial function.
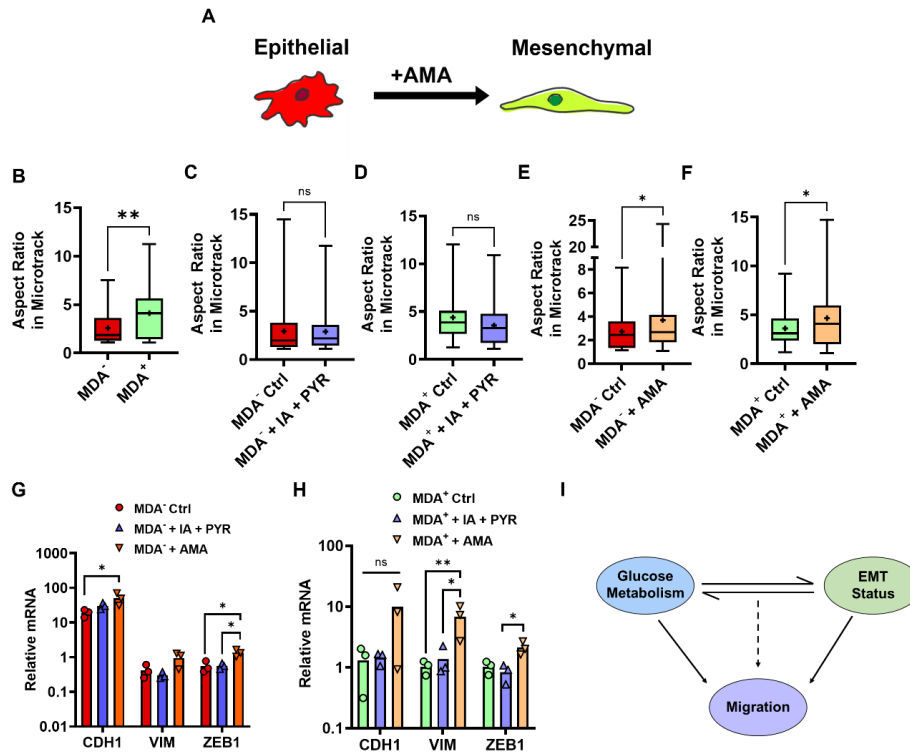
Figure 4.6. Modulation of glucose metabolism differentially regulates EMT phenotype. (A) Schematic of metabolism-regulated EMT; (B) Aspect ratio of MDA$^-$ and MDA$^+$ (N=3, n=30-39); (C) Aspect ratio of MDA$^-$ 6-12 h after vehicle control (Ctrl) or IA+PYR application (+IA+PYR) (N=3+, n=34-36); (D) Aspect ratio of MDA$^+$ 6-12 h after vehicle control or IA+PYR (N=3+, n=34-67); (E) Aspect ratio of MDA$^-$ 6-12 h after vehicle control or AMA (+AMA) (N=3+, n=61-64); (F) Aspect ratio of MDA$^+$ 6-12 h after vehicle control or AMA (N=3+, n=48-85); (G) Relative mRNA of MDA$^-$ treated with vehicle control, IA+PYR, or AMA for 12 h. Normalized to β-actin. (N=3). (H) Relative mRNA of MDA$^+$ treated with vehicle control, IA+PYR, or AMA for 12 h. Normalized to β-actin. (N=3); (I) Schematic of link between glucose metabolism and EMT driving cell migration; * denotes $p<0.05$, ** denotes $p<0.01$, ns = not significant. Mean + individual data points shown for bar graphs and min to max for box-and-whisker plots with mean represented as "+".

4.5   Discussion

Cancer cell phenotypic heterogeneity is associated with poor clinical outcomes and complicates cancer therapy[426,456,457]; therefore, a better understanding of the cancer cell populations that exist and work cooperatively in the TME is essential to develop effective cancer therapies. It was recently described that primary tumors and micrometastases exhibit distinct metabolic transcriptomes, with primary tumors primarily utilizing glycolysis as described by the Warburg Effect and micrometastases displaying a preference for mitochondrial OxPhos[289]. These different metabolic behaviors indicate that metabolism is highly plastic and context-dependent, and that glycolysis and OxPhos may fuel different cell behaviors, such as proliferation and colonization, with different metastatic advantages. Here, we investigate the role of glucose metabolism in cell migration and investigate how heterogeneity in metabolism fuels migratory

87

ability in triple negative breast cancer. We identify that the interplay between glucose metabolism and EMT phenotype drives heterogeneous migratory behaviors.

Cancer cell bioenergetics and migration are linked in that ATP fuels cell progression through specific steps in the metastatic cascade[458]. As it is technically challenging to precisely quantify single cell metabolism during *in vivo* metastasis, physiologically relevant *in vitro* platforms that model steps in cancer metastasis may provide valuable insight that is otherwise unachievable. Here, we sought to isolate the independent roles of glycolysis and OxPhos in breast cancer cell migration using an engineered microtrack platform that mimics the confinement and material composition of the ECM found *in vivo*. Conflicting evidence exists as to whether breast cancer single cell migration is primarily driven by glycolysis, OxPhos, or a combination of both pathways. Glycolysis regulates cytoskeletal dynamics required by cell migration[245,446,459–461] and extracellular acidification due to lactate output increases MMP activation, matrix degradation, and the reorganization of cytoskeletal machinery[462,463], suggesting that cell migration is glycolysis driven. However, it has also been shown that enhanced OxPhos and mitochondria localization to the leading edge increases cell migratory ability[251–253]. Importantly, our results suggest that breast cancer cells rely only on glycolysis to fuel their migration in confined 3D environments. The dichotomy in these findings may result from differing *in vitro* models used to monitor cell migration. 3D hydrogels, transwell assays, and microfabricated systems have different mechanical parameters, including stiffness, confinement, and alignment, all of which are known to impact cell metabolism[382,464,465]. Importantly, our microtrack system models protease-independent migration as cells do not need to degrade the matrix to migrate[97]. While our results suggest that protease-independent migration is solely glycolysis-dependent, other forms of single cell migration may require mitochondrial energy utilization.

Using this microtrack platform, we show that OxPhos inhibition did not elicit a homogenous migratory response. While highly migratory cells showed no change in migration, weakly migratory cells displayed increased migration in response to AMA treatment, suggesting that highly and weakly migratory cancer cells utilize different metabolic pathways. We further investigated this phenomenon by phenotypically sorting MDA-MB-231 triple negative breast cancer cells based on their *in vitro* migratory potential. Highly migratory cancer cells demonstrated a preference for glycolysis while weakly migratory cells exhibited higher levels of OxPhos. We previously showed that phenotypically sorted weakly migratory MDA-MB-231 and SUM159 are more metastatic in a mouse model of breast cancer metastasis than their highly migratory counterparts[377]. These findings are in agreement with other groups reporting that weakly migratory cancer cells can be highly metastatic[389,390,392]. Our results reveal that even within a single cancer cell line, heterogeneity in migratory ability and metastatic ability[377] is accompanied by heterogeneity in bioenergetics. These findings also highlight that while glycolysis may fuel cancer cells to escape from the primary tumor, OxPhos utilization may regulate other behaviors required for metastasis. In agreement,

OxPhos inhibition has been shown to have little effect on primary tumor growth, but significantly decreased metastatic seeding of breast cancer cells, indicating a role for OxPhos in later colonization steps of the cascade[250]. These data, in addition to others showing that OxPhos is upregulated in secondary metastatic sites[253,284,285,292], correspond with our previous findings that weakly migratory cells that preferentially utilize OxPhos are more metastatic than their glycolysis-dependent counterparts.

RNA sequencing of phenotypically sorted triple negative breast cancer cell lines revealed that highly migratory cells were both more glycolytic and more mesenchymal than their weaky migratory counterparts, which were more reliant on OxPhos and more epithelial. To determine if EMT status regulates glucose metabolism to control migratory potential, EMT of the highly and weakly migratory cancer cells was modulated and metabolic and migratory changes were assessed. Inducing a mesenchymal phenotype with TGFβ caused a metabolic switch towards glycolysis and was accompanied by increased migration velocity. Inducing a more epithelial phenotype by knocking in E-cadherin resulted in a switch towards increased OxPhos and decreased migration velocity. These findings are consistent with previous studies that drivers of EMT can upregulate glycolysis [247,438,440–444]. While others have reported that E-cadherin overexpression can increase OxPhos[466], the mechanism and consequences of this signaling is unclear. Here, we show that these metabolic changes can regulate downstream migration, revealing that the link between cell metabolism and EMT fuels different migratory potentials. It is important to note that while we can manipulate EMT status in our subpopulations, we do not recapitulate a fully epithelial or fully mesenchymal status; rather, we are able to push cells in either direction on the EMT spectrum to acquire properties of an epithelial-like or mesenchymal-like phenotype. We show that even minute changes to EMT status result in robust migratory or metabolic changes. Our ability to move cells along this spectrum rather than inducing one state or the other allows us to capture the intermediate partial-EMT phenotypes that may be essential in cooperative progression through the metastatic cascade.

We last investigated whether changes to glucose metabolism mechanistically signal through EMT to control migration. Inhibition of glycolysis decreased migration of the highly migratory cells while inhibition of OxPhos increased migration of the weakly migratory cells. While inhibiting glycolysis may weaken migratory potential through reduced ATP availability[230,245,467], it was unclear why inhibition of OxPhos would promote migration of weakly migratory cells. As such, we investigated whether metabolic changes induce changes to EMT status to subsequently affect migration. While inhibiting glycolysis had little effect on EMT status as evidenced by cell aspect ratio and mRNA expression of EMT markers, we were able to induce changes to EMT phenotype by inhibiting mitochondrial energy, suggesting that the link between metabolism and EMT may be more dependent on mitochondrial ability than glucose metabolism as a whole.

The role of metabolism in cell migration is still being explored in the context of cancer progression and metastasis. Here, we highlight a novel link between glucose metabolism and EMT status as the driving factor in migratory heterogeneity in breast cancer cells. We show that while highly and weakly migratory breast cancer cells exhibit unique metabolic and EMT profiles, we are able to control migration by manipulating either metabolism or EMT. Specifically, weakly migratory cells dependent on OxPhos for ATP can be pushed to a more migratory phenotype by inhibiting mitochondrial respiration and forcing cells to utilize glycolysis instead, or by inducing a more mesenchymal phenotype with TGFβ. Similarly, migration of highly migratory cells can be attenuated by blocking their main ATP source, glycolysis, or inducing an epithelial phenotype with E-cadherin. While our primary focus here is single cell migration in a representative engineered model of the primary tumor microenvironment, our data in combination with further characterization of the relationship between EMT and glucose metabolism pathways in each step of the metastatic cascade may reveal key therapeutic targets for inhibiting cancer metastasis.

CHAPTER 5: ADDITIONAL STUDIES AND DATA

5.1 MV-induced fibronectin deposition by fibroblasts is dependent upon matrix stiffness

In Chapter 2, our findings revealed that matrix stiffness effects of MV-induced fibroblast activation. CAFs are abundantly present in the breast tumor microenvironment and contribute extensively to matrix deposition and matrix remodeling[404]. Thus, we next investigated how matrix stiffness impacts MV-induced fibronectin deposition by fibroblasts. NIH 3T3 fibroblasts were seeded on 1, 5, or 20 kPa PA gels in 1.6 mL of DMEM + 1% FBS. Cells were treated with either 400 µL of serum-free media or approximately $4*10^7$ MVs suspended in 400 µL serum-free media for 24 hours. Cells were first fixed with 3.2% v/v paraformaldehyde and subsequently permeabilized with a 3:7 ratio of methanol to acetone. Cells were incubated with goat anti-fibronectin (sc6953, 1:100) overnight at 4°C. The cells were washed and incubated with AlexFluor 548 conjugated to donkey anti-goat (1:200), AlexFluor 488 phalloidin (1:500), and DAPI (1:500) for 1 hour. To image, gels were inverted onto a drop of Vectashield Mounting Media placed on a glass slide. Fluorescent images were acquired with a 20x/1.0 N.A. water-immersion objective on a Zeiss LSM700 Upright laser-scanning microscope. Cells stained with phalloidin were outlined in ImageJ to calculate cell area. Area of deposited fibronectin was calculated by using the threshold function in ImageJ to calculate area of positive stain. The ratio of deposited fibronectin area to cell area was calculated.

Our findings indicate the breast cancer MVs increase fibroblast fibronectin deposition only on stiff 20 kPa gels (**Figure 5.1A-C**). No change in total fibronectin deposition or fibronectin deposition per cell area was observed on 1 kPa or 5 kPa gels (**Figure 5.1A-C**). These results are consistent with our previous findings that matrix stiffness mediates MV-induced fibroblast activation[17] and additionally suggest a role for matrix stiffness in mediating fibronectin deposition by fibroblasts.
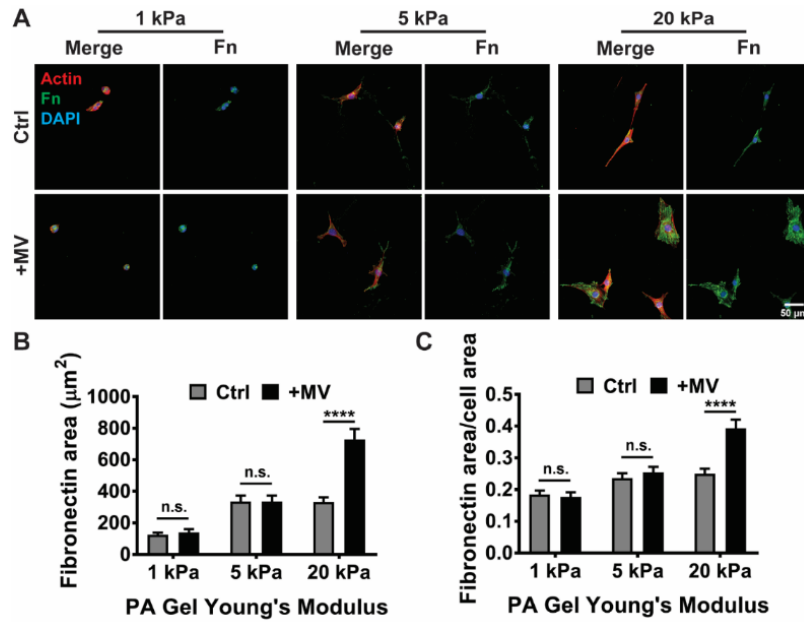
Figure 5.1. MV-induced fibronectin deposition by fibroblasts is dependent upon matrix stiffness. (A) Representative images of fibronectin (green), actin (red), and DAPI (blue) staining of fibroblasts cultured in control (Ctrl) or with MVs (+MV) on 1 kPa, 5 kPa, and 20 kPa PA gels. (B) Fibronectin area deposited per cell (N=3; n = 43, 43, 42, 53, 53, 60). (C) Fibronectin area normalized to cell area (cell (N=3; n = 43, 43, 42, 53, 53, 60). Bar graphs show mean +/- SEM. P-values determined using a two-way ANOVA with Tukey test for multiple comparisons. ****$p<0.0001$, n.s. = not significant.

5.2   Tg2 splice variants are enriched in MVs

In Chapter 3, we showed that weakly migratory metastatic breast cancer cells release MVs rich in Tg2 which activates fibroblasts to increase cancer cell dissemination and metastasis. Western blots of whole cell and MV lysates revealed different enrichment of Tg2 splice variants between cells and MVs. MV$^-$ appeared enriched for 55 kDa and 37 kDa Tg2 splice variants compared to MV$^+$ and cell lysates (**Figure 5.2A**). These identified proteins correspond with known splice variants of Tg2 (**Figure 5.2B**). The splice variants of Tg2 identified are predicted to be TGM2_v2 (~55-60 kDa) and TGM2_V3 (~38 kDa)[468]. The mechanism of Tg2 splice variant enrichment in MV$^-$ and the functional role they play in MV signaling is unknown.
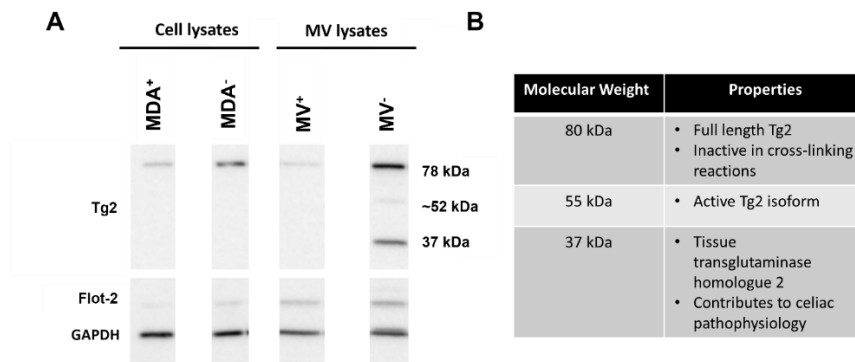
Figure 5.2. Tg2 splice variants are enriched in MV⁻. (A) Western blot for Tg2, Flot-2, and GAPDH in MDA⁺, MDA⁻, MV⁺, and MV⁻. (B) Table of Tg2 isoforms and properties.

5.3 Cooperative interactions between highly and weakly migratory SUM159 enhance weakly migratory spheroid compaction and migration

Previous work in the Reinhart-King Lab indicated that highly migratory MDA-MB-231 enhance the migration of weakly migratory MDA-MB-231 (Hapach, Schwager et al., *in prep*). We next extended these findings to the SUM159 (SUM^PAR) human triple negative breast cancer cell line. SUM^PAR were phenotypically sorted based on migratory ability using a transwell assay, resulting in highly migratory (SUM⁺) and weakly migratory (SUM⁻) subpopulations.

Tumor spheroids were used to investigate the cooperative interactions between SUM⁺ and SUM⁻. SUM⁺, SUM⁻, and SUM^MIX (1:1 ratio of SUM⁺:SUM⁻) spheroids were formed over 72 hours. Spheroids compacted to different extents with SUM⁺ and SUM^MIX compacting more than SUM⁻ (**Figure 5.3A-B**). When observing fully compacted SUM^MIX spheroids at 72 hours, SUM⁺ preferentially located towards the exterior of the spheroids while SUM⁻ appear to localize towards the core of the spheroid (**Figure 5.3C**).

We next assessed cancer cell migration in tumor spheroids. After 72 hours of compaction, SUM⁺, SUM⁻, and SUM^MIX spheroids were embedded in 1.5 mg/ml collagen gels and cultured for 72 hours. Both SUM⁺ and SUM^MIX spheroids exhibited single and collective modes of migration, while only low levels of collective migration were observed in SUM⁻ spheroids (**Figure 5.3D**). SUM⁻ of SUM^MIX spheroids exhibited greater migration area than SUM⁻ only spheroids. Migrating SUM⁻ in SUM^MIX spheroids were identified in collectively migrating strands (**Figure 5.3E**). Together, these results reveal that cooperative interactions between highly and weakly migratory SUM159 triple negative breast cancer cells can promote the migration of weakly migratory cancer cells.
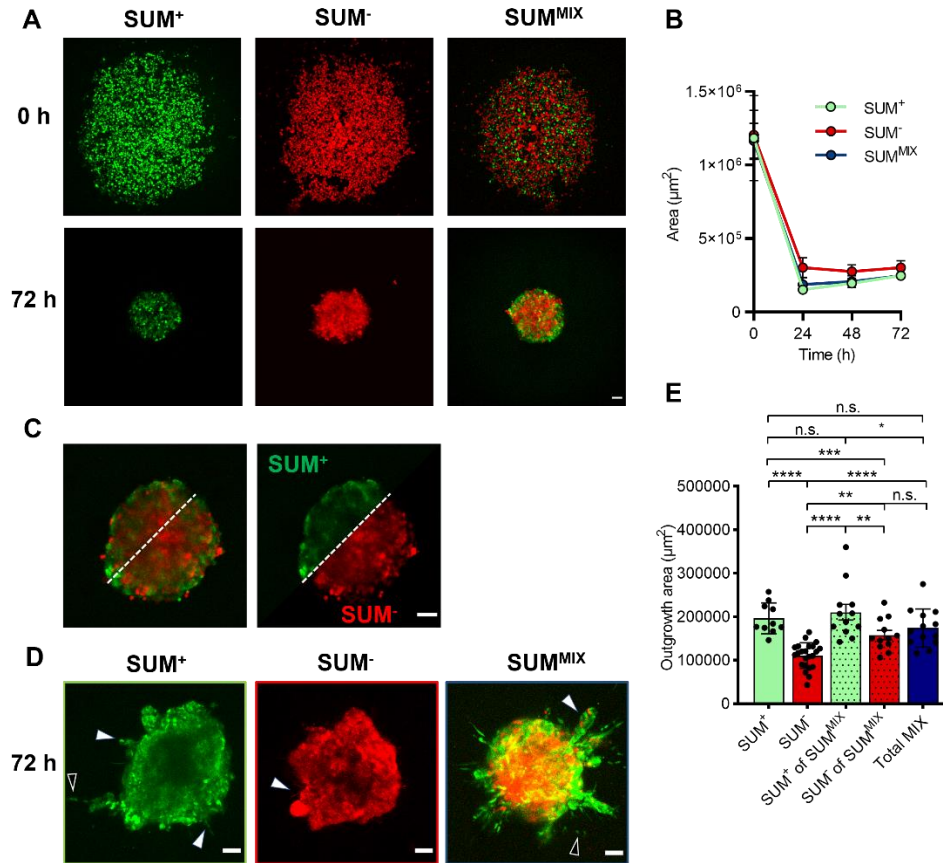
Figure 5.3. Cooperative interactions between highly and weakly migratory SUM159 enhance weakly migratory spheroid compaction and migration. (A) Representative images of *in vitro* tumor spheroids immediately after seeding (0 h) and before embedding (72 h) with SUM+ (green), SUM- (red), and SUM^{MIX} (1:1 SUM+:SUM- co-culture) subpopulations; scale bar: 100 µm. (B) Compaction curve of SUM+, SUM-, and SUM^{MIX} spheroids from 0 h to 72 h. (N=3+, n = 12, 11, 12) (C) Representative image of fully compacted SUM^{MIX} spheroid (left) with individual SUM+ (green) and SUM- (red) channels shown across spheroid diameter (right); scale bar: 100 µm. (D) Representative images of SUM+, SUM-, and SUM^{MIX} tumor spheroids in 1.5 mg mL^{-1} collagen at 72 h post-embedding. Black arrows mark single cell migration while white arrows mark collective strand migration; scale bar: 100 µm. (E) Spheroid outgrowth at 72 h post-embedding (N=3+, n = 10, 23, 12, 12, 13). * $p < 0.05$, **$p<0.01$, ***$p<0.001$, **** $p < 0.0001$, n.s. = not significant.

5.4 Metabolic proteins in MVs reflect metabolism of releasing cell

iTRAQ proteomics of MV+ and MV- was completed as previously described (**Chapter 3**). Metabolic proteins involved in mitochondrial OxPhos and glycolysis were identified in the MVs. Proteins involved in glycolysis were enriched in MV+ while proteins involved in OxPhos were enriched in MV- (**Figure 5.4A**). These differences in metabolic cargo reflect the metabolism of the releasing cancer cell (**Chapter 4**). GO Term analysis of the proteomics identified mitochondrial matrix as enriched in MV- (**Figure 5.4B**). The wide variety of glucose metabolism cargo identified in the MVs, including glucose transports, lactate

transporters, glycolytic, TCA cycle, and ETC proteins, suggests that MVs are involved in metabolic signaling and may be capable of generating their own ATP.
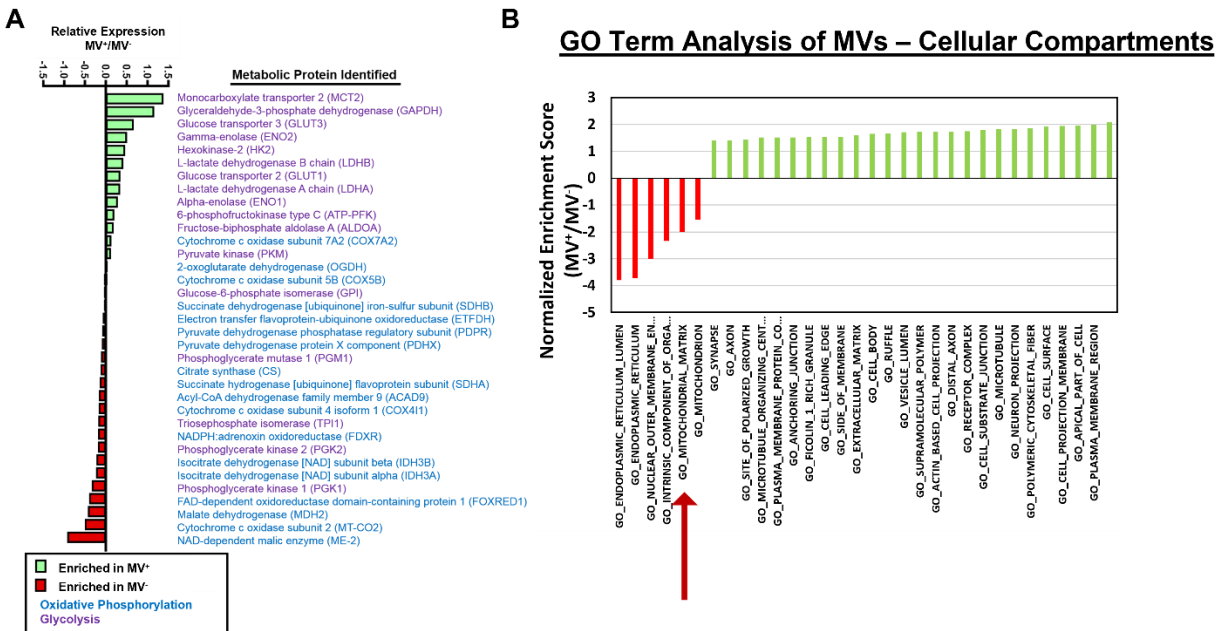
Figure 5.4. Metabolic cargo identified in MVs isolated from highly and weakly migratory breast cancer subpopulations. (A) Relative expression of glucose metabolism proteins (glycolysis (blue), OxPhos (red)) identified with iTRAQ proteomics in MV$^+$ and MV$^-$. (B) GO Term Analysis of MV$^+$ and MV$^-$ iTRAQ proteomics. The cellular compart GO Term of Mitochondrial Matrix denoted with red arrow.

5.5   Highly and weakly migratory cancer cells release MVs that regulate fibroblast metabolism

Previous work suggests that MVs released by tumor cells can reprogram stromal cell metabolism[16]. Thus, we investigated whether MVs released by phenotypically sorted highly and weakly migratory subpopulations of MDA-MB-231 breast cancer cells differentially regulated fibroblast metabolism. For 2-NBDG glucose uptake studies, NIH 3T3 fibroblasts were seeded on 20 kPa PA gels in 1.6 mL of DMEM + 1% FBS. After 24 hours, media was refreshed and cells were treated with 0.146 mM 2-NBDG and either 400 μL of serum-free media or approximately $3*10^7$ MVs suspended in 400 μL serum-free media. After 24 hours, cells were fixed with 3.2% v/v paraformaldehyde and washed 3x5 min with PBS. Images were acquired using a 20x/0.4 N.A. objective on a Zeiss LSM800 laser-scanning microscope. For TMRM mitochondrial membrane potential studies, NIH 3T3 fibroblasts were seeded on 20 kPa PA gels in 1.6 mL of DMEM + 1% FBS. After 24 hours, media was refreshed and cells were treated with either 400 μL of serum-free media or approximately $3*10^7$ MVs suspended in 400 μL serum-free media. After 24 hours, 150 nM of TMRM was added for 30 min. Cells were fixed with 3.2% v/v paraformaldehyde and washed with PBS. Images were acquired using a 10x/0.3 N.A. objective on a Zeiss LSM800 laser-scanning microscope. Fluorescence was quantified using corrected total cell fluorescence measurements as previously described (Chapter 3, 4).

Fibroblasts cultured with MV$^+$ or MV$^-$ exhibited an increase in glucose uptake and a decrease in mitochondrial membrane potential (**Figure 5.5A-B**), indicating that cancer derived MVs induce increased glycolysis in fibroblasts, consistent with the Reverse Warburg Effect[272]. Culture with MV$^-$ induced a greater metabolic change in fibroblasts than culture with MV$^+$ (**Figure 5.5A-B**), suggesting that MVs that are more potent activators of fibroblasts (**Chapter 3**) also have a greater effect on reprogramming fibroblast metabolism. While this is consistent with other results correlating a metabolic switch to glycolysis with fibroblast activation[16,469], it suggests that the metabolic programming in fibroblasts is not a result of metabolic cargo transfer via MVs as we previously showed that MV$^+$ contained higher levels of glycolytic cargo than MV$^-$ (**Figure 5.4A**).
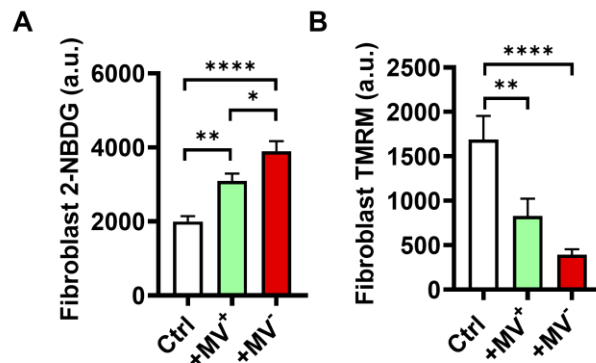
Figure 5.5. MVs from highly and weakly migratory breast cancer cells differentially regulate fibroblast glucose metabolism. (A) Fibroblast glucose uptake after culture in control conditions (Ctrl), with MV$^+$ (+MV$^+$), or with MV$^-$ (+MV$^-$) (N=3; n = 71, 71, 73). (B) Fibroblast mitochondrial membrane potential after culture in Ctrl, + MV$^+$, or +MV$^-$ conditions (N=3; n = 53, 53, 48). Bar graphs show mean +/- SEM. P-values determined using a one-way ANOVA with Tukey test for multiple comparisons. *$p<0.05$, **$p<0.01$, ****$p<0.0001$.

CHAPTER 6: CONCLUSIONS AND FUTURE DIRECTIONS

6.1   Conclusions

Intratumor heterogeneity is an emerging hallmark of cancer that complicates both clinical diagnostics and therapy. Intratumor heterogeneity describes the state in which breast tumors are made up of a dynamic extracellular matrix and a heterogeneous collection of cells, including cancer and stromal cells[8]. In this thesis, we investigated how heterogeneity in matrix stiffness and migratory phenotype contribute to breast cancer progression.

6.1.1   *Matrix stiffness enhances breast cancer MV-mediated fibroblast activation*

In Chapter 2, we studied how soft and stiff matrices affect MV signaling to fibroblasts in breast cancer. Polyacrylamide gels, ranging from 1 kPa to 20 kPa, were used to mimic the range of stiffness in physiologically relevant breast tissue. Using time-lapse microscopy, immunofluorescent staining, EdU proliferation assay, and traction force microscopy, we determined that breast cancer derived MVs have different effects on fibroblast function on soft and stiff matrices. On soft 1 kPa PA gels, mimicking the stiffness of healthy breast tissue, MVs had no effect on fibroblast spreading, activation, proliferation, or traction stress. As stiffness increased to 5 kPa and 20 kPa, MVs had increasingly greater effects and significantly increased fibroblast spreading, activation, proliferation, and traction stress on 20 kPa PA gels. We next extended our findings to a 3D engineered environment that more accurately recapitulates the geometry sensed by cells in the body. Stiffness of 3D collagen gels was modulated using non-enzymatic glycation. we determined that even in 3D collagen gels, fibroblasts treated with MVs in stiffer gels displayed increased contractility compared to fibroblasts in softer gels.

As cancer cells release a variety of components into the extracellular space, including growth factors, proteases, and cytokines, in addition to extracellular vesicles, we sought to determine whether MVs are a physiologically significant regulator of fibroblast function. MVs resuspended in breast cancer conditioned media had significantly greater effects on fibroblast spreading and traction force compared to conditioned media alone, indicating that MVs are not outcompeted by other components of the cancer secretome.

Lastly, we investigated whether the cell type from which MVs are shed influences the matrix stiffness-dependent effect of MVs on fibroblasts. MVs isolated from MCF10A breast epithelial cells had no effect on fibroblast spreading or contractility on 5 or 20 kPa PA gels. MVs isolated from weakly metastatic MCF7 cells exhibited no change in cell spreading on 5 or 20 kPa PA gels but did increase fibroblast contractility on stiff 20 kPa gels. These results indicate that the effects of MVs on fibroblast function is indeed cell-type dependent and may correlate with cancer cell metastatic potential.

The findings in Chapter 2 reveal a novel mediator in the bidirectional relationship between cancer cells and fibroblasts in the TME. As fibroblast activation is associated with cancer progression, cancer-derived MVs appear to play a role in transforming fibroblasts to an activated state to prime the TME for metastasis. The robust response of fibroblasts to MVs on stiff matrices ranging highlights the sensitivity of fibroblasts to MV contents at the tumor periphery. Importantly, this region is where fibroblasts form tracks in the matrix or align fibers to promote cancer cell invasion.

6.1.2 *Weakly migratory metastatic breast cancer cells active fibroblasts in a MV-Tg2 dependent manner to mediate cancer cell dissemination*

In Chapter 3, we investigated how weakly migratory metastatic breast cancer cells escape the primary tumor to metastasize. Previously, MDA-MB-231 were phenotypically sorted based on migration into 'highly migratory' and 'weakly migratory' subpopulations[377]. The highly migratory subpopulation was weakly metastatic in mice and the weakly migratory subpopulation was highly metastatic in mice[377]. These surprising findings led us to investigate the mechanism by which weakly migratory cancer cells can escape the primary tumor and metastasize.

We first investigated the primary tumors formed by MDA$^+$ and MDA$^-$. MDA$^-$ tumors were stiffer, had higher levels of mouse-derived ECM, and had higher levels of CAF markers than MDA$^+$ tumors, indicating that CAFs in MDA$^-$ tumors may contribute to MDA$^-$ dissemination and metastasis. As it is known that MVs from cancer cells can induce fibroblast activation, we isolated MVs from MDA$^+$ and MDA$^-$ and assessed fibroblast function after treatment with MVs. MVs released from MDA$^-$ induced a variety of phenotypes associated with fibroblast activation, including FAK activation, αSMA expression, fibronectin deposition, and contractility at significantly greater levels than MVs released from MDA$^+$. We then extended these findings into a 3D tumor spheroid model which mimics cancer cell dissemination away from the primary tumor. Treatment of weakly migratory cancer cell and fibroblast coculture spheroids with MVs released from MV$^-$ greatly enhanced cancer cell migration in spheroids, indicating the MV$^-$ signals to fibroblasts to enhance weakly migratory cancer cell migration.

Proteomics data revealed that MV$^-$ were enriched for the enzyme Tg2. Knockdown of Tg2 in MDA$^-$ reduced *in vivo* metastasis and knockdown of Tg2 in MV$^-$ reduced fibroblast activation and spheroid outgrowth *in vitro*. Repeated injections of Tg2-rich wildtype MV$^-$ were sufficient to induce the metastasis of Tg2 knockdown MDA$^-$. Lastly, we show that Tg2 is a clinical indicator of breast cancer progression and identify Tg2 as an important therapeutic target to prevent metastasis.

Altogether, we show that the relationship between cancer cell migratory ability and dissemination away from the primary tumor is complex. We identify a population of weakly migratory, highly metastatic breast cancer cells which escape the primary tumor via MV-Tg2-mediated fibroblast activation. As we further define the relationship between cancer cell migration and metastatic potential and the consequences

of MV signaling on cancer progression, these findings are likely to have broader implications in designing modalities and therapies to detect and target metastatic cancer cells.

6.1.3   *Link between glucose metabolism and EMT regulates migratory heterogeneity in breast cancer*

In Chapter 4, we explore the relationship between glucose metabolism, EMT state, and migratory ability. We began by investigating the mode of glucose metabolism that fuels single cell breast cancer migration *in vitro*. Time-lapse microscopy of single cell MDA-MB-231 breast cancer migration in microfabricated collagen microtracks and treatment with metabolic inhibitors of glycolysis and OxPhos indicate that glycolysis primarily fuels confined single cell MDA-MB-231 migration *in vitro*. During this investigation, migratory heterogeneity in response OxPhos inhibition was observed, prompting us to investigate whether highly and weakly migratory cells primarily utilize different modes of glucose metabolism to fuel their different phenotypes.

We further investigated this by phenotypically sorting MDA-MB-231 based on their *in vitro* migratory potential. Our data revealed that highly migratory cells were both more glycolytic and more mesenchymal than their weaky migratory counterparts, which were more reliant on OxPhos and more epithelial, suggesting that EMT state and glucose metabolism may be linked to drive cancer cell migration. Inducing a mesenchymal phenotype in the weakly migratory cells caused a metabolic switch towards glycolysis and was accompanied by increased migration velocity. Inducing a more epithelial phenotype in the highly migratory cells resulted in increased OxPhos and decreased migration velocity. We lastly show that while modulating glucose metabolism can change the migration potential of highly and weakly migratory cells, inhibition of glycolysis had no effect on EMT status while inhibition of OxPhos induced changes to EMT phenotype, suggesting that the link between metabolism and EMT may be more dependent on mitochondrial ability than glucose metabolism as a whole.

Altogether, we highlight a novel link between glucose metabolism and EMT status as the driving factor in migratory heterogeneity in breast cancer cells. While we focused on single cell migration in an engineered model of the tumor microenvironment, our data in combination with further characterization of the relationship between EMT and glucose metabolism pathways in each step of the metastatic cascade may reveal key therapeutic targets for inhibiting cancer metastasis.

6.2   Future Directions

6.2.1   *Expanding to other cell types*

Most of the studies presented in this dissertation were completed with MDA-MB-231 triple negative breast cancer cells and NIH 3T3 fibroblasts; thus, these findings should be expanded to additional cancer types. In Chapter 2, we show that breast cancer MVs induce 3T3 fibroblast activation on stiff substrates rather than soft substrates. We propose future studies investigating MV-fibroblast signaling in pancreatic adenocarcinoma and hepatocellular carcinoma, both cancers in which CAFs have been described

as mediating pro-cancer functions[470–472]. First, we should investigate whether MVs isolated from pancreatic and hepatocellular cancer cells transform fibroblasts. Next, it should be investigated whether MV-fibroblast signaling from these other cancer types is stiffness-dependent. While primary breast tumors and primary pancreatic adenocarcinoma tumors range from 1–20 kPa, hepatocellular primary tumors can range from 20 – 75 kPa[8,473–475]. Therefore, it should be investigated whether the same stiffness enhances MV signaling in all cancer types or whether the stiffness is tissue dependent (i.e., do hepatocellular cancer MVs activate fibroblasts on all physiologically relevant stiffnesses?). This can be assessed *in vitro* by isolating MVs from pancreatic and hepatocellular carcinoma cell lines and assessing fibroblast phenotype, such as αSMA expression, proliferation, and contractility, after MV treatment on PA gels ranging from 1-20 kPa or 20-75 kPa for pancreatic and hepatocellular carcinoma, respectively. These studies should also investigate how fibroblasts derived from different tissues, such as the pancreas or liver, respond to MV signaling. Importantly, human primary liver fibroblasts are available for purchase and would be suitable for these studies. We additionally propose studies comparing the phenotypes of MV-activated normal fibroblasts to primary CAFs.

In Chapter 3, we show that highly and weakly migratory MDA-MB-231 have different metastatic potentials and that weakly migratory cells release MVs rich in Tg2 which are potent activators of fibroblasts. These studies should be expanded to other cancer types to determine if (1) the inverse relationship between migration and metastasis exists after phenotype sorting, (2) MVs released by weakly migratory metastatic cancer cells activate fibroblasts, and (3) weakly migratory metastatic cancer cells and their MVs are enriched in Tg2. To begin to address these questions, human hepG2 hepatocellular carcinoma cells should be sorted based on migratory ability using a Transwell assay. As collagen I is abundant is the liver[476], the collagen I coated Transwell described in Chapters 3 and 4 is likely sufficient. After phenotypic sorting, metastatic potential of highly and weakly migratory cancer cells can be investigated using an orthotopic model for hepatocellular carcinoma metastasis. Next, MVs should be isolated from the highly and weakly migratory subpopulations. Transformation of fibroblasts after MV treatment can be quantified with αSMA expression, proliferation, and contractility. While in Chapter 4, 20 kPa gels were used for all experiments, different stiffness gels will likely be required to mimic liver stiffness, as described above. Lastly, RNAseq, proteomics, and western blots can be used to quantify Tg2 expression as it relates to migratory and metastatic potential. These experiments should also be repeated in a mouse cell line and an immunocompetent mouse model to assess the effects of MVs on immune cells and the ramifications of these interactions on metastasis. Importantly, a syngeneic orthotopic hepatocellular carcinoma model has recently been established[477] and can be utilized for these studies.

In Chapter 4, we show that phenotypically sorted MDA-MB-231 and SUM159 triple negative breast cancer cells similarly vary in migratory, metabolic, and EMT phenotype. These findings should

similarly be expanded to other cell types to determine the how glucose metabolism fuels migration in other cancer types. We hypothesize that while glycolysis fuels single cell MDA-MB-231 migration in *in vitro* confinement, different metabolic pathways may fuel migration of different cancer cell types. Using a similar Transwell-based invasion assay, highly invasive human cervix squamous cell carcinoma cells actually displayed increased mitochondrial activity compared to their parental cell lines[253]. This suggests that OxPhos may contribute to cervix squamous cell carcinoma migration and invasion.

6.2.2   *Assessing MV uptake by fibroblasts*

In Chapter 2, our findings reveal that matrix stiffness enhances MV-induced fibroblast activation. However, it remains unclear whether matrix stiffness enhances MV uptake by fibroblasts. As matrix stiffness increases fibroblast contractility[17], and MV uptake is dependent upon actin polymerization and cell contractility[3], we hypothesize that fibroblasts on stiffer substrates may uptake higher amount of MVs and this may enhance MV-induced fibroblast activation.

While our studies focused on fibroblast functional changes induced by breast cancer MVs, the dynamics of MV uptake by fibroblasts remains unclear. The current standard for fluorescently labeling MVs is fluorescent dyes, such as DiD or PKH[478,479]. However, repeated washing and filtration steps resulted in significant loss of sample (data not shown). Additionally, excess dye in suspension can be non-specifically taken up by recipient cells and dyes can trigger an enlargement of EVs due to membrane fusion[478]. Other groups have reported that luciferase expressing cells release EVs that can be imaged with BLI[480]; however, the MVs isolated in our system were not detected using BLI (data not shown). We propose labeling the MVs via palmGFP which fluorescently encodes the plasma membrane[481]. This will permit quantification of recipient cell uptake via fluorescence using confocal microscopy or flow cytometry.

Our studies would also be enhanced by determining if MV uptake is required for MV-induced signaling. In Chapter 3, we show that MVs released by highly and weakly migratory breast cancer cells differentially regulate fibroblast activation. While equal numbers of MVs were applied to fibroblasts during these studies, it is possible that differences in MV surface proteins may result in differences in fibroblast signaling independent of MV uptake. We show that pre-treatment of MVs with a cell impermeable Tg2 inhibitor reduced MV activation of fibroblasts, suggesting that Tg2 is located on the surface of the MVs, consistent with previous findings[15]. This suggests that external MV cargo, such as Tg2, can signal to integrins or other receptors on recipient cells to induce functional changes.

To further determine if MV-Tg2 can signal to recipient cells without cellular uptake of MVs, we propose fluorescently tagging Tg2 in cells before isolation of MVs. Isolated MVs can be imaged to verify that Tg2 is located on the surface of the MV and fibroblasts can subsequently be cultured with Tg2-labelled MVs. Fibroblast transformation and fluorescent changes can be assessed to determine if MV uptake is required for Tg2-mediated signaling.

It is also possible that MVs may rupture in the extracellular space and release their contents. It has been shown *in vitro* that when force is applied, the lipid membrane of EVs can rupture[482]. Thus, we hypothesize that MVs may signal to recipient cells through a combination of uptake, cell surface signaling, and cargo released upon rupture. To assess MV rupture, an external force can be applied to rupture MVs, such as AFM as previously described[482]. Fibroblasts can be cultured with ruptured MVs and the transfer of Tg2 fluorescence and functional changes can be assessed. As Tg2 is known to crosslink fibronectin to activate integrins on recipient cells[15], FAK and ERK activation, which are downstream of integrin activation in fibroblasts, could be assessed to determine if ruptured MVs can successfully activate fibroblast integrins.

6.2.3   Therapeutically targeting matrix stiffness and MV signaling

Our work in Chapter 2 identifies matrix stiffness as a potential therapeutic target to reduce MV-signaling, fibroblast activation, and ultimately cancer cell metastatic potential. A variety of therapies targeting matrix stiffening are currently being investigated, including fresolimumab targeting TGFβ, marimastat to activate MMPs, and vitaxin and volociximab targeting integrins αvβ3 and α5β1, respectively[483]. Increased matrix stiffness and matrix density in tumors may also serve as a barrier to effective drug delivery. For example, while CAR-T cell therapy has proven successful in blood-based cancers, it has largely been unsuccessful in solid tumors due poor trafficking and infiltration into tumor tissue[484]. Softening of tumor tissue may reduce MV signaling, fibroblast activation, and may permit other therapies such as CAR-T cell therapy to better penetrate solid tumors. However, concerns exist regarding matrix-targeting cancer therapies as matrix degradation may facilitate tumor cell invasion and may release growth factors and cytokines which could initiate inflammatory signals[483].

Chapters 2 and 3 identify cancer-derived MVs as therapeutic targets for breast cancer metastasis. Targeting MV release serves to reduce cancer cell-induced fibroblast activation in the tumor microenvironment. A variety of compounds have been reported to reduce MV release *in vitro*, including calpeptin targeting calpains, Y27632 targeting ROCK, D-Pantethine targeting cholesterol synthesis, and imipramine targeting aSMase[485]. Reducing MV signaling may also promote immune activation as EV signaling can be immunosuppressive[486,487]. However, the efficacy and side effects of these treatments *in vivo* are largely unknown.

The mechanical memory of fibroblasts should also be considered when designing cancer therapies that target matrix stiffness and MV signaling. As the median time to treatment initiation was 29 days in 2013[488], prior to treatment, fibroblasts will have been exposed to increased matrix stiffness which may affect their future behavior. Fibroblasts exhibit memory of their past mechanical microenvironment, and can exhibit sustained activation for up to two weeks after returning to soft cultures after priming on stiff matrices[489]. This finding emphasizes the importance of early cancer detection and designing therapeutics that may target both matrix stiffness and activated fibroblasts.

6.2.4 Cell phenotype and MV cargo

In Chapter 3, our findings indicate that Tg2 is not uniformly packaged into all breast cancer-derived MVs but rather depends upon the migratory phenotype of the MDA-MB-231 subpopulation. While others have shown that highly migratory cancer cells transfer migration-promoting cargo to weakly migratory cancer cells using EVs[419], our results reveal heterogeneity in MV cargo based on migratory phenotype within a single cell line, furthering highlighting a novel aspect of heterogeneity in cancer. In Chapter 5, we show preliminary findings that Tg2 splice variants are enriched in weakly migratory MVs compared to weakly migratory cells. This suggests that MV cargo may not be a direct reflection of the composition of the MV releasing cell, but rather cargo is differentially packaged into MVs by intracellular mechanisms. This is consistent with other studies suggesting that MVs are not a sampling of cellular components, but rather that certain proteins are selectively packaged into MVs[490]. Future work should investigate the relationship between cell phenotype and MV cargo, including phenotypes other than migratory ability, and should investigate the mechanisms of MV cargo trafficking. These findings will identify which cell phenotypes release MVs that contribute to specific pro-cancer phenotypes and provide insight into engineering MVs with specific cargo for regenerative medicine applications.

6.2.5 Tg2 and cell migration

Our findings in Chapter 4 implicate MV-Tg2 in weakly migratory cancer cell metastasis. Tg2 expression is generally positively correlated with cancer cell invasion and migration[58,59]. In MDA-MB-231 cells, Tg2-high subclones exhibit increased Transwell invasion compared to Tg2-low subclones[420]. While our finding that enhanced Tg2 expression correlates with metastatic capability is consistent with previous work[15,413,418,491,492], high Tg2 expression in the weakly migratory subpopulation raises questions on the role of Tg2 in mediating migration. Our results suggest that high Tg2 expression alone is not sufficient to induce migration. Unexpectedly, our weakly migratory subpopulation was enriched for both Tg2 and E-cadherin[377]. As it has previously been shown that Tg2 and E-cadherin expression are anticorrelated[493,494], it remains unclear how the phenotypic Transwell-based sorting produced a weakly migratory population enriched for both Tg2 and E-cadherin.

Tg2 was recently identified as a marker of epithelial-mesenchymal plasticity and was found to be upregulated in cancer cells undergoing EMT only after a reversion to a secondary epithelial state[413]. This finding is consistent with our results that a weakly migratory subpopulation of the highly mesenchymal MDA-MB-231 cell line is enriched for both Tg2 and E-cadherin. Taken together, these results suggest that our highly migratory population of MDA-MB-231 has undergone EMT while the weakly migratory population has undergone EMT and a subsequent reversion back to an epithelial phenotype. Together, these findings reveal that Tg2 is expressed by a population of cells that exhibit a partial-EMT phenotype and it is this population of cancer cells that is capable of robust metastasis via MV-fibroblast signaling.

Throughout the 20 rounds of Transwell phenotypic sorting, the highly migratory cells repeatedly migrate through 3D collagen and then grow in complete media on tissue culture plastic under the Transwell. The weakly migratory cells are continuously cultured on a 3D collagen gel on top of the Transwell in serum-starved conditions. We propose future studies tracking EMT status throughout the 20 rounds of phenotypic sorting, such as E-cadherin, Tg2, and vimentin staining.

It is additionally important to determine if we can induce Tg2 expression in the highly migratory subpopulation by inducing MET, potentially by mimicking the culture conditions experienced by the weakly migratory cells during sorting. To additionally determine whether the differences in Tg2 in the highly and weakly migratory cells are solely due to differences in cell migration or whether different culture conditions during sorting, we can utilize a secondary method to isolate highly and weakly migratory cancer cells, such as photoactivation, or sorting cells based on migration machinery and assess Tg2 expression.

6.2.6   *MV signaling to pre-metastatic niche*

In Chapter 3, we identify a novel mechanism by which weakly migratory cancer cells can escape the primary tumor through MV-Tg2-mediated fibroblast activation. As cancer derived EVs have been identified in the bloodstream and can travel to distant regions in the body[495], MVs released by the primary tumor likely reach secondary sites where they can transform resident cells. In colorectal cancer (CRC), exosomes released by CRC cells promote vascular permeability and angiogenesis to enhance CRC metastasis[422]. CRC EVs have been found to enter the circulation and activate lung fibroblasts to induce premetastatic niche formation[496]. Additionally, hepatocellular cancer EV-mediated CAF signaling promoted liver to lung metastasis[213]. While exosomes have clear roles in angiogenesis and pre-metastatic niche formation, the role of MVs in these processes are largely unknown. MVs and exosomes have been found to contain many of the same cancer-promoting signaling proteins, such as VEGF and TGFβ[344,423,424]. Thus, we hypothesize that primary tumor-derived MVs travel to the lungs and liver where they activate local fibroblasts to induce matrix remodeling of the pre-metastatic niche to prime the secondary site for metastasis.

In the context of intratumor heterogeneity, certain cells within the primary tumor may release MVs that are more equipped to enter the blood stream and reach secondary sites to signal to recipient cells. While our study suggests that the more metastatic cancer cells release MVs that are more potent activators of fibroblasts, it remains possible that other cells within the primary tumor release MVs better equipped to transform recipient cells. For example, MVs released from primary tumor CAFs may also travel to secondary sites and induce functional changes. A better understanding of MV heterogeneity within a primary tumor and how this heterogeneity relates to cell signaling and cancer metastasis, including premetastatic niche formation, is essential to understand the mechanisms of cancer metastasis.

6.2.7   Limitations to MV in vivo studies

In Chapters 2 and 3, our findings reveal that cancer derived MVs induce functional changes in fibroblasts. The majority of these studies were completed *in vitro* due to limitations in MV labeling. *In vivo* labeling mechanisms that selectively label and track MVs in mice will be essential to investigate the interplay between MV signaling and metastasis *in vivo*.

To address these concerns, we propose utilizing a membrane-bound luciferase probe which can be used to track MV signaling *in vitro* and *in vivo*[497]. Luciferase-labelled MVs that can be tracked using IVIS imaging could be used to quantify MV distribution in mice after injection, such as which tissues MVs localize to, as well as degradation times, will be crucial to investigate MV dynamics *in vivo*. Additionally, cells labeled with membrane-bound luciferase release EVs *in vivo* which can then be isolated and characterized[497]. This may allow purification for only luciferase-expressing EVs rather than a mixture of cancer, stromal, and other resident cell EVs to be isolated from mouse tissues. Additionally, developments to MV uptake studies, as outlined above, may permit *in vivo* studies of MV uptake by recipient cells. If luciferase-labeled MVs transfer their luciferase back to recipient cells, such as immune cells or fibroblasts, it may be possible to track from primary tumor to secondary site *in vivo*.

6.2.8   Mitochondrial dysfunction and EMT

In Chapter 4, our findings suggest that inhibition of OxPhos in breast cancer cells induces changes to EMT status while inhibition of glycolysis does not affect EMT. This indicates that EMT phenotype is more dependent on mitochondrial function rather than glucose metabolism utilization as a whole. Similar to our studies, MCF10A breast epithelial cells with mitochondrial stress adopted a fibroblast-like mesenchymal morphology and were highly motile[498]. Additionally, preliminary results reveal that OxPhos inhibition of the weakly migratory cancer cells decreases overall ATP and does not increase glucose uptake (data not shown), suggesting that it is not an increase in glycolysis that is enhancing migration and inducing EMT. The mechanisms by which mitochondrial dysfunction induces a mesenchymal and migratory phenotype is still unclear.

A Seahorse Mito Stress test could be used on the highly and weakly migratory cancer cells, as well as cells transformed to be more epithelial or more mesenchymal, to further characterize mitochondrial function as it relates to EMT. The effect of additional OxPhos inhibitors that target different enzymes, such as oligomycin, which inhibits ATP synthase, AG-881, which targets IDH, or rotenone, which inhibits complex I of the electron transport chain, on EMT status should be determined to evaluate whether the EMT shift observed is due to mitochondrial dysfunction as a whole or is the result of inhibition of certain steps in OxPhos.

6.2.9   *Role of glutamine metabolism in cell migration*

In Chapter 4, we focus on the role of glucose metabolism in cell migration. However, cancer metabolism encompasses a wide range of pathways and intermediates that contribute to cellular energetics. Recently glutamine metabolism has gained increasing attention as one of the main sources for cancer cell energy[219,499–501]. As glutamine metabolism feeds into the TCA cycle[219], it may fuel similar cell behaviors to OxPhos. Certain studies report that glutamine fuels proliferation but not migration in endothelial cells[501], while others report that a metabolic shift towards glutamine regulates growth and invasion in ovarian cancer[500]. Studies suggesting differing roles of glutamine in cancer migration may be due to different *in vitro* models as chemical and mechanical signals likely alter glutamine metabolism.

We propose future studies that investigate the role of glutamine metabolism in single cell migration and EMT. A Seahorse Mito Fuel Flex Test can be used to determined differences in glutamine metabolism between highly and weakly migratory cells. Cell migration can be analyzed after inhibition of glutamine signaling via L-γ-glutamyl-p-nitroanilide, to inhibit glutamine uptake, or 968 and BPTES to disrupt glutamine catabolism[502]. We hypothesize that inhibition of glutamine metabolism in weakly migratory cancer cells may also induce EMT through metabolic dysregulation. However, in hepatocellular carcinoma, inhibition of glutaminase, the enzyme that converts glutamine into glutamate, was found to inhibit migration and invasion through Snail inhibition[503], suggesting that inhibition of glutamine may induce a more epithelial phenotype.

6.2.10   *Oxidative phosphorylation, metastasis, and metabolic plasticity*

In Chapters 3 and 4, our findings reveal that weakly migratory, OxPhos MDA-MB-231 are more metastatic than highly migratory, glycolytic MDA-MB-231. This observation is consistent with other studies that OxPhos is upregulated at metastatic sites[289]. While our work in Chapter 4 shows that glycolysis fuels the migration of the highly migratory cells, we do not explore how OxPhos contributes to weakly migratory cancer cell metastasis.

To determine if OxPhos is required for weakly migratory cancer cell metastasis, cells can be pre-treated *in vitro* with oligomycin, a selective inhibitor of OxPhos, before injection into mice. It has previously been shown that pre-treatment of MDA-MB-231 with oligomycin resulted in decreased lung metastasis[289]. As such, we anticipate that OxPhos inhibition will decrease weakly migratory cancer cell metastasis. To determine whether OxPhos is important in the early or later stages of the metastatic cascade, progression through the metastatic cascade could be monitored *in vitro* and *in vivo*. *In vitro* assays, including proliferation assays, intravasation assays, viscometers to mimic fluid shear experienced in circulation, and colonization of *ex vivo* tissues can be used to investigate weakly migratory cancer cells behavior with and without OxPhos inhibition. Additionally, mice injected with control and oligomycin pre-treated cells can

be monitored for progression through the metastatic cascade with experiments including *en bloc* primary tumor sections to monitor cancer cell dissemination and CTC isolation to quantify survival in circulation.

It is important to note that cancer cell glucose metabolism is highly plastic and changes throughout metastatic cascade progression. While the highly and weakly migratory MDA-MB-231 subpopulations exhibit different metabolic phenotypes *in vitro*, these phenotypes may be plastic and change throughout metastasis. Characterizing and tracking cancer cell glucose metabolism *in vivo* throughout the metastatic cascade will provide insight on the most relevant metabolic pathways to therapeutically target in metastasis. In addition to the *in vitro* and *in vivo* experiments outlined above, cancer cell metabolism should be monitored during these various stages to determine how environmental cues shift metabolism during metastasis.

6.2.11   *MVs and metabolic signaling*

In Chapter 5, we show preliminary data that MVs contain a wide array of metabolic cargo and that MVs can induce metabolic programming in fibroblasts. Our proteomics data identifies proteins and enzymes involved in glycolysis and OxPhos in MVs, indicating that MVs may be capable of generating ATP. Future work can be completed to determine whether MVs can generate ATP, whether the ATP is utilized or degraded via ATPases, and the potential ramifications of these metabolic enzymes in MV signaling.

In Chapter 5, we show that MVs can metabolically reprogram fibroblasts to be more glycolytic; however, the changes in fibroblast metabolism do not appear to correlate with the metabolic cargo in the MVs. The MVs with more OxPhos-related proteins induced a larger switch towards glycolysis in fibroblasts than the more glycolytic-rich MVs. This suggests that MVs reprogram fibroblast metabolism independently of metabolic cargo. Future work can determine the role of Tg2 in MV-mediated fibroblast metabolic reprogramming. As Tg2 activates HIF-1α[504], we hypothesize that breast cancer MV-induced fibroblast glycolysis may be through Tg2-HIF-1α signaling.

APPENDIX A: MICROVESICLE ISOLATION

Microvesicle Extraction from MDAs
1. Seed 3 million MDA-MB-231 cells in a T150 flask
2. Grow cells for 2 days
3. After 2 days, serum starve in 14 mL serum-free DMEM for 18 hours (O/N)
4. Remove media from flask and place in 15 mL conical tube
5. Centrifuge @ 400 rpm for 5 minutes. Place supernatant in new tube, leaving pellet and ~250 uL of media at the bottom of the old tube
6. Repeat
7. Filter solution with steriflip tubes using a weak vacuum (~1 drip/second)
8. When almost filtered, use 1000 uL pipet to pipet solution surrounding "wagon wheel" back into filter
9. Wash with 10 mL serum-free DMEM. Allow to filter. When almost finished, pipet solution off "wagon wheel" rim again
10. Turn off vacuum. Remove filter
11. Re-suspend microvesicles on top of filter in 1 mL serum-free media. To do so, wash filter repeatedly in a circular formation.
12. Place in cryo tube and store in -80C freezer
Tip: Make sure vacuum is OFF before attaching it to steriflip tube.

Other cell lines:
- Seed 3 million cells into T150 flask. Grow cells for 2 days. Serum-starve in respective serum-free media (MCF10A = DMEM/F12 + P/S). Collect MVs as described. Re-suspend in 1 mL respective serum-free media. Count MVs with ZetaView to determine volume of MVs to apply to cells.

To collect MV lysate:
1. Seed 3 million MDA-MB-231 cells per T150 flask. Use 3 T150 flasks to get concentrated lysate.
2. Grow cells for 2 days
3. After 2 days, serum starve each flask in 14 mL serum-free DMEM for 12-18 hours (O/N)
4. Remove media from flasks and place in 50 mL conical tube. You'll have just under 45 mL.
5. Centrifuge @ 400 rpm for 5 minutes. Place supernatant in new tube, leaving pellet and ~1 mL of media at the bottom of the old tube
6. Repeat
7. Filter solution with steriflip tubes using a weak vacuum (~1 drip/second)
8. When almost filtered, use 1000 uL pipet to pipet solution surrounding "wagon wheel" back into filter
9. Wash with 10 mL PBS. Allow to filter. When almost finished, pipet solution off "wagon wheel" rim again
10. Turn off vacuum. Remove filter
11. Lyse MVs in 200 uL 4x SDS (preheated to 95C on heating block). To do so, wash filter repeatedly in a circular formation.
12. Place in 1.7 mL Eppendorf tube and store in -80C freezer
   a. I normally have to load ~10 uL to get a good band on a western

APPENDIX B: AFM OF PRIMARY TUMORS

Materials:
- MFP3D-BIO inverted optical AFM (Asylum Research, USA)
    - IGOR PRO Software (Asylum Research, USA)
- Silicon nitride cantilever (diameter = 5 um, spherical borosilicate glass tip, 0.06 N/m) (Novascan Tech, USA)
    - Length of cantilever determines compliance
    - Use spherical tip for tissue
    - 1-1 rule: want similar cantilever/material compliance
- Hoechst Nuclei Stain (Thermofisher, H3570)
- ImmEdge Hydrophobic Barrier Pen (Vector, H4000)
- 24 x 30 mm Thermoplastic coverslips (ThermoFisher, 150067)
- Halt Protease Inhibitor Cocktail, EDTA-free (100X) (Thermofisher, 78439)
- Frozen, mounted, tumors embedded in OCT, 20 um thick
- Biopsy punch (2-6 mm)
- Super glue
- 1X PBS

Procedure:
1. AFM set up
    - Turn on AFM microscope (under AFM)
    - Turn on light source (BF lamp, on switch is to right of computer)
    - Turn on laser (key switch turn)
    - Image → Integral gain (feedback loop between deflection and set up) → **set = 1** (slower than 10)
    - Force → fix velocity (**2 um/s for glass**), fix force distance (**10 um for glass**)
    - Press "video" → want svideo input
    - Find cantilever and bring into focus with brass knob
    - Find laser with LDX and LDY knobs
    - Zero deflection with PD knob
2. Calibrate cantilever on infinitely hard surface
    a. Sensitivity calibration
        i. Click engage (engages z feedback loop)
        ii. Lower head until cantilever is close to glass surface. Lower until ding. Click withdraw.
        iii. Single force → cantilever will touch until set point (Ex: 1 Volt)
            1. Red line = approach, blue line = retraction
            2. CTRL + I → drag A to bottom of red line and B to top (of linear overlap)
            3. Right click → update inVOLS (inverse optical lever sensitivity → X volts = 1 nm deflection)
        iv. Force calibration subtab → print screen, paste into paint, record cantilever number in file
    b. Thermal calibration
        i. Move holder up ~10 knob turns, zero deflection with PDX
        ii. Close doors
        iii. Thermal → capture thermal data. Wait until curve stops moving.
            1. Draw fit → click top of curve → fit thermal data
            2. Force calibration subtab → see spring constant → print screen, paste into paint, save

3. Prepare sample for AFM
    a. Remove frozen, sectioned tumor slide from freezer
    b. Wait ~20-30 seconds for sample to thaw. Remove excess OCT with kimwipe.
    c. Wash thermoplastic coverslip with DI water. Use air duster to remove excess water.
    d. Using biopsy punch of desired size, punch hole in center of coverslip.
    e. Add superglue ring around tumor section. Carefully place coverslip down and lightly press to glue down.
    f. Using hydrophobic pen, draw a circle around the hole in the coverslip. Circle should have a diameter of about 1.5 cm.
    g. Add ~200 uL of PBS+ 1:200 Halt protease inhibitor cocktail for 2 min. Discard.
    h. Add ~200 uL of solution from step G + 1:500 hoeschst for 5 min. Discard.
    i. 2 x 3 min wash with PBS+PIC.
    j. Ready to AFM.
4. Calibrate cantilever in liquid (do this in the liquid your sample will be in!)
    a. Place your sample on AFM stage. Apply PBS + PIC to sample inside hydrophobic ring.
    b. Ensure front leg of AFM head is at its maximum length
    c. Place AFM head onto of sample. Slowly enter cantilever into liquid bubble.
    d. Sensitivity calibration
        i. Once cantilever is in liquid, readjust laser so that laser is focused on cantilever tip
        ii. Thermal tab → lock spring constant
        iii. Capture thermal data, fit to curve, examine new sensitivity calculation.
    e. Virtual Deflection calibration
        i. Change trigger channel to "none"
        ii. Zero deflection
        iii. Force → setup → show virtual deflection 2nd term
        iv. Change force distance to max, drag red bar to top
        v. Single force → CTRL + I → Place A and B → calculate virtual deflection poly
5. Poking your sample
    a. Set trigger point = 1 nN
    b. Using objective, find sample of tumor you want to poke (change video to composite mode)
    c. Engage → lower until beep → withdraw
    d. Single force (re-lower force distance after virtual deflection calibration)
    e. Review → graph → last curve → elastic
        i. Tip = sphere
        ii. Radius = 2.5 um
        iii. Poisson (of sample) = 0.5
    f. When you find an area that is giving you good pokes, do a force map
        i. Fmap tab
        ii. Change force points and force lines (# of x/y squares on grid)
        iii. Change cyan square to change scanning area
        iv. "Do Fmap"

NIR-AZA Fluorophore
- Received from Donal O'Shea at Royal College of Surgeons in Ireland
Info:
- BF$_2$-azadipyrromethene (NIR-AZA) are NIR-fluorophores
- NIR-AZA 1 is amphiphilic, has good chemical and photo-stability, and is internalized by cells

Preparation:
1. Take Eppendorf from freezer and warm up to RT for 20 min on benchtop
2. Add 1 mL sterile PBS into Eppendorf (prepares a stock solution of 200 uM)
3. Keep stock solution in 4C refrigerator, use within 1 week

Absorbance = 692 nm
Fluorescence = 720 nm

Collection of MVs from NIR-AZA labelled cells:
1. Grow cancer cells in complete media until 70-80% confluent
2. Wash 3X with PBS
3. Incubate for 2 hours with 10 mL medium with 5 uM NIR-AZA
4. Wash 3X with PBS
5. Add 14 mL SF media O/N
6. Collect MVs

Validation:
1. Compare MV release #'s to ensure MVs are still being released and collected
2. Image tube of labelled MVs

IVIS presets
       Excitation = 680, 700 nm
       Emission = 710, 790 nm

APPENDIX D: LYSIS OF MVS FOR PROTEOMICS

Buffer components:
- 150 mM NaCl
- 2% NP-40
- 0.5% sodium deoxycholate
- 50 mM Tris, pH 8

Lysing MVs:
- Collect MVs on 0.2um filter, wash with cold PBS
- Remove filter top and place on ice
- Add lysis buffer for 5 minutes, swirling occasionally
- Pipet up lysis buffer and transfer to a 1.7 mL Eppendorf tube
- Incubate lysate in 4C for 30 minutes
    o Can sonicate before centrifugation if very viscous
- Micro-centrifuge at 14,000g for 5-15 minutes at 4C (time and speed may change depending on cell type)
- Collect supernatant (avoid pellet) and put into fresh Eppendorf tube
- Store in -80C and avoid multiple freeze/thaw cycles

APPENDIX E: LACTATE ASSAY

Purpose: To determine the concentration of lactate in cells or in conditioned media. This assay can also be used for mouse tissues. Refer to the online protocols for the kit for this use.

Materials:
- Clear 96-well plate
- Eppendorf tubes

Item	Tube Label	Amount	Preparation when received	Aliquot Size	Storage
Lactate Assay Buffer	B	25 mL	Ready to use	1 mL	-20C
Lactate Enzyme Mix	E	1 vial	Reconstitute with 220 uL of lactate assay buffer. Keep on ice.	15 uL	-20C
Lactate Substrate Mix	S	1 vial	Reconstitute with 220 uL lactate assay buffer. Keep on ice.	15 uL	4C
100 mM L(+)-Lactate Standard	1 mM	100 uL	Dilute to 1 mM by adding 10 uL standard to 990 uL of lactate assay buffer.	35 uL	-20C

Protocol:
1. Standard Preparation:
   a. Prepare fresh standards for every use
   b. Carry out each dilution twice to run standard in duplicate

Standard #	1 mM Std Vol (uL)	Buffer (uL)	Final volume in well (uL)	End lactate concentration (nmol/well)
1	0	25	25	0
2	1	24	25	1
3	2	23	25	2
4	3	22	25	3
5	4	21	25	4
6	5	20	25	5

2. Sample Preparation:
   a. Cell Samples (adherent or suspension)
      i. Harvest cells for each assay (1-2 million recommended)
      ii. Wash cells with **cold** PBS
      iii. Resuspend pellet in 4X volumes of **buffer** (~200 uL)
      iv. Centrifuge 2-5 min @ 4C, top speed
      v. Collect supernatant. Transfer to clean tube. Keep on ice.
      vi. Deproteinize (either use a deproteinization kit or follow instructions bellow)
         1. Requires:
            a. Perchloric acid (PCA) 4M, ice cold
            b. Potassium hydroxide (KOH) 2M, ice cold
         2. Add ice cold PCA 4 M to a final concentration of 1 M in the homogenate solution and vortex. (high protein samples might need more PCA)
         3. Incubate on ice for 5 min
         4. Centrifuge samples at 13,000g for 2 min at 4C. Transfer supernatant to fresh tube. Measure volume of supernatant.

5. Precipitate excess PCA by adding ice-cold 2 M KOH that equals 34% of the supernatant to your sample (ex: 34 uL of 2 M KOH to 100 uL sample). Vortex. This will neutralize and precipitate excess PCA.
6. Use pH paper to ensure that pH is between 6.5-8. If necessary adjust with 0.1 M KOH or PCA.
7. Note: the deproteinization will dilute your samples. To calculate the dilution factor, apply the following formula: % original concentration = 100* (initial sample volume/ (initial sample volume + Vol PCA + Vol KOH))

b. Serum Samples
   i. Can be tested directly. Do not require additional preparation.
   ii. Deproteinization is recommended but not required.
   iii. Example:
      1. Culture 100,000 MDA-MB-231 in 500 uL 231 CM in 24 well plate for 24 hours.
      2. Collect 500 uL conditioned media in 15 mL tube.
      3. Dilute with 500 uL 231 CM. (1:2 dilution)

3. Assay Procedure:
a. Tips:
   i. Equilibrate all materials and reagents to RT
   ii. Work all standards and samples in duplicate
   iii. To save supplies, run all samples at once so you only waste materials on one set of standards.
b. Prepare samples and standards as previously described. **Keep on ice.**
c. Set up reaction wells in 96 well plate (clear plate)
   i. **Standard wells**: add 25 uL of standards. Run in duplicate.
   ii. **Sample wells**: Add 2-25 uL of sample. Adjust to 25 uL with **buffer**. Run in duplicate.
      1. 2 uL of your 1:2 dilution of conditioned media should give you numbers in a good range.
   iii. **Sample background controls**: Add 2-25 uL sample of one sample. Adjust to 25 uL with **buffer**. (These numbers of usually very stable. It's just how much the media color impacts the reading. To save reagents, I would consider running with just 1 sample).

	1	2	3	4	5	6	7	8	9	10	11	12
A	Std1	Std2	Std3	Std4	Std5	Std6						
B	Std1	Std2	Std3	Std4	Std5	Std6						
C	S1	S2	S3									
D	S1	S2	S3									
E	SB											
F												
G												
H												

d. Prepare reaction mix
   i. Prepare 50 uL of reaction mix for each reaction. Mix enough reagents for the number of assays. Prepare a master mix to ensure consistency.
   ii. x uL * number of assays + 1

Components	Reaction Mix (uL)	Background Reaction Mix (uL)
Lactate Assay Buffer	23	24

Lactate Substrate Mix	1	1
Lactate Enzyme Mix	1	0

iii. Example calculations:
1. NOTE: Reaction Mix calculations include running the standards in either single or duplicate as well. All calculations have a buffer of reagents for 1 extra reaction to account for pipet error.

	Reaction Mix			Background Reaction Mix (just run 1x to save reagents)	
	Buffer (uL)	Substrate (uL)	Enzyme (uL)	Buffer (uL)	Substrate (uL)
2 samples (singles) (x9)	207	9	9	24	1
2 samples (duplicates) (x17)	391	17	17	24	1
3 samples (singles) (x10)	230	10	10	24	1
3 samples (duplicate) (x19)	437	19	19	24	1
6 samples (singles) (x13)	299	13	13	24	1
6 samples (duplicates) (x25)	575	25	25	24	1
9 samples (singles) (x16)	368	16	16	24	1
9 samples (duplicates) (x31)	713	31	31	24	1

e. Add 25 uL of reaction mix and 25 uL of background reaction mix to appropriate wells.
f. Incubate 30 minutes at room temperature.
g. Measure OD 450 nm. Stable for 4 hours.

Data Analysis:
1. Transfer data to excel
2. Average all duplicate reading
3. Subtract absorbance from standard 1 from all other standards
4. Plot standard absorbance readings against lactate concentration. Linear fit.
5. Substrate background sample absorbance readings from sample readings.
6. Using linear fit equation, calculate the amount of lactate in each well.
7. Calculate the lactate concentration in your sample based on dilutions.
   a. 1:2 dilution
   b. 2 uL in 23 uL (1:12.5 dilution)

APPENDIX F: GIBSON ASSEMBLY TO GENERATE FUW-TG2 PLASMID

Plasmids
1. pHis-Tg2: https://www.addgene.org/100719/
2. FUW backbone: https://www.addgene.org/14882/

Designing Gibson PCR Primers
1. Used SnapGene on AFM computer
2. Modeled linearizing FUW backbone with XbaI and BamH1
3. Designed Gibson primers that overlap with both Tg2 fragment and FUW backbone
   a. Forward: ggctgcaggtcgactatatggccgaggagctgg
   b. Reverse: ccctcgaggttaactgatcaattagtggtggtggtggtg
4. Used NEB calculator to calculate annealing temperature: http://tmcalculator.neb.com/#!/main
   a. ONLY input parts that bind to your desired fragment – NOT the backbone
   b. Calculated annealing temperature = 64C

Gibson PCR
1. Dilute template DNA to10 ng/uL
2. Turn on T100 Thermal Cycler and start Phusion program. Once started, click 'pause'. This allows the hid to pre-heat.

Step	Temp	Time (s)	Cycles
Initial Denaturization	98	60	1
Denaturization	98	10	30
Annealing	64	30	30
Extension	72	30	30
Final Extension	72	600	1
Hold	4	Forever	

3. Mix PCR reaction tubes.
   a. **keep Phusion polymerase on yellow cold block and do not add to tubes until thermal cycler is heated up**

1	Nuclease-free Water	32.5 uL
2	Template DNA (10 ng/uL)	1 uL
3	Fprimer 10 uM	2.5 uL
4	Rprimer 10 uM	2.5 uL
5	dNTPs	1 uL
6	Phusion 5X buffer	10 uL
7	Phusion polymerase	0.5 uL

4. Place tubes on Thermal Cycler → Start → run will take about 1 hr 10 min.

Running a Gel:
1. While waiting for PCR to run, cast gel.
   a. 1.8 agarose + 60 mL TAE buffer.
2. Add 3 uL of 1 Kbp plus ladder to well 1
3. Add PCR product 5uL + 1 uL of loading dye to well 2
4. Add cut FUW vector 3 uL + 1 uL of loading dye to well 3
5. Run at 100 V for ~30 min

Gel Extraction:
1. If band is messy, you will need to do gel extraction
2. Rerun gel. Fuse together 5 lanes with tape so you get 1 large band.
   a. Fill well with a lot of PCR product.
   b. Run at 100 V until well separately.
3. Using UV block and face shield, cut out desired band using sharp razor. Place in **pre-weighed** 1.7 mL centrifuge tube.
   a. Ideally don't want more than ~350 mg of gel per tube.
4. Follow wizard gel clean-up kit directions.

PCR Cleanup:
1. If bands on gel look good, use Wizard PCR/Gel Clean-Up Kit to clean-up the PCR product.
2. Follow manufacturer directions.
3. Takes ~20 minutes.
4. Measure concentration on nanodrop.
5. Freeze at -20.

Gibson Assembly Calculations:
- Tg2 Fragment: 115.56 ng/uL, 2132 bp
  o 50 ng = 0.43 uL = _____ pmol DNA
    ▪ pmol = (50 ng x 1000) / (2132 x 650 Da) = 50,000/127,920 = 0.39 pmol
  o 100 ng = 0.865 uL = _____ pmol DNA
    ▪ Pmol = (100 ng x 1000) / (2312 x 650 Da) = 100,000/127,920 = .781 pmol
- FUW backbone: 135.645 ng/uL
  o 50 ng = 0.369 uL
  o 100 ng = 0.737 uL
  o *Diluting FUW to 50 ng/uL* → 11.05 uL FUW + 18.95 uL water
    ▪ 50 ng = 1 uL = 0.083 pmol DNA
    ▪ 100 ng = 2 uL = 0.0171 pmol DNA
- **For the reaction:** Need 100 ng template (FUW) and 5x that of insert.
  o 100 ng of FUW is 0.0171 pmol, so I need 0.85 pmol of Tg2 = 0.94 uL

Gibson Assembly:
1. Diluted cut FUW (135.645 ng/ul) to 50ng/uL (11.05uL of FUW to 28.95 uL of water)
2. Added 5.02 uL of water, 0.94 uL of Tg2 fragment (115.56 ng/uL), and 2 uL of FUW to a PCR tube.

Ingredient	100 ng template
Water	7.06 uL
Tg2	0.94 uL
FUW	2 uL
Master Mix	10 uL
Total	20 uL

3. Take MasterMix out of freezer, **place on cold block**.
4. Add 10uL MasterMix to tube.
5. Place on PCR machine incubating at **50 degrees for four hours**.

Transformation:
1. Acquire 5 LB+Amp plates

2. Dilute FUW (1000ng/uL) uncut and FUW cut (50 ng/uL) both to 1 ng/uL.
3. Label 4 tubes: Tg2-FUW Gibson Assembly, Pos Ctrl, Neg Ctrl, Produc
4. Label a tube for Tg2-FUW Gibson product, filled with 15 uL water.
5. Remove Gibson product from PCR machine and added 5 uL to tube
6. Put 2 uL of uncut FUW into a tube labelled positive control
7. Put 2 uL of cut FUW into a tube labelled negative control
8. Put 2 uL of diluted Gibson product into a labelled tube
9. Thaw **COMPETENT DH5alpha** on ice immediately
10. Thaw SOC media on benchtop
11. Add 50 uL of bacteria to each of the three tubes, tap three times, and immediately put on ice.
12. Incubate 30 min on ice. MAKE SURE WATER BATH IS AT 42 DEGREES
13. At 30 min, heat shock at 42 degrees for exactly 45 seconds in special water bath. NO LONGER
14. Shove on ice for 2 min.
15. At 2 min, **add 250 uL of SOC media**.
16. Place on bacterial shaker for 1hr.
17. Warm three labelled plates in bacteria incubator.
18. At 1 hr, pipette mixture on to respective plate, let air dry, then place upside down in incubator (no shaker).
19. Check in 16 hr and remove plates from incubator

Colony PCR – grow up colonies with PCR and run on gel to see which ones are the correct length
1. Remove plate from bacterial incubator at
2. Label 10 medium bacteria tubes and 10 PCR tubes
3. Aliquot 50 mL LB + 50 uL ampicillin (stored in -20C). Cover in foil.
4. Add 2 mL LB+amp to each bacterial tube.
5. Prepare and aliquot mastermix into PCR tubes *ON ICE*

	1 reaction (20 uL each)	12 reactions
Nuclease Free Water	8 uL	96 uL
10 uM Forward Primer (UbC)	1 uL	12 uL
10 uM Rev Primer (WRE)	1 uL	12 uL
DreamTaq or GoTaq Pol	10 uL	120 uL

6. Inoculate each PCR tube with a single colony each
   a. Touch a pipette tip to a colony, dip it in the PCR tubes, eject it into a 17x100 mm culture tube filled with 2 mL LB+amp
7. Run on thermocycler (**WANT A HOT START**)

Step	# cycles	Time	Temperature
Initial denaturation	1	60s	95C
Denature	25	10s	95C
Anneal	25	30s	Variable
Extension	25	30s	72C
Final Extension	1	10 min	72C
Hold	infinity	infinity	4C

8. Annealing temp = 5C below Gibson PCR (64-5 = 59)
9. Ran on gel with 1 kb plus ladder
   a. 3 uL ladder
   b. 5 uL PCR product
   c. 120V for 30 min
   d. Add extra broth to best bands

Miniprep of Colonies
1. Remove bacterial tubes from incubator
2. Create bacterial stock from 500 uL bacteria and 500 uL 50% glycerol/DI water. Place in -80C
3. Spin down bacteria in 1.7 mL tube (1.4 mL at a time)
   a. Reserve 100-300 uL for inoculation
4. Discard supernatant after spinning down
5. Add 250 uL resuspension buffer and break up pellet
6. Add 250 uL cell lysis buffer, invert 6-8 times, let sit until clear or 5 min (NO LONGER)
7. Add 10 uL of alkaline phosphatase, invert 10 times
   a. Let set for 5 min at RT
8. Add 350 uL neutralization buffer. Spin max speed 5 min
   a. Label final elution tube + columns
9. Place supernatant on column. Let sit 1 min, then spin max speed 30s.
10. Discard flow through. Add 750 uL wash buffer. 30s spin.
11. Discard flow through. Add 250 uL wash buffer. 30s spin.
12. 1 final empty spin. Diacard bottom and place column on new tube.
13. Warm elution water in microwave.
14. Add 50 uL water to column over new tube. Spin 1 min.
15. Add 30 uL water to column. Spin 2 min.
16. Nanodrop

Restriction Digest
1. Need 1 ug of DNA – calculate this based on nanodrop.
2. Follow restriction digest protocol.
   a. Restriction digest of colonies
      i. Used ECoRI, XbaI, and KpnI
- Inoculated large culture O/N (100 mL LB + 100 uL AMP + 100 uL #2 culture)
- Midiprep
- Nanodrop

REFERENCES

1. Schwager, S. C., Taufalele, P. V. & Reinhart-King, C. A. Cell–Cell Mechanical Communication in Cancer. *Cell. Mol. Bioeng.* **12**, 1–14 (2019).

2. Mosier, J. A., Schwager, S. C., Boyajian, D. A. & Reinhart-King, C. A. Cancer cell metabolic plasticity in migration and metastasis. *Clin. Exp. Metastasis* (2021) doi:10.1007/s10585-021-10102-1.

3. Schwager, S. C. & Reinhart-King, C. A. Mechanobiology of microvesicle release, uptake, and microvesicle-mediated activation. in *Current Topics in Membranes* (Academic Press, 2020). doi:10.1016/bs.ctm.2020.08.004.

4. Centers for Disease Control and Prevention. CDC - Basic Information About Breast Cancer. *Cent. Diesae Control Prev.* (2017).

5. American Cancer Society. Cancer Facts & Figures 2015. *American Cancer Society* 56 (2015).

6. Hanahan, D. & Weinberg, R. A. Hallmarks of Cancer: The Next Generation. *Cell* **144**, 646–674 (2011).

7. Sun, X. & Yu, Q. Intra-tumor heterogeneity of cancer cells and its implications for cancer treatment. *Acta Pharmacol. Sin.* **36**, 1219 (2015).

8. Plodinec, M. *et al.* The nanomechanical signature of breast cancer. *Nat. Nanotechnol.* **7**, 757–765 (2012).

9. Kim, J. & DeBerardinis, R. J. Mechanisms and Implications of Metabolic Heterogeneity in Cancer. *Cell Metab.* **30**, 434–446 (2019).

10. Lawson, D. A., Kessenbrock, K., Davis, R. T., Pervolarakis, N. & Werb, Z. Tumour heterogeneity and metastasis at single-cell resolution. *Nat. Cell Biol.* **20**, 1349 (2018).

11. Alkasalias, T., Moyano-Galceran, L., Arsenian-Henriksson, M. & Lehti, K. Fibroblasts in the Tumor Microenvironment: Shield or Spear? *Int. J. Mol. Sci.* **19**, (2018).

12. Erdogan, B. *et al.* Cancer-associated fibroblasts promote directional cancer cell migration by aligning fibronectin. *J Cell Biol* **216**, 3799–3816 (2017).

13. Erdogan, B. & Webb, D. J. Cancer-associated fibroblasts modulate growth factor signaling and extracellular matrix remodeling to regulate tumor metastasis. *Biochem. Soc. Trans.* **45**, 229–236 (2017).

14. Kalluri, R. The biology and function of fibroblasts in cancer. *Nat. Rev. Cancer* **16**, 582–598 (2016).

15. Antonyak, M. A. *et al.* Cancer cell-derived microvesicles induce transformation by transferring tissue transglutaminase and fibronectin to recipient cells. *Proc. Natl. Acad. Sci. U. S. A.* **108**, 4852–4857 (2011).

16. Jiang, E. *et al.* Tumoral microvesicle–activated glycometabolic reprogramming in fibroblasts promotes the progression of oral squamous cell carcinoma. *FASEB J.* **33**, 5690–5703 (2019).

17. Schwager, S. C. *et al.* Matrix stiffness regulates microvesicle-induced fibroblast activation. *Am. J. Physiol.-Cell Physiol.* **317**, C82–C92 (2019).

18. Balaban, N. Q. *et al.* Force and focal adhesion assembly: a close relationship studied using elastic micropatterned substrates. *Nat. Cell Biol.* **3**, 466–472 (2001).

19. Horwitz, A., Duggan, K., Buck, C., Beckerle, M. C. & Burridge, K. Interaction of plasma membrane fibronectin receptor with talin--a transmembrane linkage. *Nature* **320**, 531–533 (1986).

20. Oria, R. *et al.* Force loading explains spatial sensing of ligands by cells. *Nature* **552**, 219–224 (2017).

21. Roca-Cusachs, P., Gauthier, N. C., Del Rio, A. & Sheetz, M. P. Clustering of alpha(5)beta(1) integrins determines adhesion strength whereas alpha(v)beta(3) and talin enable mechanotransduction. *Proc. Natl. Acad. Sci. U. S. A.* **106**, 16245–16250 (2009).

22. Wang, N., Butler, J. P. & Ingber, D. E. Mechanotransduction across the cell surface and through the cytoskeleton. *Science* **260**, 1124–1127 (1993).

23. Zaidel-Bar, R., Cohen, M., Addadi, L. & Geiger, B. Hierarchical assembly of cell–matrix adhesion complexes. *Biochem. Soc. Trans.* **32**, 416–420 (2004).

24. Zamir, E. *et al.* Dynamics and segregation of cell-matrix adhesions in cultured fibroblasts. *Nat. Cell Biol.* **2**, 191–196 (2000).

25. Choquet, D., Felsenfeld, D. P. & Sheetz, M. P. Extracellular matrix rigidity causes strengthening of integrin-cytoskeleton linkages. *Cell* **88**, 39–48 (1997).

26. Cavalcanti-Adam, E. A. *et al.* Lateral spacing of integrin ligands influences cell spreading and focal adhesion assembly. *Eur. J. Cell Biol.* **85**, 219–224 (2006).

27. Heino, J. & Käpylä, J. Cellular receptors of extracellular matrix molecules. *Curr. Pharm. Des.* **15**, 1309–1317 (2009).

28. Schwarz, U. S. & Gardel, M. L. United we stand: integrating the actin cytoskeleton and cell-matrix adhesions in cellular mechanotransduction. *J. Cell Sci.* **125**, 3051–3060 (2012).

29. Katz, B.-Z. *et al.* Physical State of the Extracellular Matrix Regulates the Structure and Molecular Composition of Cell-Matrix Adhesions. *Mol. Biol. Cell* **11**, 1047–1060 (2000).

30. Seong, J., Wang, N. & Wang, Y. Mechanotransduction at focal adhesions: from physiology to cancer development. *J. Cell. Mol. Med.* **17**, 597–604 (2013).

31. Chaudhuri, O. *et al.* Extracellular matrix stiffness and composition jointly regulate the induction of malignant phenotypes in mammary epithelium. *Nat. Mater.* **13**, 970–978 (2014).

32. Hotchin, N. A. & Hall, A. The assembly of integrin adhesion complexes requires both extracellular matrix and intracellular rho/rac GTPases. *J. Cell Biol.* **131**, 1857–1865 (1995).

33. Paszek, M. J. *et al.* Tensional homeostasis and the malignant phenotype. *Cancer Cell* **8**, 241–254 (2005).

34. Provenzano, P. P., Inman, D. R., Eliceiri, K. W. & Keely, P. J. Matrix density-induced mechanoregulation of breast cell phenotype, signaling, and gene expression through a FAK-ERK linkage. *Oncogene* **28**, 4326–4343 (2009).

35. Riveline, D. *et al.* Focal contacts as mechanosensors: externally applied local mechanical force induces growth of focal contacts by an mDia1-dependent and ROCK-independent mechanism. *J. Cell Biol.* **153**, 1175–1186 (2001).

36. Webb, D. J., Parsons, J. T. & Horwitz, A. F. Adhesion assembly, disassembly and turnover in migrating cells -- over and over and over again. *Nat. Cell Biol.* **4**, E97-100 (2002).

37. Wozniak, M. A., Desai, R., Solski, P. A., Der, C. J. & Keely, P. J. ROCK-generated contractility regulates breast epithelial cell differentiation in response to the physical properties of a three-dimensional collagen matrix. *J Cell Biol* **163**, 583–595 (2003).

38. Amano, M. *et al.* Phosphorylation and Activation of Myosin by Rho-associated Kinase (Rho-kinase). *J. Biol. Chem.* **271**, 20246–20249 (1996).

39. Kaneko-Kawano, T. *et al.* Dynamic Regulation of Myosin Light Chain Phosphorylation by Rho-kinase. *PLOS ONE* **7**, e39269 (2012).

40. Alexander, N. R. *et al.* Extracellular matrix rigidity promotes invadopodia activity. *Curr. Biol. CB* **18**, 1295–1299 (2008).

41. Connell, L. E. & Helfman, D. M. Myosin light chain kinase plays a role in the regulation of epithelial cell survival. *J. Cell Sci.* **119**, 2269–2281 (2006).

42. Kassianidou, E., Hughes, J. H., Kumar, S. & Wang, Y.-L. Activation of ROCK and MLCK tunes regional stress fiber formation and mechanics via preferential myosin light chain phosphorylation. *Mol. Biol. Cell* **28**, 3832–3843 (2017).

43. Pelham, R. J. & Wang, Y. High Resolution Detection of Mechanical Forces Exerted by Locomoting Fibroblasts on the Substrate. *Mol. Biol. Cell* **10**, 935–945 (1999).

44. Wyckoff, J. B., Pinner, S. E., Gschmeissner, S., Condeelis, J. S. & Sahai, E. ROCK- and Myosin-Dependent Matrix Deformation Enables Protease-Independent Tumor-Cell Invasion In Vivo. *Curr. Biol.* **16**, 1515–1523 (2006).

45. Glentis, A. *et al.* Cancer-associated fibroblasts induce metalloprotease-independent cancer cell invasion of the basement membrane. *Nat. Commun.* **8**, (2017).

46. Provenzano, P. P. *et al.* Collagen reorganization at the tumor-stromal interface facilitates local invasion. *BMC Med.* **4**, 38 (2006).

47. Provenzano, P. P., Inman, D. R., Eliceiri, K. W., Trier, S. M. & Keely, P. J. Contact Guidance Mediated Three-Dimensional Cell Migration is Regulated by Rho/ROCK-Dependent Matrix Reorganization. *Biophys. J.* **95**, 5374–5384 (2008).

48. Riching, K. M. *et al.* 3D Collagen Alignment Limits Protrusions to Enhance Breast Cancer Cell Persistence. *Biophys. J.* **107**, 2546–2558 (2014).

49. Shi, Q. *et al.* Rapid disorganization of mechanically interacting systems of mammary acini. *Proc. Natl. Acad. Sci.* **111**, 658–663 (2014).

50. Carey, S. P. *et al.* Local extracellular matrix alignment directs cellular protrusion dynamics and migration through Rac1 and FAK. *Integr. Biol. Quant. Biosci. Nano Macro* **8**, 821–835 (2016).

51. Han, W. *et al.* Oriented collagen fibers direct tumor cell intravasation. *Proc. Natl. Acad. Sci.* **113**, 11208–11213 (2016).

52. Provenzano, P. P. *et al.* Collagen density promotes mammary tumor initiation and progression. *BMC Med.* **6**, 11 (2008).

53. Wang, T.-H., Hsia, S.-M. & Shieh, T.-M. Lysyl Oxidase and the Tumor Microenvironment. *Int. J. Mol. Sci.* **18**, (2016).

54. Albinger-Hegyi, A. *et al.* Lysyl oxidase expression is an independent marker of prognosis and a predictor of lymph node metastasis in oral and oropharyngeal squamous cell carcinoma (OSCC). *Int. J. Cancer* **126**, 2653–2662 (2010).

55. Erler, J. T. *et al.* Lysyl oxidase is essential for hypoxia-induced metastasis. *Nature* **440**, 1222–1226 (2006).

56. Collighan, R. J. & Griffin, M. Transglutaminase 2 cross-linking of matrix proteins: biological significance and medical applications. *Amino Acids* **36**, 659–670 (2009).

57. Ayinde, O., Wang, Z. & Griffin, M. Tissue transglutaminase induces Epithelial-Mesenchymal-Transition and the acquisition of stem cell like characteristics in colorectal cancer cells. *Oncotarget* **8**, 20025–20041 (2017).

58. Wang, Z. & Griffin, M. The Role of TG2 in Regulating S100A4-Mediated Mammary Tumour Cell Migration. *PLOS ONE* **8**, e57017 (2013).

59. Lee, H.-T. *et al.* Transglutaminase 2 Promotes Migration and Invasion of Lung Cancer Cells. *Oncol. Res.* **26**, 1175–1182 (2018).

60. Fullár, A. *et al.* Remodeling of extracellular matrix by normal and tumor-associated fibroblasts promotes cervical cancer progression. *BMC Cancer* **15**, (2015).

61. Muranen, T. *et al.* Starved epithelial cells uptake extracellular matrix for survival. *Nat. Commun.* **8**, 13989 (2017).

62. Naba, A. *et al.* The matrisome: in silico definition and in vivo characterization by proteomics of normal and tumor extracellular matrices. *Mol. Cell. Proteomics MCP* **11**, M111.014647 (2012).

63. Chang, H. Y. *et al.* Diversity, topographic differentiation, and positional memory in human fibroblasts. *Proc. Natl. Acad. Sci. U. S. A.* **99**, 12877–12882 (2002).

64. Kalluri, R. & Zeisberg, M. Fibroblasts in cancer. *Nat. Rev. Cancer* **6**, 392–401 (2006).

65. Rodemann, H. P. & Müller, G. A. Characterization of human renal fibroblasts in health and disease: II. In vitro growth, differentiation, and collagen synthesis of fibroblasts from kidneys with interstitial fibrosis. *Am. J. Kidney Dis. Off. J. Natl. Kidney Found.* **17**, 684–686 (1991).

66. Lo, C. M., Wang, H. B., Dembo, M. & Wang, Y. L. Cell movement is guided by the rigidity of the substrate. *Biophys. J.* **79**, 144–152 (2000).

67. Sawada, Y. *et al.* Force sensing by mechanical extension of the Src family kinase substrate p130Cas. *Cell* **127**, 1015–1026 (2006).

68. Tamada, M., Sheetz, M. P. & Sawada, Y. Activation of a signaling cascade by cytoskeleton stretch. *Dev. Cell* **7**, 709–718 (2004).

69. Kraning-Rush, C. M., Califano, J. P. & Reinhart-King, C. A. Cellular Traction Stresses Increase with Increasing Metastatic Potential. *PLoS ONE* **7**, (2012).

70. Guo, W., Frey, M. T., Burnham, N. A. & Wang, Y. Substrate rigidity regulates the formation and maintenance of tissues. *Biophys. J.* **90**, 2213–2220 (2006).

71. Reid, S. E. *et al.* Tumor matrix stiffness promotes metastatic cancer cell interaction with the endothelium. *EMBO J.* **36**, 2373–2389 (2017).

72. Schrader, J. *et al.* Matrix Stiffness Modulates Proliferation, Chemotherapeutic Response and Dormancy in Hepatocellular Carcinoma Cells. *Hepatol. Baltim. Md* **53**, 1192–1205 (2011).

73. Ulrich, T. A., de Juan Pardo, E. M. & Kumar, S. The mechanical rigidity of the extracellular matrix regulates the structure, motility, and proliferation of glioma cells. *Cancer Res.* **69**, 4167–4174 (2009).

74. Yeh, Y.-C., Ling, J.-Y., Chen, W.-C., Lin, H.-H. & Tang, M.-J. Mechanotransduction of matrix stiffness in regulation of focal adhesion size and number: reciprocal regulation of caveolin-1 and β1 integrin. *Sci. Rep.* **7**, 15008 (2017).

75. Acerbi, I. *et al.* Human breast cancer invasion and aggression correlates with ECM stiffening and immune cell infiltration. *Integr. Biol. Quant. Biosci. Nano Macro* **7**, 1120–1134 (2015).

76. Georges, P. C. *et al.* Increased stiffness of the rat liver precedes matrix deposition: implications for fibrosis. *Am. J. Physiol. Gastrointest. Liver Physiol.* **293**, G1147-1154 (2007).

77. Cawston, T. E. & Young, D. A. Proteinases involved in matrix turnover during cartilage and bone breakdown. *Cell Tissue Res.* **339**, 221 (2010).

78. Itoh, Y. & Nagase, H. Matrix metalloproteinases in cancer. *Essays Biochem.* **38**, 21–36 (2002).

79. Kessenbrock, K., Plaks, V. & Werb, Z. Matrix Metalloproteinases: Regulators of the Tumor Microenvironment. *Cell* **141**, 52–67 (2010).

80. Page-McCaw, A., Ewald, A. J. & Werb, Z. Matrix metalloproteinases and the regulation of tissue remodelling. *Nat. Rev. Mol. Cell Biol.* **8**, 221–233 (2007).

81. Gialeli, C., Theocharis, A. D. & Karamanos, N. K. Roles of matrix metalloproteinases in cancer progression and their pharmacological targeting. *FEBS J.* **278**, 16–27 (2011).

82. Xu, X. *et al.* Matrix Metalloproteinase-2 Contributes to Cancer Cell Migration on Collagen. *Cancer Res.* **65**, 130–136 (2005).

83. Nabeshima, K., Inoue, T., Shimao, Y. & Sameshima, T. Matrix metalloproteinases in tumor invasion: role for cell migration. *Pathol. Int.* **52**, 255–264 (2002).

84. Zhu, X. *et al.* Galectin-1 knockdown in carcinoma-associated fibroblasts inhibits migration and invasion of human MDA-MB-231 breast cancer cells by modulating MMP-9 expression. *Acta Biochim. Biophys. Sin.* **48**, 462–467 (2016).

85. Endres, M. *et al.* Regulation of matrix metalloproteinases (MMPs) expression and secretion in MDA-MB-231 breast cancer cells by LIM and SH3 protein 1 (LASP1). *Oncotarget* **7**, 64244–64259 (2016).

86. Laghezza Masci, V., Taddei, A. R., Gambellini, G., Giorgi, F. & Fausto, A. M. Microvesicles shed from fibroblasts act as metalloproteinase carriers in a 3-D collagen matrix. *J. Circ. Biomark.* **5**, (2016).

87. Hakulinen, J., Sankkila, L., Sugiyama, N., Lehti, K. & Keski-Oja, J. Secretion of active membrane type 1 matrix metalloproteinase (MMP-14) into extracellular space in microvesicular exosomes. *J. Cell. Biochem.* **105**, 1211–1218 (2008).

88. Angelucci, A. *et al.* Vesicle-associated urokinase plasminogen activator promotes invasion in prostate cancer cell lines. *Clin. Exp. Metastasis* **18**, 163 (2000).

89. Di Vizio, D. *et al.* Large oncosomes in human prostate cancer tissues and in the circulation of mice with metastatic disease. *Am. J. Pathol.* **181**, 1573–1584 (2012).

90. Antonyak, M. A. & Cerione, R. A. Microvesicles as Mediators of Intercellular Communication in Cancer. in *Cancer Cell Signaling* 147–173 (Humana Press, New York, NY, 2014). doi:10.1007/978-1-4939-0856-1_11.

91. Costa-Silva, B. *et al.* Pancreatic cancer exosomes initiate pre-metastatic niche formation in the liver. *Nat. Cell Biol.* **17**, 816–826 (2015).

92. Peinado, H. *et al.* Melanoma exosomes educate bone marrow progenitor cells toward a pro-metastatic phenotype through MET. *Nat. Med.* **18**, 883–891 (2012).

93. Monsky, W. L. *et al.* A Potential Marker Protease of Invasiveness, Separase, Is Localized on Invadopodia of Human Malignant Melanoma Cells. *Cancer Res.* **54**, 5702–5710 (1994).

94. Zegers, M. M. & Friedl, P. Rho GTPases in collective cell migration. *Small GTPases* **5**, e983869 (2014).

95. Artym, V. V., Zhang, Y., Seillier-Moiseiwitsch, F., Yamada, K. M. & Mueller, S. C. Dynamic Interactions of Cortactin and Membrane Type 1 Matrix Metalloproteinase at Invadopodia: Defining the Stages of Invadopodia Formation and Function. *Cancer Res.* **66**, 3034–3043 (2006).

96. Wolf, K. *et al.* Compensation mechanism in tumor cell migration: mesenchymal–amoeboid transition after blocking of pericellular proteolysis. *J. Cell Biol.* **160**, 267–277 (2003).

97. Kraning-Rush, C. M., Carey, S. P., Lampi, M. C. & Reinhart-King, C. A. Microfabricated collagen tracks facilitate single cell metastatic invasion in 3D. *Integr. Biol. Quant. Biosci. Nano Macro* **5**, 606–616 (2013).

98. Carey, S. P. *et al.* Comparative mechanisms of cancer cell migration through 3D matrix and physiological microtracks. *Am. J. Physiol.-Cell Physiol.* **308**, C436–C447 (2015).

99. Gaggioli, C. *et al.* Fibroblast-led collective invasion of carcinoma cells with differing roles for RhoGTPases in leading and following cells. *Nat. Cell Biol.* **9**, 1392–1400 (2007).

100. Parsons, J. T., Horwitz, A. R. & Schwartz, M. A. Cell adhesion: integrating cytoskeletal dynamics and cellular tension. *Nat. Rev. Mol. Cell Biol.* **11**, 633–643 (2010).

101. Vasquez, C. G. & Martin, A. C. Force transmission in epithelial tissues. *Dev. Dyn.* **245**, 361–371 (2016).

102. Sivasankar, S., Gumbiner, B. & Leckband, D. Direct Measurements of Multiple Adhesive Alignments and Unbinding Trajectories between Cadherin Extracellular Domains. *Biophys. J.* **80**, 1758–1768 (2001).

103. Bertocchi, C. *et al.* Nanoscale architecture of cadherin-based cell adhesions. *Nat. Cell Biol.* **19**, 28–37 (2017).

104. Gomez, G. A., McLachlan, R. W. & Yap, A. S. Productive tension: force-sensing and homeostasis of cell–cell junctions. *Trends Cell Biol.* **21**, 499–505 (2011).

105. Martin, A. C., Kaschube, M. & Wieschaus, E. F. Pulsed contractions of an actin-myosin network drive apical constriction. *Nature* **457**, 495–499 (2009).

106. Martin, A. C., Gelbart, M., Fernandez-Gonzalez, R., Kaschube, M. & Wieschaus, E. F. Integration of contractile forces during tissue invagination. *J. Cell Biol.* **188**, 735–749 (2010).

107. Wheelock, M. J., Shintani, Y., Maeda, M., Fukumoto, Y. & Johnson, K. R. Cadherin switching. *J Cell Sci* **121**, 727–735 (2008).

108. Panorchan, P. *et al.* Single-molecule analysis of cadherin-mediated cell-cell adhesion. *J. Cell Sci.* **119**, 66–74 (2006).

109. Labernadie, A. *et al.* A mechanically active heterotypic E-cadherin/N-cadherin adhesion enables fibroblasts to drive cancer cell invasion. *Nat. Cell Biol.* **19**, 224–237 (2017).

110. Fritz, G., Just, I. & Kaina, B. Rho GTPases are over-expressed in human tumors. *Int. J. Cancer* **81**, 682–687 (1999).

111. Burridge, K. & Wennerberg, K. Rho and Rac take center stage. *Cell* **116**, 167–179 (2004).

112. Jaffe, A. B. & Hall, A. Rho GTPases: biochemistry and biology. *Annu. Rev. Cell Dev. Biol.* **21**, 247–269 (2005).

113. Levental, K. R. *et al.* Matrix Crosslinking Forces Tumor Progression by Enhancing Integrin Signaling. *Cell* **139**, 891–906 (2009).

114. Mekhdjian, A. H. *et al.* Integrin-mediated traction force enhances paxillin molecular associations and adhesion dynamics that increase the invasiveness of tumor cells into a three-dimensional extracellular matrix. *Mol. Biol. Cell* **28**, 1467–1488 (2017).

115. Plotnikov, S. V., Pasapera, A. M., Sabass, B. & Waterman, C. M. Force Fluctuations within Focal Adhesions Mediate ECM-Rigidity Sensing to Guide Directed Cell Migration. *Cell* **151**, 1513–1527 (2012).

116. Lintz, M., Muñoz, A. & Reinhart-King, C. A. The Mechanics of Single Cell and Collective Migration of Tumor Cells. *J. Biomech. Eng.* **139**, 0210051–0210059 (2017).

117. Li, L. *et al.* E-cadherin plays an essential role in collective directional migration of large epithelial sheets. *Cell. Mol. Life Sci.* **69**, 2779–2789 (2012).

118. Reffay, M. *et al.* Interplay of RhoA and mechanical forces in collective cell migration driven by leader cells. *Nat. Cell Biol.* **16**, 217–223 (2014).

119. Trepat, X. & Fredberg, J. J. Plithotaxis and emergent dynamics in collective cellular migration. *Trends Cell Biol.* **21**, 638–646 (2011).

120.   Tambe, D. T. *et al.* Collective cell guidance by cooperative intercellular forces. *Nat. Mater.* **10**, 469–475 (2011).

121.   Vishwakarma, M. *et al.* Mechanical interactions among followers determine the emergence of leaders in migrating epithelial cell collectives. *Nat. Commun.* **9**, 3469 (2018).

122.   Sunyer, R. *et al.* Collective cell durotaxis emerges from long-range intercellular force transmission. *Science* **353**, 1157–1161 (2016).

123.   van Helvert, S. & Friedl, P. Strain Stiffening of Fibrillar Collagen during Individual and Collective Cell Migration Identified by AFM Nanoindentation. *ACS Appl. Mater. Interfaces* **8**, 21946–21955 (2016).

124.   Wendler, F. *et al.* Extracellular vesicles swarm the cancer microenvironment: from tumor–stroma communication to drug intervention. *Oncogene* **36**, 877 (2017).

125.   Vader, P., Breakefield, X. O. & Wood, M. J. A. Extracellular vesicles: Emerging targets for cancer therapy. *Trends Mol. Med.* **20**, 385–393 (2014).

126.   Doyle, L. M. & Wang, M. Z. Overview of Extracellular Vesicles, Their Origin, Composition, Purpose, and Methods for Exosome Isolation and Analysis. *Cells* **8**, (2019).

127.   Colombo, M., Raposo, G. & Théry, C. Biogenesis, secretion, and intercellular interactions of exosomes and other extracellular vesicles. *Annu. Rev. Cell Dev. Biol.* **30**, 255–289 (2014).

128.   Minciacchi, V. R., Freeman, M. R. & Di Vizio, D. Extracellular Vesicles in Cancer: Exosomes, Microvesicles and the Emerging Role of Large Oncosomes. *Semin. Cell Dev. Biol.* **40**, 41–51 (2015).

129.   Wolf, P. The Nature and Significance of Platelet Products in Human Plasma. *Br. J. Haematol.* **13**, 269–288 (1967).

130.   Dickhout, A. & Koenen, R. R. Extracellular Vesicles as Biomarkers in Cardiovascular Disease; Chances and Risks. *Front. Cardiovasc. Med.* **5**, (2018).

131.   György, B. *et al.* Detection and isolation of cell-derived microparticles are compromised by protein complexes resulting from shared biophysical parameters. *Blood* **117**, e39-48 (2011).

132. Menck, K. *et al.* Characterisation of tumour-derived microvesicles in cancer patients' blood and correlation with clinical outcome. *J. Extracell. Vesicles* **6**, (2017).

133. Bordeleau, F. *et al.* Microvesicles released from tumor cells disrupt epithelial cell morphology and contractility. *J. Biomech.* **49**, 1272–1279 (2016).

134. Menck, K. *et al.* Tumor-derived microvesicles mediate human breast cancer invasion through differentially glycosylated EMMPRIN. *J. Mol. Cell Biol.* **7**, 143–153 (2015).

135. Huaitong, X. *et al.* Microvesicles releasing by oral cancer cells enhance endothelial cell angiogenesis via Shh/RhoA signaling pathway. *Cancer Biol. Ther.* **18**, 783–791 (2017).

136. Kawamoto, T. *et al.* Tumor-Derived Microvesicles Induce Proangiogenic Phenotype in Endothelial Cells via Endocytosis. *PLOS ONE* **7**, e34045 (2012).

137. Tricarico, C., Clancy, J. & D'Souza-Schorey, C. Biology and biogenesis of shed microvesicles. *Small GTPases* **8**, 220–232 (2016).

138. Sedgwick, A. E., Clancy, J. W., Balmert, M. O. & D'Souza-Schorey, C. Extracellular microvesicles and invadopodia mediate non-overlapping modes of tumor cell invasion. *Sci. Rep.* **5**, 14748 (2015).

139. Li, B., Antonyak, M. A., Zhang, J. & Cerione, R. A. RhoA triggers a specific signaling pathway that generates transforming microvesicles in cancer cells. *Oncogene* **31**, 4740–4749 (2012).

140. Muralidharan-Chari, V. *et al.* ARF6-regulated shedding of tumor cell-derived plasma membrane microvesicles. *Curr. Biol. CB* **19**, 1875–1885 (2009).

141. Gallagher, P. J., Herring, B. P. & Stull, J. T. Myosin light chain kinases. *J. Muscle Res. Cell Motil.* **18**, 1–16 (1997).

142. Franz, C. M., Jones, G. E. & Ridley, A. J. Cell Migration in Development and Disease. *Dev. Cell* **2**, 153–158 (2002).

143. Bear, J. E. & Haugh, J. M. Directed migration of mesenchymal cells: where signaling and the cytoskeleton meet. *Curr. Opin. Cell Biol.* **0**, 74–82 (2014).

144. Xuan, Y. H. *et al.* High-Glucose Inhibits Human Fibroblast Cell Migration in Wound Healing via Repression of bFGF-Regulating JNK Phosphorylation. *PLOS ONE* **9**, e108182 (2014).

145. O'Neill, P. R. *et al.* Membrane Flow Drives an Adhesion-Independent Amoeboid Cell Migration Mode. *Dev. Cell* **46**, 9-22.e4 (2018).

146. Charras, G. & Paluch, E. Blebs lead the way: how to migrate without lamellipodia. *Nat. Rev. Mol. Cell Biol.* **9**, 730–736 (2008).

147. Caswell, P. T. & Zech, T. Actin-Based Cell Protrusion in a 3D Matrix. *Trends Cell Biol.* **28**, 823–834 (2018).

148. Paluch, E. K. & Raz, E. The role and regulation of blebs in cell migration. *Curr. Opin. Cell Biol.* **25**, 582–590 (2013).

149. Pollard, T. D. & Borisy, G. G. Cellular motility driven by assembly and disassembly of actin filaments. *Cell* **112**, 453–465 (2003).

150. Nguyen, L. K., Kholodenko, B. N. & von Kriegsheim, A. Rac1 and RhoA: Networks, loops and bistability. *Small GTPases* **9**, 316–321 (2016).

151. Lorentzen, A., Bamber, J., Sadok, A., Elson-Schwab, I. & Marshall, C. J. An ezrin-rich, rigid uropod-like structure directs movement of amoeboid blebbing cells. *J. Cell Sci.* **124**, 1256–1267 (2011).

152. Pertz, O., Hodgson, L., Klemke, R. L. & Hahn, K. M. Spatiotemporal dynamics of RhoA activity in migrating cells. *Nature* **440**, 1069–1072 (2006).

153. Tucher, C. *et al.* Extracellular Vesicle Subtypes Released From Activated or Apoptotic T-Lymphocytes Carry a Specific and Stimulus-Dependent Protein Cargo. *Front. Immunol.* **9**, (2018).

154. Clancy, J. W., Tricarico, C. J., Marous, D. R. & D'Souza-Schorey, C. Coordinated Regulation of Intracellular Fascin Distribution Governs Tumor Microvesicle Release and Invasive Cell Capacity. *Mol. Cell. Biol.* **39**, (2019).

155. Huang, C., Hays, F. A., Tomasek, J. J., Benyajati, S. & Zhang, X. A. Tetraspanin CD82 interaction with cholesterol promotes extracellular vesicle–mediated release of ezrin to inhibit tumour cell movement. *J. Extracell. Vesicles* **9**, 1692417 (2020).

156.   Charras, G., Hu, C.-K., Coughlin, M. & Mitchison, T. Reassembly of contractile actin cortex in cell blebs. *J. Cell Biol.* **175**, 477–490 (2006).

157.   Kim, S.-Y. *et al.* Coordinated balance of Rac1 and RhoA plays key roles in determining phagocytic appetite. *PLoS ONE* **12**, (2017).

158.   Chauhan, B. K., Lou, M., Zheng, Y. & Lang, R. A. Balanced Rac1 and RhoA activities regulate cell shape and drive invagination morphogenesis in epithelia. *Proc. Natl. Acad. Sci.* **108**, 18289–18294 (2011).

159.   Moorman, J. P., Luu, D., Wickham, J., Bobak, D. A. & Hahn, C. S. A balance of signaling by Rho family small GTPases RhoA, Rac1 and Cdc42 coordinates cytoskeletal morphology but not cell survival. *Oncogene* **18**, 47–57 (1999).

160.   Hart, M. J. *et al.* Cellular transformation and guanine nucleotide exchange activity are catalyzed by a common domain on the dbl oncogene product. *J. Biol. Chem.* **269**, 62–65 (1994).

161.   Olivo, C. *et al.* Distinct involvement of Cdc42 and RhoA GTPases in actin organization and cell shape in untransformed and Dbl oncogene transformed NIH3T3 cells. *Oncogene* **19**, 1428–1436 (2000).

162.   Antonyak, M. A., Wilson, K. F. & Cerione, R. A. R(h)oads to microvesicles. *Small GTPases* **3**, 219–224 (2012).

163.   Taddei, M. L. *et al.* Mesenchymal to amoeboid transition is associated with stem-like features of melanoma cells. *Cell Commun. Signal. CCS* **12**, 24 (2014).

164.   Sonbol, H. S. Extracellular Matrix Remodeling in Human Disease. *J. Microsc. Ultrastruct.* **6**, 123–128 (2018).

165.   Gkretsi, V. & Stylianopoulos, T. Cell Adhesion and Matrix Stiffness: Coordinating Cancer Cell Invasion and Metastasis. *Front. Oncol.* **8**, (2018).

166.   Califano, J. P. & Reinhart-King, C. A. Substrate Stiffness and Cell Area Predict Cellular Traction Stresses in Single Cells and Cells in Contact. *Cell. Mol. Bioeng.* **3**, 68–75 (2010).

167. Kraning-Rush, C. M., Califano, J. P. & Reinhart-King, C. A. Cellular Traction Stresses Increase with Increasing Metastatic Potential. *PLOS ONE* **7**, e32572 (2012).

168. Polte, T. R., Eichler, G. S., Wang, N. & Ingber, D. E. Extracellular matrix controls myosin light chain phosphorylation and cell contractility through modulation of cell shape and cytoskeletal prestress. *Am. J. Physiol. Cell Physiol.* **286**, C518-528 (2004).

169. Paszek, M. J. *et al.* Tensional homeostasis and the malignant phenotype. *Cancer Cell* **8**, 241–254 (2005).

170. Peng, Y. *et al.* ROCK isoforms differentially modulate cancer cell motility by mechanosensing the substrate stiffness. *Acta Biomater.* **88**, 86–101 (2019).

171. Sugimoto, W. *et al.* Substrate rigidity-dependent positive feedback regulation between YAP and ROCK2. *Cell Adhes. Migr.* **12**, 101–108 (2018).

172. Ebata, T. *et al.* Substrate Stiffness Influences Doxorubicin-Induced p53 Activation via ROCK2 Expression. *BioMed Research International* vol. 2017 e5158961 https://www.hindawi.com/journals/bmri/2017/5158961/ (2017).

173. Hoon, J. L., Tan, M. H. & Koh, C.-G. The Regulation of Cellular Responses to Mechanical Cues by Rho GTPases. *Cells* **5**, (2016).

174. Peyton, S. R., Kim, P. D., Ghajar, C. M., Seliktar, D. & Putnam, A. J. The effects of matrix stiffness and RhoA on the phenotypic plasticity of smooth muscle cells in a 3-D biosynthetic hydrogel system. *Biomaterials* **29**, 2597–2607 (2008).

175. Mosier, J. A. *et al.* Extent of Cell Confinement in Microtracks Affects Speed and Results in Differential Matrix Strains. *Biophys. J.* **117**, 1692–1701 (2019).

176. Nishida, K. *et al.* Cigarette smoke disrupts monolayer integrity by altering epithelial cell-cell adhesion and cortical tension. *Am. J. Physiol. - Lung Cell. Mol. Physiol.* **313**, L581–L591 (2017).

177. Goh, N. S. L. *et al.* Increased epithelial permeability in pulmonary fibrosis in relation to disease progression. *Eur. Respir. J.* **38**, 184–190 (2011).

178.   Groschwitz, K. R. & Hogan, S. P. Intestinal Barrier Function: Molecular Regulation and Disease Pathogenesis. *J. Allergy Clin. Immunol.* **124**, 3–22 (2009).

179.   Soler, A. P. *et al.* Increased tight junctional permeability is associated with the development of colon cancer. *Carcinogenesis* **20**, 1425–1431 (1999).

180.   Cui, W. *et al.* Tumor necrosis factor alpha increases epithelial barrier permeability by disrupting tight junctions in Caco-2 cells. *Braz. J. Med. Biol. Res.* **43**, 330–337 (2010).

181.   Brennan, K., Offiah, G., McSherry, E. A. & Hopkins, A. M. Tight Junctions: A Barrier to the Initiation and Progression of Breast Cancer? *Journal of Biomedicine and Biotechnology* vol. 2010 e460607 https://www.hindawi.com/journals/bmri/2010/460607/ (2009).

182.   Ivanov, A. I., Parkos, C. A. & Nusrat, A. Cytoskeletal Regulation of Epithelial Barrier Function During Inflammation. *Am. J. Pathol.* **177**, 512–524 (2010).

183.   VanderBurgh, J. A., Hotchkiss, H., Potharazu, A., Taufalele, P. V. & Reinhart-King, C. A. Substrate stiffness heterogeneities disrupt endothelial barrier integrity in a micropillar model of heterogeneous vascular stiffening. *Integr. Biol. Quant. Biosci. Nano Macro* **10**, 734–746 (2018).

184.   Bordeleau, F. *et al.* Matrix stiffening promotes a tumor vasculature phenotype. *Proc. Natl. Acad. Sci.* **114**, 492–497 (2017).

185.   Huynh, J. *et al.* Age-Related Intimal Stiffening Enhances Endothelial Permeability and Leukocyte Transmigration. *Sci. Transl. Med.* **3**, 112ra122-112ra122 (2011).

186.   Reid, S. E. *et al.* Tumor matrix stiffness promotes metastatic cancer cell interaction with the endothelium. *EMBO J.* **36**, 2373–2389 (2017).

187.   Harney, A. S. *et al.* Real-Time Imaging Reveals Local, Transient Vascular Permeability, and Tumor Cell Intravasation Stimulated by TIE2hi Macrophage–Derived VEGFA. *Cancer Discov.* **5**, 932–943 (2015).

188.   Mulcahy, L. A., Pink, R. C. & Carter, D. R. F. Routes and mechanisms of extracellular vesicle uptake. *J. Extracell. Vesicles* **3**, (2014).

189. Costa Verdera, H., Gitz-Francois, J. J., Schiffelers, R. M. & Vader, P. Cellular uptake of extracellular vesicles is mediated by clathrin-independent endocytosis and macropinocytosis. *J. Control. Release Off. J. Control. Release Soc.* **266**, 100–108 (2017).

190. Toribio, V. *et al.* Development of a quantitative method to measure EV uptake. *Sci. Rep.* **9**, 1–14 (2019).

191. Durak-Kozica, M., Baster, Z., Kubat, K. & Stępień, E. 3D visualization of extracellular vesicle uptake by endothelial cells. *Cell. Mol. Biol. Lett.* **23**, (2018).

192. Ofir-Birin, Y. *et al.* Monitoring Extracellular Vesicle Cargo Active Uptake by Imaging Flow Cytometry. *Front. Immunol.* **9**, (2018).

193. French, K. C., Antonyak, M. A. & Cerione, R. A. Extracellular vesicle docking at the cellular port: Extracellular vesicle binding and uptake. *Semin. Cell Dev. Biol.* **67**, 48–55 (2017).

194. Parolini, I. *et al.* Microenvironmental pH is a key factor for exosome traffic in tumor cells. *J. Biol. Chem.* **284**, 34211–34222 (2009).

195. Montecalvo, A. *et al.* Mechanism of transfer of functional microRNAs between mouse dendritic cells via exosomes. *Blood* **119**, 756–766 (2012).

196. Morelli, A. E. *et al.* Endocytosis, intracellular sorting, and processing of exosomes by dendritic cells. *Blood* **104**, 3257–3266 (2004).

197. Escrevente, C., Keller, S., Altevogt, P. & Costa, J. Interaction and uptake of exosomes by ovarian cancer cells. *BMC Cancer* **11**, 108 (2011).

198. Schneider, D. J. *et al.* Mechanisms and modulation of microvesicle uptake in a model of alveolar cell communication. *J. Biol. Chem.* **292**, 20897–20910 (2017).

199. Mettlen, M., Pucadyil, T., Ramachandran, R. & Schmid, S. L. Dissecting dynamin's role in clathrin-mediated endocytosis. *Biochem. Soc. Trans.* **37**, 1022–1026 (2009).

200. Sundborger, A. C. & Hinshaw, J. E. Regulating dynamin dynamics during endocytosis. *F1000Prime Rep.* **6**, (2014).

201. Dai, J., Ting-Beall, H. P. & Sheetz, M. P. The secretion-coupled endocytosis correlates with membrane tension changes in RBL 2H3 cells. *J. Gen. Physiol.* **110**, 1–10 (1997).

202. Raucher, D. & Sheetz, M. P. Membrane expansion increases endocytosis rate during mitosis. *J. Cell Biol.* **144**, 497–506 (1999).

203. Mandal, K. *et al.* Soft hyaluronic gel promotes cell spreading, stress fibers, focal adhesion, membrane tension by phosphoinositide signaling, not traction force. *ACS Nano* **13**, 203–214 (2019).

204. Nambiar, R., McConnell, R. E. & Tyska, M. J. Control of cell membrane tension by myosin-I. *Proc. Natl. Acad. Sci.* **106**, 11972–11977 (2009).

205. Thottacherry, J. J. *et al.* Mechanochemical feedback control of dynamin independent endocytosis modulates membrane tension in adherent cells. *Nat. Commun.* **9**, 1–14 (2018).

206. Narumiya, S., Tanji, M. & Ishizaki, T. Rho signaling, ROCK and mDia1, in transformation, metastasis and invasion. *Cancer Metastasis Rev.* **28**, 65–76 (2009).

207. Paňková, K., Rösel, D., Novotný, M. & Brábek, J. The molecular mechanisms of transition between mesenchymal and amoeboid invasiveness in tumor cells. *Cell. Mol. Life Sci.* **67**, 63–71 (2010).

208. Kreger, B. T., Dougherty, A. L., Greene, K. S., Cerione, R. A. & Antonyak, M. A. Microvesicle Cargo and Function Changes upon Induction of Cellular Transformation. *J. Biol. Chem.* **291**, 19774–19785 (2016).

209. Zhao, X.-P. *et al.* Membrane microvesicles as mediators for melanoma-fibroblasts communication: roles of the VCAM-1/VLA-4 axis and the ERK1/2 signal pathway. *Cancer Lett.* **360**, 125–133 (2015).

210. Lee, H., Zhang, D., Zhu, Z., Dela Cruz, C. S. & Jin, Y. Epithelial cell-derived microvesicles activate macrophages and promote inflammation via microvesicle-containing microRNAs. *Sci. Rep.* **6**, 35250 (2016).

211. Kim, J.-H. & Asthagiri, A. R. Matrix stiffening sensitizes epithelial cells to EGF and enables the loss of contact inhibition of proliferation. *J Cell Sci* **124**, 1280–1287 (2011).

212. LaValley, D. J. *et al.* Matrix stiffness enhances VEGFR-2 internalization, signaling, and proliferation in endothelial cells. *Converg. Sci. Phys. Oncol.* **3**, 044001 (2017).

213. Fang, T. *et al.* Tumor-derived exosomal miR-1247-3p induces cancer-associated fibroblast activation to foster lung metastasis of liver cancer. *Nat. Commun.* **9**, 191 (2018).

214. Attieh, Y. *et al.* Cancer-associated fibroblasts lead tumor invasion through integrin-β3–dependent fibronectin assembly. *J. Cell Biol.* **216**, 3509–3520 (2017).

215. Schillaci, O. *et al.* Exosomes from metastatic cancer cells transfer amoeboid phenotype to non-metastatic cells and increase endothelial permeability: their emerging role in tumor heterogeneity. *Sci. Rep.* **7**, 1–15 (2017).

216. Webster, K. A. Evolution of the coordinate regulation of glycolytic enzyme genes by hypoxia. *J. Exp. Biol.* **206**, 2911–2922 (2003).

217. Hay, N. Reprogramming glucose metabolism in cancer: can it be exploited for cancer therapy? *Nat. Rev. Cancer* **16**, 635–649 (2016).

218. Ge, T. *et al.* The Role of the Pentose Phosphate Pathway in Diabetes and Cancer. *Front. Endocrinol.* **11**, (2020).

219. Cluntun, A. A., Lukey, M. J., Cerione, R. A. & Locasale, J. W. Glutamine Metabolism in Cancer: Understanding the Heterogeneity. *Trends Cancer* **3**, 169–180 (2017).

220. Paudel, B. B. & Quaranta, V. Metabolic plasticity meets gene regulation. *Proc. Natl. Acad. Sci. U. S. A.* **116**, 3370–3372 (2019).

221. Koczula, K. M. *et al.* Metabolic plasticity in CLL: adaptation to the hypoxic niche. *Leukemia* **30**, 65–73 (2016).

222. Jia, D. *et al.* Elucidating cancer metabolic plasticity by coupling gene regulation with metabolic pathways. *Proc. Natl. Acad. Sci.* **116**, 3909–3918 (2019).

223. Warburg, O. The Metabolism of Carcinoma Cells. *J. Cancer Res.* **9**, 148–163 (1925).

224. Ward, P. S. & Thompson, C. B. Metabolic Reprogramming: A Cancer Hallmark Even Warburg Did Not Anticipate. *Cancer Cell* **21**, 297–308 (2012).

225. Vaupel, P., Schmidberger, H. & Mayer, A. The Warburg effect: essential part of metabolic reprogramming and central contributor to cancer progression. *Int. J. Radiat. Biol.* **95**, 912–919 (2019).

226. Elstrom, R. L. *et al.* Akt Stimulates Aerobic Glycolysis in Cancer Cells. *Cancer Res.* **64**, 3892–3899 (2004).

227. Vander Heiden, M. G., Cantley, L. C. & Thompson, C. B. Understanding the Warburg Effect: The Metabolic Requirements of Cell Proliferation. *Science* **324**, 1029–1033 (2009).

228. Shim, H. *et al.* c-Myc transactivation of LDH-A: implications for tumor metabolism and growth. *Proc. Natl. Acad. Sci. U. S. A.* **94**, 6658–6663 (1997).

229. van Zijl, F., Krupitza, G. & Mikulits, W. Initial steps of metastasis: Cell invasion and endothelial transmigration. *Mutat. Res. Mutat. Res.* **728**, 23–34 (2011).

230. Zanotelli, M. R. *et al.* Regulation of ATP utilization during metastatic cell migration by collagen architecture. *Mol. Biol. Cell* **29**, 1–9 (2018).

231. Giampieri, S. *et al.* Localized and reversible TGFbeta signalling switches breast cancer cells from cohesive to single cell motility. *Nat. Cell Biol.* **11**, 1287–1296 (2009).

232. Boekhorst, V. te *et al.* Calpain-2 regulates hypoxia/HIF-induced amoeboid reprogramming and metastasis. *bioRxiv* 2020.01.06.892497 (2020) doi:10.1101/2020.01.06.892497.

233. Chung, Y.-C. *et al.* Rab11 collaborates E-cadherin to promote collective cell migration and indicates a poor prognosis in colorectal carcinoma. *Eur. J. Clin. Invest.* **46**, 1002–1011 (2016).

234. Friedl, P. & Wolf, K. Tumour-cell invasion and migration: diversity and escape mechanisms. *Nat. Rev. Cancer* **3**, 362–374 (2003).

235. Emad, A. *et al.* Superior breast cancer metastasis risk stratification using an epithelial-mesenchymal-amoeboid transition gene signature. *Breast Cancer Res.* **22**, 74 (2020).

236. Tolde, O. *et al.* Quantitative phase imaging unravels new insight into dynamics of mesenchymal and amoeboid cancer cell invasion. *Sci. Rep.* **8**, 12020 (2018).

237. Parri, M., Taddei, M. L., Bianchini, F., Calorini, L. & Chiarugi, P. EphA2 reexpression prompts invasion of melanoma cells shifting from mesenchymal to amoeboid-like motility style. *Cancer Res.* **69**, 2072–2081 (2009).

238.   Haga, H., Irahara, C., Kobayashi, R., Nakagaki, T. & Kawabata, K. Collective movement of epithelial cells on a collagen gel substrate. *Biophys. J.* **88**, 2250–2256 (2005).

239.   Friedl, P. & Alexander, S. Cancer Invasion and the Microenvironment: Plasticity and Reciprocity. *Cell* **147**, 992–1009 (2011).

240.   Polacheck, W. J., Zervantonakis, I. K. & Kamm, R. D. Tumor cell migration in complex microenvironments. *Cell. Mol. Life Sci. CMLS* **70**, 1335–1356 (2013).

241.   Friedl, P. & Wolf, K. Plasticity of cell migration: a multiscale tuning model. *J. Cell Biol.* **188**, 11–19 (2010).

242.   Aiello, N. M. *et al.* EMT subtype influences epithelial plasticity and mode of cell migration. *Dev. Cell* **45**, 681-695.e4 (2018).

243.   Wang, Y. & Zhou, B. P. Epithelial-mesenchymal Transition---A Hallmark of Breast Cancer Metastasis. *Cancer Hallm.* **1**, 38–49 (2013).

244.   Vincent-Salomon, A. & Thiery, J. P. Host microenvironment in breast cancer development: Epithelial–mesenchymal transition in breast cancer development. *Breast Cancer Res.* **5**, 101–106 (2003).

245.   Shiraishi, T. *et al.* Glycolysis is the primary bioenergetic pathway for cell motility and cytoskeletal remodeling in human prostate and breast cancer cells. *Oncotarget* **6**, 130–143 (2015).

246.   Berx, G., Raspé, E., Christofori, G., Thiery, J. P. & Sleeman, J. P. Pre-EMTing metastasis? Recapitulation of morphogenetic processes in cancer. *Clin. Exp. Metastasis* **24**, 587–597 (2007).

247.   Kim, N. H. *et al.* Snail reprograms glucose metabolism by repressing phosphofructokinase PFKP allowing cancer cell survival under metabolic stress. *Nat. Commun.* **8**, 14374 (2017).

248.   Cooke, V. G. *et al.* Pericyte depletion results in hypoxia-associated epithelial-to-mesenchymal transition and metastasis mediated by met signaling pathway. *Cancer Cell* **21**, 66–81 (2012).

249.   Yang, M.-H. *et al.* Direct regulation of TWIST by HIF-1alpha promotes metastasis. *Nat. Cell Biol.* **10**, 295–305 (2008).

250.   LeBleu, V. S. *et al.* PGC-1α mediates mitochondrial biogenesis and oxidative phosphorylation in cancer cells to promote metastasis. *Nat. Cell Biol.* **16**, 992–1003 (2014).

251.   Kelley, L. C. *et al.* Adaptive F-Actin Polymerization and Localized ATP Production Drive Basement Membrane Invasion in the Absence of MMPs. *Dev. Cell* **48**, 313-328.e8 (2019).

252.   Cunniff, B., McKenzie, A. J., Heintz, N. H. & Howe, A. K. AMPK activity regulates trafficking of mitochondria to the leading edge during cell migration and matrix invasion. *Mol. Biol. Cell* **27**, 2662–2674 (2016).

253.   Porporato, P. E. *et al.* A mitochondrial switch promotes tumor metastasis. *Cell Rep.* **8**, 754–766 (2014).

254.   Yoshida, S. *et al.* Molecular chaperone TRAP1 regulates a metabolic switch between mitochondrial respiration and aerobic glycolysis. *Proc. Natl. Acad. Sci.* **110**, E1604–E1612 (2013).

255.   Krakhmal, N. V., Zavyalova, M. V., Denisov, E. V., Vtorushin, S. V. & Perelmuter, V. M. Cancer Invasion: Patterns and Mechanisms. *Acta Naturae* **7**, 17–28 (2015).

256.   Duda, D. G. *et al.* Malignant cells facilitate lung metastasis by bringing their own soil. *Proc. Natl. Acad. Sci.* (2010) doi:10.1073/pnas.1016234107.

257.   Klameth, L. *et al.* Small cell lung cancer: model of circulating tumor cell tumorospheres in chemoresistance. *Sci. Rep.* **7**, 5337 (2017).

258.   Plou, J. *et al.* From individual to collective 3D cancer dissemination: roles of collagen concentration and TGF-β. *Sci. Rep.* **8**, 12723 (2018).

259.   Aceto, N. *et al.* Circulating Tumor Cell Clusters are Oligoclonal Precursors of Breast Cancer Metastasis. *Cell* **158**, 1110–1122 (2014).

260.   Wu, J.-S. *et al.* Cathepsin B defines leader cells during the collective invasion of salivary adenoid cystic carcinoma. *Int. J. Oncol.* **54**, 1233–1244 (2019).

261.   Wolf, K. *et al.* Multi-step pericellular proteolysis controls the transition from individual to collective cancer cell invasion. *Nat. Cell Biol.* **9**, 893–904 (2007).

262. Glentis, A. *et al.* Cancer-associated fibroblasts induce metalloprotease-independent cancer cell invasion of the basement membrane. *Nat. Commun.* **8**, 924 (2017).

263. Shih, W. & Yamada, S. N-cadherin as a key regulator of collective cell migration in a 3D environment. *Cell Adhes. Migr.* **6**, 513–517 (2012).

264. Elisha, Y., Kalchenko, V., Kuznetsov, Y. & Geiger, B. Dual role of E-cadherin in the regulation of invasive collective migration of mammary carcinoma cells. *Sci. Rep.* **8**, 4986 (2018).

265. Zhang, J. *et al.* Energetic regulation of coordinated leader–follower dynamics during collective invasion of breast cancer cells. *Proc. Natl. Acad. Sci.* **116**, 7867–7872 (2019).

266. Commander, R. *et al.* Subpopulation targeting of pyruvate dehydrogenase and GLUT1 decouples metabolic heterogeneity during collective cancer cell invasion. *Nat. Commun.* **11**, 1–17 (2020).

267. De Bock, K. *et al.* Role of PFKFB3-Driven Glycolysis in Vessel Sprouting. *Cell* **154**, 651–663 (2013).

268. Cruys, B. *et al.* Glycolytic regulation of cell rearrangement in angiogenesis. *Nat. Commun.* **7**, 12240 (2016).

269. Carmeliet, P., De Smet, F., Loges, S. & Mazzone, M. Branching morphogenesis and antiangiogenesis candidates: tip cells lead the way. *Nat. Rev. Clin. Oncol.* **6**, 315–326 (2009).

270. Sotgia, F. *et al.* Caveolin-1 and Cancer Metabolism in the Tumor Microenvironment: Markers, Models, and Mechanisms. *Annu. Rev. Pathol. Mech. Dis.* **7**, 423–467 (2012).

271. Mougeolle, A. *et al.* Oxidative Stress Induces Caveolin 1 Degradation and Impairs Caveolae Functions in Skeletal Muscle Cells. *PLOS ONE* **10**, e0122654 (2015).

272. Pavlides, S. *et al.* The reverse Warburg effect: aerobic glycolysis in cancer associated fibroblasts and the tumor stroma. *Cell Cycle Georget. Tex* **8**, 3984–4001 (2009).

273. Martinez-Outschoorn, U. E. *et al.* Anti-estrogen resistance in breast cancer is induced by the tumor microenvironment and can be overcome by inhibiting mitochondrial function in epithelial cancer cells. *Cancer Biol. Ther.* **12**, 924–938 (2011).

274. Sedgwick, A. E., Clancy, J. W., Olivia Balmert, M. & D'Souza-Schorey, C. Extracellular microvesicles and invadopodia mediate non-overlapping modes of tumor cell invasion. *Sci. Rep.* **5**, 14748 (2015).

275. Begum, H. M. *et al.* Spatial Regulation of Mitochondrial Heterogeneity by Stromal Confinement in Micropatterned Tumor Models. *Sci. Rep.* **9**, 11187 (2019).

276. Otranto, M. *et al.* The role of the myofibroblast in tumor stroma remodeling. *Cell Adhes. Migr.* **6**, 203–219 (2012).

277. Menk, A. V. *et al.* Early TCR Signaling Induces Rapid Aerobic Glycolysis Enabling Distinct Acute T Cell Effector Functions. *Cell Rep.* **22**, 1509–1521 (2018).

278. Bantug, G. R., Galluzzi, L., Kroemer, G. & Hess, C. The spectrum of T cell metabolism in health and disease. *Nat. Rev. Immunol.* **18**, 19–34 (2018).

279. Lim, A. R., Rathmell, W. K. & Rathmell, J. C. The tumor microenvironment as a metabolic barrier to effector T cells and immunotherapy. *eLife* **9**, e55185 (2020).

280. Macintyre, A. N. *et al.* The Glucose Transporter Glut1 Is Selectively Essential for CD4 T Cell Activation and Effector Function. *Cell Metab.* **20**, 61–72 (2014).

281. Angiari, S. *et al.* Regulation of T cell activation and pathogenicity by dimeric pyruvate kinase M2 (PKM2). *J. Immunol.* **202**, 125.11-125.11 (2019).

282. Cavalli, L. R., Varella-Garcia, M. & Liang, B. C. Diminished tumorigenic phenotype after depletion of mitochondrial DNA. *Cell Growth Differ. Mol. Biol. J. Am. Assoc. Cancer Res.* **8**, 1189–1198 (1997).

283. Morais, R. *et al.* Tumor-forming ability in athymic nude mice of human cell lines devoid of mitochondrial DNA. *Cancer Res.* **54**, 3889–3896 (1994).

284. Chen, E. I. *et al.* Adaptation of energy metabolism in breast cancer brain metastases. *Cancer Res.* **67**, 1472–1486 (2007).

285. Porporato, P. E. & Sonveaux, P. Paving the way for therapeutic prevention of tumor metastasis with agents targeting mitochondrial superoxide. *Mol. Cell. Oncol.* **2**, e968043 (2015).

286. Li, A. M. *et al.* Metabolic Profiling Reveals a Dependency of Human Metastatic Breast Cancer on Mitochondrial Serine and One-Carbon Unit Metabolism. *Mol. Cancer Res.* **18**, 599–611 (2020).

287. Rademaker, G. *et al.* Myoferlin Contributes to the Metastatic Phenotype of Pancreatic Cancer Cells by Enhancing Their Migratory Capacity through the Control of Oxidative Phosphorylation. *Cancers* **11**, (2019).

288. Zhang, T. *et al.* A small molecule targeting myoferlin exerts promising anti-tumor effects on breast cancer. *Nat. Commun.* **9**, 3726 (2018).

289. Davis, R. T. *et al.* Transcriptional diversity and bioenergetic shift in human breast cancer metastasis revealed by single-cell RNA sequencing. *Nat. Cell Biol.* **22**, 310–320 (2020).

290. Huang, M., Xiong, H., Luo, D., Xu, B. & Liu, H. CSN5 upregulates glycolysis to promote hepatocellular carcinoma metastasis via stabilizing the HK2 protein. *Exp. Cell Res.* **388**, 111876 (2020).

291. Wiel, C. *et al.* BACH1 Stabilization by Antioxidants Stimulates Lung Cancer Metastasis. *Cell* **178**, 330-345.e22 (2019).

292. Dupuy, F. *et al.* PDK1-Dependent Metabolic Reprogramming Dictates Metastatic Potential in Breast Cancer. *Cell Metab.* **22**, 577–589 (2015).

293. Kim, H. M., Jung, W. H. & Koo, J. S. Site-specific metabolic phenotypes in metastatic breast cancer. *J. Transl. Med.* **12**, 354 (2014).

294. Stein, E. M. *et al.* Enasidenib in mutant IDH2 relapsed or refractory acute myeloid leukemia. *Blood* **130**, 722–731 (2017).

295. Saraei, P., Asadi, I., Kakar, M. A. & Moradi-Kor, N. The beneficial effects of metformin on cancer prevention and therapy: a comprehensive review of recent advances. *Cancer Manag. Res.* **11**, 3295–3313 (2019).

296. El-Mir, M. Y. *et al.* Dimethylbiguanide inhibits cell respiration via an indirect effect targeted on the respiratory chain complex I. *J. Biol. Chem.* **275**, 223–228 (2000).

297.   Mediani, L. *et al.* Reversal of the glycolytic phenotype of primary effusion lymphoma cells by combined targeting of cellular metabolism and PI3K/Akt/ mTOR signaling. *Oncotarget* **7**, 5521–5537 (2016).

298.   Raez, L. E. *et al.* A phase I dose-escalation trial of 2-deoxy-D-glucose alone or combined with docetaxel in patients with advanced solid tumors. *Cancer Chemother. Pharmacol.* **71**, 523–530 (2013).

299.   Chapiro, J. *et al.* Systemic delivery of microencapsulated 3-bromopyruvate for the therapy of pancreatic cancer. *Clin. Cancer Res. Off. J. Am. Assoc. Cancer Res.* **20**, 6406–6417 (2014).

300.   Baggstrom, M. Q. *et al.* A phase II study of AT-101 (gossypol) in chemotherapy-sensitive recurrent extensive stage small cell lung cancer (ES-SCLC). *J. Thorac. Oncol. Off. Publ. Int. Assoc. Study Lung Cancer* **6**, 1757–1760 (2011).

301.   Beloueche-Babari, M. *et al.* Monocarboxylate transporter 1 blockade with AZD3965 inhibits lipid biosynthesis and increases tumour immune cell infiltration. *Br. J. Cancer* **122**, 895–903 (2020).

302.   Lycan, T. W. *et al.* A Phase II Clinical Trial of CPI-613 in Patients with Relapsed or Refractory Small Cell Lung Carcinoma. *PloS One* **11**, e0164244 (2016).

303.   Velpula, K. K., Bhasin, A., Asuthkar, S. & Tsung, A. J. Combined targeting of PDK1 and EGFR triggers regression of glioblastoma by reversing the Warburg effect. *Cancer Res.* **73**, 7277–7289 (2013).

304.   Chu, Q. S.-C. *et al.* A phase I open-labeled, single-arm, dose-escalation, study of dichloroacetate (DCA) in patients with advanced solid tumors. *Invest. New Drugs* **33**, 603–610 (2015).

305.   Moore, Z. *et al.* NAMPT inhibition sensitizes pancreatic adenocarcinoma cells to tumor-selective, PAR-independent metabolic catastrophe and cell death induced by β-lapachone. *Cell Death Dis.* **6**, e1599 (2015).

306.   Golub, D. *et al.* Mutant Isocitrate Dehydrogenase Inhibitors as Targeted Cancer Therapeutics. *Front. Oncol.* **9**, (2019).

307.   DiNardo, C. D. *et al.* Durable Remissions with Ivosidenib in IDH1-Mutated Relapsed or Refractory AML. *N. Engl. J. Med.* **378**, 2386–2398 (2018).

308. Amadori, D. *et al.* Modulating effect of lonidamine on response to doxorubicin in metastatic breast cancer patients: results from a multicenter prospective randomized trial. *Breast Cancer Res. Treat.* **49**, 209–217 (1998).

309. Nath, K. *et al.* Lonidamine induces intracellular tumor acidification and ATP depletion in breast, prostate and ovarian cancer xenografts and potentiates response to doxorubicin. *NMR Biomed.* **28**, 281–290 (2015).

310. Spencer, A. *et al.* A phase 1 clinical trial evaluating marizomib, pomalidomide and low-dose dexamethasone in relapsed and refractory multiple myeloma (NPI-0052-107): final study results. *Br. J. Haematol.* **180**, 41–51 (2018).

311. Raninga, P. V. *et al.* Marizomib suppresses triple-negative breast cancer via proteasome and oxidative phosphorylation inhibition. *Theranostics* **10**, 5259–5275 (2020).

312. Gee, J. R. *et al.* A Phase II Randomized, Double-blind, Presurgical Trial of Polyphenon E in Bladder Cancer Patients to Evaluate Pharmacodynamics and Bladder Tissue Biomarkers. *Cancer Prev. Res. Phila. Pa* **10**, 298–307 (2017).

313. Berman, A. Y., Motechin, R. A., Wiesenfeld, M. Y. & Holz, M. K. The therapeutic potential of resveratrol: a review of clinical trials. *NPJ Precis. Oncol.* **1**, (2017).

314. Sato, A., Asano, T., Ito, K. & Asano, T. Ritonavir interacts with bortezomib to enhance protein ubiquitination and histone acetylation synergistically in renal cancer cells. *Urology* **79**, 966.e13–21 (2012).

315. Vander Heiden, M. G. *et al.* Identification of small molecule inhibitors of pyruvate kinase M2. *Biochem. Pharmacol.* **79**, 1118–1124 (2010).

316. Clem, B. F. *et al.* Targeting 6-phosphofructo-2-kinase (PFKFB3) as a therapeutic strategy against cancer. *Mol. Cancer Ther.* **12**, 1461–1470 (2013).

317. Redman, R. A., Pohlmann, P. R., Kurman, M. R., Tapolsky, G. & Chesney, J. A. A phase I, dose-escalation, multi-center study of PFK-158 in patients with advanced solid malignancies explores a first-in-man inhbibitor of glycolysis. *J. Clin. Oncol.* **33**, TPS2606–TPS2606 (2015).

318. Clem, B. *et al.* Small-molecule inhibition of 6-phosphofructo-2-kinase activity suppresses glycolytic flux and tumor growth. *Mol. Cancer Ther.* **7**, 110–120 (2008).

319. Ocaña, M. C., Martínez-Poveda, B., Marí-Beffa, M., Quesada, A. R. & Medina, M. Á. Fasentin diminishes endothelial cell proliferation, differentiation and invasion in a glucose metabolism-independent manner. *Sci. Rep.* **10**, 6132 (2020).

320. Wang, Y. *et al.* GEN-27, a Newly Synthetic Isoflavonoid, Inhibits the Proliferation of Colon Cancer Cells in Inflammation Microenvironment by Suppressing NF-κB Pathway. *Mediators Inflamm.* **2016**, 2853040 (2016).

321. Kumagai, S., Narasaki, R. & Hasumi, K. Glucose-dependent active ATP depletion by koningic acid kills high-glycolytic cells. *Biochem. Biophys. Res. Commun.* **365**, 362–368 (2008).

322. Ozerlat, I. Targeted therapy of glucose uptake via GLUT1 kills RCC cells. *Nat. Rev. Urol.* **8**, 471–471 (2011).

323. Liu, Y. *et al.* A small-molecule inhibitor of glucose transporter 1 downregulates glycolysis, induces cell-cycle arrest, and inhibits cancer cell growth in vitro and in vivo. *Mol. Cancer Ther.* **11**, 1672–1682 (2012).

324. Heredia, V. *et al.* AG-120, a novel IDH1 targeted molecule, inhibits invasion and migration of chondrosarcoma cells in vitro. *Ann. Oncol.* **28**, v538 (2017).

325. Kong, S. C. *et al.* Monocarboxylate Transporters MCT1 and MCT4 Regulate Migration and Invasion of Pancreatic Ductal Adenocarcinoma Cells. *Pancreas* **45**, 1036–1047 (2016).

326. Gao, L. *et al.* CPI-613 rewires lipid metabolism to enhance pancreatic cancer apoptosis via the AMPK-ACC signaling. *J. Exp. Clin. Cancer Res. CR* **39**, (2020).

327. National Library of Medicine (U.S.). *A Study of CPI-613 for Patients With Relapsed or Refractory Burkitt Lymphoma/Leukemia or High-Grade B-Cell Lymphoma With High-Risk Translocations.* https://clinicaltrials.gov/ct2/show/NCT03793140 (2019).

328. Alimova, I. N. *et al.* Metformin inhibits breast cancer cell growth, colony formation and induces cell cycle arrest in vitro. *Cell Cycle Georget. Tex* **8**, 909–915 (2009).

329. Jang, S. Y. *et al.* Metformin inhibits tumor cell migration via down-regulation of MMP9 in tamoxifen-resistant breast cancer cells. *Anticancer Res.* **34**, 4127–4134 (2014).

330. Huang, Q. *et al.* Novel ginsenoside derivative 20(S)-Rh2E2 suppresses tumor growth and metastasis in vivo and in vitro via intervention of cancer cell energy metabolism. *Cell Death Dis.* **11**, 1–19 (2020).

331. Quail, D. & Joyce, J. Microenvironmental regulation of tumor progression and metastasis. *Nat. Med.* **19**, 1423–1437 (2013).

332. Webber, J., Steadman, R., Mason, M. D., Tabi, Z. & Clayton, A. Cancer Exosomes Trigger Fibroblast to Myofibroblast Differentiation. *Cancer Res.* **70**, 9621–9630 (2010).

333. Suetsugu, A. *et al.* Imaging exosome transfer from breast cancer cells to stroma at metastatic sites in orthotopic nude-mouse models. *Adv. Drug Deliv. Rev.* **65**, 383–390 (2013).

334. Song, Y. H. *et al.* Breast cancer-derived extracellular vesicles stimulate myofibroblast differentiation and pro-angiogenic behavior of adipose stem cells. *Matrix Biol.* **60**, 190–205 (2017).

335. Raposo, G. & Stoorvogel, W. Extracellular vesicles: Exosomes, microvesicles, and friends. *J Cell Biol* **200**, 373–383 (2013).

336. Balaj, L. *et al.* Tumour microvesicles contain retrotransposon elements and amplified oncogene sequences. *Nat. Commun.* **2**, 180 (2011).

337. Erdogan, B. & Webb, D. J. Cancer-associated fibroblasts modulate growth factor signaling and extracellular matrix remodeling to regulate tumor metastasis. *Biochem. Soc. Trans.* **45**, 229–236 (2017).

338. El-Mohri, H., Wu, Y., Mohanty, S. & Ghosh, G. Impact of matrix stiffness on fibroblast function. *Mater. Sci. Eng. C* **74**, 146–151 (2017).

339. Marinković, A., Mih, J. D., Park, J.-A., Liu, F. & Tschumperlin, D. J. Improved throughput traction microscopy reveals pivotal role for matrix stiffness in fibroblast contractility and TGF-β responsiveness. *Am. J. Physiol. Lung Cell. Mol. Physiol.* **303**, L169-180 (2012).

340. Califano, J. P. & Reinhart-King, C. A. A Balance of Substrate Mechanics and Matrix Chemistry Regulates Endothelial Cell Network Assembly. *Cell. Mol. Bioeng.* **1**, 122 (2008).

341. Reinhart-King, C. A., Dembo, M. & Hammer, D. A. The Dynamics and Mechanics of Endothelial Cell Spreading. *Biophys. J.* **89**, 676–689 (2005).

342. Dembo, M. & Wang, Y. L. Stresses at the cell-to-substrate interface during locomotion of fibroblasts. *Biophys. J.* **76**, 2307–2316 (1999).

343. Mason, B. N., Starchenko, A., Williams, R. M., Bonassar, L. J. & Reinhart-King, C. A. Tuning 3D Collagen Matrix Stiffness Independently of Collagen Concentration Modulates Endothelial Cell Behavior. *Acta Biomater.* **9**, 4635–4644 (2013).

344. Feng, Q. *et al.* A class of extracellular vesicles from breast cancer cells activates VEGF receptors and tumour angiogenesis. *Nat. Commun.* **8**, 14450 (2017).

345. Chen, C. S., Mrksich, M., Huang, S., Whitesides, G. M. & Ingber, D. E. Geometric Control of Cell Life and Death. *Science* **276**, 1425–1428 (1997).

346. Folkman, J. & Moscona, A. Role of cell shape in growth control. *Nature* **273**, 345–349 (1978).

347. Sarker, B. *et al.* Evaluation of Fibroblasts Adhesion and Proliferation on Alginate-Gelatin Crosslinked Hydrogel. *PLoS ONE* **9**, (2014).

348. Wakatsuki, T., Wysolmerski, R. B. & Elson, E. L. Mechanics of cell spreading: role of myosin II. *J. Cell Sci.* **116**, 1617–1625 (2003).

349. Hinz, B., Celetta, G., Tomasek, J. J., Gabbiani, G. & Chaponnier, C. Alpha-Smooth Muscle Actin Expression Upregulates Fibroblast Contractile Activity. *Mol. Biol. Cell* **12**, 2730–2741 (2001).

350. Nishishita, R. *et al.* Expression of cancer-associated fibroblast markers in advanced colorectal cancer. *Oncol. Lett.* **15**, 6195–6202 (2018).

351. Shinde, A. V., Humeres, C. & Frangogiannis, N. G. The role of α-smooth muscle actin in fibroblast-mediated matrix contraction and remodeling. *Biochim. Biophys. Acta* **1863**, 298–309 (2017).

352. Rhee, S. Fibroblasts in three dimensional matrices: cell migration and matrix remodeling. *Exp. Mol. Med.* **41**, 858–865 (2009).

353. Malandrino, A., Mak, M., Kamm, R. D. & Moeendarbary, E. Complex mechanics of the heterogeneous extracellular matrix in cancer. *Extreme Mech. Lett.* **21**, 25–34 (2018).

354. Yuan, Y. Spatial Heterogeneity in the Tumor Microenvironment. *Cold Spring Harb. Perspect. Med.* **6**, a026583 (2016).

355. Denis, M. *et al.* Correlating Tumor Stiffness with Immunohistochemical Subtypes of Breast Cancers: Prognostic Value of Comb-Push Ultrasound Shear Elastography for Differentiating Luminal Subtypes. *PLoS ONE* **11**, (2016).

356. Baker, E. L., Bonnecaze, R. T. & Zaman, M. H. Extracellular matrix stiffness and architecture govern intracellular rheology in cancer. *Biophys. J.* **97**, 1013–1021 (2009).

357. Patel, S., Wetie, A. G. N., Darie, C. C. & Clarkson, B. D. Cancer Secretomes and Their Place in Supplementing Other Hallmarks of Cancer. in *Advancements of Mass Spectrometry in Biomedical Research* (eds. Woods, A. G. & Darie, C. C.) 409–442 (Springer International Publishing, 2014). doi:10.1007/978-3-319-06068-2_20.

358. Steenbeek, S. C. *et al.* Cancer cells copy migratory behavior and exchange signaling networks via extracellular vesicles. *EMBO J.* e8357 (2018) doi:10.15252/embj.201798357.

359. Sung, B. H. & Weaver, A. M. Exosome secretion promotes chemotaxis of cancer cells. *Cell Adhes. Migr.* **11**, 187–195 (2017).

360. Demory Beckler, M. *et al.* Proteomic analysis of exosomes from mutant KRAS colon cancer cells identifies intercellular transfer of mutant KRAS. *Mol. Cell. Proteomics MCP* **12**, 343–355 (2013).

361. Kahlert, C. & Kalluri, R. Exosomes in tumor microenvironment influence cancer progression and metastasis. *J. Mol. Med.* **91**, 431–437 (2013).

362. Sung, B. H., Ketova, T., Hoshino, D., Zijlstra, A. & Weaver, A. M. Directional cell movement through tissues is controlled by exosome secretion. *Nat. Commun.* **6**, 7164 (2015).

363. Fabbri, M. *et al.* MicroRNAs bind to Toll-like receptors to induce prometastatic inflammatory response. *Proc. Natl. Acad. Sci. U. S. A.* **109**, E2110-2116 (2012).

364. Wang, Y., Gong, T., Zhang, Z.-R. & Fu, Y. Matrix Stiffness Differentially Regulates Cellular Uptake Behavior of Nanoparticles in Two Breast Cancer Cell Lines. *ACS Appl. Mater. Interfaces* **9**, 25915–25928 (2017).

365. Stranford, D. M., Hung, M. E., Gargus, E. S., Shah, R. N. & Leonard, J. N. A Systematic Evaluation of Factors Affecting Extracellular Vesicle Uptake by Breast Cancer Cells. *Tissue Eng. Part A* **23**, 1274–1282 (2017).

366. Brugnano, J. L. & Panitch, A. Matrix Stiffness Affects Endocytic Uptake of MK2-Inhibitor Peptides. *PLoS ONE* **9**, (2014).

367. Liu, F. *et al.* Mechanosignaling through YAP and TAZ drives fibroblast activation and fibrosis. *Am. J. Physiol.-Lung Cell. Mol. Physiol.* **308**, L344–L357 (2014).

368. Li, B., Antonyak, M. A., Zhang, J. & Cerione, R. A. RhoA triggers a specific signaling pathway that generates transforming microvesicles in cancer cells. *Oncogene* **31**, 4740–4749 (2012).

369. Hoshino, A. *et al.* Tumour exosome integrins determine organotropic metastasis. *Nature* **527**, 329–335 (2015).

370. Zhang, X. H.-F. *et al.* Selection of Bone Metastasis Seeds by Mesenchymal Signals in the Primary Tumor Stroma. *Cell* **154**, 1060–1073 (2013).

371. Schwager, S. C. *et al. Weakly migratory metastatic breast cancer cells activate fibroblasts via microvesicle-Tg2 to facilitate dissemination and metastasis*. 2021.10.27.466095 https://www.biorxiv.org/content/10.1101/2021.10.27.466095v1 (2021) doi:10.1101/2021.10.27.466095.

372. Clark, A. G. & Vignjevic, D. M. Modes of cancer cell invasion and the role of the microenvironment. *Curr. Opin. Cell Biol.* **36**, 13–22 (2015).

373. De Pascalis, C. & Etienne-Manneville, S. Single and collective cell migration: the mechanics of adhesions. *Mol. Biol. Cell* **28**, 1833–1846 (2017).

374. Kwon, T., Kwon, O.-S., Cha, H.-J. & Sung, B. J. Stochastic and Heterogeneous Cancer Cell Migration: Experiment and Theory. *Sci. Rep.* **9**, 16297 (2019).

375. Summerbell, E. R. *et al.* Epigenetically heterogeneous tumor cells direct collective invasion through filopodia-driven fibronectin micropatterning. *Sci. Adv.* **6**, eaaz6197 (2020).

376. Hallou, A., Jennings, J. & Kabla, A. J. Tumour heterogeneity promotes collective invasion and cancer metastatic dissemination. *R. Soc. Open Sci.* **4**, 161007 (2017).

377. Hapach, L. A. *et al.* Phenotypic Heterogeneity and Metastasis of Breast Cancer Cells. *Cancer Res.* **81**, 3649–3663 (2021).

378. Dai, X., Cheng, H., Bai, Z. & Li, J. Breast Cancer Cell Line Classification and Its Relevance with Breast Tumor Subtyping. *J. Cancer* **8**, 3131–3141 (2017).

379. Wu, Y., Siadaty, M. S., Berens, M. E., Hampton, G. M. & Theodorescu, D. Overlapping gene expression profiles of cell migration and tumor invasion in human bladder cancer identify metallothionein 1E and nicotinamide N-methyltransferase as novel regulators of cell migration. *Oncogene* **27**, 6679–6689 (2008).

380. Patsialou, A. *et al.* Selective gene-expression profiling of migratory tumor cells in vivo predicts clinical outcome in breast cancer patients. *Breast Cancer Res.* **14**, R139 (2012).

381. Walkiewicz, K. *et al.* Expression of Migration-Related Genes in Human Colorectal Cancer and Activity of a Disintegrin and Metalloproteinase 17. *BioMed Res. Int.* **2016**, 8208904 (2016).

382. Zanotelli, M. R. *et al.* Energetic costs regulated by cell mechanics and confinement are predictive of migration path during decision-making. *Nat. Commun.* **10**, 1–12 (2019).

383. Fuchigami, T. *et al.* Fibroblasts promote the collective invasion of ameloblastoma tumor cells in a 3D coculture model. *FEBS Open Bio* **7**, 2000–2007 (2017).

384. Gaggioli, C. *et al.* Fibroblast-led collective invasion of carcinoma cells with differing roles for RhoGTPases in leading and following cells. *Nat. Cell Biol.* **9**, 1392–1400 (2007).

385. Labernadie, A. *et al.* A mechanically active heterotypic E-cadherin/N-cadherin adhesion enables fibroblasts to drive cancer cell invasion. *Nat. Cell Biol.* **19**, 224–237 (2017).

386. Palmer, T. D., Ashby, W. J., Lewis, J. D. & Zijlstra, A. Targeting tumor cell motility to prevent metastasis. *Adv. Drug Deliv. Rev.* **63**, 568–581 (2011).

387. Fares, J., Fares, M. Y., Khachfe, H. H., Salhab, H. A. & Fares, Y. Molecular principles of metastasis: a hallmark of cancer revisited. *Signal Transduct. Target. Ther.* **5**, 1–17 (2020).

388. Liu, Z. *et al.* Cancer cells display increased migration and deformability in pace with metastatic progression. *FASEB J.* **34**, 9307–9315 (2020).

389. Chen, A. *et al.* Reduction in Migratory Phenotype in a Metastasized Breast Cancer Cell Line via Downregulation of S100A4 and GRM3. *Sci. Rep.* **7**, 3459 (2017).

390. Fietz, E. R. *et al.* Glucocorticoid resistance of migration and gene expression in a daughter MDA-MB-231 breast tumour cell line selected for high metastatic potential. *Sci. Rep.* **7**, 43774 (2017).

391. Johnstone, C. N. *et al.* Functional and genomic characterisation of a xenograft model system for the study of metastasis in triple-negative breast cancer. *Dis. Model. Mech.* **11**, dmm032250 (2018).

392. Padmanaban, V. *et al.* E-cadherin is required for metastasis in multiple models of breast cancer. *Nature* **573**, 439–444 (2019).

393. Kubens, B. S. & Zänker, K. S. Differences in the migration capacity of primary human colon carcinoma cells (SW480) and their lymph node metastatic derivatives (SW620). *Cancer Lett.* **131**, 55–64 (1998).

394. Tormoen, G. W., Cianchetti, F. A., Bock, P. E. & McCarty, O. J. T. Development of Coagulation Factor Probes for the Identification of Procoagulant Circulating Tumor Cells. *Front. Oncol.* **2**, 110 (2012).

395. Zanotelli, M. R., Zhang, J. & Reinhart-King, C. A. Mechanoresponsive metabolism in cancer cell migration and metastasis. *Cell Metab.* **33**, 1307–1321 (2021).

396. Zhou, Z. *et al.* VCAM-1 secreted from cancer-associated fibroblasts enhances the growth and invasion of lung cancer cells through AKT and MAPK signaling. *Cancer Lett.* **473**, 62–73 (2020).

397. Miyazaki, K. *et al.* Collective cancer cell invasion in contact with fibroblasts through integrin-α5β1/fibronectin interaction in collagen matrix. *Cancer Sci.* **111**, 4381–4392 (2020).

398. Dumont, N. *et al.* Breast fibroblasts modulate early dissemination, tumorigenesis, and metastasis through alteration of extracellular matrix characteristics. *Neoplasia N. Y. N* **15**, 249–262 (2013).

399. Goetz, J. G. *et al.* Biomechanical remodeling of the microenvironment by stromal caveolin-1 favors tumor invasion and metastasis. *Cell* **146**, 148–163 (2011).

400. Lavallée-Adam, M., Rauniyar, N., McClatchy, D. B. & Yates, J. R. PSEA-Quant: A Protein Set Enrichment Analysis on Label-Free and Label-Based Protein Quantification Data. *J. Proteome Res.* **13**, 5496–5509 (2014).

401. Supek, F., Bošnjak, M., Škunca, N. & Šmuc, T. REVIGO Summarizes and Visualizes Long Lists of Gene Ontology Terms. *PLOS ONE* **6**, e21800 (2011).

402. Piersma, B., Hayward, M.-K. & Weaver, V. M. The fibrotic tumor stroma. *Biochim. Biophys. Acta BBA - Rev. Cancer* 188356 (2020) doi:10.1016/j.bbcan.2020.188356.

403. Fenner, J. *et al.* Macroscopic Stiffness of Breast Tumors Predicts Metastasis. *Sci. Rep.* **4**, 5512 (2014).

404. Liu, T., Zhou, L., Li, D., Andl, T. & Zhang, Y. Cancer-Associated Fibroblasts Build and Secure the Tumor Microenvironment. *Front. Cell Dev. Biol.* **7**, (2019).

405. Öhlund, D. *et al.* Distinct populations of inflammatory fibroblasts and myofibroblasts in pancreatic cancer. *J. Exp. Med.* **214**, 579–596 (2017).

406. Wu, S. Z. *et al.* Stromal cell diversity associated with immune evasion in human triple-negative breast cancer. *EMBO J.* **39**, e104063 (2020).

407. Bartoschek, M. *et al.* Spatially and functionally distinct subclasses of breast cancer-associated fibroblasts revealed by single cell RNA sequencing. *Nat. Commun.* **9**, 5150 (2018).

408. Kieffer, Y. *et al.* Single-Cell Analysis Reveals Fibroblast Clusters Linked to Immunotherapy Resistance in Cancer. *Cancer Discov.* **10**, 1330–1351 (2020).

409. Merlino, G. *et al.* Stromal Activation by Tumor Cells: An in Vitro Study in Breast Cancer. *Microarrays* **5**, 10 (2016).

410. Belhabib, I., Zaghdoudi, S., Lac, C., Bousquet, C. & Jean, C. Extracellular Matrices and Cancer-Associated Fibroblasts: Targets for Cancer Diagnosis and Therapy? *Cancers* **13**, 3466 (2021).

411.   Wu, F. *et al.* Signaling pathways in cancer-associated fibroblasts and targeted therapy for cancer. *Signal Transduct. Target. Ther.* **6**, 1–35 (2021).

412.   Linares, J., Marín-Jiménez, J. A., Badia-Ramentol, J. & Calon, A. Determinants and Functions of CAFs Secretome During Cancer Progression and Therapy. *Front. Cell Dev. Biol.* **8**, (2021).

413.   Shinde, A. *et al.* Transglutaminase-2 facilitates extracellular vesicle-mediated establishment of the metastatic niche. *Oncogenesis* **9**, 1–12 (2020).

414.   Bartha, Á. & Győrffy, B. TNMplot.com: A Web Tool for the Comparison of Gene Expression in Normal, Tumor and Metastatic Tissues. *Int. J. Mol. Sci.* **22**, 2622 (2021).

415.   Győrffy, B. Survival analysis across the entire transcriptome identifies biomarkers with the highest prognostic power in breast cancer. *Comput. Struct. Biotechnol. J.* **19**, 4101–4109 (2021).

416.   Cerami, E. *et al.* The cBio cancer genomics portal: an open platform for exploring multidimensional cancer genomics data. *Cancer Discov.* **2**, 401–404 (2012).

417.   Gao, J. *et al.* Integrative analysis of complex cancer genomics and clinical profiles using the cBioPortal. *Sci. Signal.* **6**, pl1 (2013).

418.   Oh, K. *et al.* Transglutaminase 2 facilitates the distant hematogenous metastasis of breast cancer by modulating interleukin-6 in cancer cells. *Breast Cancer Res. BCR* **13**, R96 (2011).

419.   Steenbeek, S. C. *et al.* Cancer cells copy migratory behavior and exchange signaling networks via extracellular vesicles. *EMBO J.* **37**, e98357 (2018).

420.   Mangala, L. S., Arun, B., Sahin, A. A. & Mehta, K. Tissue transglutaminase-induced alterations in extracellular matrix inhibit tumor invasion. *Mol. Cancer* **4**, 33 (2005).

421.   Loh, C.-Y. *et al.* The E-Cadherin and N-Cadherin Switch in Epithelial-to-Mesenchymal Transition: Signaling, Therapeutic Implications, and Challenges. *Cells* **8**, 1118 (2019).

422.   Zeng, Z. *et al.* Cancer-derived exosomal miR-25-3p promotes pre-metastatic niche formation by inducing vascular permeability and angiogenesis. *Nat. Commun.* **9**, 5395 (2018).

423.   Goulet, C. R. *et al.* Exosomes Induce Fibroblast Differentiation into Cancer-Associated Fibroblasts through TGFβ Signaling. *Mol. Cancer Res.* **16**, 1196–1204 (2018).

424. Ko, S. Y. *et al.* Cancer-derived small extracellular vesicles promote angiogenesis by heparin-bound, bevacizumab-insensitive VEGF, independent of vesicle uptake. *Commun. Biol.* **2**, 1–17 (2019).

425. Yang, S.-S. *et al.* Breast cancer-derived exosomes regulate cell invasion and metastasis in breast cancer via miR-146a to activate cancer associated fibroblasts in tumor microenvironment. *Exp. Cell Res.* 111983 (2020) doi:10.1016/j.yexcr.2020.111983.

426. Fisher, R., Pusztai, L. & Swanton, C. Cancer heterogeneity: implications for targeted therapeutics. *Br. J. Cancer* **108**, 479–485 (2013).

427. Lunt, S. Y. & Vander Heiden, M. G. Aerobic Glycolysis: Meeting the Metabolic Requirements of Cell Proliferation. *Annu. Rev. Cell Dev. Biol.* **27**, 441–464 (2011).

428. Engbring, J. A. & Kleinman, H. K. The basement membrane matrix in malignancy. *J. Pathol.* **200**, 465–470 (2003).

429. Hapach, L. A., Mosier, J. A., Wang, W. & Reinhart-King, C. A. Engineered models to parse apart the metastatic cascade. *Npj Precis. Oncol.* **3**, 1–8 (2019).

430. Lambert, A. W., Pattabiraman, D. R. & Weinberg, R. A. Emerging Biological Principles of Metastasis. *Cell* **168**, 670–691 (2017).

431. Banyard, J. & Bielenberg, D. R. The Role of EMT and MET in Cancer Dissemination. *Connect. Tissue Res.* **56**, 403–413 (2015).

432. Son, H. & Moon, A. Epithelial-mesenchymal Transition and Cell Invasion. *Toxicol. Res.* **26**, 245–252 (2010).

433. Wang, Y., Liu, J., Ying, X., Lin, P. C. & Zhou, B. P. Twist-mediated Epithelial-mesenchymal Transition Promotes Breast Tumor Cell Invasion via Inhibition of Hippo Pathway. *Sci. Rep.* **6**, 24606 (2016).

434. Polireddy, K. *et al.* Targeting Epithelial-Mesenchymal Transition for Identification of Inhibitors for Pancreatic Cancer Cell Invasion and Tumor Spheres Formation. *PLOS ONE* **11**, e0164811 (2016).

435. Funasaka, T., Hogan, V. & Raz, A. Phosphoglucose isomerase/autocrine motility factor mediates epithelial and mesenchymal phenotype conversions in breast cancer. *Cancer Res.* **69**, 5349–5356 (2009).

436. Liu, K. *et al.* Glyceraldehyde-3-phosphate dehydrogenase promotes cancer growth and metastasis through upregulation of SNAIL expression. *Int. J. Oncol.* **50**, 252–262 (2017).

437. Ahmad, A. *et al.* Phosphoglucose isomerase/autocrine motility factor mediates epithelial-mesenchymal transition regulated by miR-200 in breast cancer cells. *Cancer Res.* **71**, 3400–3409 (2011).

438. Kang, H., Kim, H., Lee, S., Youn, H. & Youn, B. Role of Metabolic Reprogramming in Epithelial–Mesenchymal Transition (EMT). *Int. J. Mol. Sci.* **20**, 2042 (2019).

439. Chen, G. *et al.* Deregulation of Hexokinase II Is Associated with Glycolysis, Autophagy, and the Epithelial-Mesenchymal Transition in Tongue Squamous Cell Carcinoma under Hypoxia. *BioMed Res. Int.* **2018**, e8480762 (2018).

440. Sciacovelli, M. & Frezza, C. Metabolic reprogramming and epithelial-to-mesenchymal transition in cancer. *FEBS J.* **284**, 3132–3144 (2017).

441. Sun, N.-Y. & Yang, M.-H. Metabolic Reprogramming and Epithelial-Mesenchymal Plasticity: Opportunities and Challenges for Cancer Therapy. *Front. Oncol.* **10**, 792 (2020).

442. Zhang, J. *et al.* TGF-β1 induces epithelial-to-mesenchymal transition via inhibiting mitochondrial functions in A549 cells. *Free Radic. Res.* **52**, 1432–1444 (2018).

443. Masin, M. *et al.* GLUT3 is induced during epithelial-mesenchymal transition and promotes tumor cell proliferation in non-small cell lung cancer. *Cancer Metab.* **2**, 11 (2014).

444. Han, S.-Y. *et al.* Mitochondrial dysfunction induces the invasive phenotype, and cell migration and invasion, through the induction of AKT and AMPK pathways in lung cancer cells. *Int. J. Mol. Med.* **42**, 1644–1652 (2018).

445. Carey, S. P. *et al.* Comparative mechanisms of cancer cell migration through 3D matrix and physiological microtracks. *Am. J. Physiol. Cell Physiol.* **308**, C436-447 (2015).

446.   Kondo, H. *et al.* Single-cell resolved imaging reveals intra-tumor heterogeneity in glycolysis, transitions between metabolic states, and their regulatory mechanisms. *Cell Rep.* **34**, 108750 (2021).

447.   Thejer, B. M. *et al.* PGRMC1 phosphorylation affects cell shape, motility, glycolysis, mitochondrial form and function, and tumor growth. *BMC Mol. Cell Biol.* **21**, 24 (2020).

448.   Dad, A., Jeong, C. H., Pals, J. A., Wagner, E. D. & Plewa, M. J. Pyruvate Remediation of Cell Stress and Genotoxicity Induced by Haloacetic Acid Drinking Water Disinfection By-Products. *Environ. Mol. Mutagen.* **54**, 629 (2013).

449.   Lam, W. Y. *et al.* Mitochondrial Pyruvate Import Promotes Long-Term Survival of Antibody-Secreting Plasma Cells. *Immunity* **45**, 60–73 (2016).

450.   Shah, A. T., Cannon, T. M., Higginbotham, J. N., Coffey, R. J. & Skala, M. C. Autofluorescence flow sorting of breast cancer cell metabolism. *J. Biophotonics* **10**, 1026–1033 (2017).

451.   Shen, Y. *et al.* Detecting heterogeneity in and between breast cancer cell lines. *Cancer Converg.* **4**, 1 (2020).

452.   Zhang, X., Chan, T. & Mak, M. Morphodynamic signatures of MDA-MB-231 single cells and cell doublets undergoing invasion in confined microenvironments. *Sci. Rep.* **11**, 6529 (2021).

453.   Leggett, S. E. *et al.* Morphological Single Cell Profiling of the Epithelial-Mesenchymal Transition. *Integr. Biol. Quant. Biosci. Nano Macro* **8**, 1133–1144 (2016).

454.   Maier, J., Traenkle, B. & Rothbauer, U. Visualizing Epithelial–Mesenchymal Transition Using the Chromobody Technology. *Cancer Res.* **76**, 5592–5596 (2016).

455.   Ribatti, D., Tamma, R. & Annese, T. Epithelial-Mesenchymal Transition in Cancer: A Historical Overview. *Transl. Oncol.* **13**, 100773 (2020).

456.   Deshmukh, S. & Saini, S. Phenotypic Heterogeneity in Tumor Progression, and Its Possible Role in the Onset of Cancer. *Front. Genet.* **11**, 604528 (2020).

457.   Ramón y Cajal, S. *et al.* Clinical implications of intratumor heterogeneity: challenges and opportunities. *J. Mol. Med. Berl. Ger.* **98**, 161–177 (2020).

458. Bergers, G. & Fendt, S.-M. The metabolism of cancer cells during metastasis. *Nat. Rev. Cancer* **21**, 162–180 (2021).

459. Park, J. S. *et al.* Mechanical regulation of glycolysis via cytoskeleton architecture. *Nature* **578**, 621–626 (2020).

460. Costanza, B. *et al.* Transforming growth factor beta-induced, an extracellular matrix interacting protein, enhances glycolysis and promotes pancreatic cancer cell migration. *Int. J. Cancer* **145**, 1570–1584 (2019).

461. DeCamp, S. J. *et al.* Epithelial layer unjamming shifts energy metabolism toward glycolysis. *Sci. Rep.* **10**, 18302 (2020).

462. Gatenby, R. A. & Gawlinski, E. T. The glycolytic phenotype in carcinogenesis and tumor invasion: insights through mathematical models. *Cancer Res.* **63**, 3847–3854 (2003).

463. Lardner, A. The effects of extracellular pH on immune function. *J. Leukoc. Biol.* **69**, 522–530 (2001).

464. Ponce, I. *et al.* Matrix Stiffness Modulates Metabolic Interaction between Human Stromal and Breast Cancer Cells to Stimulate Epithelial Motility. *Metabolites* **11**, 432 (2021).

465. Sullivan, W. J. *et al.* Extracellular Matrix Remodeling Regulates Glucose Metabolism through TXNIP Destabilization. *Cell* **175**, 117-132.e21 (2018).

466. Park, S. Y., Shin, J. & Kee, S. E-cadherin expression increases cell proliferation by regulating energy metabolism through nuclear factor-κB in AGS cells. *Cancer Sci.* **108**, 1769–1777 (2017).

467. Garde, A. & Sherwood, D. R. Fueling Cell Invasion through Extracellular Matrix. *Trends Cell Biol.* **31**, 445–456 (2021).

468. Sestito, C. *et al.* Differential Expression of Tissue Transglutaminase Splice Variants in Peripheral Blood Mononuclear Cells of Primary Progressive Multiple Sclerosis Patients. *Med. Sci.* **6**, 108 (2018).

469. Avagliano, A. *et al.* Metabolic Reprogramming of Cancer Associated Fibroblasts: The Slavery of Stromal Fibroblasts. *BioMed Res. Int.* **2018**, 6075403 (2018).

470.   Geng, X. *et al.* Cancer-Associated Fibroblast (CAF) Heterogeneity and Targeting Therapy of CAFs in Pancreatic Cancer. *Front. Cell Dev. Biol.* **9**, (2021).

471.   Jia, W., Liang, S., Cheng, B. & Ling, C. The Role of Cancer-Associated Fibroblasts in Hepatocellular Carcinoma and the Value of Traditional Chinese Medicine Treatment. *Front. Oncol.* **11**, (2021).

472.   Liu, T. *et al.* Cancer-associated fibroblasts: an emerging target of anti-cancer immunotherapy. *J. Hematol. Oncol.J Hematol Oncol* **12**, 86 (2019).

473.   Nguyen, A. V. *et al.* Stiffness of pancreatic cancer cells is associated with increased invasive potential. *Integr. Biol. Quant. Biosci. Nano Macro* **8**, 1232–1245 (2016).

474.   Nia, H. T. *et al.* Solid stress and elastic energy as measures of tumour mechanopathology. *Nat. Biomed. Eng.* **1**, 1–11 (2016).

475.   Masuzaki, R. *et al.* Assessing liver tumor stiffness by transient elastography. *Hepatol. Int.* **1**, 394–397 (2007).

476.   Ma, H.-P. *et al.* Collagen 1A1 (COL1A1) Is a Reliable Biomarker and Putative Therapeutic Target for Hepatocellular Carcinogenesis and Metastasis. *Cancers* **11**, 786 (2019).

477.   Kasashima, H. *et al.* An Orthotopic Implantation Mouse Model of Hepatocellular Carcinoma with Underlying Liver Steatosis. *STAR Protoc.* **1**, 100185 (2020).

478.   Shimomura, T. *et al.* New Lipophilic Fluorescent Dyes for Labeling Extracellular Vesicles: Characterization and Monitoring of Cellular Uptake. *Bioconjug. Chem.* **32**, 680–684 (2021).

479.   Takov, K., Yellon, D. M. & Davidson, S. M. Confounding factors in vesicle uptake studies using fluorescent lipophilic membrane dyes. *J. Extracell. Vesicles* **6**, (2017).

480.   Gangadaran, P. *et al.* A new bioluminescent reporter system to study the biodistribution of systematically injected tumor-derived bioluminescent extracellular vesicles in mice. *Oncotarget* **8**, 109894–109914 (2017).

481.   Lai, C. P. *et al.* Visualization and tracking of tumour extracellular vesicle delivery and RNA translation using multiplexed reporters. *Nat. Commun.* **6**, 7029 (2015).

482. LeClaire, M., Gimzewski, J. & Sharma, S. A review of the biomechanical properties of single extracellular vesicles. *Nano Sel.* **2**, 1–15 (2021).

483. Huang, J. *et al.* Extracellular matrix and its therapeutic potential for cancer treatment. *Signal Transduct. Target. Ther.* **6**, 1–24 (2021).

484. Marofi, F. *et al.* CAR T cells in solid tumors: challenges and opportunities. *Stem Cell Res. Ther.* **12**, 81 (2021).

485. Catalano, M. & O'Driscoll, L. Inhibiting extracellular vesicles formation and release: a review of EV inhibitors. *J. Extracell. Vesicles* **9**, 1703244 (2020).

486. Taylor, D. D. & Gercel-Taylor, C. Exosomes/microvesicles: mediators of cancer-associated immunosuppressive microenvironments. *Semin. Immunopathol.* **33**, 441–454 (2011).

487. Liu, J. *et al.* Immune suppressed tumor microenvironment by exosomes derived from gastric cancer cells via modulating immune functions. *Sci. Rep.* **10**, 14749 (2020).

488. Khorana, A. A. *et al.* Time to initial cancer treatment in the United States and association with survival over time: An observational study. *PloS One* **14**, e0213209 (2019).

489. Balestrini, J. L., Chaudhry, S., Sarrazy, V., Koehler, A. & Hinz, B. The mechanical memory of lung myofibroblasts. *Integr. Biol. Quant. Biosci. Nano Macro* **4**, 410–421 (2012).

490. D'Souza-Schorey, C. & Clancy, J. W. Tumor-derived microvesicles: shedding light on novel microenvironment modulators and prospective cancer biomarkers. *Genes Dev.* **26**, 1287–1299 (2012).

491. Delaine-Smith, R. *et al.* Transglutaminase-2 Mediates the Biomechanical Properties of the Colorectal Cancer Tissue Microenvironment that Contribute to Disease Progression. *Cancers* **11**, 701 (2019).

492. Lee, J. *et al.* Tissue Transglutaminase Mediated Tumor–Stroma Interaction Promotes Pancreatic Cancer Progression. *Clin. Cancer Res.* **21**, 4482–4493 (2015).

493. HE, W., SUN, Z. & LIU, Z. Silencing of TGM2 reverses epithelial to mesenchymal transition and modulates the chemosensitivity of breast cancer to docetaxel. *Exp. Ther. Med.* **10**, 1413–1418 (2015).

494. Kumar, A. *et al.* Tissue Transglutaminase Promotes Drug Resistance and Invasion by Inducing Mesenchymal Transition in Mammary Epithelial Cells. *PLOS ONE* **5**, e13390 (2010).

495. Meng, X., Pan, J., Sun, S. & Gong, Z. Circulating exosomes and their cargos in blood as novel biomarkers for cancer. *Transl. Cancer Res.* **7**, (2018).

496. Ji, Q. *et al.* Primary tumors release ITGBL1-rich extracellular vesicles to promote distal metastatic tumor growth through fibroblast-niche formation. *Nat. Commun.* **11**, 1–18 (2020).

497. Zaborowski, M. P. *et al.* Membrane-bound Gaussia luciferase as a tool to track shedding of membrane proteins from the surface of extracellular vesicles. *Sci. Rep.* **9**, 17387 (2019).

498. Guha, M. *et al.* Mitochondrial retrograde signaling induces epithelial–mesenchymal transition and generates breast cancer stem cells. *Oncogene* **33**, 5238–5250 (2014).

499. Hwang, S. *et al.* Mitochondrial glutamine metabolism regulates sensitivity of cancer cells after chemotherapy via amphiregulin. *Cell Death Discov.* **7**, 1–11 (2021).

500. Yang, L. *et al.* Metabolic shifts toward glutamine regulate tumor growth, invasion and bioenergetics in ovarian cancer. *Mol. Syst. Biol.* **10**, (2014).

501. Kim, B., Li, J., Jang, C. & Arany, Z. Glutamine fuels proliferation but not migration of endothelial cells. *EMBO J.* **36**, 2321–2333 (2017).

502. Lukey, M. J., Wilson, K. F. & Cerione, R. A. Therapeutic strategies impacting cancer cell glutamine metabolism. *Future Med. Chem.* **5**, 1685–1700 (2013).

503. Kuo, T.-C. *et al.* Glutaminase 2 stabilizes Dicer to repress Snail and metastasis in hepatocellular carcinoma cells. *Cancer Lett.* **383**, 282–294 (2016).

504. Kumar, S. & Mehta, K. Tissue transglutaminase constitutively activates HIF-1α promoter and nuclear factor-κB via a non-canonical pathway. *PloS One* **7**, e49321 (2012).